Light Propagation in Paint and Prostate Human Tissues Using Visible to Mid-IR Spectroscopy and Imaging Techniques

by

Jamal Hafiez Ali

A dissertation submitted to the Graduate Faculty in Physics in partial fulfillment of the requirements for the degree of Doctor in Philosophy, The City University of New York.

2004

INFORMATION TO USERS

The quality of this reproduction is dependent upon the quality of the copy submitted. Broken or indistinct print, colored or poor quality illustrations and photographs, print bleed-through, substandard margins, and improper alignment can adversely affect reproduction.

In the unlikely event that the author did not send a complete manuscript and there are missing pages, these will be noted. Also, if unauthorized copyright material had to be removed, a note will indicate the deletion.

ProQuest Information and Learning Company
300 North Zeeb Road
P.O. Box 1346
Ann Arbor, MI 48106-1346

This manuscript has been read and accepted for the Graduate
Faculty in Physics in satisfaction of the dissertation requirement

9/21/04 Robert R Alfano

Date **Chair of Examining Committee**

Date **Chair of Examining Committee**

9/22/04 Sultan Cattu

Date **Executive Officer**

Dr. Wubao Wang _____

Prof. Joel Gersten _____

Prof.Ping-Pei Ho _____

Dr. Francesco Pellegrino _____

Dr. Jason Koutcher

Supervisory Committee

THE CITY UNIVERSITY OF NEW YORK

Abstract

Light Propagation in Paint and Prostate Human Tissues Using Visible to Mid-IR Spectroscopy and Imaging Techniques

by

Jamal Hafiez Ali

Advisor: Prof R. R. Alfano

The topic of the thesis is to understand the structural and molecular changes in scattering media for bio-medical applications such as animal, and human prostate tissues and non-biomedical applications such as corrosion and cracks beneath paint using steady and time-resolved light spectroscopy and imaging techniques in the visible to mid-IR spectral region. The thesis focuses also on understanding the randomization of coherence and polarization in thin scattering paint medium.

Temporal polarization emission profiles of Fluorescein dye attached to different molecular weight ranging from 4 K to 500 K were measured. Images of an object containing varying molecular weight of Fluorescein dye embedded inside intralipid media were investigated.

The non-invasive spectral polarization difference imaging and the fluorescence polarization difference imaging techniques using Cardio Green dye are introduced in the optical imaging studies to enhance the image quality.

The measured transport length for prostate tissues using time-resolved pulse transmission is ℓ_{tr} = 0.86 mm. Four modeling samples of human rectum-membrane-prostate tissue were investigated using the near-infrared spectral polarization imaging technique to detect small foreign objects at different depths inside prostate tissues.

The content of water in cancerous and normal human prostate tissues was shown to be different using near infrared spectroscopy and imaging techniques. The OH stretching vibrational overtone mode at 980 nm, 1195 nm, 1444 nm and other water overtone modes provide key spectroscopic fingerprints to detect non-invasively cancer in prostate tissue.

The value of the transport length (ℓ_{tr}) for paint medium obtained from time-resolved pulse transmission, steady state, and degree of polarization measurements is 28 μm, 34 μm, and 29 μm, respectively. The correlation of time-resolved interference (coherence) and polarization in a scattering thin paint medium has been determined for the first time for the ballistic, snake, and diffusive regions in terms of the mean transport length. The measured linear depolarization length in paint is not in agreement with the current theoretical understanding in scattering media.

The visible to mid-infrared transmission window of paint between 0.5 - 5.5 μm has been used for the first time to detect corrosion beneath commercial and military paint using spectral polarization imaging and confocal scanning imaging techniques.

Acknowledgments

I would like to thank my thesis supervisor Prof. R. R. Alfano, Distinguished Professor of Science and Engineering, for his excellent supervision, continuous guidance, and support throughout the work of my thesis. I'm extremely grateful to my co-thesis advisor, Dr. W. Wang, for his advice, discussions, and teaching me many experimental techniques in the thesis work. I deeply appreciate my advisors patience on my acquiring the needed skills to do my thesis work.

Many thanks to Prof. Joel Gersten, Prof. Ping-Pei Ho, Dr. Jason Koutcher, and Dr. Francesco Pellegrino for serving on my thesis committee and reviewing the manuscript. It is with deep sadness that we have lost wonderful colleagues: Prof. Melvin Lax and Prof. L. Mitchell, who were my thesis committee in my second exam.

To my colleagues at the Institute of Ultrafast Spectroscopy and Lasers (IUSL) and the physics department, thank you for the help and advice. Special thanks go to Dr. W. Cai and Dr. Min Xu for the fruitful discussion and help in the theoretical physics of light scattering in highly scattering media.

This work was possible with the financial support and help from the IUSL, Physics Department at the City College of New York, New York STAR, U. S. Army Medical Research and Materiel Command, Lockheed Martin, and Hackensack University Medical Center (HUMC).

My acknowledgment is extended to my best friends: Janice Allen, Rola Moulhem, Mazin Yousef, Yara Abu-Ammouneh, Reema Dauod, Mirna Khori, Emad El-Khateeb, Noor El-Deen Malkawi, Snezana Bogdanovich, Kevin Mertes and Francesca Ruta for their help and support in many aspects of my life. I want to thank deeply Ms. Allida Gupton at the City University of New York, Ms. Megan Gibbs, Ms. Joan Brijlall, and Ms. Lauren Gohara at IUSL for their help and support during my thesis work.

Last but not least, I would like to thank my lovely parents (Hafiz Bashtawi and Feryal Bakar), brothers (Ra2d, Ghassan, Abdallah, Mohamad), sisters (Seham, Abeer, Sana2, Hana2, Tagreed, Ameera, and 7aneen) for their constant support, encouragement, and endless love throughout my studies.

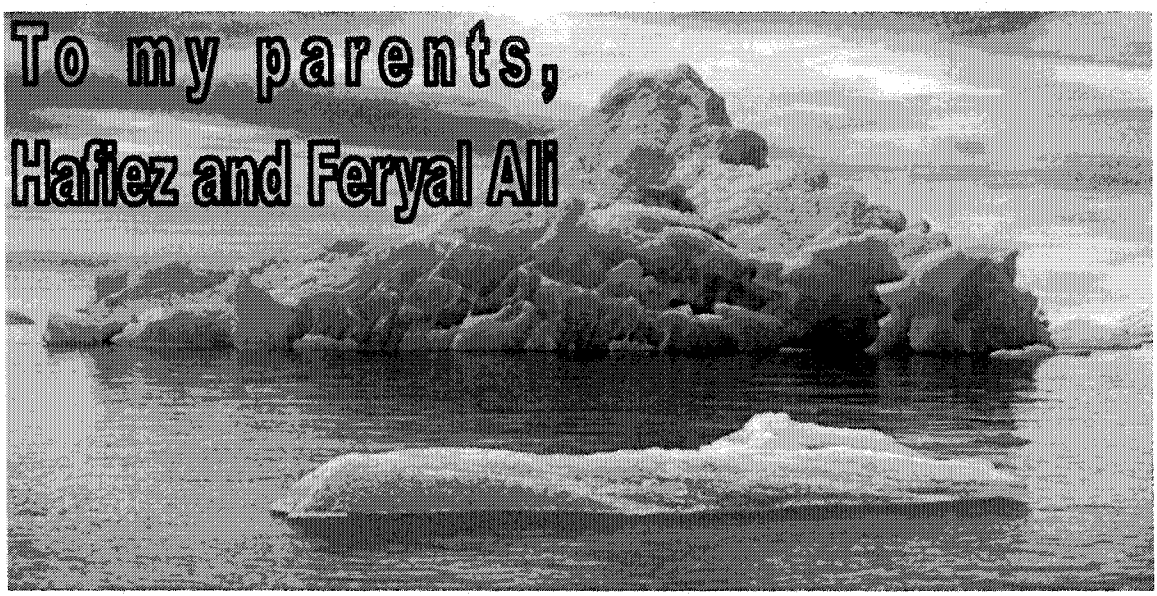

Table of Contents

List of Figures

Chapter 2

Chapter 3

Chapter 4

Chapter 5

Chapter 6

Chapter 7

Chapter 8

List of Tables

Chapter 5

Chapter 6

Chapter 7

Chapter 1

Introduction

1.1 Background

Optics plays a major role in today's medical, communications, and military fields [1-8]. The study of light transport in random scattering media provides non-invasive way to obtain information about the optical properties of materials. A random medium is a system where the dielectric constant ε depends on the position (r) and time (t). Light propagating through such a medium is scattered by the fluctuations in $\varepsilon(r,t)$, where $\varepsilon = \varepsilon' + i\varepsilon''$ (related to index of refraction n by $\varepsilon=(n+ik)^2$). ε'' represents absorption when it is positive value or amplification when it is negative value. Paint and tissues are highly scattered media with chromophors in a host. Tissues are composed of many cells connected by extracellular matrix. In different organs the cells vary in size and shape. The cell is mainly composed of the nucleus, mitochondria, golgi and other small particles dispersed in the cytoplasm of the cell. The typical cell size is about $12\,\mu m$. The nucleus size is about $3\,\mu m$ and the mitochondria size is between 0.4 and $1\,\mu m$ [9]. Paint is mainly composed of binder and pigments mixed in a solvent. The Pigments in the paint play a major role in light scattering and the degree of color. The pigment particles vary in size depends on the paint product. Pigments vary between 0.2 and $10\,\mu m$ and in some cases they may form clusters of much larger size.

Light scattering is sensitive to the structure and the chemical composition of the media. Structural and molecular changes occur in space causing the index of refraction

and absorption changes. Degree of light scattering is very sensitive to the size of the particle relative to the wavelength of the light and the shape of the scatterer. The scattering of light from particles much smaller than the wavelength of light is called Rayleigh scattering. Rayleigh scattering has very strong wavelength (λ) dependence, proportional to λ^{-4}, the shorter the wavelength the stronger the scattering. It also has a marked dependence on the polarization of the light, where scattering along a line perpendicular to the incident light is linearly polarized normal to the plane containing the incident and scattered light. In other directions the light will appear partially polarized. Mie scattering is responsible for particles that are larger than the wavelength of incident light. The wavelength dependence in Mie scattering (proportional to λ^{-2}) is much weaker than that seen in Rayleigh scattering. Mie scattering tends to depolarize the polarized light.

The propagation of light in optically dense random scattering media is characterized by multiple scattering, which randomizes the direction, phase, and polarization of the incident wave. A fundamental understanding of light scattering in biological tissues (such as prostate tissues) and paint is crucial to develop new techniques to detect hidden objects in highly scattering media, such as tumors in prostate and corrosion beneath a paint layer.

When light enters scattering media, the light can be absorbed, transmitted, and scattered. These interactions are wavelength dependent. The light emerging from the scattering medium consists of three components – the ballistic, the snake and the diffusive photons [10]. These components differ in their paths through the medium, and consequently in their imaging properties. The transmitted (unscattered) photons travel

undeviated and emerge first. These preserve the characteristics of the incident light, namely direction of propagation, and polarization, and are hence best for imaging. The diffusive photons emerge later than the ballistic photons because of their increased path lengths. Their polarization, direction of propagation and phase are completely randomized. Snake photons are those that travel in near-forward paths, consequently, they retain the image bearing characteristics to some extent. A basic understanding of the underlying physics of these optical interactions, photon scattering and absorption leads to a natural description of light propagation in biological and non biological turbid media.

Steady state and time-resolved optical techniques [10-15] will be used to determine the absorption and luminescence of materials. Time-resolved spectroscopy provides information on the excited state of a material. It can be used to determine luminescence lifetimes, molecular motion, possible decay mechanisms, and energy transfer processes, which are not available from steady state measurements. Photo-physics of contrast agents [16-18] such as Indocyanine Green (Cardio Green) and Fluorescien in highly scattering host media in human tissues is used to enhance the imaging quality in terms of contrast and resolution of luminous objects hidden deep inside the tissues. The measurement of the fluorescence depolarization will provide information about the rotational motion and the orientation of the macromolecules. It is important to investigate the degree of scattering, fluorescence polarization, and coherence memory in steady and time-resolved measurements for the dyes to be used in human tissues. A reasonable approach to obtain the larger parallel (II) and perpendicular ($\perp$) polarization intensity difference, $I_{\parallel}$-$I_{\perp}$, is increasing the molecular weight (MW) of the emission molecules by attaching polymers to the dye, because for heavy MW dye-

polymer conjugates, nonradiative rotational motion is expected to be inhibited given rise to a longer polarization decay time of the dye emission, and therefore, a larger difference of $I_{\parallel}$-$I_{\perp}$. As a result, imaging can be enhanced by attachment of specific molecular weight (MW) to the dye. Understanding the underlying physics of the MW attachment and their use in optical tissue imaging is important and crucial to the medical imaging applications.

On the non-medical use side, detection of corrosion and cracks beneath a paint layer on a metallic and other materials surface is important in determining structural failures. It uses the same principles of approach as in medical applications. Surfaces on aging aircraft, bridges, cars, or boats are subject to corrosion. Photonic techniques [19-20] offer a potentially rapid, noninvasive and easy approach to detect corrosion in situ. At the present time, there is no optical method for early detection of corrosion under paint. Understanding of the underlying physics of light scattering in paint will be important obtaining better results in corrosion imaging beneath a thick layer of paint. Infrared spectroscopy is very useful for the identification of organic components in paint. The penetration depth in mid-IR is normally high due to the low scattering power and low absorption of most paints in this region. Confocal detection methods [21-25] are based on the property that weakly scattered light emerges from the scattering medium at positions and angles close to the optical axis. The basic optical components of the confocal microscope are similar to a conventional light microscope except that a laser is the source of light and a small pinhole is used to focus the light at a single point in the specimen.

The degree of scattering depends on the depth of imaging and the type of material (such as prostate tissues or paint). It is interesting to correlate the number of the scattering events (at a certain wavelength) as a function of depth or sample thicknesses. In highly

scattering media, such as paint and tissue, the ability to image relies on the ability of the system to reject photons that are multiply scattered. Comparison between different imaging techniques, such as spectral polarization imaging and confocal scanning imaging as they relate to scattering events, or transport lengths is important.

Understanding the propagation of light at short time and length scales has become a key issue for the rapid development of micro and nano-technologies. The study of dynamic wave transport through thin scattering media of few orders of transport mean free path (ℓ_t) is a very interesting problem [5, 26]. The propagation can be described by the diffusion equation in which the rate of propagation is characterized by the diffusion constant $D = \upsilon_E \ell_t / 3$ where υ_E is the energy velocity. The visibility or coherence of incoherent source is described by the Van Cittert-Zernike theorem, which implies the existence of spatial coherence region from a completely incoherent source. Multiple scattering of light from particles in highly scattering media randomizes the direction of propagation and the state of polarization. The validity of the diffusion equation for thin scattering media will be investigated for short and long time scales. We will present the experimental and the theoretical fit of the pulse transition from the ballistic to the diffusive regime in the dynamic light transmission through different thicknesses of paint slabs. Recently, a correlation between the degree of polarization and the degree of coherence has been theoretically predicted [27]. Experimentally this correlation has not yet been explored in scattering media. It is interesting to investigate the transition from the ballistic-snake-diffusion in the time domain and the relation between the loss of visibility (coherence) and depolarization through the paint media. This thesis sheds light on some of these issues.

1.2 Thesis Statement

This thesis focuses on studying of the structural and molecular changes in bio-medical applications such as animal, normal and cancer human prostate tissues and non-biomedical applications such as cracks and corrosion beneath paint. The visible to mid-IR spectral regions are investigated using steady and time-resolved light absorption, fluorescence and scattering measurements techniques. The thesis focuses also on understanding the randomization of coherence and polarization from ballistic to snake to diffusive region for thin scattering paint media using double slit time-resolved measurements techniques. The correlation between coherence (visibility) and depolarization in paint media will be investigated for the first time. The coherence and polarization lengths in terms of the transport scattering length for highly scattering paint media will be investigated.

The following major objectives will be focused on in this thesis:

1. Optical properties of human prostate tissues, paint, and Cardio Green and Fluorescein dyes from visible to mid-IR were investigated.
2. Fluorescein dye attached to different molecular weight chains and their impact on imaging using time-resolved fluorescence polarization dynamics was investigated.
3. Novel methods such as spectral fluorescence difference and spectral polarization difference imaging were used to enhance the visibility of hidden objects or to detect normal and cancer human prostate tissues.
4. Dyes such as Cardio Green and Fluorescein were used in detecting foreign objects in prostate human tissues.

5. Near infrared transmission and backscattered imaging were used to detect water (H_2O bonding) content in normal and cancer human prostate tissues at different stages of cancer.
6. The randomization of coherence and polarization in paint from ballistic-snake-diffusive region were investigated using steady and time resolved measurements.
7. Detection of corrosion and cracks hidden beneath the top coat and primer paint layers using visible to Mid-IR (0.5 - 5.5 μm) spectral polarization imaging and confocal scanning imaging techniques.

The common connection among these objectives is to investigate light propagation in biomedical (animals and normal-cancer human prostate tissues) and non-biomedical (corrosion beneath paint) scattering media using visible to Mid-IR spectroscopy and imaging techniques to obtain a better understanding of underlying on going physics.

This thesis is concerned with two problems, which at first sight appear quite different. The first problem involves prostate cancer detection and is obviously related to medicine and biology. The second problem involves the detection of corrosion beneath paint, which is a materials science phenomenon. However, both topics bear some similarities. These include the fact that they both are scattering media involving similar microstructures. Most importantly, we may learn about both using similar diagnostic techniques. In this thesis we show that optical spectroscopy and imaging are tools ideally suited for the study of these diverse random scattering phenomena.

1.3 Thesis Organization

This section presents an overall summary of chapters in the thesis. Chapter 2 describes the theoretical background of the research work. The theoretical description will cover absorption, single and multiple scattering, polarization, scanning techniques, and the general theory of the steady and time-resolved measurements.

Chapter 3 presents the experimental work of the time-resolved light scattering in animal and human tissues. Fluorescence depolarization of Cardio Green dye using Nd-YAG ultrashort laser pulses will be investigated. The optical properties of human prostate tissue using Ti:Sapphire femtosecond laser pulses will be measured. Time-resolved fluorescence polarization dynamics and imaging of Fluorescein dye attached to different molecular weight chains will be investigated for the first time.

Chapter 4 represents the experimental work of steady state imaging through animal and human prostate tissues. The visibility enhancement of fluorescent objects hidden in animal tissues using the spectral fluorescence difference method will be explained. Fluorescence imaging measurements of foreign objects embedded in human prostate tissues using Cardio Green dye will be investigated. The spectral polarization imaging of human rectum-membrane prostate tissues will be studied. Near Infrared transmission and backscattered imaging to detect water content in tissues for the first time as a new fingerprint marker in normal and cancer human prostate tissues will be investigated.

Chapter 5 describes the time-resolved photon scattering measurements in highly scattering paint medium. The optical properties of paint will be obtained using steady state transmission measurements, polarization measurements, and time-resolved

measurements techniques. The randomization and correlation of coherence and polarization from ballistic to diffusive in paint using steady-state and time-resolved measurements will be investigated for the first time.

Chapter 6 describes imaging through paint to detect cracks and corrosion using spectral polarization and confocal scanning imaging techniques from visible to mid-IR for the first time. The detection of corrosion and micro-cracks hidden beneath top coat and primer paint layers using visible to mid-IR spectral polarization imaging techniques will be investigated. This chapter also describes imaging of corrosion beneath paint using confocal scanning imaging techniques.

In chapter 7, I summarize my work and present the future direction to continue the research.

1.4 References

1. A. Ishimaru, Wave propagation and scattering in random media, **Vol. 1** and **2**, Academic Press, NY, 1978.

2. P. Sheng, Introduction to wave scattering, localization, and mesoscopic phenomena, Academic Press, NY, 1995.

3. K. M. Yoo, Feng Liu, and R. R. Alfano, Phy. Rev. Lett. **64**, 2647, 1990.

4. B. B. Das, Feng Liu and R. R. Alfano, Rep. Prog. Phys. **60**, 227, 1997.

5. Rik H. J. Kop, Pedro de Vries, Rudolf Sprik, and Ad Lagendijk , Phys. Rev. Lett **79**, 4369, 1997

6. W. Rudolph; M. Kempe , J. Mod. Opt. **44**, 1617, 1997.

7. Luther E. Preuss, A. Edward Profio, Appl. Opt. **28**, 2207, 1989.

8. R. R. Alfano, D. Tata, J. Cordero, P. Tomashefsky, F. Longo, and M. Alfano, IEEE J. Quantum Electron, Vol. 20, 1507, 1984.

9. E. Solomon and P. Davis, Human anatomy and physiology, CBS college publishing, 1983.

10. L. Wang, P. P. Ho, C. Liu, G. Zhang, R. R. Alfano, Science 253, 769, 1991.

11. N. Ometto, Ed. , Analytical Laser Spectroscopy, NY Wiley, 1979.

12. R. R. Alfano and L. L. Shapiro, Physics Today, **28**, 7, 1975.

13. R. R. Alfano and S. S. Yao, J. Dent. Res. **60**, 120, 1981.

14. K. M. Yoo and R. R. Alfano, Opt. Lett. 15, 320, 1990.

15. B. B. Das, Feng Liu and R. R. Alfano, Rep. Prog. Phys. **60**, 235, 1997.

16. F. J. Green, The Sigma-Aldrich Handbook of Stains Dyes and Indicators, Sigma-Aldrich Corporation, 1991.

17. P. S. Anderson, S. Montan, S. Svanberg, IEEE J. Q. E. **23**, 1798, 1987.

18. K. M. Yoo, Zhi-Wei Zang, S. A. Ahmed, R. R. Alfano, Opt. Lett. **16**, 1252, 1991.

19. Xu, F., Pudavar, H.E.,Prasad, P.N., and Dickensheets, D., Opt. Lett., **24**, 1808, 1999.

20. Ying, J., Liu, F., Ho, P.P., and Alfano, R. R., Opt. Lett., **25**, 1189, 2000.

21. Michael R. Hee, Joseph A. Izatt, Joseph M. Jacobson, James G. Fujimoto, and Eric A. Swanson, Opt. Lett. **18**, 950, 1993.

22. Faming Xu, Haridas E. Pudavar, Paras N. Prasad, and David Dickensheets, Opt. Lett. **24**, 1808, 1999.

23. M. Kempe, W. Rudolph, and E. Welsch , J. Opt. Soc. Am. A **13**, 46, 1996.

24. T. Wilson and C. J. R. Sheppard, Theory and practice of scanning optical microscopy, Academic, London, 1984.

25. T. Wilson, ed., Confocal Microscopy, Academic, London, 1991.

26. J. M. Drake and A. Z. Genack, Phys. Rev. Lett. **63**, 259, 1989.

27. Emil Wolf, Opt. Lett. **28**, 1078, 2003.

Chapter 2

Background

2.1 Introduction

When light propagates through tissue or paint, a number of processes occur. The light can be absorbed, transmitted and scattered. Changes in polarization, coherence and reflection can be attributed to scattering processes. These interactions processes are wavelength dependent. A basic understanding of photon scattering and absorption leads to a clear description of light propagation in biological and non biological materials. This chapter briefly describes the physics involved in light interaction with scattering media. The propagation of CW and short pulses in scattering and absorption media is analyzed and discussed. Multiple scattering and absorption are responsible for laser broadening and intensity decay as it travels through scattering media such as tissues and paint. Polarization phenomena in scattering tissues and paint media are described.

This chapter discusses the background to the experimental work using CW and pulse light sources, signal detection spectroscopy, and imaging techniques.

2.2 What is Paint and Tissue?

Paint is a mixture of a pigment and a vehicle (a mix of solvent and solid binder) such as oil, that together form a liquid as shown in Fig. 2.1. In some cases liquid is oil, in others it evaporates and leaves the pigment exposed as in watercolor. The structure of the paint is mainly composed of solvent, binder, and pigment. These are the major structures that cause light scattering and absorption in the paint medium. But as we mentioned

earlier different types of paint have different geometric and molecular structures. In paint coating, the primary role of pigments is to provide the optical properties of hiding and color. In practice, it is the difference in

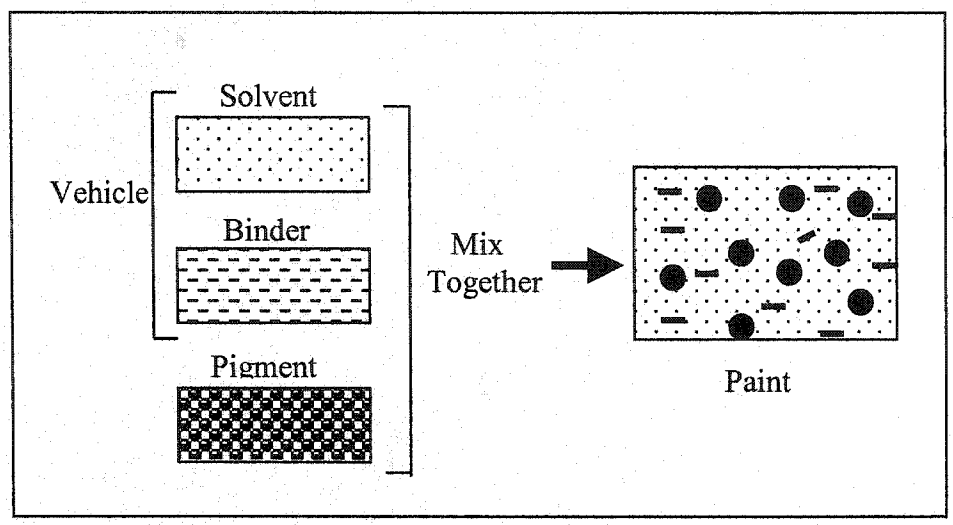

Fig. 2.1 Paint is composed of a pigment, solvent and solid binder.

refractive index between the pigments and the surrounding medium (binder) that decide the opacity. The greater the difference the more the light will be scattered or bent and the higher the opacity. Pigments impact hiding by virtue of their light absorption and scattering abilities. The color comes from particles called pigments suspended in a fluid medium, which is sufficiently viscous to keep the pigments in suspension. Light passes through the dried linseed oil and strikes the pigments particles as shown in Fig. 2.2. A portion of the light is reflected/scattered while the rest is transmitted to the next particle. Pigments absorb selectively in certain regions of the spectrum when light passes through them. The reflection from the surface of these pigment particles influence the color of the media. Reflection (R) is very sensitive to the difference between the refractive index of pigment (n_1) and its surrounding medium (n_2), i.e. $R = \frac{(n_1 - n_2)^2}{(n_1 + n_2)^2}$ at normal incidence. If

there is a small difference between indices the paint will be transparent unless the pigment itself is sufficiently absorbing to attenuate light before it penetrates to the underlying surface and back. The larger the number of pigment particles within a given thickness or travel distance the more reflection will occur giving a more solid paint layer.

The solvent particles are very small and they have a diameter size of less than 0.1 μm, while the pigments vary in size between 1 and 20 μm. The pigment particles are the main cause for Mie scattering in the NIR and mid-IR range. The oil solvent is the main cause for absorption.

Tissue is a complex structure composed of many different substances. A tissue is a group of cells that perform a specific function and the basic types of tissues in the human body include epithelial, muscle, nervous, and connective tissues. The four primary tissue

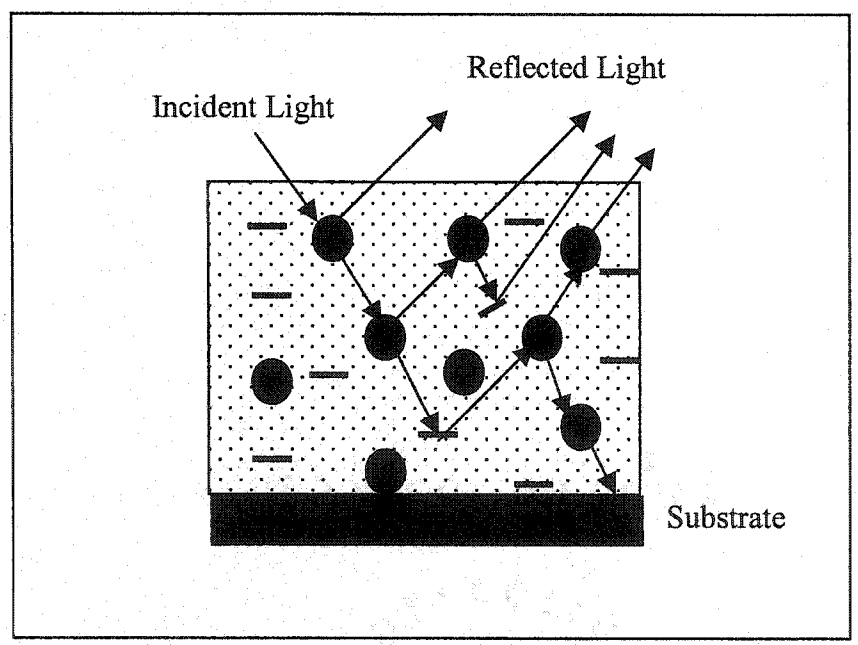

Fig. 2.2 Light propagation through a paint layer.

types and their basic function are: epithelial (covering of all body surfaces), connective (support and bind structures together), muscle (ability to shorten or contract in order to produce movement of the body parts), and nervous (coordinating and controlling many body activities and plays a major role in emotions, memory, and reasoning). The index of refraction of each component is determined by the biochemical making of the tissue and will influence the amplitude of the scattered light. There are two primary types of cells: prokaryotic cells and eukaryotic cells. Only bacteria and cyanobacteria are prokaryotes. Animals, plants, fungi and protists are eukaryotes.

Fig. 2.3 shows a typical human or eukaryotic cell with mean diameter approximately 12 μm [1]. Prokaryotic cells are about 10 times smaller in diameter than eukaryotic cells. Prokaryotic cells do not have a nucleus whereas eukaryotic cells do. The cell consists of a plasma cell membrane, cytoplasm, golgi, mitochondria, lysosome,

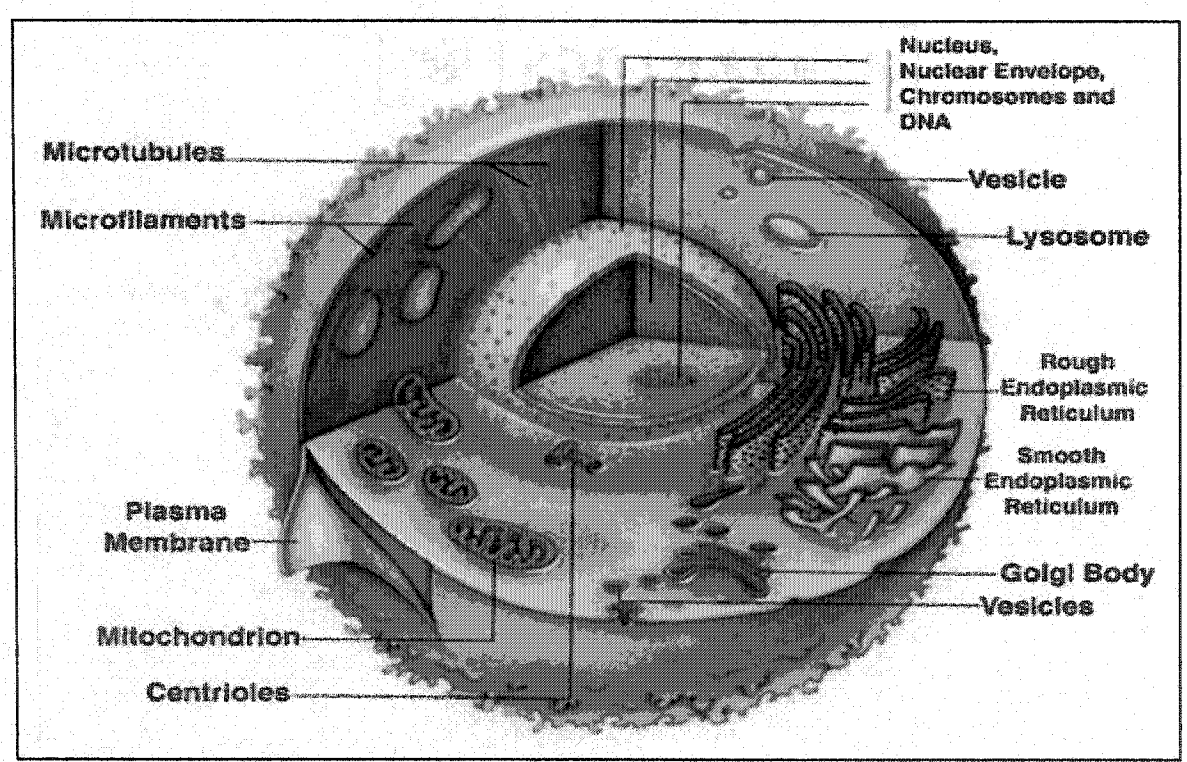

Fig. 2.3: A schematic view of a typical human cell [1].

ribsome, nucleus and other components. The nucleus is composed mainly of chromatin and nucleolus. The diameter of the nucleus is ~ 5 μm, while the size of mitochondria is between 0.4 and 1 μm. The different cells make up the human body tissues.

The major constituents of the tissue are water, fat, hemoglobin, melanin, collagen, elastin, flavins, NADH, tryptophan, tyrosine, etc. The main contributors in the ultraviolet (UV) and visible spectral properties are collagen, elastin, flavins, NADH, and tryptophan. The main constituents of the biological tissue that contribute towards absorption in the near infrared (NIR) are water, fat, solutions between cells as sugar, melanin, hemoglobin. However, melanin and hemoglobin can be ignored in the NIR, but not in the visible regime as melanin contributes a little to the overall attenuation and hemoglobin is the main contributor. Water and fat have an absorption peak at around 940 nm, but water is a significant contributor to the overall attenuation as its concentration is very high in biological tissue. The skin is the largest organ that covers the body. The skin is composed of three layers as shown in Fig. 2.4 [2]: 1) The epidermis—stratified squamous epithelium, 2) The dermis—supportive connective tissue matrix, and 3) The hypodermis layer—loose connective tissue and fat. The epidermis is a very thin layer responsible for the production of melanin and skin color. Its thickness varies from 1.6 mm on the soles of the feet to 0.04 mm on the eyelids. The second skin layer, or dermis, lies below the epidermis and is connected to it by the basement membrane. Normally, the dermis is approximately five to seven times thicker than the epidermis. It is made of connective tissues, collagen, and elastin, and contains most of the nerve endings, blood vessels, and immune and lymphatic systems of the skin. The third skin layer, the hypodermis or

subcutaneous, is the deepest of the three layers. Comprised primarily of connective and fatty tissues, the hypodermis is much thicker than the epidermis.

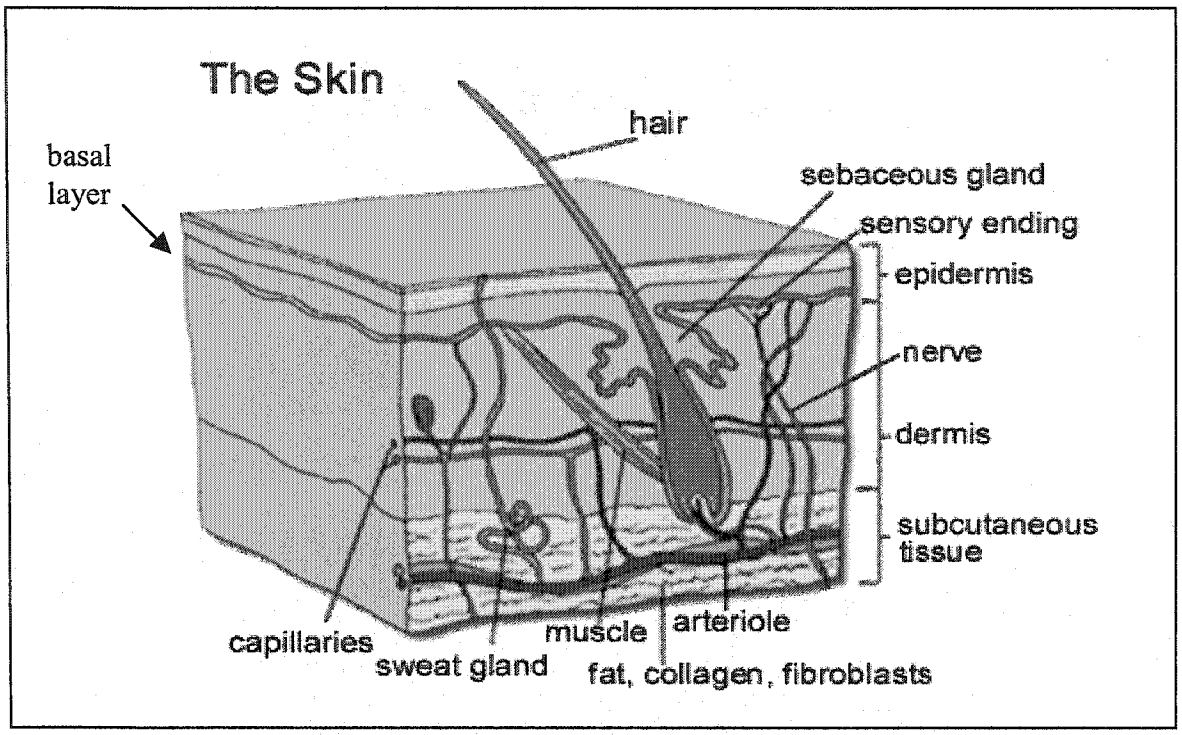

Fig. 2.4: A schematic view shows a typical skin layer [2].

Measurements of light transport through tissue are sensitive to the morphology (structural) and molecular changes in the tissue. Pathologists are often using these structural features for disease diagnoses. Noninvasive optical techniques could have several advantages over conventional pathology methods. Important questions such as the following need to be addressed: what structures scatter light? How sensitive is light scattering to changes in structural features? Can we correlate the structural and molecular changes to the measurements of light scattering?

Scattering and absorption are the main mechanism in light-tissue interaction. When light is scatter in tissue, it does penetrate the surface of the skin. Long wavelength

light penetrates deep into the tissue, while short wavelengths light get scattered. Between 400 nm and 1100 nm non-pigmented tissues have scattering dominating over absorption. Under these circumstances the transport equation can be approximated by a diffusion model. In the strong absorption case the fluence rate in tissue can be written as:

$$I(z,r) = I_0(r)(1 - R)e^{-\mu z}, \qquad (2.1)$$

where I is the intensity in the tissue at coordinates z, r and R ($R(0) = \frac{(n-1)^2}{(n+1)^2}$, n is the relative refractive index) is the specular reflection coefficient (Fresenel reflection) and μ is the attenuation coefficient ($\mu_s + \mu_a \approx \mu_a$, where $\mu_a >> \mu_s$). The absorption of the incident light in tissue or paint media depends on the chromophores in both media. There is no simplified solution to the transport equation if the scattering is about equal to the absorption. Generally, a medium component whose size is small compared to the wavelength will exhibit Rayleigh scattering. It will scatter light more isotropically than larger components, but the total amount of scattered light will be less for the smaller component due to its smaller size. The larger particle, (Mie scattering), will scatter the light mostly in the forward direction.

Mammalian cells sizes are typically of the order of 10-30 μm in diameter, with nuclei of the order of 3-10 μm in diameter [3]. The cells structures as shown in Fig. 2.3 vary in size between 0.1 and 30 μm. It is well known that larger particles scatter light stronger in the forward direction. Mie theory provides a strong evidence of this fact ($\phi \sim \frac{\lambda}{a}$, where ϕ is the scattering angle, λ is the incident wavelength and a is the size of the scattering particle). The majority of light scattering from a cell at small angles is due

to the nucleus, with the smaller organelles such as the mitochondria being responsible for scattering at larger angles.

Biological tissues are optically inhomogeneous and absorbing media whose average index of refraction is close to water and generally is given by, n = 1.5 – (1.5 - 1.33)*W, where W is the volume fraction of water [4]. Cellular organelles such as mitochondria, golgi, and nuclei are the main scatterers in various tissues. Scattering of light in tissue is caused by inhomogeneities such as cell membranes or intracellular structures. The scattering arises due to a relative refractive index mismatch at the boundaries between two such media or structures.

2.3 Prostate Cancer

The male prostate gland is located below the bladder. The seminal vesicles are located posterior to the prostate. The urethra exits from the bladder and traverses the prostate before exiting to the penile urethra (see Fig. 2.5) [5].

Cancer is a group of many related diseases. There are over one hundred different kinds of cancer, which originate from different types of normal cells. Most cancers fall into one of three main groups: carcinomas, sarcomas, and leukemias/lymphomas [6]. Carcinomas, which constitute approximately 90 percent of all human cancers, arise from cells that cover the surface of the body (skin), line the internal organs (such as the lungs, stomach, and intestine), and form glands (such as the breast and prostate). Sarcomas, which are rare in humans, are cancers of connective tissues, such as muscle and bone. Leukemias and lymphomas, which constitute about 8 percent of all human cancers, arise from the blood forming cells and cells of the immune system, respectively. Each of these

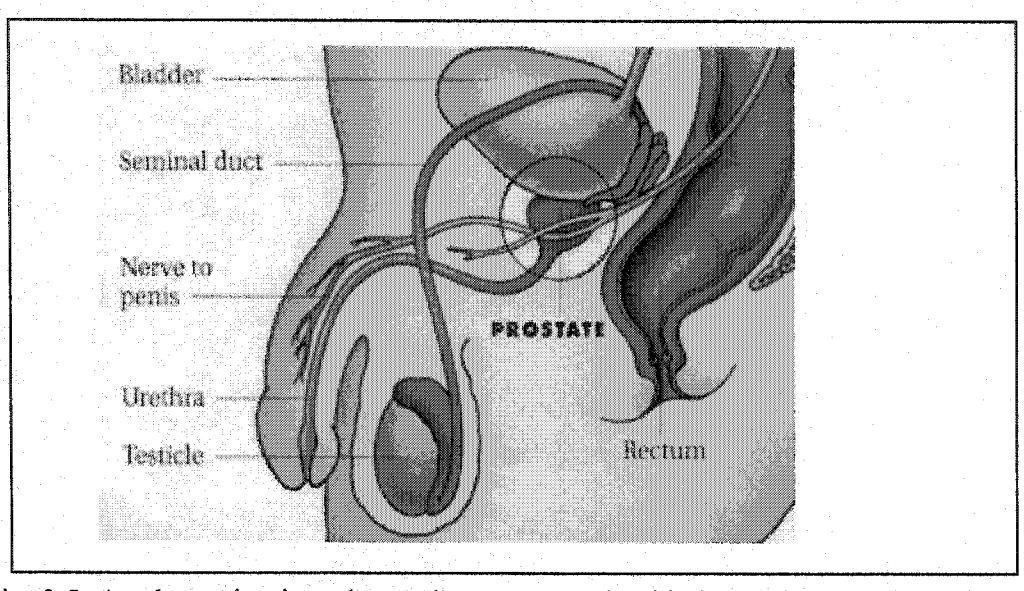

Fig. 2.5: A schematic view shows that prostate gland is located below the bladder [5].

main groups of cancers is further subdivided according to its site of origin (e.g., lung carcinoma) and a more detailed description of the type of cell involved. These diseases begin in cells, the body's basic unit of life. Cells have many important functions throughout the body. Normally, cells grow and divide to form new cells in an orderly way. They perform their functions for a while, and then they die. This process helps keep the body healthy. Sometimes, however, cells do not die. Instead, they keep dividing and creating new cells that the body does not need. They form a mass of tissue, called a growth or tumor. Tumors can be benign or malignant. Benign tumors are not cancer. They can usually be removed, and in most cases, they do not come back. Cells from benign tumors do not spread to other parts of the body. Most important, benign tumors of the prostate are not a threat to life. Benign prostate hyperplasia (BPH) is the abnormal growth of benign prostate cells. In BPH, the prostate grows larger and presses against the urethra and bladder, interfering with the normal flow of urine. Malignant tumors are

cancer. Cells in these tumors are abnormal. They divide without control or order, and they do not die. They can invade and damage nearby tissues and organs. Also, cancer cells can break away from a malignant tumor and enter the bloodstream and lymphatic system. This is how cancer spreads from the original (primary) cancer site to form new (secondary) tumors in other organs. The spread of cancer is called metastasis. When cancer spreads from its original location to another part of the body such as the bones, bladder, or rectum, the new tumor has the same kind of abnormal cells and the same name as the primary tumor. For example, if prostate cancer spreads to the bones, the cancer cells in the new tumor are prostate cancer cells. The disease is metastatic prostate cancer; it is not bone cancer.

Prostate cancer is detected using: 1) Digital rectal examination (DRE): the doctor inserts a lubricated, gloved finger into the rectum and feels the prostate through the rectal wall to check for lumps, enlargements, or areas of hardness that might indicate prostate cancer, see Fig. 2.6 [7]. A digital rectal examination allows a doctor to feel only the back wall of the prostate gland, so any abnormalities located in the middle or front part of the gland cannot be felt. For this reason, the DRE is performed in conjunction with prostate specific antigen (PSA) testing. 2) Prostate specific antigen (PSA): is a protein present in the prostate gland of men. It is normally present in the blood at very low levels. Increased levels of PSA suggest the presence of prostate cancer, however, PSA can be also elevated due to prostate infection, irritation, benign prostatic hypertrophy (enlargement) or hyperplasia (BPH), recent ejaculation, etc. If test results suggest that cancer may be present, the man will need to have a biopsy. During a biopsy, the doctor removes tissue samples from the prostate, usually with a needle. A pathologist looks at the tissue under

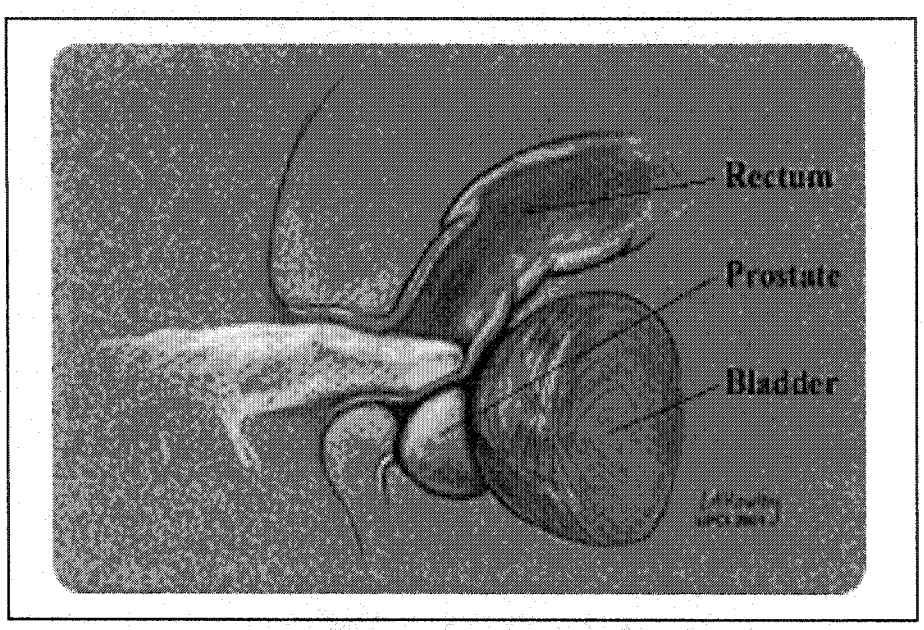

Fig. 2.6: DRE exam is done by feeling the prostate through the rectum [7].

a microscope to check for cancer cells. If cancer is present, the pathologist usually reports the grade of the tumor.

The grade tells how much the tumor tissue differs from normal prostate tissue and suggests how fast the tumor is likely to grow. One way of grading prostate cancer, called the Gleason system [8,9] uses A through E (see Fig. 2.7). Another system uses scores of 2 to 10. Tumors with higher scores or grades are more likely to grow and spread than tumors with lower scores. Normal body tissue cells are well-formed and differentiated *to meet the* functions of the specific body part. As long as the cancer is well differentiated then it looks more similar to normal cells. If the cells become progressively random and chaotic, the tumor is poorly differentiated or undifferentiated, and to a pathologist the stage of abnormality is visible under a microscope. A tumor whose structure is nearly normal (well differentiated) will probably have a biological behavior relatively close to normal.

Prostate cancers may be detected by digital examination, by ultrasonography (transrectal ultrasound), or by screening with a blood test for prostate specific antigen (PSA). None of these methods can reliably detect all prostate cancers, particularly the small cancers. New non-invasive techniques for early cancer detection are needed in prostate cancer detection.

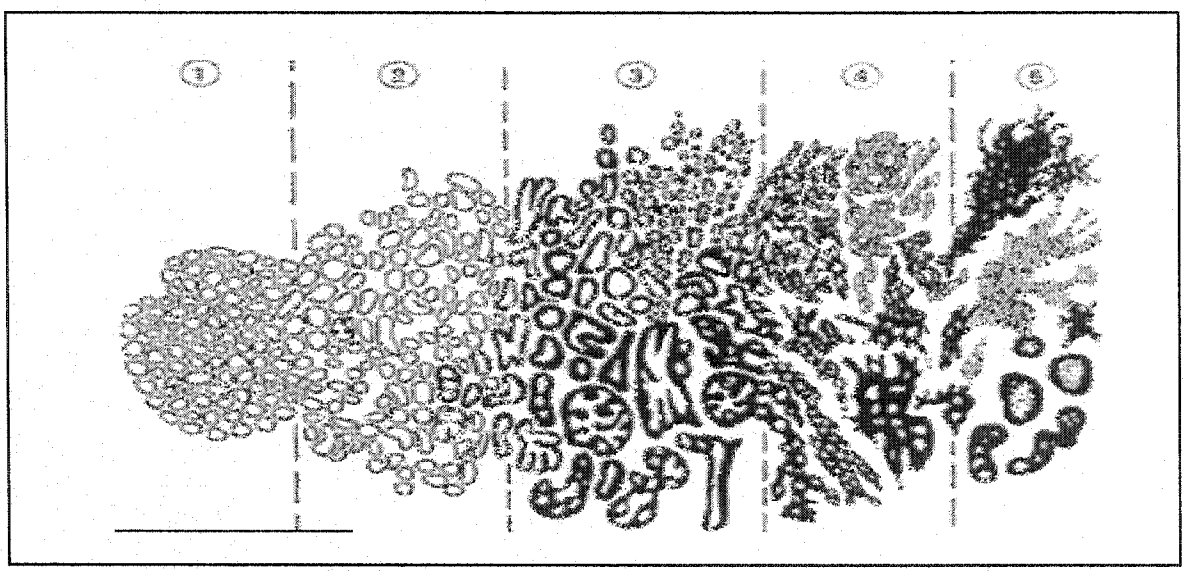

Fig. 2.7: Histologic grading of adenocarcinoma of prostate according to Gleason and the Veterans Administration Cooperative Urologic Research Group. A, Grade 1: single, separate, closely packed, uniform glands. B, Grade 2: single, separate, loosely arranged, fairly uniform glands. C, Grade 3: single, separate, irregularly spaced, very variable glands. D, Grade 4: raggedly infiltrating masses of fused glandular epithelium. E, Grade 5: anaplastic tumor and/or "comedocarcinoma". [9].

2.4 Absorption, Emission, and Polarization Anisotropy

When electromagnetic radiation or light interacts with matter, it can be absorbed, transferring the energy of the radiation to the medium. The wave energy is transferred from EM wave energy into energy modes in the absorbing medium. The absorption process is divided into categories that correspond to modes of molecular energy storage

that include vibrational, rotational, and electronic modes as shown in Fig 2.8. How energy is absorbed depends on the frequency of the radiation, the intensity of the beam, and the duration of exposure.

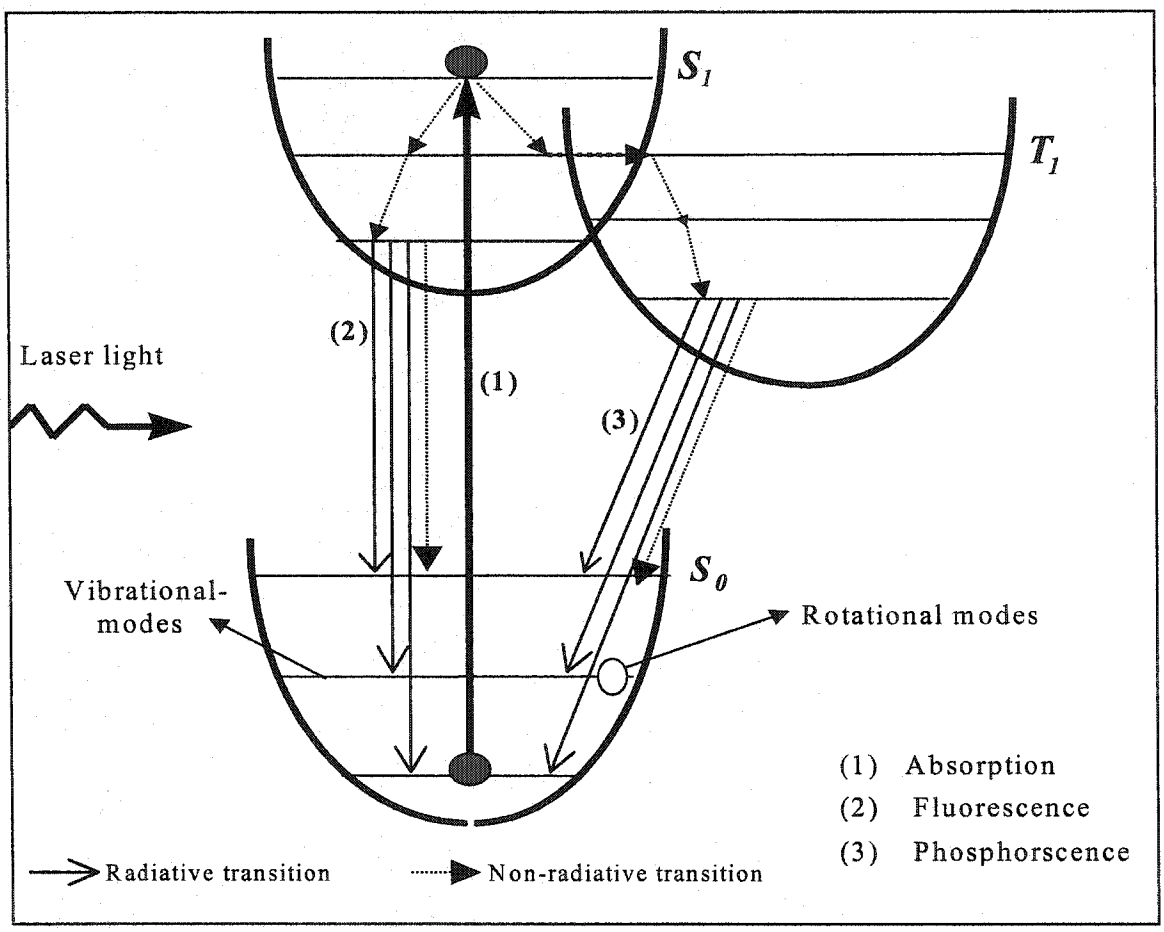

Fig 2.8: Schematic diagram shows the energy levels of a molecule and the physical processes of transitions between energy levels.

When a collimated beam of light of intensity I and wavelength λ transverse a non- scattering medium (as shown in Fig 2.9) of infinitesimal path dx with absorption coefficient $\mu_a(\lambda)$, the emerging differential change of the intensity I can be written as [10-13]:

$$dI = -\mu_a I dx \ . \tag{2.2}$$

Integration over the thickness of the medium (x) yields the intensity of emerging ballistic light I,

$$I = I_0 e^{-\mu_a(\lambda)x} . \tag{2.3}$$

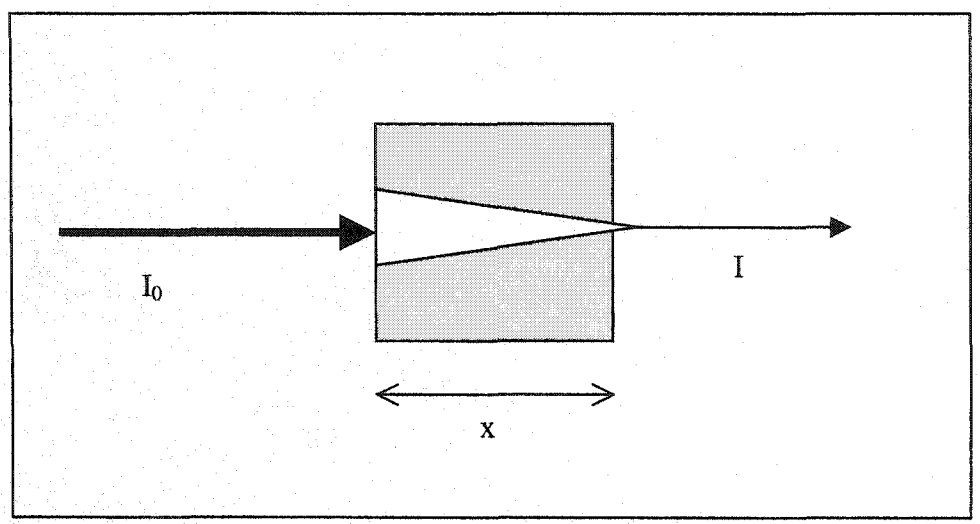

Fig 2.9: A collimated beam transverse a non-scattering media represents the ballistic light.

The absorption coefficient $\mu_a(\lambda)$ represents the probability per unit length of a photon being absorbed. The $\mu_a(\lambda)$ of the medium may be due to a number of absorbing substances (chromophores) mixed together. The absorption coefficient of a mixture of chromophores can be expressed as the sum of the products of the concentration of each chromophore C_n with its extinction coefficient ε_n

$$\mu_a(\lambda) = \sum_n \varepsilon_n(\lambda) c_n . \tag{2.4}$$

The absorption coefficient can also be expressed in terms of particle density n and absorption cross section σ_a as

$$\mu_a = n\sigma_a , \tag{2.5}$$

giving the Beer Lambert law

$$I = I_0 e^{-n\sigma_a x} . \tag{2.6}$$

The Beer Lambert law is only valid under certain conditions: the light entering the medium must be monochromatic and collimated beam, and the medium itself must be uniformly absorbing. Therefore tissues are approximated as a homogenous mixture of compounds or chromophores (such as water, hemoglobin, lipids, melanin, and proteins) each of which has its unique spectrum. The reciprocal, $1/\mu_a$, is called the absorption path length, the distance required for the intensity of the beam to fall to 1/e of the initial intensity, and equals the mean free path a photon travels between consecutive absorption events. Equation 2.2 can be rewritten in terms of optical density (OD) as

$$I = I_0 10^{-OD} . \tag{2.7}$$

The transmission, T, is defined as the ratio of transmitted to incident intensity

$$T = \frac{I}{I_0}, \tag{2.8}$$

and the attenuation, or optical density (OD) of an attenuating medium is given by

$$OD = \log_{10}(\frac{I_0}{I}) = \frac{1}{2.3} Ln(\frac{I_0}{I}) . \tag{2.9}$$

Hence

$$OD = \frac{\mu_a d}{2.3} . \tag{2.10}$$

The rate of light absorption by a molecule depends on a number of factors. It is a necessity that the energy of the incident light is "matched" to the energy difference between the two states (ϕ_g, ϕ_e). In addition, the integral (transition of the dipole moments) must be non-zero, that is to say [14-17]

$$\int_{-\infty}^{\infty} \phi_e \mu \phi_g dr \neq 0 \quad . \tag{2.11}$$

The latter defines the selection rule for absorption of light, namely the transition dipole, μ, must transform ϕ_g into a state of ϕ_e. The actual expression for the transition rate also depends on the relative orientation of the electric field of the incident light with respect to the transition dipole, $\mu, \sim \left|\vec{\mu}.\vec{E}\right|^2$. The absorption will depend on $\cos^2(\theta)$, where θ is the angle between the transition dipole and the direction of the oscillation of the electric field. Therefore, if one passes linear polarized light through an oriented sample it is possible to obtain information on the relative orientation of the transition dipole and the incident light. If the orientation of the molecule is also known then it is possible to determine the direction of the transition dipole with respect to the molecular coordinate system. The changes in absorption as a function of the orientation of the transition dipole with respect to the direction of light polarization is usually described as *the* dichroism:

$$d = \frac{\Lambda_{11} - \Lambda_{\perp}}{\Lambda_{11} + \Lambda_{\perp}}, \tag{2.12}$$

and absorption anisotropy

$$\alpha = \frac{\Lambda_{11} - \Lambda_{\perp}}{\Lambda_{11} + 2\Lambda_{\perp}}, \tag{2.13}$$

where Λ_{II} and $\Lambda_{\perp}$ represent the absorption intensity when the beam is parallel and perpendicular to the sample, respectively. To measure d or α, the sample is oriented in the polarized light and the absorption intensity is measured when the beam is parallel (Λ_{II}) and perpendicular ($\Lambda_{\perp}$) to the sample. To relate the measured d or α to the

molecular geometry of the sample it is necessary to determine the relationship between these observables and the direction of the transition dipole within the sample. If the molecule is fluorescent it is also possible to measure *the* fluorescence polarization, which results from excitation with polarized light. This involves measuring the polarization of the fluorescence, which is emitted parallel (I_{11}) and perpendicular ($I_{\perp}$) to the incident beam. In this case the polarization anisotropy is defined as

$$r = \frac{I_{11} - I_{\perp}}{I_{11} + 2I_{\perp}}. \tag{2.14}$$

The fluorescence polarization is defined as

$$P = \frac{I_{11} - I_{\perp}}{I_{11} + I_{\perp}}. \tag{2.15}$$

Note that α and r differs from d and p by an additional $\Lambda_{\perp}$ or $I_{\perp}$ in the denominator such that the denominator is equal to the total light absorbed (α) or emitted (r). This actually simplifies the use of α and r in analysis.

Orientational dynamics is aimed at understanding the motions of solute molecules in their solvent environment. The nature and time scale of molecular motions is changed dramatically when a molecule is placed in solution. One of the simplest approaches for probing solute-solvent interactions is to determine how simple molecular motions are altered by the solvent. Since optical spectroscopic methods are capable of measuring reorientational dynamics on the time scales that are relevant to solute-solvent interactions, we use time-resolved spectroscopy to probe reorientational motions. The two decays in our experiments are a result of emission polarized parallel and perpendicular to the laser excitation polarization. By measurement of the decays of fluorescence polarized parallel and perpendicular to the polarization of the excitation

pulse, fluorescence depolarization can be measured in order to determine the rates of molecular reorientation (e.g. by rotational diffusion)[18].

If the light used to excite fluorescence is polarized, absorption will be most probable for those molecules that happen to lie with their transition moments parallel to the plane of polarization. The state of polarization of the emitted light, however will depend on a number of factors, the most important factor is the orientation of the emitting dipole and the rapidity of the molecular rotation compared to the fluorescence life-time. In general the fluorescent will be partially or wholly depolarized, we define the fluorescence depolarization or anisotropy (as defined in 2.15) by the formula [19],

$$r(t) = \frac{I_{11}(t) - I_{\perp}(t)}{I_{11}(t) + 2I_{\perp}(t)}, \tag{2.16}$$

where I_{11} and $I_{\perp}$ are the parallel and perpendicular intensity components of the emitted light at time t respectively (as shown in Fig. 2.10). Theoretically the maximum of anisotropy (or fluorescence depolarization) from equation (2.17) is 1, but this is not the case in the experimental world since the direction of the dipole moment absorption is not

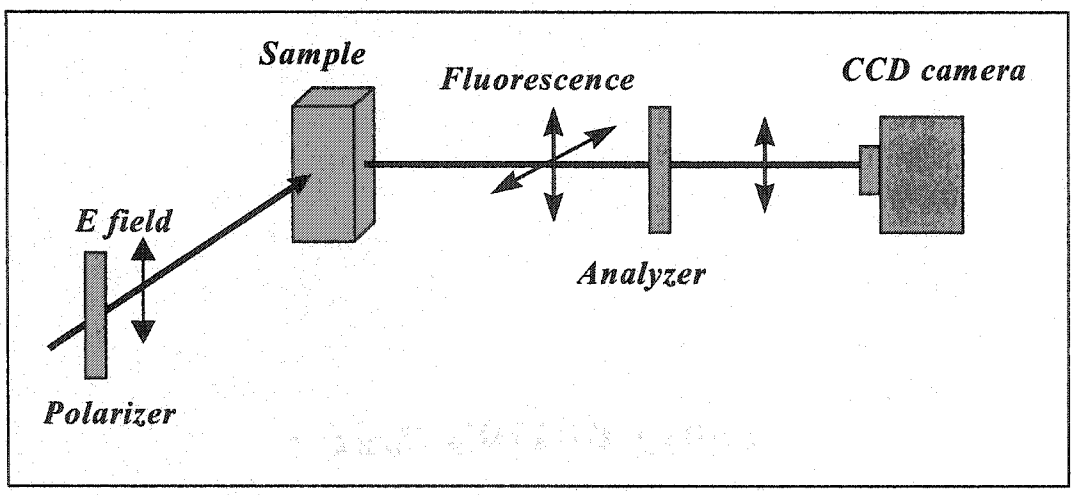

Fig. 2.10: Schematic diagram showing the fluorescence polarization dependent of the sample measured by a CCD camera detector.

as the direction of the dipole moment emission due to the rotation of the molecule. Also the attachment of the macromolecules makes it almost impossible to align perfectly with the external field.

Due to the rotational motion and the direction of the dipole before and after the emission the anisotropy will decrease, the decay will be (for a simple systems) exponential described by,

$$r(t) = Ae^{-t/\tau}, \tag{2.17}$$

where τ is the rotational relaxation time and related to the rotational diffusion constant(D) by

$$\tau = \frac{1}{6D}. \tag{2.18}$$

The measurement of the time decay of fluorescence anisotropy provides information about the rotational motion and the orientation of the macromolecules.

It has been shown [18-21] that r(t) is a single exponential function for spherical rotators and for symmetric oblate(disc shaped) and prolate (rod shaped) rotators where the transition moment is parallel to the symmetry axis. Fleming et al. [18] have demonstrated numerically that an oblate rotator with its transition moment perpendicular to the symmetry axis will have an r(t) function that approximates to a single exponential. The case that r(t) will be a sum of exponentials is for a prolate rotator with a transition moment perpendicular to the symmetry axis. The general formula that is valid for any shape of molecule is given by [18]

$$r(t) = \frac{2}{5} < p_2[\hat{e}(0).\hat{e}(t)] >, \tag{2.19}$$

where the correlation function P_2 is the second Legendre polynomial of the dipole reorientation angle and e's are the unit vectors along the transition dipole at times 0 and t, respectively. In the case of Brownian rotation as an Einstein sphere, then equation (2.20) become [18, 22]

$$r(t) = \frac{2}{5} e^{-6Dt}, \tag{2.20}$$

where D is the rotational diffusion constant and is given by

$$D = \frac{KT}{6V\eta}, \tag{2.21}$$

where K is the Boltzmann constant, T is the temperature, V is the volume of Einstein sphere and η is the viscosity of the medium. By substituting equation (2.22) into equation (2.19) we will get the relation

$$\tau = \frac{V\eta}{KT}. \tag{2.22}$$

If we are talking about symmetric shape (sphere) then we can substitute $V = \frac{4}{3}\pi a^3$ where a is the radius of the sphere in equation (2.23), then we will receive

$$\tau = \frac{4\pi a^3 \eta}{3KT}. \tag{2.23}$$

The rotational time depend on temperature, viscosity, and the radius of the molecule (size). For a random distribution of spherical molecule in solution r(t) is equal or less than 0.4 ($r(t) \leq 0.4$, maximum at t=0 so r(t)=2/5) which is viscosity dependent under the same temperature T and same molecules.

2.5 Scattering

2.5.1 Single Scattering

Elastic scattering of light occurs when charged particles in a medium are set into oscillatory motion by the electric field of the incident wave and re-emit light of the same frequency as the primary wave. In most solids and liquids, intermolecular interactions broaden the absorption frequencies such that both scattering and absorption of light occur at different wavelengths. The real refractive index of a medium is given by $n = c/v$ where c is the speed of light in vacuum and v the speed of light in the medium. The complex refractive index is defined as

$$N = n + ik, \tag{2.24}$$

where the real part, n, determines the speed of wave and the imaginary part, k, determines the absorption of the wave as it propagates through the medium. From Maxwell's equation k can be related to absorption coefficient μ_a, defined as follows

$$k = \frac{\mu_a \lambda}{4\pi}, \tag{2.25}$$

where λ is the incident light wavelength. The refractive index depends on the number of molecules per unit volume and their polarizibility. Scattering of light in turbid media is caused by refractive index mismatches at macroscopic (e.g. air skin or air paint) and microscopic boundaries (e.g. nucleus cytoplasm in tissue or pigments solvent in paint).

Mammalian cells sizes are typically of the order of 10 - 30 μm in diameter, with nuclei of the order of 3 - 10 μm in diameter. Mitochondria are 1 - 4 μm in length and 0.3 - 0.7 μm in diameter. Lysosomes and peroxisomes are spherically in shape and its size is 0.2-0.5 μm in diameter. Golgi apparatus have complicated shapes and containing a high

proportion of lipid membranes. The scattering from the nuclei most closely resembles that from the cells. The scattering at small angles is mainly attributed to the to the nuclei, while small objects such as mitochondria in the cell contribute to the large scattering angles (see $P(\theta)$ dependent) [10,11,23]. Various theories have been put forward to describe the scattering of light by particles of different shapes and sizes. In general these fall into two classes: single scattering and multiple scattering theories. In single scattering theory it is assumed that the particle separation is sufficiently large, or the number of particles is sufficiently small, such that the total scattered wave due to all the particles is small compared to the incident wave [10-11,13]. Single scattering by particles small in diameter compared to the wavelength of the incident light is often known as Rayleigh scattering, which varies with the inverse fourth power of the incident wavelength. Determining the scattered field patterns from particles that are large compared to the incident wavelength, Mie scattering, is a complicated task, due to phase differences between the scattered wavelets, which must be taken into consideration. If the optical depth $\mu x \langle 0.1$ then single scattering prevails; for $0.1 \langle \mu x \langle 0.3$ a correction for double scattering may be necessary [10]. For larger values of the optical depth the full complexities of multiple scattering becomes a factor. In the case of single scattering, the scattering properties of a medium are described by its scattering coefficient μ_s. The scattering coefficient is the product of the number density of scattering particles n and the scattering cross section σ_s of the particles or $\mu_s = n\sigma_s$ attenuating through simple scattering materials can be described by

$$I = I_0 e^{-\mu_s x}, \tag{2.26}$$

where I is the non-scattered component of light after traversing a non-absorbing sample of thickness x as shown in Fig. 2.11. The scattering pathlength, $1/\mu_s$, is the average distance a photon travels between consecutive scattering events and the quantity $\mu_s x$ is the optical thickness of a sample expressed in terms of scattering path lengths.

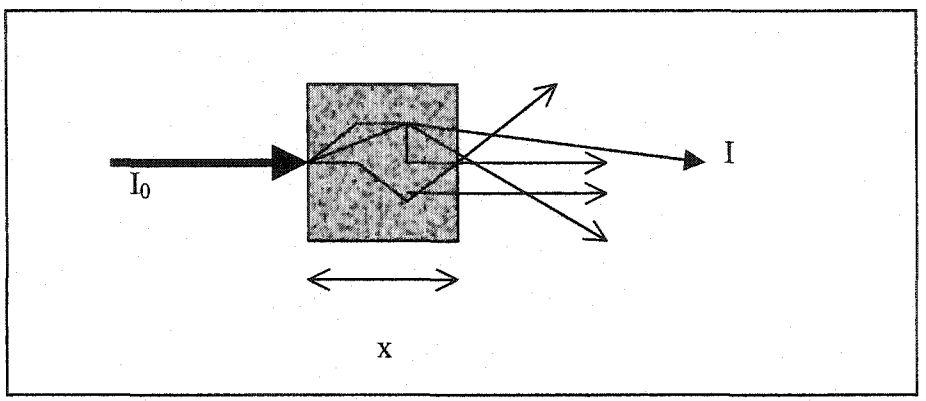

Fig. 2.11: Light traversing a non-absorbing medium of thin thickness (x).

Compared to the non-scattering case above, if a medium is scattering the paths taken by the photons traversing it are no longer direct. This has two effects: photons are scattered in all directions, so one no longer detect all the emerging photons and photons have traveled varying distances through the scattering media. In a scattering and absorbing thin media, the transmitted signal can be written as

$$I = I_0 e^{-\mu_t x} \quad , \tag{2.27}$$

where μ_t is the total attenuation coefficient, given by $\mu_t = \mu_a + \mu_s$. For thin samples, the reciprocal of the total attenuation coefficient, $1/\mu_t$, is known as the mean free path, and the distance traveled by a photon between interactions. There are many systems such as biological tissues for which the assumption that the particles are independent of one another is invalid and multiple scattering becomes important [24]. On encountering a scattering particle within a medium, photons traveling in a direction $\hat{s}$ are scattered into a

new direction $\hat{s}'$. The new directions generally do not occur with equal probability and can be described by the differential scattering coefficient, $d\mu_s(\hat{s},\hat{s}')$. Integrating over all angles gives μ_s, the total scattering coefficient

$$\mu_s = \int_{4\pi} d\mu_s(\hat{s},\hat{s}')d\hat{s}' . \tag{2.28}$$

The scattering phase function p is the normalized version of the differential scattering coefficient

$$p(\hat{s},\hat{s}') = \frac{d\mu_s(\hat{s},\hat{s}')}{\mu_s} , \tag{2.29}$$

such that $\int_{4\pi} p(\hat{s},\hat{s}')d\hat{s}' = 1$. The mean cosine g of the scattering angle θ, the angle between the incident $\hat{s}$ and scattered $\hat{s}'$ directions, is known as the anisotropy factor

$$g = \int_{4\pi} p(\theta)\cos(\theta)d\hat{s}' . \tag{2.30}$$

If the scattering is completely isotropic then p is equal for all angles and g will be equal to zero. As the particle size increases, the intensity distribution increases in the forward direction and p for small angles is much higher than for all other angles. Therefore, the mean cosine tends towards a unity value, the higher the g value the more forward peaked the scattering. Most tissues have a high g value in the range 0.7-0.97 [25]. Combining the scattering coefficient and the anisotropy factor gives the transport scattering coefficient $\mu_s' = (1-g)\mu_s$. The transport attenuation coefficient $\mu_{tr} = \mu_a + \mu_s'$ and its reciprocal, μ_{tr}^{-1}, the transport mean free path (ℓ_{tr}).

2.5.2 Multiple Scattering

The previous section have discussed the scattering of light from a small collection of particles, or one in which the particles are far enough apart, so that their individual scattered fields do not significantly interfere with one other. In a biological tissue or a pigmented paint sample, the scattering particle density is such that the interaction of scattered waves between neighboring particles cannot be ignored and multiple scattering is present. This section will discuss light propagation to describe absorption and scattering in turbid media such as prostate tissue and pigmented paint.

A short pulse of collimated light incident on a highly scattering medium such as tissue or paint will diffuse and disperse in time for a given thickness as shown in Fig. 2.12. It is possible to describe light transport in a regime where multiple scattering dominates using Maxwell's electromagnetic theory [10]. But it has been noted that solutions to multiple scattering theory will be complex [26-27]. However, such a

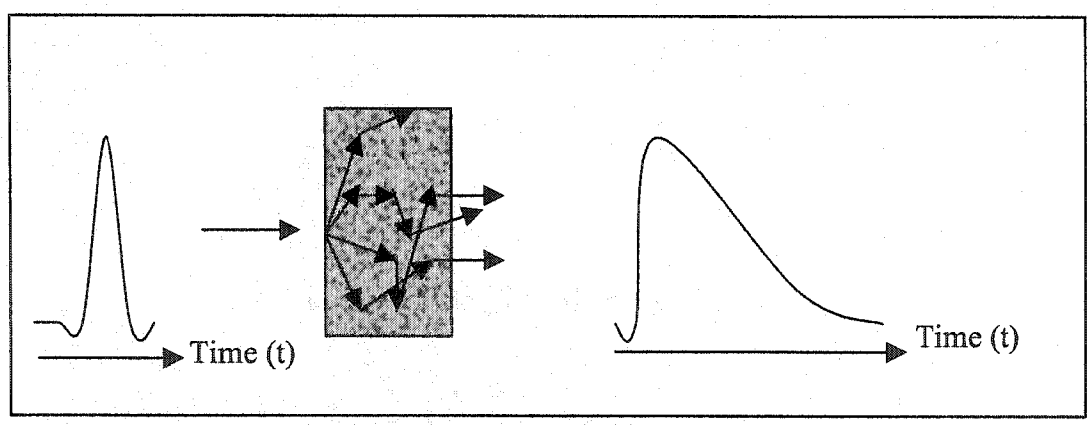

Fig. 2.12: Transmission of a short pulse through a scattered medium.

treatment in this case is complex and a lack of $\varepsilon(r)$ makes it unfeasible. Instead the problem can be simplified by ignoring wave phenomena such as polarization and interference, and particle properties such as inelastic collisions and the transport of

individual photons (absorbed or scattered) is considered. This is good approximation for large thicknesses in tissue or paint which are highly scattering media. The propagation of the electromagnetic waves in scattering media can be described with the Boltzmann transport equation also known as the radiative transfer equation (RTE). The basic assumption in radiative transfer theory is that only flow of energy through the medium is considered.

The RTE is written as [28]:

$$\frac{1}{\upsilon}\frac{\partial L(r,\hat{s},t)}{\partial t}+\nabla.L(r,\hat{s},t)\hat{s}=-(\mu_s+\mu_a)L(r,\hat{s},t)+\mu_s\iint_{4\pi}L(r,\hat{s}',t)f(\hat{s}.\hat{s}')d\Omega'+S(r,\hat{s},t), \qquad (2.31)$$

where the radiance $L(r,\hat{s},t)$ has units W/(m^2 sr) and where $\hat{s}$ is a unit vector pointing in the direction of interest. The linear scattering and absorption coefficients, μ_s and μ_a, are the inverse of the mean free paths for scattering and absorption, respectively, and the normalized differential scattering cross section $f(\hat{s},\hat{s}')$ satisfies $\iint_{4\pi}f(\hat{s}.\hat{s}')d\Omega'=1$. The source term $S(r,\hat{s},t)$ represents power injected into a unit solid angle centered on $\hat{s}$ in a unit volume at r. Equation (2.31) provides a mathematical description of incoherent photons. The similarity of the transport equation to a continuity equation is emphasized by integration over all solid angles and making use of the definition of the fluence rate ϕ and flux J

$$\frac{1}{\upsilon}\frac{\partial U(r,t)}{\partial t}+\nabla\cdot J(r,t)=-\mu_a U(r,t)+S_0(r,t), \qquad (2.32)$$

where

$$S_0(r,t)\equiv\iint_{4\pi}S(r,\hat{s},t)d\Omega, \qquad (2.33)$$

$$U(r,t) \equiv \iint_{4\pi} L(r,\hat{s},t)d\Omega, \tag{2.34}$$

$$J(r,t) \equiv \iint_{4\pi} L(r,\hat{s},t)\hat{s}d\Omega. \tag{2.35}$$

When scattering is much stronger than absorption ($(1-g)\mu_s >> \mu_a$), the radiance can be expressed as an isotropic fluence rate U plus a small directional flux J, and transport equation (2.31) reduces to a diffusion equation [29-31]. We first expand the radiance as

$$L(r,\hat{s},t) = \frac{\upsilon}{4\pi}U(r,t) + \frac{3}{4\pi}J(r,t)\cdot\hat{s}, \tag{2.36}$$

then substitute this diffusion approximation into equation (2.32) and then multiplying by $\hat{s}$ and integrating over all solid angles yields (for U part)

$$\frac{\partial U(r,t)}{\partial t} + \upsilon\mu_a U(r,t) + \nabla\cdot J(r,t) = S_0(r,t). \tag{2.37}$$

Assuming that the source S is isotropic and the point of interest is far from sources or boundaries and using equation of continuity, then equation (2.31) can be reduced to diffusion equation [32]:

$$D\nabla^2 U(r,t) - \mu_a\upsilon U(r,t) - \frac{\partial U(r,t)}{\partial t} = -S_0(r,t), \tag{2.38}$$

$$D \equiv \frac{\upsilon}{3[(1-g)\mu_s]} \equiv \frac{\upsilon}{3\sigma_{tr}} \equiv \frac{\ell_{tr}\upsilon}{3}, \tag{2.39}$$

where D is the photon-diffusion coefficient, g is the average cosine of the scattering angle, $\sigma_{tr} = (1-g)\mu_s$ is the linear transport coefficient, and $\ell_{tr} = 1/\sigma_{tr}$ is the transport mean free path. We are interested in the solution to diffusion equation for a slab geometry.

We can use this Green's function to solve the problem of slab geometry as shown in Fig. 2.13 by making two further assumptions. First, we assume that all the incident photons are initially scattered at some depth from the interface (as an example glass-tissue interface), which is called the extrapolated depth ($z=z_0=0.71\ell_{tr}$). The second assumption is that $U(r,0,t)=0$ and $U(r,L+2Z_0,t)=0$ on the physical boundary condition. This condition can be achieved by adding two point sources near z=2L, but then the boundary condition at z=0 is violated for t>2L/c. Both boundary conditions can be met at all times only by adding an infinite number of dipole sources as shown in Fig. 2.13. In practice, the number of sources required depends on the optical properties of the slab and the maximum time at which transmittance (or reflectance if one interested to calculate reflectance) must be calculated. Solving the diffusion equation (2.38) for a slab geometry using Green's function is shown in Fig. 2.13. With the above boundary conditions, the

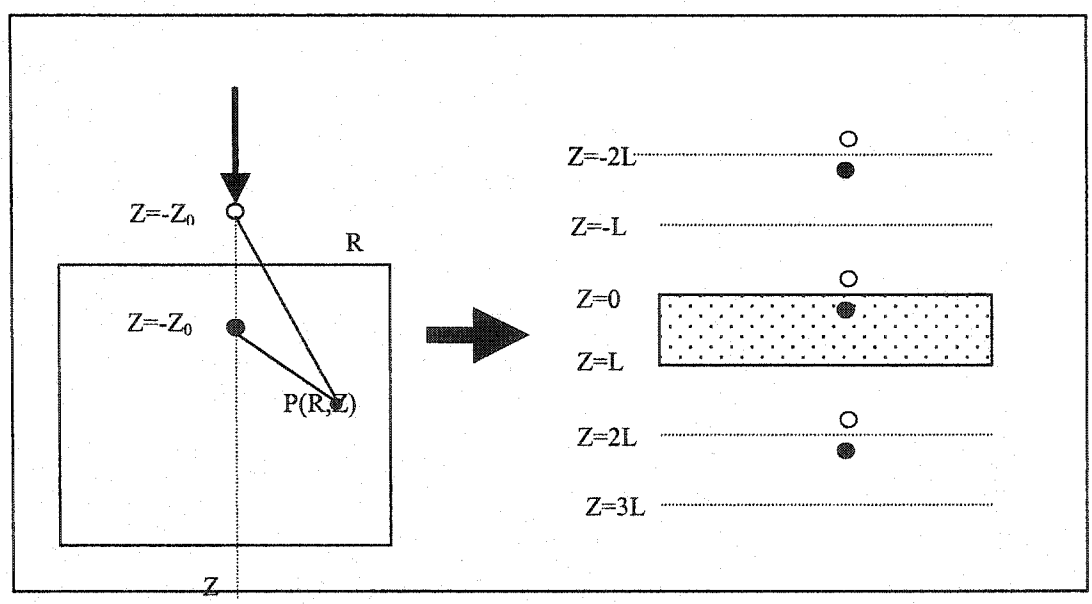

Fig. 2.13: Solving the diffusion equation for a slab geometry using Green's function.

photon fluence rate or density in three-dimension (3D) with the source at z' can be obtained with the method of images as [33]

$$U(\vec{r},t)=\frac{e^{-R^2/4Dt}}{(4\pi Dt)^{3/2}}\sum_{n=-\infty}^{\infty}[e^{-(2nd+z'-z)^2/4\pi Dt}-e^{-(2nd-z'-z)^2/4\pi Dt}]e^{-\mu_a vt}, \tag{2.40}$$

where $R=x^2+y^2$, $z=L+z_0$, and $d=L+2z_0$. The transmitted intensity of a laser pulse on the opposite side of a slab of thickness L can be obtained by integrating the photon flux over the whole surface of the slab related to equation (2.40) [34-35]

$$I_Z=\frac{1}{4td^2}\exp(-\mu_a vt)\sum_{n=1}^{\infty}m\cdot\sin[\frac{m\pi L}{d}]\cdot\exp(-(m\pi)^2Dt/d^2). \tag{2.41}$$

Equation (2.41) can be used to fit the temporal profiles of the transmitted pulses to obtain the transport and the absorption lengths of the scattered medium.

For a thin slab, for a short pulse from a point source at $z'=0$, the corresponding 1D photon density in an infinite medium in the diffusion model

$$U(z,t)=\frac{1}{(4\pi Dt)^{1/2}}\exp(-\frac{z^2}{4\pi Dt}-\mu_a vt), \tag{2.42}$$

is replaced by that of the cumulative solution as the following:

$$U(z,t)=\frac{1}{(4\pi Dvt)^{1/2}}\exp\left[-\frac{(z-R_Z)^2}{4Dvt}\right]\exp(-\mu_a vt) \tag{2.43}$$

where the center of particles, R_Z , $R_Z=c[1-\exp(-g_1t)]/g_1$ and the diffusion coefficients

$$D=\frac{v}{3t}\left\{\frac{t}{g_1}-\frac{3g_1-g_2}{g_1^2(g_1-g_2)}[1-\exp(-g_1t)]+\frac{2}{g_2(g_1-g_2)}[1-\exp(-g_2t)]-\frac{3}{2g_1^2}[1-\exp(-g_1t)]^2\right\} \tag{2.44}$$

where $g_l = \mu_s[1 - a_l/(2l+1)]$ and a_l is coefficients of the Legendre's expansion of the phase function, $P(s, s') = \frac{1}{4\pi}\sum l\, a_l P_l[\cos(s \cdot s')]$.

The dynamic wave transport for diffusion approximation for different thickness of samples has been investigated. There is no clear picture about the dynamic in the multiple scattering media such as paint film at different thickness especially for thin samples and in the short time domain effect. For long time exponential decay, the transmitted pulse is proportional to exp $(-t/\tau)$. The transmitted pulse in the diffusion approximation equation is proportional to exp $(-(\pi^2 D_{eff} t/L^2) + \mu_a v t)$ yields [33, 36-37]

$$D_{eff} = \frac{L^2}{\pi^2}\left(\frac{1}{\tau} - \mu_a v\right) \tag{2.45}$$

where D_{eff} is the effective diffusion coefficient, L is the sample thickness, τ is the decay time, μ_a is the absorption coefficient, and v is the energy velocity.

Since for thin samples, there is a strong internal reflection at the boundary condition of the scattered medium, the extrapolation length Z will be added to the transmission in the diffusion equation. The transmission for varying length samples (slab of thickness L) is described by the diffusion theory as [38]

$$T = \frac{\ell_{tr} + z}{L + 2z}, \tag{2.46}$$

and for small relative index of refraction (say $n_r \sim 1.1$) gives

$$T(z \sim 0.71\ell_{tr}) = \frac{1.71\ell_{tr}}{L + 1.4\ell_{tr}}, \tag{2.47}$$

for thickness where ballistic intensity is much smaller than the diffusive light. The extrapolation length is defined as,

$$z = (2/3)\frac{1+R}{1-R}, \tag{2.48}$$

Where R is the average diffusive reflectivity. The average diffusive reflectivity R, which determines the extrapolation length is given by [39],

$$R = \frac{3C_2 + 2C_1}{3C_2 - 2C_1 + 2}, \tag{2.49}$$

where $C_n = \int_0^1 r(\mu)\mu^n d\mu$. (2.50)

The angular dependent reflectivity, $r(\mu)$, of the entire boundary is

$$r(\mu) = \frac{r_{12} + r_{23} - 2r_{12}r_{23}}{1 - r_{12}r_{23}}, \tag{2.51}$$

where r_{ij} is the average Fresnel reflectivity of the ij interface where a photon strikes the boundary at an angle $\cos^{-1}(\theta)$ from the normal. For light incident on air-paint-glass surface, where n=1.35 for paint and n=1.45 for glass, equation (2.44) becomes

$$T(z \sim 1.8\ell_{tr}) = \frac{2.81\ell_{tr}}{L + 5.6\ell_{tr}}. \tag{2.52}$$

Plotting the inverse of transmission (1/T) versus sample thickness (L), enables the transport mean free path l_{tr} for the paint to be obtained. In addition, the degree of linear polarization (P_L) can be used to measure the transport length and the polarization length of the scattered media as will be explained in the next section.

2.5.3 Polarization in Scattering Media

The characteristics of an incident light pulse propagating through paint, namely, intensity, duration, coherence, and polarization, change as the pulse is scattered inside the medium. The pulse that emerges has very different characteristics than that of the incident pulse. The transmitted light propagating in a turbid medium such as paint or tissue can be viewed as consisting of three components: ballistic, snake, and diffusive as described earlier. Ballistic photons traverse the shortest path, retain most of the incident photons characteristics and carry direct information about the interior structure of the scattering medium. Diffusive light, consists of multiply scattered photons, takes the longest path or time to exit the medium. It provides little information about the internal structure of the medium. Similar components occur for the backscattered light reflected from the medium.

The degree of polarization of the scattered light is defined as

$$P_L = \left| \frac{P_{11} - P_{\perp}}{P_{11} + P_{\perp}} \right|, \tag{2.53}$$

where P_{11} is the intensity of light maintaining its original polarization state, and $P_{\perp}$ is the intensity of light in the orthogonal polarization state. P_L=1 represents linearly polarized light; P_L=0 represents totally depolarized light. It has also been suggested that the state of polarization of the emerging light can be used to discriminate photon path length, with unscattered and weakly scattered light maintaining their original polarization states, and that this can improve imaging resolution. As the scatterer concentration increases or the length of the sample increases, the unscattered attenuated light and the scattered light are depolarized at different rates, depending on the particle size and the anisotropy factor (g). Bicout et al. [36] derived an approximation, which is valid for a large number of

scattering events (greater or equal to 10), for the degree of polarization, P_L, of light transmitted through a slab of thickness L. The degree of polarization of the transmitted light percolates with contribution from many different paths. Expressions for incident linearly (P_L) and circularly (P_C) polarized light are derived. The number of steps in this path of length s is $n = s/\ell_s$ (ℓ_s represents mean free path). The number of scattering paths of length s is simply given by the Green's function G(n,d) of the diffusion equation [40]. These degrees of polarization are given by a proper weighting G(n,d) of scattering paths of length s and can be written as

$$P_i = \frac{\int_0^\infty f_i(n)G(n,d)dn}{\int_0^\infty G(n,d)dn}, \tag{2.54}$$

where i=L for linear states of polarization, and I=C for circular states of polarization. The functions f expresses the dependences of the output degree of polarization on the number of scatterings (equal to n+1 in the multiple scattering regime). In the large n limit, the f's reduce to

$$f_L(n) \cong (3/2)\exp[-n(l_s/\zeta_L)], \tag{2.55}$$

$$f_C(n) \cong (3/2)\exp[-n(l_s/\zeta_C)]. \tag{2.56}$$

The $\zeta's$ defines characteristic lengths of depolarization for a path of n+1 scattering: $\zeta_L = l_s/\ln(10/7)$ and $\zeta_C = l_s/\ln(2)$. It is clear that $\zeta_L = 2\zeta_C$. Integrating equation (2.55) will result in

$$P_i = \frac{L.\sinh(l_s/\xi_i)}{l_s.\sinh(L/\xi_i)}, \tag{2.57}$$

where $\xi_i = (\zeta_i l_s / 3)^{1/2}$, with i=L, C, define the characteristic lengths of depolarization for the slab geometry. In the far field, the degree of polarization of the transmitted light under ($L \geq 10.\ell_s$) can be approximated by [40]

$$P_i \cong \frac{2L}{\ell_s}\sinh(\frac{\ell_s}{\xi_i})\exp(-\frac{L}{\xi_i}). \tag{2.58}$$

It is clear that the characteristic polarization length for incident linearly polarized light is greater by a factor of $\sqrt{2}$ than the corresponding length for incident circularly polarized light. This analysis of degree of polarization should apply equally well for large spheres provided that ℓ_s is changed into the transport mean free path

$$\ell_{tr} = \frac{1}{\phi\sigma_{tr}} = \frac{\ell_s}{[1- < \cos(\theta) >]} \tag{2.59}$$

and the appropriate size dependence of the f's is inserted therein. The transport scattering cross section for each scatterer is defined in the usual way as

$$\sigma_{tr} = \int\sigma(\theta)[1-\cos(\theta)]d\Omega, \tag{2.60}$$

where θ is the scattering angle. The degree of linear polarization, P_L, for large particles as suggested by Bicout can be written as

$$P_i \cong \frac{2L}{\ell_{tr}}\sinh(\frac{\ell_{tr}}{\xi_i})\exp(-\frac{L}{\xi_i}), \tag{2.61}$$

where ℓ_{tr} is the transport mean free path.

$$\ell_{tr} = \frac{\ell_s}{(1-g)}, \tag{2.62}$$

where ℓ_s is the mean free path and equals $1/\mu_s$, g is the mean cosine of the scattering angle $(0 \leq g \leq 1)$; and g=0 represents isotropic scattering, whereas g=1 represents

forward scattering. The quantity g decreases as the particle size decreases. These results were in agreement with the explicit computation done in the context of the Bethe-Salpeter equation handled in the diffusion approximation [41]. It is not yet established how depolarization proceeds as the size of the particles increases from very small to large. Bicout et al. applied equation 2.57 up to a particle size factor of $ka = 2\pi a/\lambda \sim 20$. What happens beyond this limit is not established. Kim et al. [42] derived another expression for the degree of polarization, which can be written as:

$$P_L \sim \exp(-L/\ell_s \xi_i). \tag{2.63}$$

Both Kim [39] and Bicout [36] claim that the linear depolarization length is about one transport length. Both don't agree with our experimental results for the paint material, where the paint volume fraction is ~ 20%. Most recently, Min Xu et al. [43] demonstrated theoretically a new formula to evaluate the degree of polarization taking into consideration the internal reflection at the boundaries in the scattering media and the density of the medium. Min Xu et al. defined the degree of polarization in scattering media for a high volume fraction as:

$$P_L \sim \frac{2d}{\xi_L'} Sinhc(\frac{z_1}{\xi_L'}) Sinhc(\frac{z}{\xi_L'}) e^{-\frac{d}{\xi_L'}}, \tag{2.64}$$

where $Sinhc(x) = \frac{Sinhx}{x}$, $d = L + 2z$, $z_1 = z + \ell_{tr}$, z is the extrapolation length, $\xi_L' = \sqrt{\frac{\ell_{tr}\ell_s}{3\ln(1/a)}}$ is the linear depolarization length, and a is related to the material's density.

2.6 Transitions Between Energy Levels

In steady-state measurements, the light irradiation and detection are either continuous or, if chopped or pulsed, the pulse length is long compared to the propagation time of the photons, which is typically of the order of nanoseconds. The reflected light from the sample will consist of two parts; the specular reflection and the diffuse reflectance. The specular reflection is due to differences in the refractive indices between the tissue and the surrounding medium and depends on the surface texture.

The presence of internal multiple scatterers within a luminescence body can affect the luminescence observed at the surface of the body in self-absorption, the luminescence light emitted from inside a random medium will reach the surface by a random walk diffusion process. The shorter wavelength light undergoes a longer random walk and experiences more absorption. In general the larger wavelength light will scattered less and hence penetrate deeper. When molecules are illuminated by monochromatic radiation (as shown in Fig. 2.8) with a wavelength within their resonance absorption band, a portion of the radiation is absorbed (resonance absorption). Some of the absorbed radiation will be re-emitted as fluorescence radiation by the molecules over a broad spectral range characteristic of the specific molecular species. In that process, each excited molecule decays by reemitting a photon spontaneously. This fluorescence radiation will be isotropic.

Total energy of a molecule in its electronics ground state is

$$E_t = E_e + E_v + E_r , \tag{2.65}$$

where E_t, E_e, E_v, and E_r are the total, electronic, vibrational, and rotational energy respectively. Similarly the total energy of a molecule in an excited electronic state is

$$E_{tl}=E_{el}+E_{vl}+E_{rl}. \tag{2.66}$$

If we define an absorption transition as (the change in E= Δ E) then,

$$\Delta E_x=E_{x1}-E_x, \tag{2.67}$$

where x= t, e, v or r, transitions involving ΔE_e and ΔE_v yield the electronic and vibrational absorption spectrum.

The Hamiltonian of a molecule in a radiation field is $H = H^0 + H^1$, where H^0 is the Hamiltonian in the absence of the external field and H^1 is the perturbation Hamiltonian due to the field. The perturbation Hamiltonian for electro-dipole (ED) and electric-quadrupole (EQ) transitions are, respectively

$$H^1_{ED} = -er \cdot E, \tag{2.68}$$

$$H^1_{EQ} = -(1/2)er \cdot r \cdot [\nabla \cdot E], \tag{2.69}$$

where E is the electric field and r is the distance between the charges of the dipole. The equation of motion for the state function, ψ, is given by Shrodinger equation for a single particle as

$$i\hbar\frac{\partial\psi}{\partial t} = (H^0 + H^1)\psi. \tag{2.70}$$

In the limit that the perturbation, H^1 is small, it is possible to express the wave function at later time t in terms of energy eigenfunctions of the unperturbed Hamiltonian, H^0, as [44-45]

$$\psi = \sum_{n=1}^{\infty} C_n(t)e^{-(i/\hbar)E_n^0 t}\psi_n^0, \tag{2.71}$$

where E_n^0 is the energy of the eigenstate ψ_n^0, and C_n is the expansion coefficient or the wave function amplitude. Substituting equation (2.71) into equation (2.70), then equation (2.68) can be simplified to

$$i\hbar\sum_n \frac{dC_n(t)}{dt}\psi_n^0 e^{-(i/\hbar)E_n^0 t} = \sum_n C_n(t)H^1\psi_n^0 e^{-(i/\hbar)E_n^0 t} \qquad (2.72)$$

Taking the projection of the vector expressed by each side of equation (2.72) by multiplying it by $\psi_k^{0^*}$ and integrating over the space, we get

$$\frac{dC_m(t)}{dt} = \frac{1}{i\hbar}\sum_n C_n(t)H_{kn}^1 e^{(\frac{E_k^0 - E_n^0}{\hbar})t} \qquad (2.73)$$

where the matrix element for H^1, $H_{kn}^1 = <\psi_k|H^1|\psi_n>$, is between the initial ($|n>$) and final ($<k|$) eigen-states of H^0. By substituting equations (2.68) and (2.69) in (2.73) the transition rate $C_m(t)$, and absorption and emission rates, between the k-energy level and the n-energy level will be obtained.

When a beam of Light is incident on a medium such as tissue the photons undergo a variety of processes, the tissue produces fluorescence and phosphorescence. Absorption of radiation takes place in order of ($\sim 10^{-15}$ second), the exited molecule very quickly ($\sim 10^{-13}$ second) loses a part of the excitation energy to populate the lower vibrational levels of the exited electronic state S_1, in a process is known as vibrational relaxation. The molecule can then decay to the ground level by emitting fluorescence or through several non-radiative processes (Internal Conversion and Intersystem Crossing) resulting in a reduction of the fluorescence intensity. The life time of a singlet state is on the order of 10^{-10} second to 10^{-8} second, while that of a triplet state is between 10^{-6} second and 10^{2} seconds or more.

2.7 Time-Resolved Theory of Light Emission

Time-resolved spectroscopy provides information on the excited state of a material. It can be used to determine luminescence lifetimes, molecular motion, possible decay mechanisms, and energy transfer process, which is not available from steady state measurements.

When the transmitted, or diffusely reflected, light from a femto- or picosecond laser pulse is recorded as a function of time, a mathematical model can be used to assess the optical properties. The average path length can be estimated by determining the average time-of-flight of the photons. For time-resolved measurements of photon propagation, short (pico- or femtosecond) laser pulses from high-repetition-rate lasers are used to illuminate the scattering medium. A frequently used laser is the Ti:Sapphire laser, emitting ~ 150 femtosecond pulses at 82 MHz. A detection technique allowing measurements on the picosecond range involves the use of a streak camera [46-48]. It can be used to detect very weak signals. The light pulse to be measured is focused onto the adjustable entrance slit of the streak camera. This slit is then imaged onto a photo cathode. When a photon hits the photo-cathode, an electron is emitted and accelerated by a high voltage towards a phosphorus screen. A rapidly rising voltage, synchronized with the incident light pulse, is applied transversely across the direction of acceleration to deflect the electrons. The deflected electron beam is amplified in a microchannel plate before hitting the screen. An image is created on the screen, where one axis corresponds to the entrance slit and the other to time. Finally, this image is captured by a CCD camera, controlled by a computer. The streak camera can be used in two different modes; single shot or synchroscan. In the single-shot mode, signal is collected from one laser

pulse. This results in a high temporal resolution, of the order of 2ps, but low dynamic width. To achieve a better signal-to-noise ratio, it is possible to accumulate light from several laser pulses. This will, however, result in a worse temporal resolution due to internal jitter in the camera ~ 5ps. Furthermore, this is possible only for lasers having a repetition rate of less than 1 kHz. For high repetition rate lasers, the synchroscan mode can be used. An internal oscillator in the camera is phase locked to a reference signal from the laser. The deflection sweep is then driven by the sinusoidal signal from the oscillator. The signal is accumulated from several laser pulses. Due to the synchronization of the light source and the detector, a better temporal resolution is obtained, compared to the accumulation of single shots. In time-resolved measurements, the laser beam is split into two beams. Part of the laser output is taken directly to the streak camera as a time reference. The other part of the beam is directed through the sample.

The temporal reference and the signal, which has traversed the sample are recorded simultaneously on the same streak image. Picosecond time-resolved techniques enable the study of dynamics of relaxation in macromolecules. The molecule steps down from the first excited state (say S_1^*) to the lowest level of the first excited singlet state S_1 through vibrational relaxation at rate of k_{rlx} (as shown in see Fig. 2.14,also see Fig. 2.8). The constant k_R is the radiative decay rate (probability of radiative transition per second). Various nonradiative decay processes are described by the rate k_{NR} . These non-radiative decay processes may occur due to collision, quenching of emission by another species, energy with diffusion while the molecule itself relaxes to the ground state. The molecular

decay rates of internal conversion, intersystem crossing, and quenching are denoted as k_{1c} , k_{1s} , and k_q, respectively. The non-radiative decay rate is given by

$$K_{NR} = K_{1C} + K_{1S} + K_q , \tag{2.74}$$

and the fluorescence decay rate is given by

$$K_F = K_R + K_{NR} , \tag{2.75}$$

where the fluorescence life time is

$$\tau_F = (1/K_F) . \tag{2.76}$$

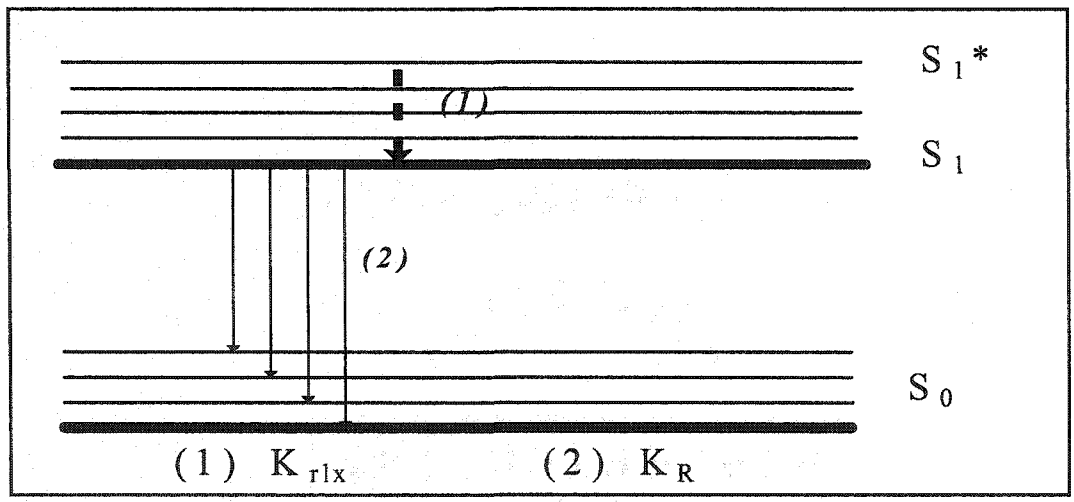

Fig. 2.14: Schematic diagram to show the vibrational relaxation (K_{rlx}) and the radiative Process (K_R).

The rate of change of a number of molecules in the emitting state S_1 can be expressed as [44,49]

$$\frac{dn_{S1}}{dt} = K_{rlx} n_{S1'} - K_F n_{S1} , \tag{2.77}$$

where n_{s_1} and $n_{s_1}^*$ are the number of molecules at the S_1 and S_1^* (vibrational excited state of S_1) levels, respectively. For a δ-pulse excitation, substituting for the number of molecules in the S^*_1 state as

$$n_{S1^*} = n_0 \exp(-K_{rlx} t) . \tag{2.78}$$

Substituting equation (2.78) into equation (2.77), equation (2.77) can be written as:

$$\frac{dn_{S1}}{dt} = K_{rlx} n_0 e^{-K_{rlx} t} - K_F n_{S1} , \tag{2.79}$$

where n_0 is the number of molecules at S_1^* at time $t = 0$. This can be written as,

$$\frac{d(n_{S1} e^{K_F t})}{dt} = K_{rlx} n_0 e^{(K_F - K_{rlx})t} . \tag{2.80}$$

Integrating equation (2.79), one can get the population at S_1,

$$n_{S1}(t) = \frac{K_{rlx} n_0}{K_{rlx} - K_F} (e^{-K_F t} - e^{-K_{rlx} t}) . \tag{2.81}$$

The two terms making up n_{s_1} are shown in Fig. 2.15. The rise time gives the vibrational relaxation from S_1^* and the decay gives the relaxation from S_1 to the ground state. The fluorescence intensity is proportional to n_{s_1} which is

$$I(t) = K_R n_{S1}(t) . \tag{2.82}$$

The time to rise to the peak t_p (maximum intensity) is given by,

$$t_P = \frac{Ln(K_{rlx} / K_F)}{(K_{rlx} - K_F)} , \tag{2.83}$$

where the solvent interaction can give rise to a more complicated time dependence of the relaxation rate to diffusion and relaxation dynamics.

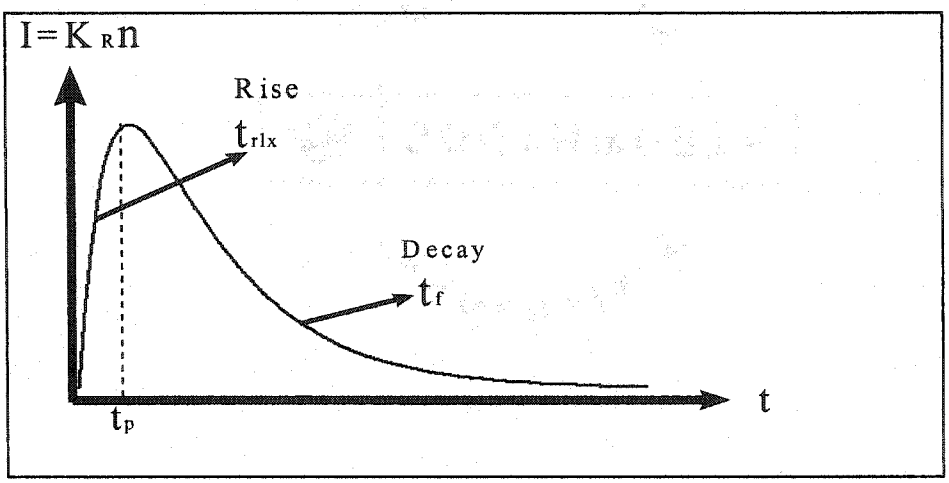

Fig. 2.15: Schematic diagram shows the decay process of state S_1.

The quantum efficiency (or quantum yield) can be written as [44]

$$Q = \frac{k_R}{(k_R + k_{NR})} = \frac{k_R}{k_F} = \frac{\tau_F}{\tau_R}. \tag{2.84}$$

2.8 Imaging and Scanning Principles

When light enters a turbid medium (such as paint or prostate tissue) it will be multiply scattered. A change in the state of tissue from normal to cancerous or change in the surface structure (corrosion or crack) beneath the paint will most likely result in a change in the light scattering such as angular intensity, polarization, and coherence.

In steady state imaging, the most common method is to use a CW light beam incident on the sample and to monitor the image using a CCD camera with the help of optical components. The back scattering geometry is a potential non-invasive technique that could be very useful for medical applications such as prostate and breast cancer detection, and non-medical applications such as cracks and corrosion detection beneath paint.

To investigate the enhancement of the imaging techniques, the contrast (or modulation) and the resolution are measured. The contrast is the difference in light intensity in an object or image, and defined as:

$$C = \left(\frac{I_{max} - I_{min}}{I_{max} + I_{min}}\right), \tag{2.85}$$

where I_{max}, I_{min} are the maximum and minimum intensity of fluorescent, absorption or the scattered light recorded from the object by the detection system.

Non-laser illumination for confocal microscopy, aside from cost and availability, wavelength flexibility and coherence are important. Non-laser light has much lower degree of coherence. Roughly speaking, we consider light to be incoherent when we don't get interference and to be coherent when we do. If the coherence of the light is too high, it gives rise to interference fringes by interacting with many optical surfaces of lenses and mirrors relaying the light from the source to the specimen. Even dust or minor surfaces defects will generate interference patterns. As a result, aside from a few special situations, low coherence illumination of specimen is desired in microscopy and this is available from non-laser sources. On the other hand, by reducing the spatial extent of the effective source emitting surface, non-laser sources can be arranged to deliver a high degree of spatial coherence. The ideal diffraction-limited objective will image an Airy disk from an infinitely small object point. The diameter of the first dark ring "d_{Airy}", generated by destructive interference [50]

$$d_{Airy} = \frac{1.22\,\lambda}{n.Sin\,\alpha}, \tag{2.86}$$

where λ is the used wavelength, n is the index of refraction of the medium, α is half angle of collected rays from object point. The product $n.Sin\alpha$ is the numerical aperture

that determine the resolution. Rayleigh set the limit for the smallest resolvable distance r_{Airy} between two points, or the radius of the airy disk, at

$$r_{Airy} = \frac{1.22\ \lambda}{2 \cdot NA}. \tag{2.87}$$

Deviation from the diffraction limited image point caused by lens aberrations can be grouped into monochromatic wavelength independent effects such as spherical aberration, astigmatism and distortions and chromatic wavelength dependent effects such as longitudinal chromatic aberration and lateral aberration. The lateral resolution $r_{Lateral}$ is given by [51-53]:

$$r_{Lateral} = \frac{1.22\lambda}{2 \cdot NA} = \frac{0.61\lambda}{NA}, \tag{2.88}$$

and the axial resolution r_{Axial} is given by

$$r_{Axial} = \frac{(1.4)\lambda . n}{NA^{2}}. \tag{2.89}$$

For an experiments with $\lambda_0 = 4.9\ \mu m$, n=1.3 (index of refraction), lens diameter of 30mm and focal length of 10mm (N.A. = $d/2f_m$ = 30 mm/20 mm = 1.5) the lateral resolution for the confocal microscope is calculated to be $\sim 2\ \mu m$, and the axial resolution is about $4\ \mu m$.

A lens which is positioned perpendicularly to the incident parallel rays brings them together at a point, known as the focal point. Thus if we want to capture an infinitely remote object on a CCD chip, the distance between the lens and the chip has to be exactly that of the focal length. In other words, the CCD chip has to lie in the focal plane as shown in Fig. 2.16. Focusing a lens means changing the distance between the lens itself and the CCD chip. Usually a lens is capable of focusing from infinity

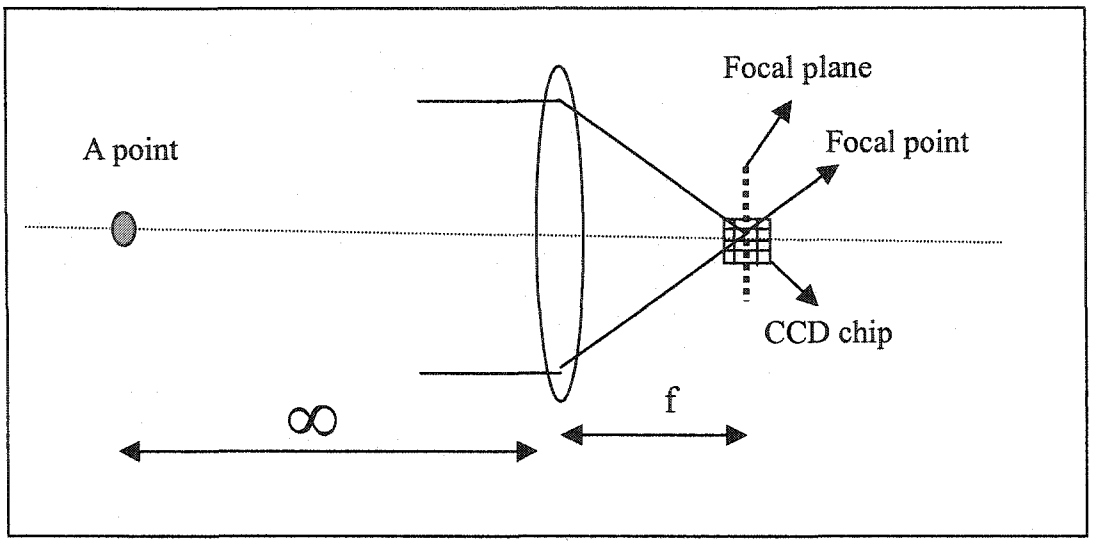

Fig. 2.16: Shows the principles of a lens, where the CDD chip lies in the focal plane.

to the so-called minimum object distance. The minimum object distance can be decreased by installing an extension tube (macro ring) between the lens and the camera. The longer the extension tube, the smaller the minimum and the maximum object distances become. A CCD pixel absorbs light (wavelength 400nm to 1000nm) and releases a charge which, during readout, is transformed into a voltage. Additional electrons are generated due to thermal effects - the so-called dark current - which is the cause of undesirable noise. As a result a CCD chip, which is not illuminated is saturated with electrons after roughly one minute of operation at room temperature. The dark current doubles approximately every 7 Kelvin, which means that the noise increases drastically with the temperature of the chip. One of the basic parameters of CCD chips is their resolution expressed in number of effective pixels or pixel elements. A sample of a typical modern high-resolution CCD chip (CH350 photometric) has 1024 pixels in the horizontal direction (columns) and 1024 pixels in vertical direction (rows). The spectral response characteristic is an important optical parameter. Quantum efficiency is the measure of the effectiveness of an imager to

produce electronic charge from incident photons. This is an especially important property when doing low-light-level imaging. Because most visible-NIR CCD imagers are made from silicon, it is useful to examine the properties of this element and the way that it interacts with light. In the high-purity crystalline form, each atom of silicon is covalently bonded to its neighbor. Energy greater than the band gap energy, about 1.1 eV, is required to break a bond and create an electron hole pair. Electron hole pairs are produced by photons in the region from 400 to 1100 nm. Within the visible spectrum, the photon to electron conversion factor is less than unity and it varies as a function of wavelength. Figure 2.17 and figure 2.18 show the spectral response of the typical Visible photometric (CH350) CCD chip and InGaAs CCD chip, respectively. Dark current arises from thermal energy within the silicon lattice comprising the CCD. Electrons are created over time that are independent of the light falling on the detector. These electrons are captured by the CCDs potential wells and counted as signal. Additionally, this increase in signal also carries a statistical fluctuation known as dark current noise. CCDs can be cooled either with thermoelectric coolers (TECs) or liquid nitrogen to reduce this effect. Ideally, the dark current noise should be reduced to a point where its contribution is negligible over a typical exposure time. Dark current, or thermally generated charge, can be measured and subtracted from data, but its noise component cannot be isolated. Dark current noise is a particular concern in low-light applications. Resolution is a term often used to mean spatial resolution, but temporal resolution and intensity resolution (dynamic range) are also important when determining the appropriate camera and the appropriate camera settings for an application. Spatial resolution is the minimum distance between two objects in a field of view, such that the objects can be resolved as being separate. If

objects are closer than the spatial resolution that the imager allows, the charge from the objects will combine in one pixel and image as one object. Temporal resolution is the maximum number of frames per second the imaging system can acquire. A high temporal resolution allows one to make multiple images quickly.

Intensity resolution (dynamic range) is the range of minimum to maximum intensity values within a field of view. It is the ability to quantitatively detect very dim and very bright pixels within a single image. A CCD of a typical full well of 45,000 electrons has an 11 electrons read noise (45,000/11=4091). This system would cooled be matched with a 12 bit A/D converter which is capable of 4095 gray scales. The other example is a 512 CCD which typically has a full well of 450,000 electrons and read noise of 7 electrons (450,000/7=64,286). This system would be matched with a 16 bit A/D converter which is capable of 65,535 gray scales. Photometrics camera systems have anywhere from 12 to 16 bits of resolution which yields 4095 to 65,535 gray scales. A workable definition of dynamic range is the ratio of the highest (lightest) signal which a scanner can record to the lowest (darkest) signal. The lightest signal would correspond to the brightest highlights in an image, the darkest signal to the deepest shadows. The units used for this measurement are density units (D) and the scale is logarithmic. The formula is: $D = \log (Io/I)$, where Io is the intensity of the light falling on the slide and I is the intensity of the light transmitted by the slide. For example, if the transmitted light signal is 50% or 0.01%, then the density (D) is 0.3 and 4, respectively. Photon noise, also known as photon or photon shot noise, is a fundamental property of the quantum nature of light. The total number of photons emitted by a steady source over any time interval varies according to a Poisson distribution. The charge collected by a CCD exhibits the

same Poisson distribution, so that the noise is equal to the square root of the signal. Photon noise is unavoidable and is always present in imaging systems; it is simply the uncertainty in the data.

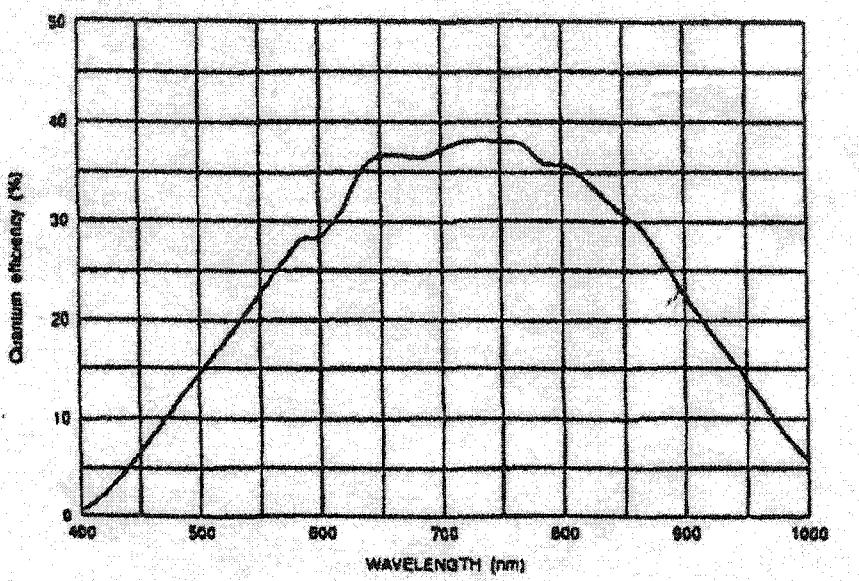

Fig. 2.17: The quantum efficiency of the silicon photometric CCD chip.

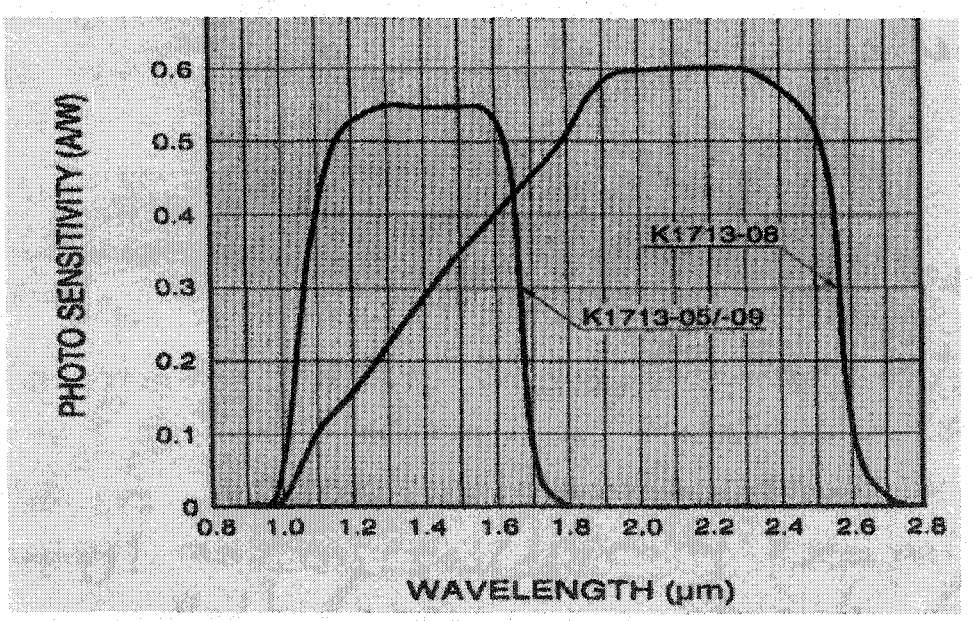

Fig. 2.18: The photo sensitivity of the InGaAs CCD chip.

2.9 References

1. http://www-class.unl.edu/bios201a/spring97/group6/
2. http://www.nku.edu/~dempseyd/SKIN.htm
3. Alberts, D. Bray, J. Lewis, M. Raff, K. Roberts, and J. D. Watson, Molecular biology of the cell, Garland, New York, 1994.
4. Private communication with Prof. Steven Jacques, 2003.
5. http://www.brucerosemanmd.com/id53.htm
6. http://www.upmccancercenters.com/cancer/prostate/dre.html
7. The Cancer Book, Geoffery M. Cooper, Jones and Bartlett Publishers, London, England, 1993.
8. Ackerman's Surgical Pathology, Juan Rosai, V. 2, Mosby Incorporated, 1998.
9. Ramzi S. Cotran, Vinay Kumar, Tucker Collins, Robbins pathology basis of disease, Elsevier Science, 6th edition, 1998.
10. H. C. Van de Hulst, Light scattering by small particles, Dover, New York, 1981.
11. C. F. Bohren and D. R. Huffman, Absorption and scattering of light by small particles, John Wiley and Sons, New York, 1983.
12. A. Ishimaru, Electromagnetic wave propagation radiation and scattering, Prentice-Hall Englewood Cliffs, New Jersey, 1995.
13. S. Chandrasekha, Radiative transfer, Dover, New York, 1960.
14. J. R. Lakowicz, Principles of fluorescence spectroscopy, 1999.
15. Oliver Howarth, Theory of spectroscopy, John Wiley and Sons, 1973.
16. R. Chang, Basic principles of spectroscopy, McGraw-Hill, 1971.
17. Cantor and Schimmel, Biophysical Chemistry, 1990.
18. G. R. Fleming, J. M. Morris and G. W. Robinson, Chem. Phys. 17, 91, 1976.
19. T. J. Chuang and K. B. Eisenthal, J. Chem. Phys. 57, 5094, 1972.
20. T. Tao, Biopolymers 8, 609, 1969.

21. F. J. Perrin, J. Phys. Radium 5, 497, 1934.

22. G. Porter, P. J. Sadkowski and C. T. Tredwell, Chem. Phys. Lett. 49, 416, 1977.

23. J. R. Mourant, J. P. Freyer, A. H. Hielscher, A. A. Eick, D. Shen, and T. M. Johnson, Apl. Opt. 37, 3586, 1998.

24. A. Ishimaru, Wave propagation and scattering in random media, New York, Academic press, 1978.

25. S. T. Flock, B. C. Wilson, and M. S. Ptterson, Med. Phys. 14(5), 835, 1987.

26. B. C. Wilson and S. L. Jacques, IEEE J. Q. Elec. 26 (12), 2186, 1990.

27. M. S. Patterson, B. C. Wilson, and D. R. Wyman, Lasers Med Sci 6, 155, 1991.

28. R. Haskell, L. Svaasand, T. Tsay, T. McAdams, and B. Tromberg, J. Opt. Soc. Am. A 11, 2727, 1994.

29. A. Ishimaru, Appl. Opt. 28, 2210, 1989.

30. K. M. Case and P. F. Zweifel, Linear Transport Theory, Addison-Wisley, Reading, Mass., Sec. 1.3, 1967.

31. J. J. Duderstandt and L. J. Hamilton, Nuclear Reactor Analysis, wiley, New York, 1976.

32. T. Durduran, A.Yodha, B. Chance, and D. Boas, J. Opt. Soc. Am. A14, 3358, 1997.

33. M. Lax, V. Nayaramamurti and R. C. Fulton in Laser Optics of Condense Matters edited by J. L. Birman, H. Z. Cummins, A. A. Kaplyaskii, Plenum, New York, 229, 1987.

34. G. H. Watson, S. L. McCall, P. A. Fleury and K. B. Lyons, Phys. Rev. B, 41, 10947, 1990.

35. X. Zhang and Z. Q. Zhang, Phys. Rev. E66, 016612, 2002.

36. R. Elalounfi, R. Carminati, and J. J. Greffet, J. Opt. A: Pure Appl. Opt. 4, S103, 2002.

37. B. B. Das, Thesis, The City University of New York, 1993.

38. Rik H. J. Kop, Pedro de Vries, Rudolf Sprik, and Ad Lagendijk, Phys. Rev. Lett. 79, 4369, 1997.

39. J. M. Drake and A. Z. Genack, Phys. Rev. Lett. 63, 259, 1989.

40. D. Bicout, C. Brosseau, A. Martinez, and J. Schmitt, Phys. Rev. E. 49, 1767, 1994.

41. D. Bicout and C. Brosseau, J. Phys. I(France) 2, 2047, 1992.

42. A. D. Kim and M. Moscoso, Phys. Rev. E., 64, 26612, 2001.

43. Ming Xu et al. to be published.

44. Parker, C. A., Photoluminescence of solution with application to photochemistry and analytical chemistry, Elsevier pub. Cor., 1968.

45. Alan G. Marshall, Biophysical Chemistry, John Wiley & Sons, 1978.

46. N. H. Schiller, A. Dagen and R. R. Alfano, Optical Spectra 15, 56, 1982.

47. R. R. Alfano, ed. " Biological events probed by ultrafast laser spectroscopy", Academic press, New York, 1982.

48. Y. Tsuchiya, Quantum Electronic QE-20, 1516, 1984.

49. B. B. Das, Feng Liu, and R. R. Alfano, Rep. Prog. Phys. 60, 235, 1997.

50. Jenkins, FA., White HE., Fundamentals of Optics, New York, McGraw-Hill, 1976.

51. T. Wilson and C. J. R. Sheppard, Theory and practice of scanning optical microscopy, Academic, London,1984.

52. T. Wilson, ed., Confocal Microscopy, Academic, London, 1991.

53. James B. Pawley, ed. "Handbook of biological confocal microscopy", Plenum press, 1995.

Chapter 3

Time-resolved Fluorescence, Polarization, and Scattering Properties of Contrast Agents and Human Prostate Tissue

3.1 Introduction

In this chapter we present the experimental work of the time resolved light fluorescence, polarization, and scattering in animal, and human prostate tissues using ultrashort laser pulses such as Nd-YAG and Ti:Sapphire lasers. Temporal polarization fluorescence of Cardio Green dye and the dipole reorientation of Cardio Green molecules in water will be investigated. Time resolved fluorescence polarization dynamics and imaging of Fluorescein dye-labeled polymers of molecular weight ranging from 4 K to 500 K at two polarization directions parallel and perpendicular to that of the linearly polarized exciting light will be investigated. The optical properties of human prostate tissue (transport mean free path and absorption lengths) using Ti:Sapphire femtosecond at 800 nm laser pulses will be measured with the pulse transmission technique using the diffusion equation.

3.2 Fluorescence Polarization Anisotropy of Cardio Green Contrast Agent

3.2.1 Background

Contrast agents are widely used in various medical imaging modalities to enhance the visibility of the desired area of the body [1]. The contrast agents dyes have been introduced in optical imaging studies to improve the image quality of objects hidden in

scattering media or tissues [2-3]. Cardio Green (CG or Indocyanine Green) dye is currently used as a diagnostic aid for blood volume determination as well as cardiac and liver function tests [4]. Dyes such as IG is useful to be used in optical tissue imaging since their absorption and emission is in the NIR region where scattering is low (compare to visible) and penetration depth is high. The absorption and fluorescence spectra of the Cardio Green dye are shown in Fig. 3.1. The Cardio Green dye has a strong absorption peak at 780 nm and a strong fluorescence peak around 815 nm. Understanding the Cardio Green dye optical properties is an important step towards better use in medical applications such as in analyzing prostate tissues.

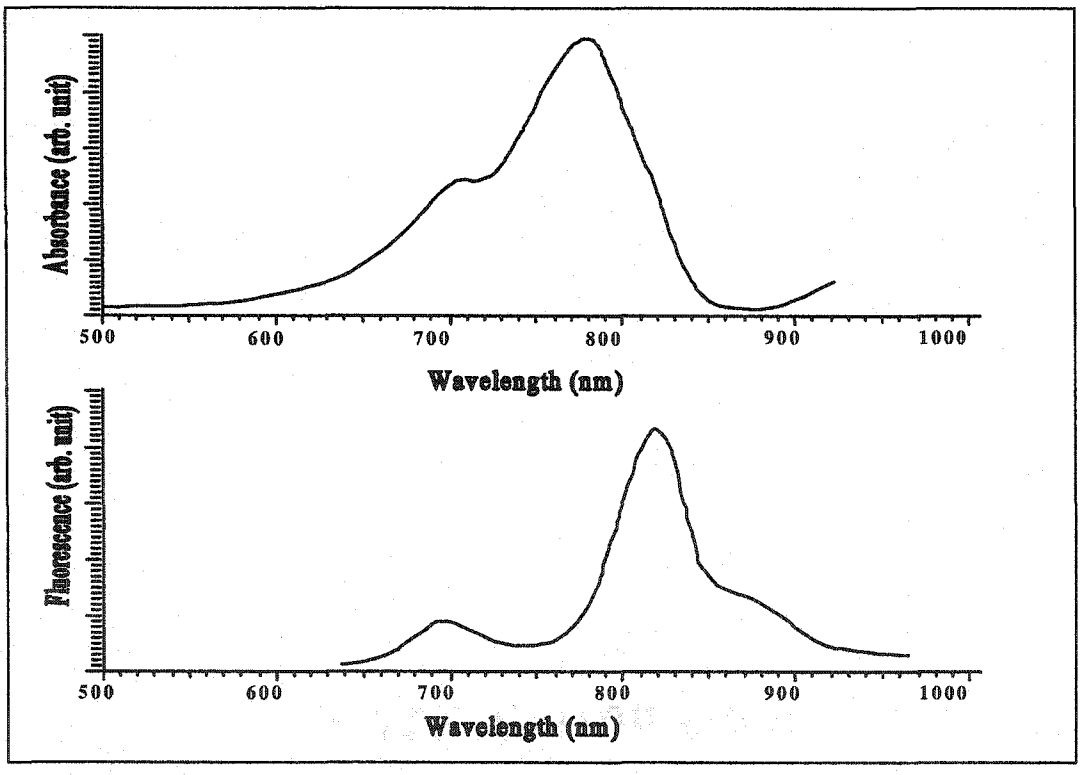

Fig. 3.1: Absorption and fluorescence spectra of Cardio Green dye in water. The Cardio Green dye has a strong absorption peak at 780 nm and a strong fluorescence peak around 815 nm.

Orientational dynamics is aimed at understanding the motion of solute molecules in their solvent environment. The nature and time scale of molecular motions is changed dramatically when a molecule is placed in solution. One of the simplest approaches for probing solute-solvent interactions is to determine how simple molecular motions are altered by the solvent. Since optical spectroscopic methods are capable of measuring reorientational dynamics on the time scales that are relevant to solute-solvent interactions, we use time-resolved spectroscopy to probe reorientational motions. The two decays in the investigated sample are a result of emission polarized parallel and perpendicular to the laser excitation polarization. A streak camera instrument records the time between a start pulse corresponding to excitation of a molecule, and the emission of a fluorescence photon. From this data, the excited-state lifetime (fluorescence lifetime) of the molecule can be determined. In addition, by measurement of the decays of fluorescence polarized parallel and perpendicular to the polarization of the excitation pulse, fluorescence depolarization can be measured in order to determine the rates of molecular reorientation (e.g. by rotational diffusion).

We present an investigation of Cardio Green dye polarization anisotropy in water (water forms 70% of the human body mass) and the potential use in medical applications such as detecting cancer tissues hidden beneath normal tissues.

3.2.2 Experimental Methods

The experimental arrangement of the time-resolved fluorescence measurement for contrast agent dyes is schematically shown in Fig. 3.2. Pulses of 500fs at 630nm output from a Rhodamine 6G dye laser, synchronously pumped by a Nd:YAG laser with a pulse compression and second harmonic generation system, were used to pump Cardio Green

dye solved in water with a concentration of 5×10^{-5} M. The fluorescence from the dye was collected by a large diameter lens (L_2) with a focus length of 5 cm and directed onto the input slit of an S-1 photo cathode in a synchroscan streak camera (Hamamatsu Model C1589). A notch filter (NF) of 630 nm and along pass (LP) filter 660 nm were used to cut off the illuminating light so that only the dye emission (> 660 nm) is recorded. Two polarizers (P_1 and P_2) were used. P_1 was used to ensure the linear polarization of the input laser pulses and P_2 used as an analyzer. P_2 was rotated with respect to P_1 to record the parallel and perpendicular polarization components of the fluorescence. The temporal profiles recorded by a silicon intensified target (SIT) vidicon camera were analyzed to obtain temporal and polarization information of the Cardio Green dye fluorescence.

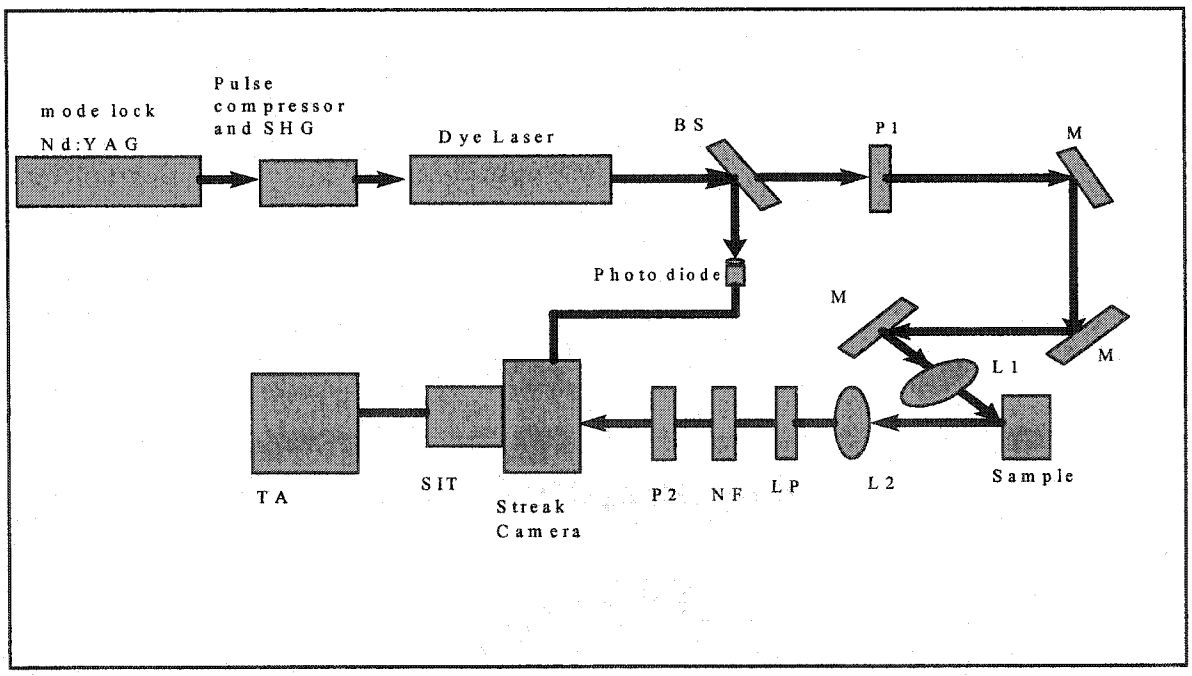

Fig. 3.2: Schematic diagram represents the experimental set up for the time-resolved fluorescence measurement. P_1, P_2: polarizers; M: mirror; BS: beam splitter; NF: notch filter of 630 nm; LP: long pass filter of 660 nm; SIT: silicon intensified target; TA: temporal analyzer.

3.2.3 Experimental Results

The measured polarized temporal profiles of the fluorescence emitted from the Cardio Green dye for two polarization orientations parallel and perpendicular to the polarization direction of the excitation light of 630 nm are shown in Fig. 3.3. The thick-line profile is the parallel emission component $(I_{//}(t))$, *and* the thin-line profile is the perpendicular one $(I_{\perp}(t))$.

3.2.4 Discussion and Outcome

The main difference for the parallel and perpendicular temporal profiles is their onset intensities. The parallel component $(I_{//}(0))$ is almost 3 times stronger than

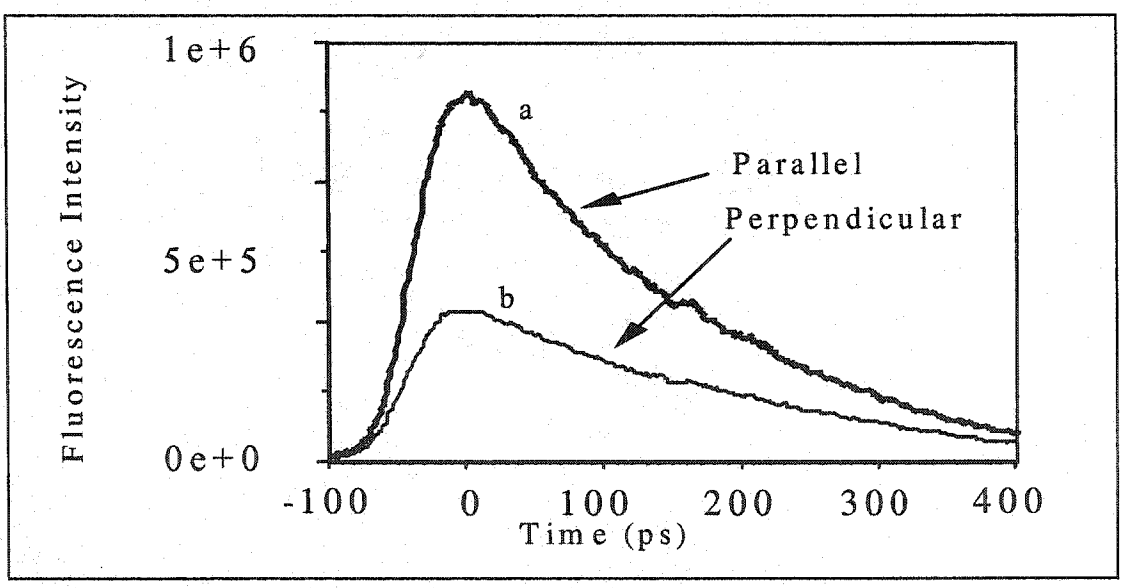

Fig.3.3: Parallel (a) and perpendicular (b) polarization temporal profiles of fluorescence emitted from Cardio Green dye in water under 630nm laser illumination.

that of the perpendicular one $(I_{\perp}(0))$ at peak intensity. This indicates that the absorption

and emission transition dipole moments are nearly parallel. In turn, the fluorescence emitted from Cardio Green has a preferred polarization direction. The time-dependent fluorescence polarization anisotropy of the emitted light was calculated from the equation:

$$r(t) = \frac{I_{//}(t) - I_{\perp}(t)}{I_{//}(t) + 2I_{\perp}(t)} \tag{3.1}$$

The r(t) can be written as [3-6]:

$$r(t) = \frac{2}{5}\left\langle P_2[\hat{e}(0)\cdot\hat{e}(t)]\right\rangle \tag{3.2}$$

where P_2 is the second Legendre polynomial of the dipole reorientation angle for any shape of molecule. The simplest possible case when the molecule undergoes Brownian rotational motion, then equation 3.2 becomes:

$$r(t) = \frac{2}{5}e^{-6Dt} \tag{3.3}$$

The temperature (T), volume of the molecule (V), and viscosity (η) of the dye solution contributes to the diffusion decay constant D by [3-6]:

$$D = \frac{KT}{6V\eta} \tag{3.4}$$

where K is the Boltzmann constant.

The calculated temporal profile of the polarization anisotropy r(t) of the fluorescence emitted from Cardio Green is shown in Fig. 3.4. The value of r(0) = 0.33 at peak position decreases to r(t) = 0.15 within t ~ 400 ps. The value of the anisotropy r(t) at t = 0 (maximum) is 0.33 which is close to the theoretical value 0.4, because of a small angle between the emission dipole moment and the absorption dipole moment. The decay behavior of *r(t)* shown in Fig. 3.4 reflects the type of the dipole reorientation of Cardio

Green molecules in water.

The experiments were also performed under 760 nm linear laser excitation. Similar results for the emission from Cardio Green were observed. The polarization preservation property of Cardio Green shown in our time-resolved polarized fluorescence measurements indicates that it can be used as a contrast agent for the different imaging techniques to enhance the conventional image quality. This implies that the emission of the transition dipole moment is parallel, which makes this dye a strong candidate for imaging enhancement.

The optical properties of the parallel and perpendicular polarization of the Cardio Green dye, related to r(t), will be used to image a dyed foreign object in animal and human prostate tissues as will be shown in the steady state measurements in chapter 4. Also the spatial resolution and contrast of the dyed foreign object embedded in highly scattering animal and human tissues will be investigated.

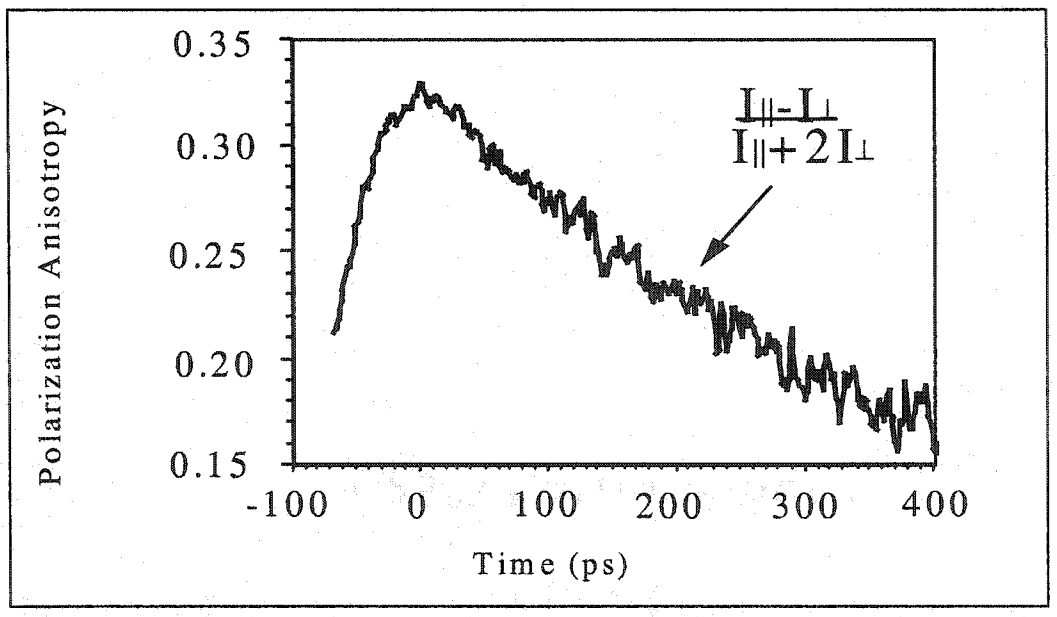

Fig. 3.4: Polarization anisotropy of fluorescence emitted from Cardio Green in water under a linear polarized 630 nm laser illumination.

3.3 Time Resolved Fluorescence Polarization Dynamics and Imaging of Different Molecular Weights Attached to Fluorescein Dye

3.3.1 Background

The polarization properties of the fluorescence from several contrast agent dyes such as Eosin, Rose Bengal, and TCTIF were investigated [3-7]. The light emitted from those dyes are partially polarized due to oriented transition dipole moments. Combining the property of polarization preservation of dye emission and the property of polarization preservation of light propagating in scattering media [8-10], novel imaging techniques can be developed and applied for imaging objects hidden inside scattering media such as human tissues.

In order to take advantage of the polarization difference imaging, dyes with a larger difference between the parallel ($I_{\parallel}$) and perpendicular ($I_{\perp}$) components of the emission are being investigated. A reasonable approach to obtain the larger difference ($I_{\parallel}$-$I_{\perp}$) is increasing the molecular weight (MW) of the emission molecules by attaching polymers to the dye, because for heavy MW dye-polymer conjugates, nonradiative rotational motion is expected to be inhibited given rise to a longer polarization decay time of the dye emission, and therefore, a larger difference of $I_{\parallel}$-$I_{\perp}$, and possibly a deeper imaging is achieved. The rotational time decay depends on the size of the molecule as proved in chapter 2, equation (2.24).

We present an investigation of MW dependence of the polarization preservation ability of the fluorescein dye-labeled polymers, using a fluorescence polarization

difference imaging "FPDI" measurement of an object containing varying MW of the dye-polymer conjugates embedded inside turbid media.

3.3.2 Experimental Methods

The dye-polymer conjugates used in our measurements were fluorescein-labeled dextrans of molecular weight range 4 K to 500 K (Sigma, St.Louis, MO). The molecular weight and length per unit dextran is ~162 daltons and ~3 angstroms, respectively. The same concentration of 50 μM in aqueous solution was made for all of the different MW conjugates.

The typical experimental setup for measuring the time-resolved fluorescence polarization profiles has been shown in Fig. 3.1. Pulses of 150 fs at 400 nm obtained from the second harmonic of a Ti:Sapphire laser were used to pump the dye-polymer samples. Fig. 3.5 shows the absorbance spectra of the Fluorescein dye. The dye strongly absorbs at 490 nm and emits in the 495-530 nm spectral range with a peak of emission located at ~515 nm. The temporal profiles of emission from the dye-polymer conjugates at two polarization directions parallel [$I_{\parallel}(t)$] and perpendicular [$I_{\perp}(t)$] to that of the linearly polarized excitation light were recorded by a synchroscan streak camera (Hamamastu Model C5680).

For imaging measurements, an Argon laser at 488 nm with average intensity of ~5 mW/cm^2 was used as an illuminating light as shown in Fig. 3.6. A 7 cm x 5 cm x 5 cm glass cell containing intralipid solution with a concentration of 0.09% was located in the sample position. In the middle of the cell, there were two 1-mm-diameter pipettes filled with the Fluorescein dye-polymer of 50 μM disolved in water at MW of 4 K (left) and 40

K (right). The two polarization images of the dye-polymer-containing pipettes were recorded by a cooled CCD camera when the detection polarization direction was parallel and perpendicular to that of the pump beam, respectively.

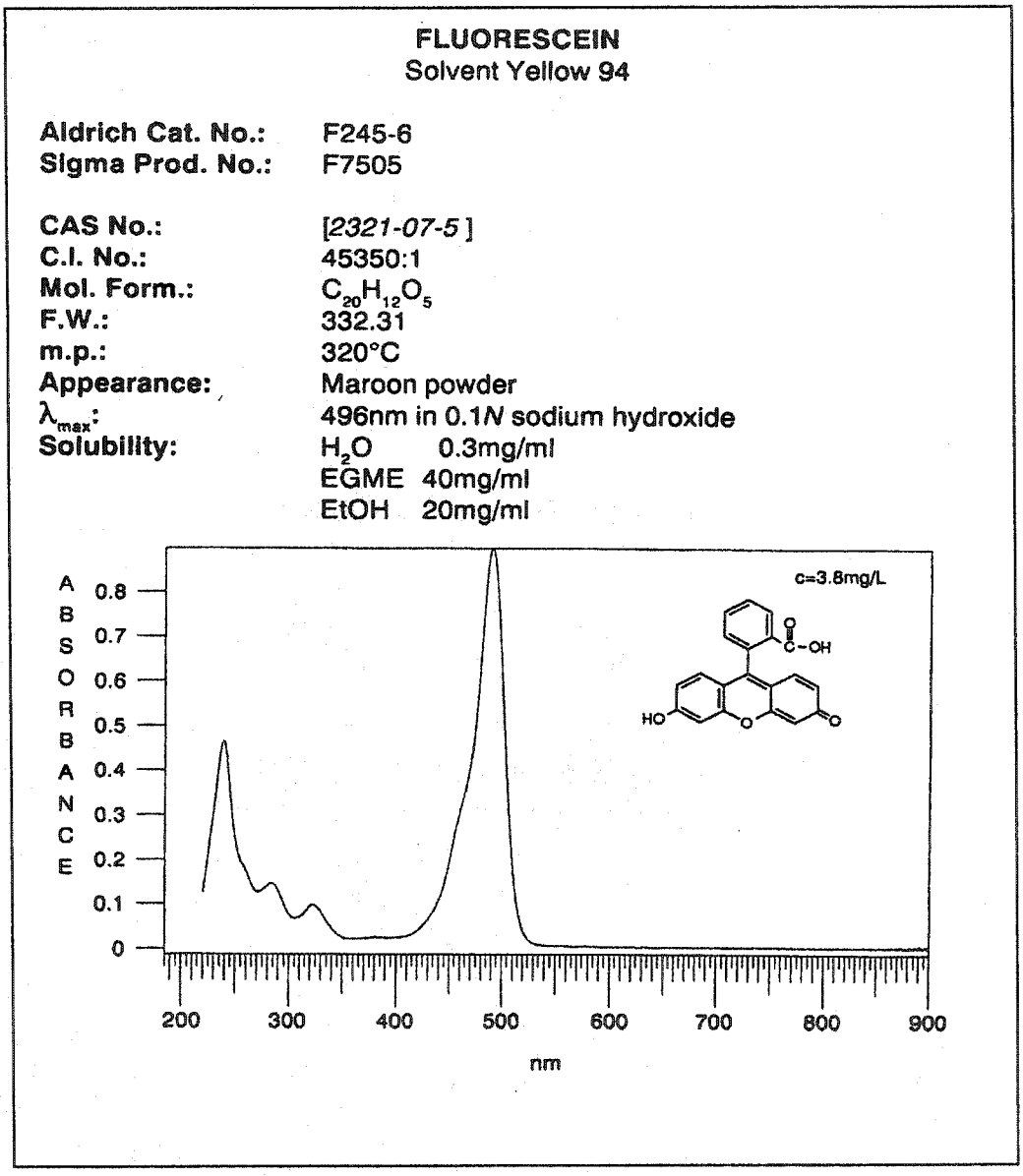

Fig. 3.5: Absorbance spectra of the Fluorescein dye.

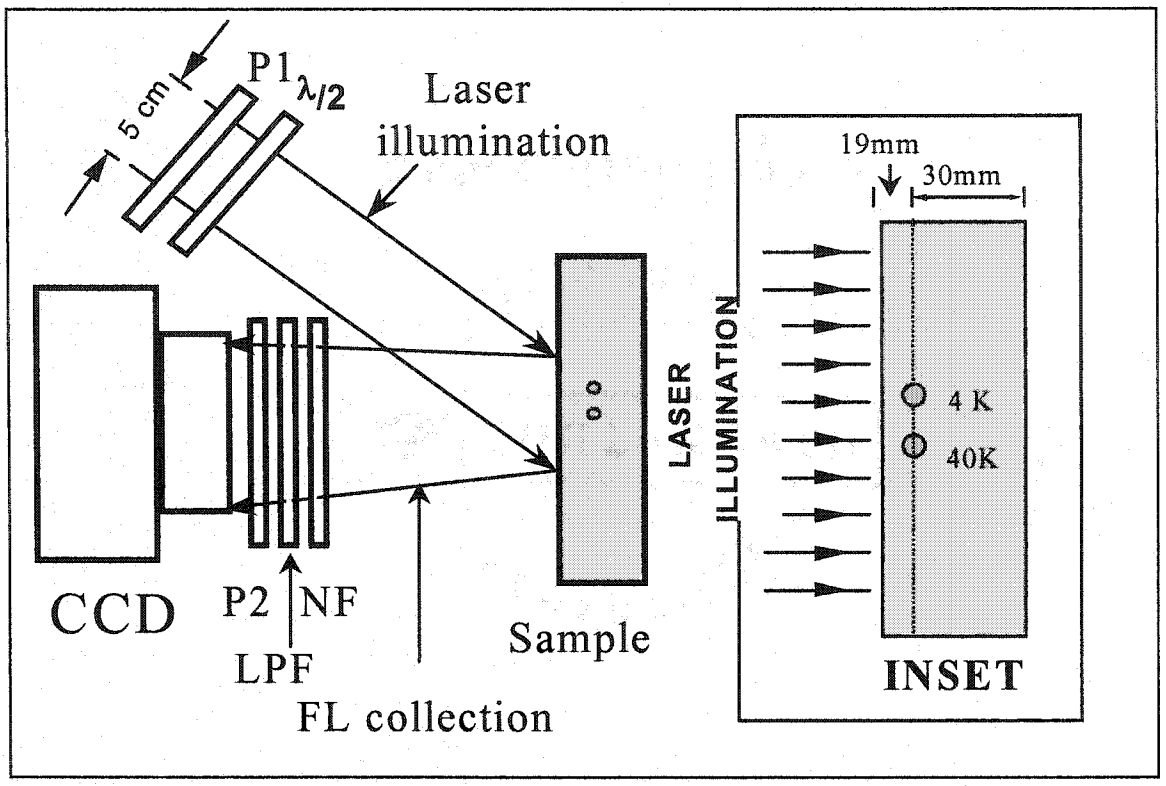

Fig. 3.6: Schematic diagram of the experimental set up for fluorescence imaging measurements.

3.3.3 Experimental Results

The time-resolved fluorescence polarization profiles were measured for pure fluorescein dye (molecular weight of 0.376 K), and the Fluorescein dye-labeled dextrans of MW of 4 K, 10 K, 20 K, 40 K, 70 K, and 500 K, respectively. As an example, Figs. 3.7a and 3.7b show the measured temporal profiles of parallel and perpendicular components of the emission from the dye-polymer conjugates at MW of 4 K and 40 K, respectively. The solid-line profiles show the parallel component [$I_{\parallel}(t)$], and the dotted-line profiles show the perpendicular one [$I_{\perp}(t)$].

3.3.4 Discussion and Outcome

It can be seen that the intensity of $I_{\|}$ is greater than that of $I_{\perp}$ for all of the different MW of the fluorescein dye-labeled dextrans at the peak position of the intensity, which indicates that the light emitted from all of the dye-polymer conjugates under a linearly polarized laser excitation are partially polarized. This indicates that their absorption and emission transition dipole moments are nearly parallel. In turn, the light emitted from these dye-polymer conjugates have a preferred polarization direction.

The salient feature of the temporal profiles is their decay behavior. The parallel profile [$I_{\|}(t)$] has a short decay followed by a long flat decay, while the perpendicular profile [$I_{\perp}(t)$] shows only a flat decay component. The short decay component of $I_{\|}(t)$ becomes longer when the MW of the dye-polymer conjugate increases. The degree of polarization (or polarization anisotropy) defined by $r(t)=[I_{\|}(t)-I_{\perp}(t)]/[I_{\|}(t)+2I_{\perp}(t)]$ was calculated for all of the dye-polymer conjugates with MW varying from 4 K to 500 K. As an example, Figs. 3.8a and 3.8b display the temporal profiles of the degree of polarization for dye-polymers with molecular weights of 4 K and 40 K, respectively. It is clear that the decay of the short component of r(t) becomes slower when the MW of the dye-polymer conjugates increases from 4 K to 40 K.

In order to obtain the MW dependence of the polarization decay, the decay time [the time for decay of r(t) from 90% to 10% of the maximum value of r(t)] was calculated for all of the dye- polymer conjugates with MW varying from 4 K to 500 K, and displayed in Fig. 3.9. The salient feature is that the polarization decay time increases with MW in the range of 0.376 K to 40 K, which can be understood because for heavy MW dye-polymer conjugates, nonradiative rotational motion is inhibited giving rise to a

longer polarization decay time of the dye emission. The polarization decay time remains unchanged when the MW increases beyond the 40 K. This can be explained because for very heavy molecules, the rotational motion is almost prohibited.

The recorded polarization images of the two pipettes filled with Fluorescein dye-labeled dextrans at MW of 4 K (left) and 40 K (right) are shown in Fig. 3.10. Fig. 3.10a displays the parallel image recorded when the detection polarization direction is parallel to that of the illuminating beam, whereas Fig. 3.10b displays the perpendicular images when the detection polarization direction is perpendicular to that of the illuminating beam. The polarization difference image for the dye-polymer conjugate of larger MW of 40 K is much brighter and clearer than that of smaller MW of 4 K. This can be understood because the polarization decay time for the dye-polymer conjugate with MW of 40 K is longer than that of MW of 4 K. Therefore, the total difference of $(I_{\parallel}-I_{\perp})$ for the dye-polymer conjugate of 40 K is larger than that of 4 K as shown in Fig. 3.10c. Fig. 3.10c shows the polarization difference image obtained by subtracting the perpendicular image [Fig. 3.10b] from the parallel image [Fig. 3.10a]. It can be seen that the difference images of 4 K and 40 K shown in Fig. 3.10c are better than their corresponding parallel and perpendicular images. This can be explained because the strong diffusion image component is canceled out when the two polarization image components are subtracted, and only ballistic and partial snake photons contribute to the formation of the polarization difference image. This observation clearly demonstrates that the high molecular weight dye-polymer conjugates can be used to enhance the imaging depth and visibility of objects hidden inside scattering media and tissues in comparison with dyes without the polymer attached.

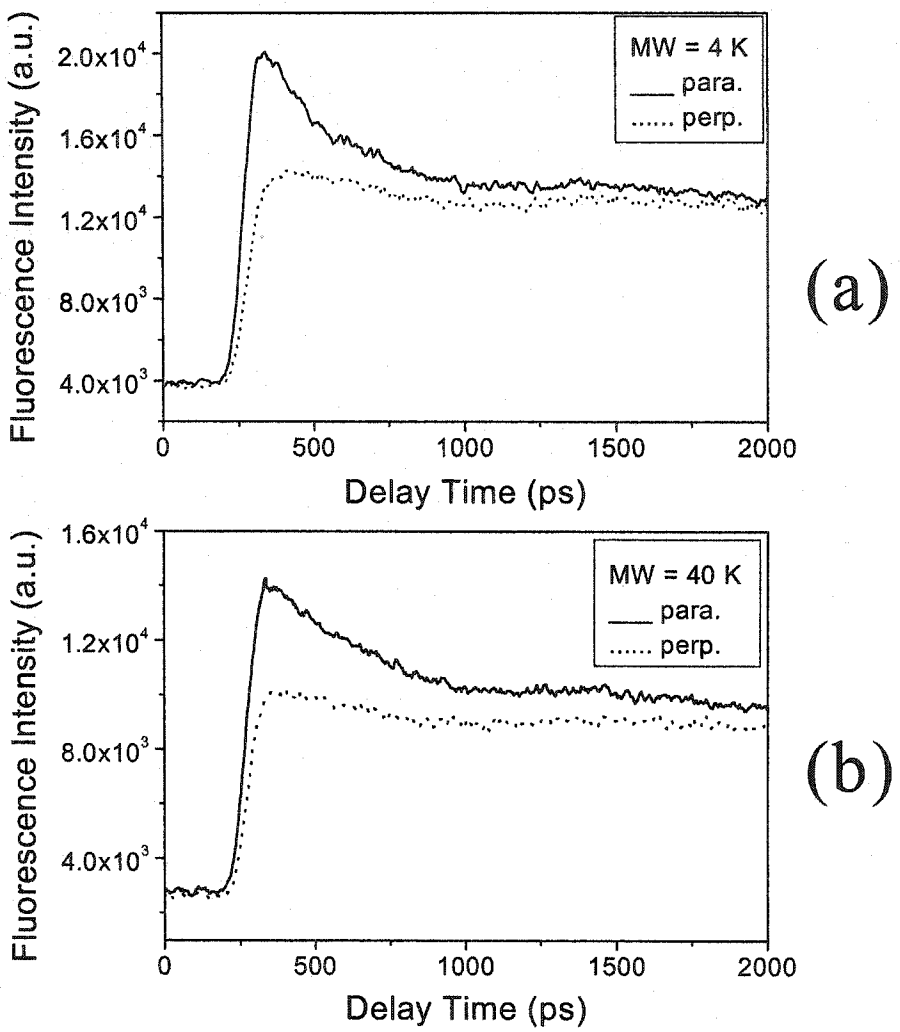

Fig. 3.7: The temporal profiles of parallel (solid line) and perpendicular (dotted line) components of emission from Fluorescein dye-polymer conjugates at molecular weights of (a) 4 K and (b) 40 K.

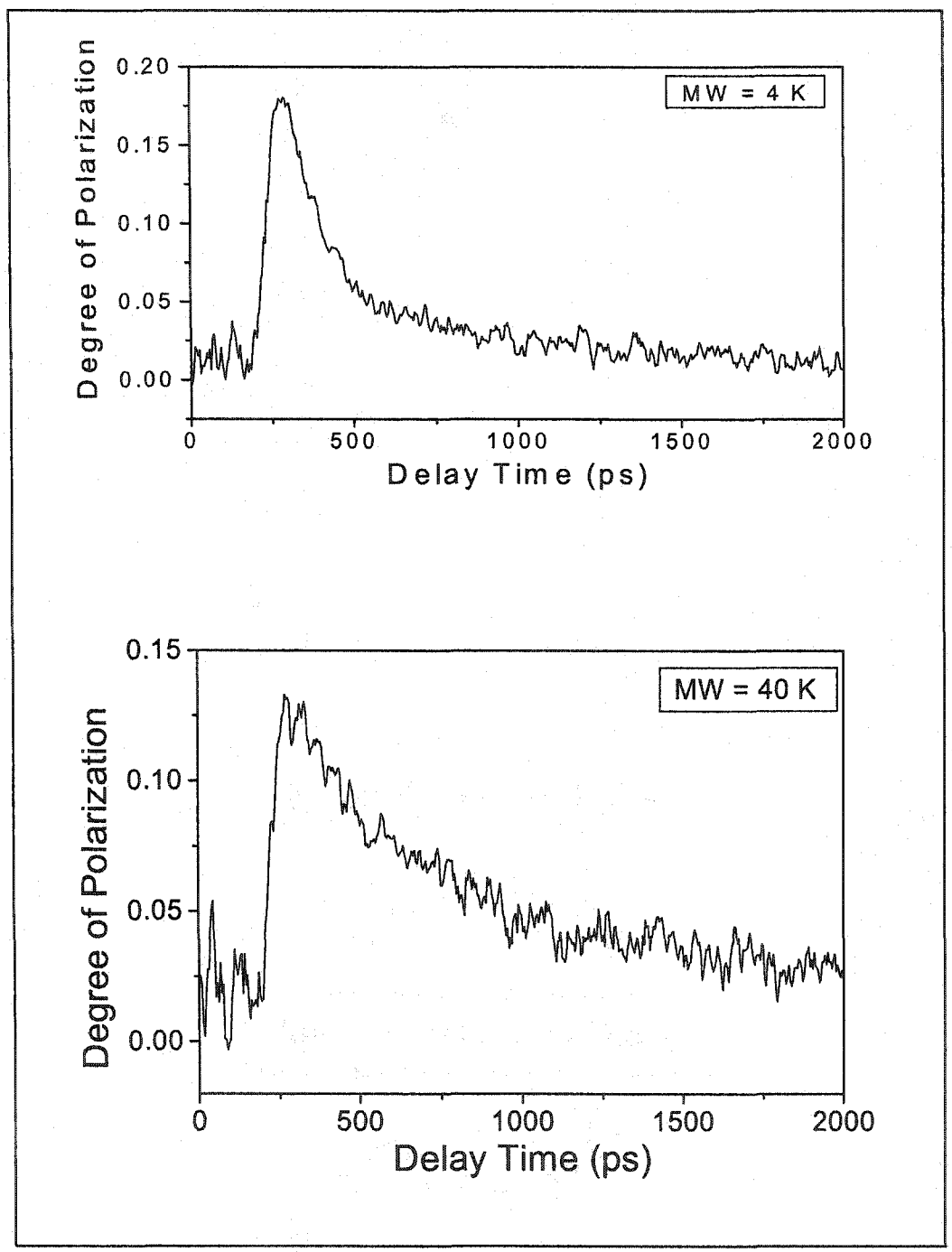

Fig. 3.8: The temporal profiles of the polarization anisotropy for dye-polymer conjugates at molecular weights of (a)4K and (b)40K.

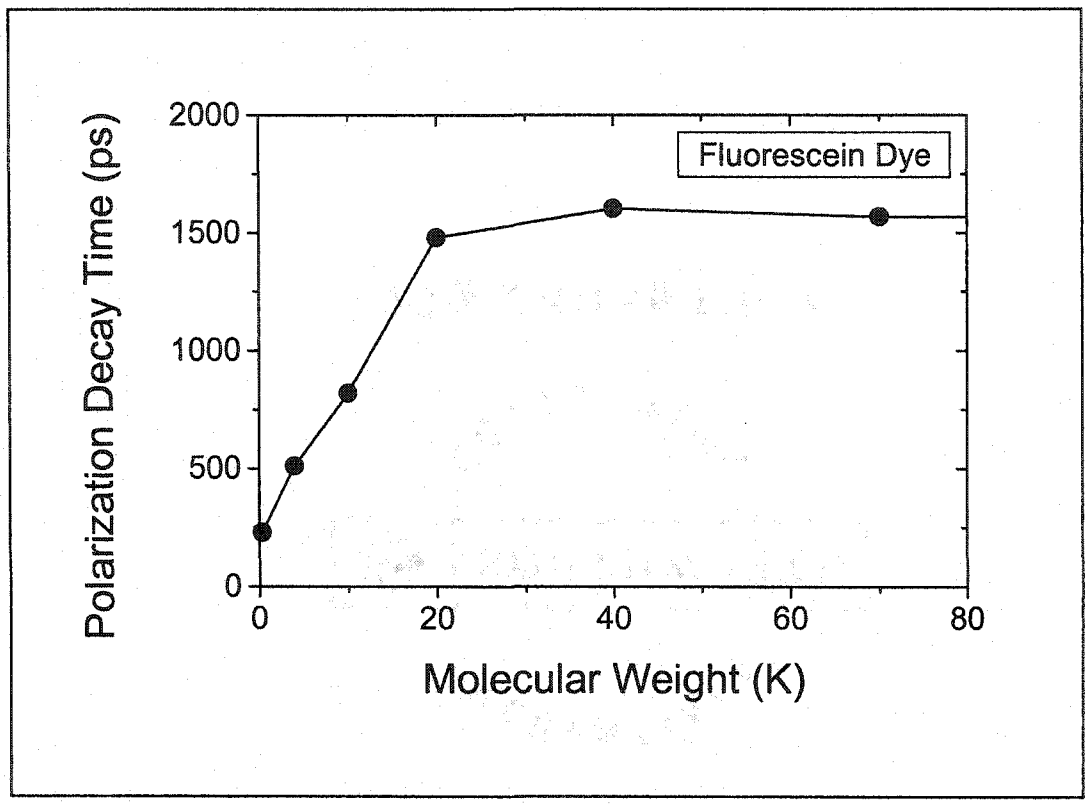

Fig. 3.9: The decay time of the polarization anisotropy r(t) [the time for decay of r(t) from 90% to 10% of its maximum value] as a function of molecular weight.

In conclusion, the temporal emission profiles of Fluorescein dye-labeled polymers of molecular weight ranging from 4 K to 500 K at two polarization directions parallel and perpendicular to that of the linearly polarized exciting light were measured. The polarization decay time of dye-polymer conjugates increases with molecular weight. Images of an object containing varying molecular weight fluorescein dye-labeled polymers embedded inside turbid media were investigated. The difference image at high polymer molecular weight was found to be much brighter and clearer than that at low molecular weight. This observation demonstrates that high molecular weight dye-

polymer conjugates can be used to enhance the imaging depth and visibility of objects hidden inside scattering media and tissues.

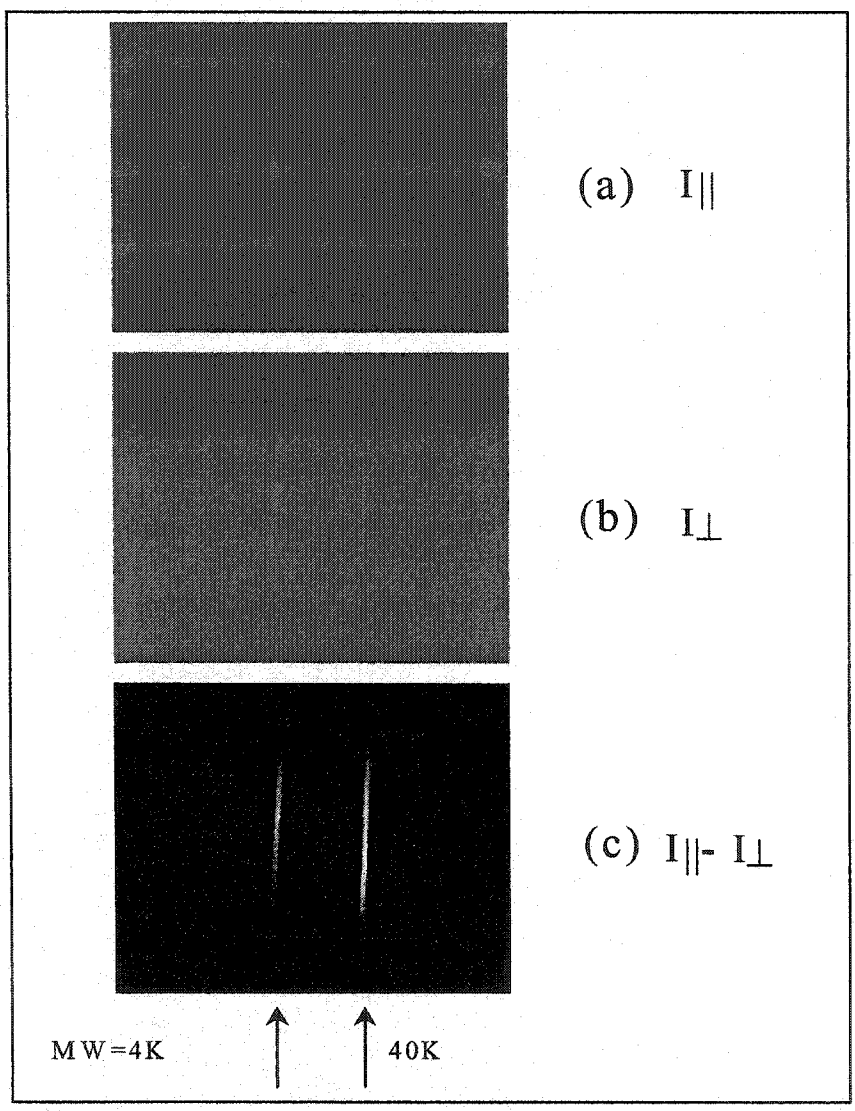

Fig. 3.10: Polarization images of the two pipettes filled with Fluorescein dye-polymer conjugates at molecular weights of 4 K (left) and 40 K (right).

3.4 Extracting the Optical Properties of Human Prostate Tissue

3.4.1 Background

Prostate cancer has a high incidence and mortality rate for men [11]. The detection and treatment of early small prostate cancers are most important to prevent death attributable to prostate cancer. Based on the spectral and polarization properties of the scattered, absorbed, and/or emitted light from prostate tissues and contrast agents, we will be able to develop novel noninvasive optical techniques for early detection of prostate cancers or to enhance the imaging qualities of objects hidden in a host of scattering media. For medical applications, such as optical tomography and spectroscopic measurements it is useful to know the maximum tissue depth that can be investigated with collimated light. Scattered photons that have lost their initial straightforward direction, temporal coherence, or polarization should not be detected. The preservation of light polarization has also been considered as an indication for forward on axis light propagation. It is critical to predict the maximum thickness of highly scattering tissue through which biological signals can be detected before the signal that carries the information is lost. The detectable ballistic light is expected to be a function of L/ℓ_S (L is the sample thickness and ℓ_S is the scattering mean free path). In the absence of absorption, we can estimate L_{Max}/ℓ_S, while the diffusive component can be related to the transport mean free path, $\ell_{tr} = \ell_S/(1-g)$, where g is the anisotropy factor. Once the transport mean free path is obtained, the maximum sample thickness L_{Max} at which the diffusive light dominates can be approximated using the diffusion theory.

Imaging of a translucent (scattering) object hidden in a highly scattering random medium with light is a challenging problem. However, strong random multiple scattering of light in tissues washes out the shadow and causes these techniques to be ineffective for imaging prostate tissues. The thickest scattering media to image or detect an object embedded in a random medium can be approximated by the number of scattering mean free lengths or the number of the transport scattering lengths. Diffusion theory is widely used to describe the transmission of light in highly scattering thick media. When ultrashort laser pulses are incident upon a slab of scattering medium (Fig. 3.11) the transmitted pulses consist of a ballistic (coherent) component, snake component, and diffusive component [10, 12-14]. The ballistic component (consisting of photons traveling along the straight-line path) is attenuated exponentially with the thickness of the

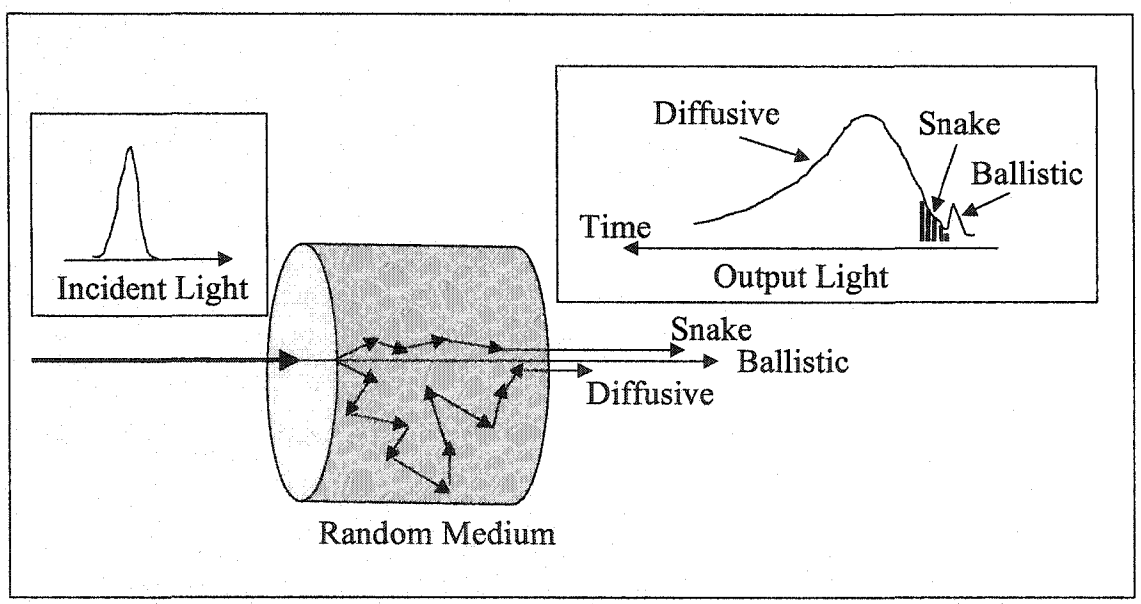

Fig. 3.11: The transmitted laser pulse through scattering random medium consists of ballistic, snake, and diffusive components.

sample, and this attenuation puts a severe limitation on its practical application, especially for medical imaging.

The intensity of the ballistic photons decreases exponentially by a factor of L/ℓ_S, where ℓ_S is the scattering mean free path of the medium and L is the medium thickness. The diffuse component is temporally broadened, as it consists of photons that have been scattered randomly in all directions and have traversed different path lengths. The temporal profile of a diffuse pulse can be approximated by the diffusion theory when the thickness of the sample is many times larger than the transport mean free path (ℓ_{tr}) of the sample. For a narrow beam of ultrashort laser pulses incident at a point on a slab, the temporal profile of a transmitted pulse at a point on the other side of the slab is predicted by the diffusion theory as [15]:

$$I(t) = \frac{1}{4td^2}\exp(-\upsilon t/\ell_a)\sum_{1}^{\infty} mSin(\frac{m\pi L}{d}) \times \exp(-(m\pi)^2 Dt/d^2), \qquad (3.5)$$

where d = L + 1.4 ℓ_{tr} for air-medium boundary, υ is the speed of light in the medium, D is the diffusion coefficient, and ℓ_a is the absorption length. The snake component, consisting of the early-arriving photons that have undergone only a few scatterings along quasi-straight-line paths (zigzag paths slightly off the straight-line path) through the turbid medium, *forms* the early portion of the diffuse pulse. The snake photons travel slightly off the straight path and, hence, carry information on the optical properties of the medium and any foreign object lying along this path line.

The transport length and absorption length are obtained from the attenuation of the transmitted diffusive photons through a prostate tissue of L thickness by fitting the experimental data to the diffusion model using equation 3.5.

3.4.2 Experimental Methods

The experimental setup is shown in Fig. 3.12. Ultrashort laser pulses from Ti:Sapphire laser of 150 fs duration, 800 nm wavelength, and 82 MHz pulse repetition rate were incident upon the sample. A part of the incident beam was used to trigger the streak camera with the use of a photodiode. The laser beam was focused by a long-focal-length lens (*f*=50 mm) into a small 1-mm-diameter spot on the sample.

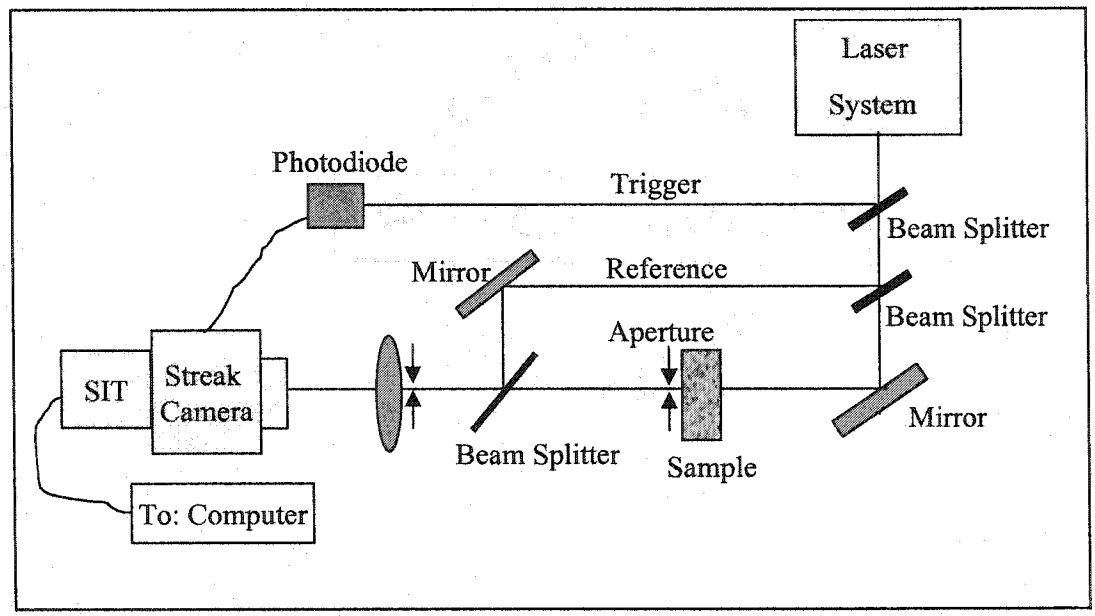

Fig. 3.12: The experimental set-up for time-resolved transmission measurements through a scattering prostate medium.

3.4.3 Experimental Results

We pressed the sample of prostate tissue between two parallel glass plates to keep them uniformly thick. The prostate sample thickness was about 2.5 cm. The transmitted signal was detected by a synchroscan streak camera. Small apertures were used to collect the transmitted photons scattered signal in the forward direction.

Figure 3.13 displays the temporal profile of the transmitted pulses propagating

through the 2.5 cm thick prostate tissue: the dotted curve represents the experimental data and the solid curve is computed from the diffusion theory.

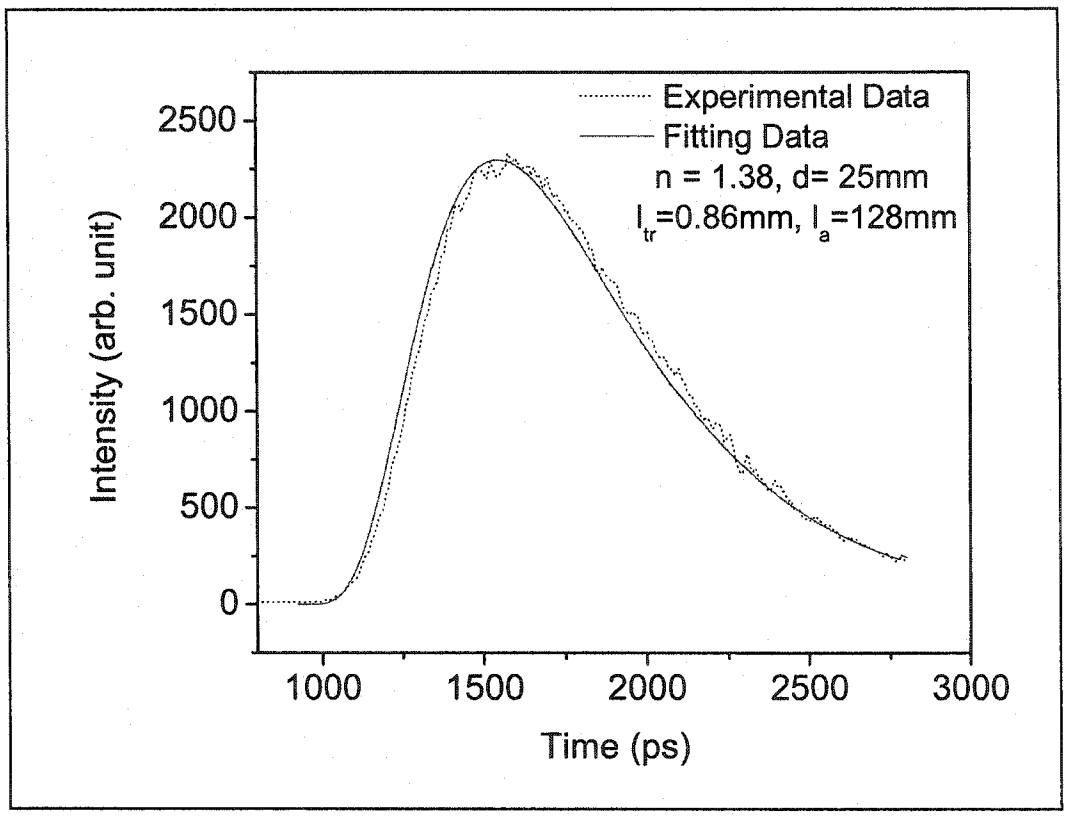

Fig. 3.13: Temporal profiles of the transmitted pulses through the 2.5-cm-thick sample: the solid curve-theoretical fitting, and the dotted curve-experimental data.

3.4.4 Discussion and Outcome

The transport mean free path was obtained by fitting the scattered pulse profile by the diffusion equation. It is shown from Fig. 3.13 that the diffusion equation fits the experimental data. The peak of the theoretical solid curve is normalized to the peak of the experimental data. The values of transport mean free path, and absorption lengths are measured at 800 nm. The ℓ_{tr} and ℓ_a for the prostate tissue were measured with the pulse transmission technique using equation (3.5). The values of the transport length and

absorption length for prostate tissues are ℓ_{tr} = 0.86 mm, *and* ℓ_a = 128 mm, respectively. It is clear from the data obtained that prostate tissue is dominated by scattering rather than by absorption at this wavelength. The previous information will be useful in the prostate imaging where the critical thickness for imaging a hidden object such as cancer in the prostate tissue can be predicted in highly scattering media using the diffusion approximation. This idea will be clearly shown in the steady state imaging of human prostate tissues measurements in the next chapter, chapter 4.

3.5 References

1. T. S. Curry III, J. E. Dowdey, R. C. Murry Jr., in: Christensen's Introduction to the Physics of Diagnostic Radiology, 3rd ed., Lea and Febiger, Philadelphia, 1984.

2. P. S. Anderson, S. Montan, S. Svanberg, IEEE J. Quantum Electron. QE-23, 1787, 1987.

3. K. M. Yoo, Zhi-Wei Zang, S. A. Ahmed, R. R. Alfano, Optics Lett. 16, 1252, 1991.

4. F. J. Green, The Sigma-Aldrich Handbook of Stains Dyes and Indicators, Sigma-Aldrich Corporation, 407, 1991.

5. G. R. Fleming, J. M. Morries and G. W. Robinson, Chemical Physics, 17, 91, 1976.

6. G. Porter, P. J. Sadkowski and C. J. Tredwell, Chem. Phys. 49, 416, 1977.

7. S. G. Demos and R. R. Alfano, Appl. Optics, 36, 150, 1997.

8. J. M. Schmitt, A. H. Gandjbakhele, and R. F. Bonner, Appl. Opt. 31, 6535, 1992.

9. S. G. Demos, W. B. Wang, and R. R. Alfano, Appl. Optics, 37, 792, 1998.

10. K. M. Yoo and R. R. Alfano, Opt. Lett. 15, 320, 1990.

11. D. J. Tindall and P. T. Scardino, "Defeating prostate cancer: Crucial directions for research-Except from the report of the Prostate Cancer Progress Review Group (Review)," Prostate, vol. 38, no. 2, pp. 166-171, 1999. P. T. Scardino, "Prostate cancer, treatment, and prevention," Newsweek, Nov. 1, 11, 1999.

12. B. B. Das, K. M. Yoo and R. R. Alfano, Opt. Lett. 18, 1002, 1993.

13. F. Liu, K. M. Yoo, and R. R. Alfano, Opt. Lett. 16, 351, 1991.

14. L. Wang, P. P. Ho, C. Liu, G. Zhang, and R. R. Alfano, Science 253, 769, 1991.

15. B. B. Das, Ph. D. Thesis, The City University of New York, 1993.

Chapter 4

Spectral Polarization Imaging of Animal Tissues, Human Prostate Tissues and the Use of Contrast Agents

4.1 Introduction

In this chapter we present the experimental work of the steady state imaging through animal tissues and human prostate tissues. The visibility enhancement of fluorescent objects hidden in animal tissues using the Spectral Fluorescence Difference Imaging (SFDI) and Polarization Fluorescence Difference Imaging (PFDI) methods using Cardio Green dye at different depths will be explained. Fluorescence imaging measurements of foreign objects embedded in human prostate tissues using Cardio Green dye will be investigated. The Spectral Polarization Imaging (SPI) method of human rectum-membrane prostate tissues will be investigated. Near infrared transmission and backscattered imaging to probe water in normal and cancer human prostate tissues will be investigated.

The degree of polarization is determined by using the relationship:

$$D = (I_{\parallel} - I_{\perp})/(I_{\parallel} + I_{\perp}), \tag{4.1}$$

where $I_{\parallel}$ and $I_{\perp}$ are the intensities for the parallel and perpendicular components of the reflected or scattered light from the object, respectively. The contrast is the difference in light intensity in an object or image, and defined as:

$$C = (I_{max} - I_{min})/(I_{max} + I_{min}), \tag{4.2}$$

where the I_{max} and I_{min} are the maximum and minimum intensities of light recorded from the object, respectively.

4.2 Imaging Enhancement of Fluorescent Objects Hidden in Animal Tissues Using Spectral Fluorescence Difference Imaging (SFDI) and Polarization Fluorescence Difference Imaging (PFDI) Methods

4.2.1 Background

When polarized light propagating inside a scattering medium reaches the dyed tissue, it's partially polarized. The dye absorbing the partially polarized light emits partially polarized light. The emitted polarized light decreases its polarization as it travels a longer path (turbid medium). Contrast agents are widely used in various medical imaging modalities to enhance the visibility of the desired area of the body [1]. Cardio Green (Indocyanine Green) dye is currently used as a diagnostic aid for blood-volume determinations as well as cardiac- and liver-function tests [2]. The contrast agent dyes have been introduced in optical imaging studies to improve the image quality of objects hidden in scattering media or tissues [3-4].

We describe novel spectral fluorescence difference imaging (SFDI) and polarization fluorescence difference imaging (PFDI) methods using the spectral properties of native fluorescence from tissues and intrinsic fluorescence from contrast agent dyes to enhance the visibility of objects embedded deeply inside animal tissues.

The difference of the fluorescence spectra emitted from Cardio Green dye and chicken breast tissue at NIR region was measured. The absorption and emission of the Cardio Green dye are shown in chapter 3 (section 3.2.3, Fig. 3.2). The wavelengths of 790 nm and 830 nm were selected as a pair of fingerprint wavelengths for imaging because at these two wavelengths, the tissue native emission intensities are almost the same while the dye intrinsic emission intensities are much different. Using the SFDI method, a 1-mm tissue object stained with Cardio Green dye located at 3.1 cm

underneath the surface of the host chicken tissue was imaged and investigated. The spatial resolution and the contrast of two 1mm diameter chicken breast tissue pieces stained with Cardio Green dye using the polarization fluorescence difference imaging (PFDI) method were imaged and compared with that of the conventional imaging approach.

4.2.2 Experimental Methods

The fluorescence spectra of the Cardio Green dye and chicken breast tissue were measured using a quarter meter spectrograph (ARC SpectroPro 275) coupled with a CCD camera (Princeton Instrument model TE/CCD-512 SF) as shown in Fig. 4.1 [5]. The laser beam of 633 nm was focused by a 20 cm focal length lens to pump the sample. The fluorescence from the sample was collected by a 85 mm focal length lens into the 0.1 mm slit of the spectrograph. A notch filter of 633 nm was placed in front of the CCD detector to block out the scattering light of the laser beam.

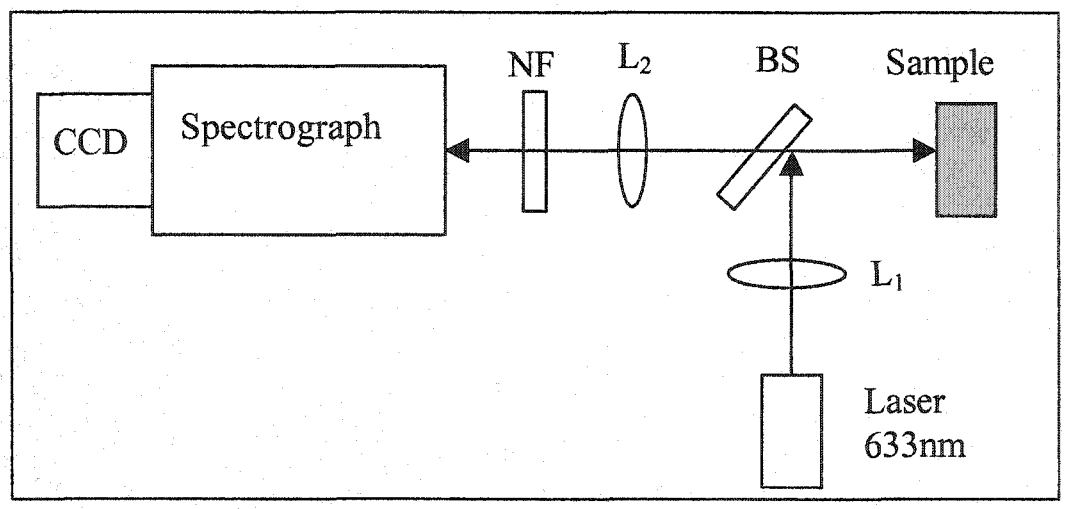

Fig. 4.1: Schematic diagram of the experimental setup of steady state spectroscopy fluorescence measurements. BS: beam splitter; L_1:excitation lens; L_2: signal collection lens; NF: notch filter.

The experimental arrangement for the imaging measurements is schematically shown in Fig. 4.2. The output beam of a Rhodamine 6G dye laser at 633 nm, synchronously pumped by a Nd:YAG laser with a pulse compression and second harmonic generation system, was expanded to a diameter of 5 cm for illuminating the tissue sample. The fluorescence light emitted from the sample was collected in the back-scattering geometry for imaging. A notch filter of 633 nm and a long pass filter of 650 nm were placed in the fluorescence path to cut off the illumination wavelength. A cooled CCD camera (Photomatrix CH250) equipped with a zoom lens placed at a distance of 50 cm from the sample was used to record the images. For the SFDI method, narrow band filters of 790 nm and 830 nm were alternatively placed in front of the detector so that the images formed by the 790 nm and 830 nm fluorescence emitted from the dye and tissue were recorded.

The sample used for the SFDI method was a small piece (1-mm diameter) of chicken breast tissue stained with Cardio Green inserted inside a large piece (6 cm x 5 cm x 4 cm) of the host chicken breast tissue. The dyed tissue object was positioned 3.1 cm underneath the surface of the host tissue as shown in Fig. 4.2. Under the 633 nm laser beam excitation, both the Cardio Green dye and chicken breast tissue emit fluorescence light in the NIR which contributes to the recorded image of the object. The purpose of the spectral fluorescence difference imaging method demonstrated in this experiment is to reduce the effect of the host tissue emission and diffusion, and to enhance the visibility of the luminous object embedded deeply inside the host tissue.

For the polarization fluorescence difference imaging (PFDI) method, the output beam of a Pyridine (LDS 698) dye laser at 760 nm was expanded to a diameter of 5 cm

and was used to illuminate the sample with an average intensity of 4 mW/cm^2, as shown in Fig. 4.3. Polarizers P_1 (to ensure the linear polarization of the input laser beam) and P_2 (analyzer) were set with their polarization axes parallel to each other. A half-wave plate for the input wavelength of 760 nm was positioned after P_1, and its optical axis was rotated from 0° to

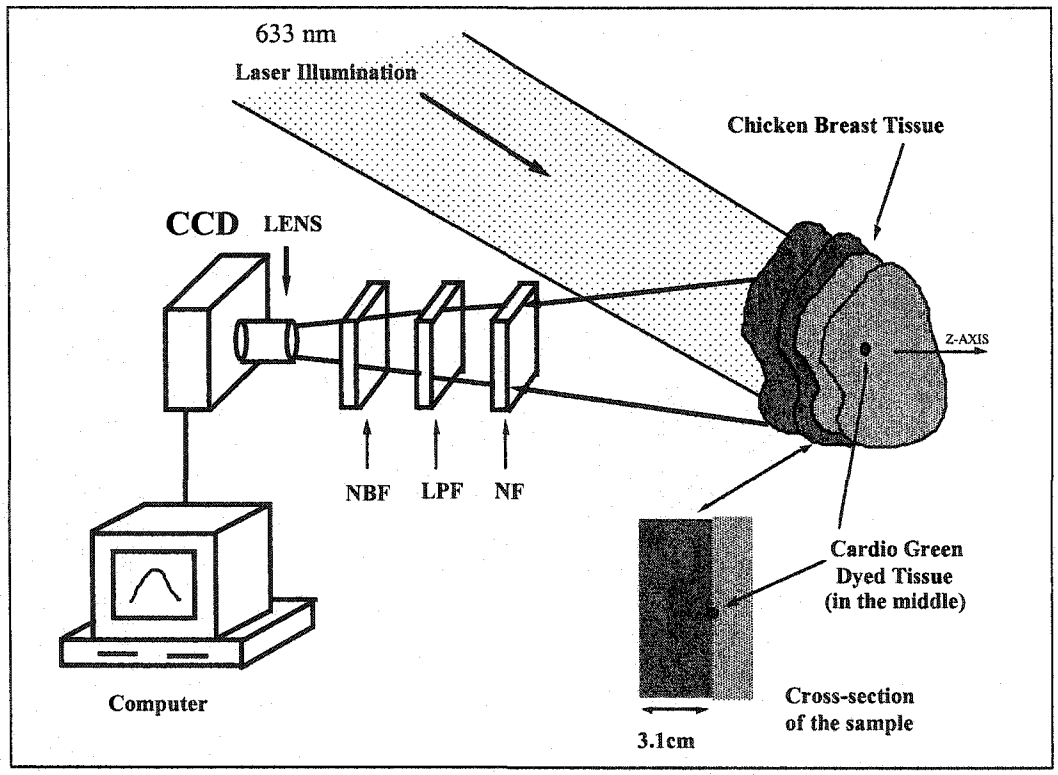

Fig. 4.2: Schematic diagram of the experimental set up used to perform the spectral fluorescence difference imaging (SFDI) measurements. NF: notch filter of 633 nm; LPF: long pass filter of 650 nm; narrow band filter of 790 nm or 830 nm placed in front of CCD to obtain the 790 nm and 830 nm images.

45° in order to illuminate the sample with linearly polarized light with polarizations parallel and perpendicular to P_2, respectively. A notch filter of 760 nm and a long pass filter of 830 nm were placed in front of the detector to cut off the illuminating light so that only the fluorescence (> 830 nm) images were recorded. A cooled CCD camera

equipped with a zoom lens and placed at a distance of 50 cm from the sample was used to record the parallel and perpendicular images. The sample used for the imaging experiments is composed of two 1 mm-diameter chicken breast tissue pieces stained with

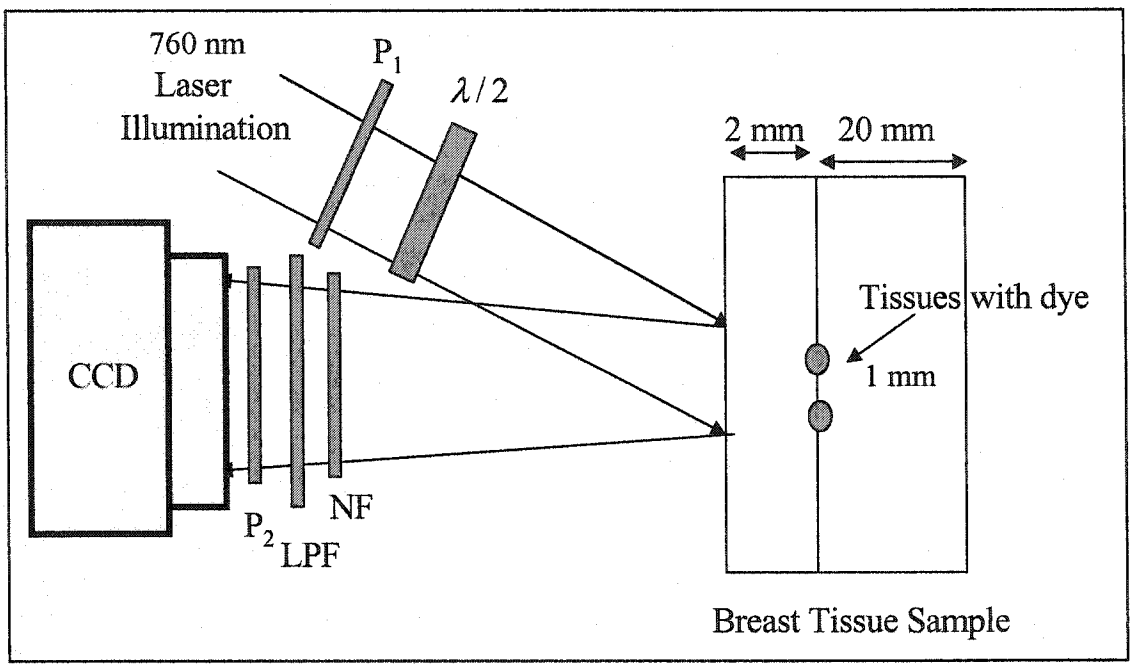

Fig. 4.3: Schematic diagram of the experimental set up used to perform the polarization fluorescence difference imaging (PFDI) measurements. The sample is composed of two 1 mm-diameter chicken breast tissue pieces (1 mm apart) stained with Cardio Green dye.

Cardio Green dye. These objects are positioned 1.5 mm apart and placed 2 mm beneath the surface of a 4 cm X 6 cm host chicken breast tissue as in Fig. 4.3.

4.2.3 Experimental Results

The measured fluorescence spectra of Cardio Green dye and chicken breast tissue under a 633 nm laser excitation are shown in Fig. 4.4. The solid curve displays the fluorescence spectrum of Cardio Green dye and the dotted curve displays the emission

from the chicken breast tissue. The emission from the Cardio Green is much stronger than that from the chicken breast tissue between 780 and 880. The native emission intensities from the tissue at the wavelengths of 790 nm and 830 nm are almost the same, while the emission intensity from the dye at 830 nm is stronger than that at 790 nm by a factor of 1.8, i.e. $I_{tissue}(830) = I_{tissue}(790)$ and $I_{dye}(830) > I_{dye}(790)$. This spectral difference at 790 nm and 830 nm of dye in comparison to the native tissue emission

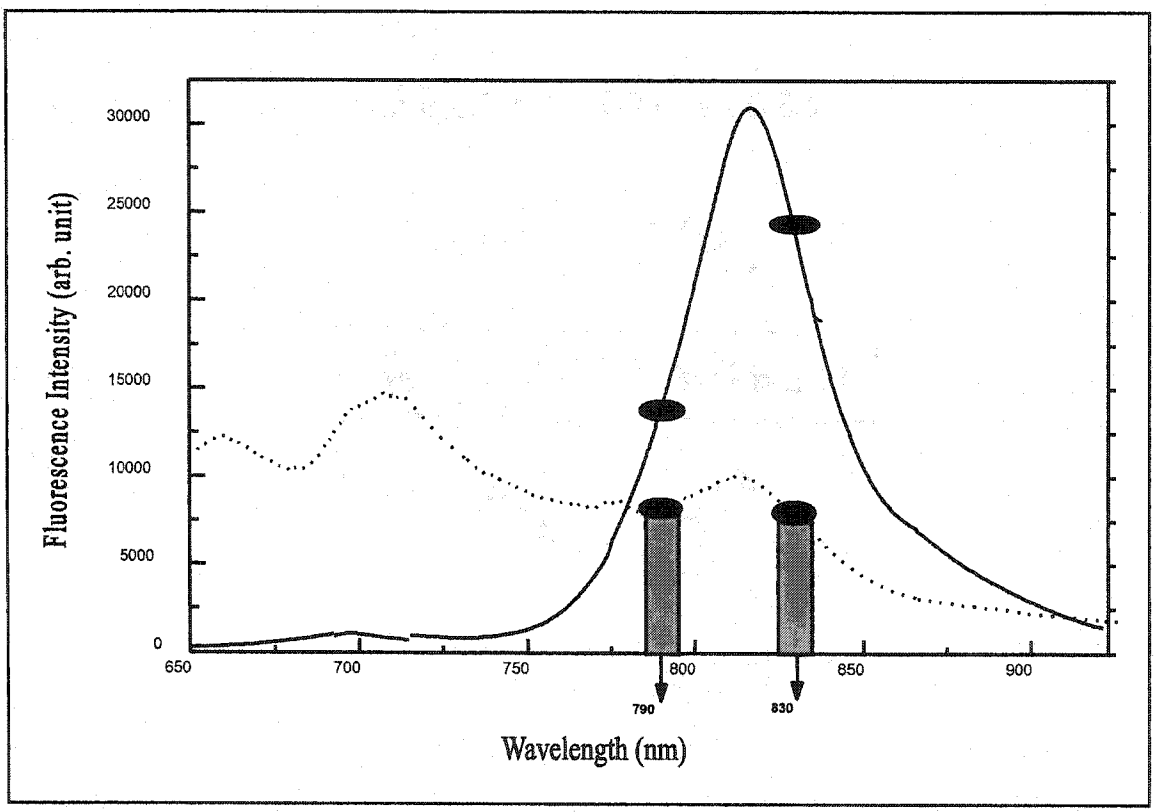

Fig. 4.4: Fluorescence spectra for Cardio Green dye in water with a concentration of $5x10^{-5}$ M (solid curve), and for chicken breast tissue (dotted curve) under 633 nm laser illumination and the use of SFDI principle.

offers us an opportunity to choose suitable imaging wavelengths for the SFDI method to reduce the contribution of the host tissue emission to the image, and highlight the hidden object better.

In SFDI method measurements, the images of the dyed 1-mm diameter tissue located 3.1 cm below the surface of the large host tissue under 633 nm laser illumination

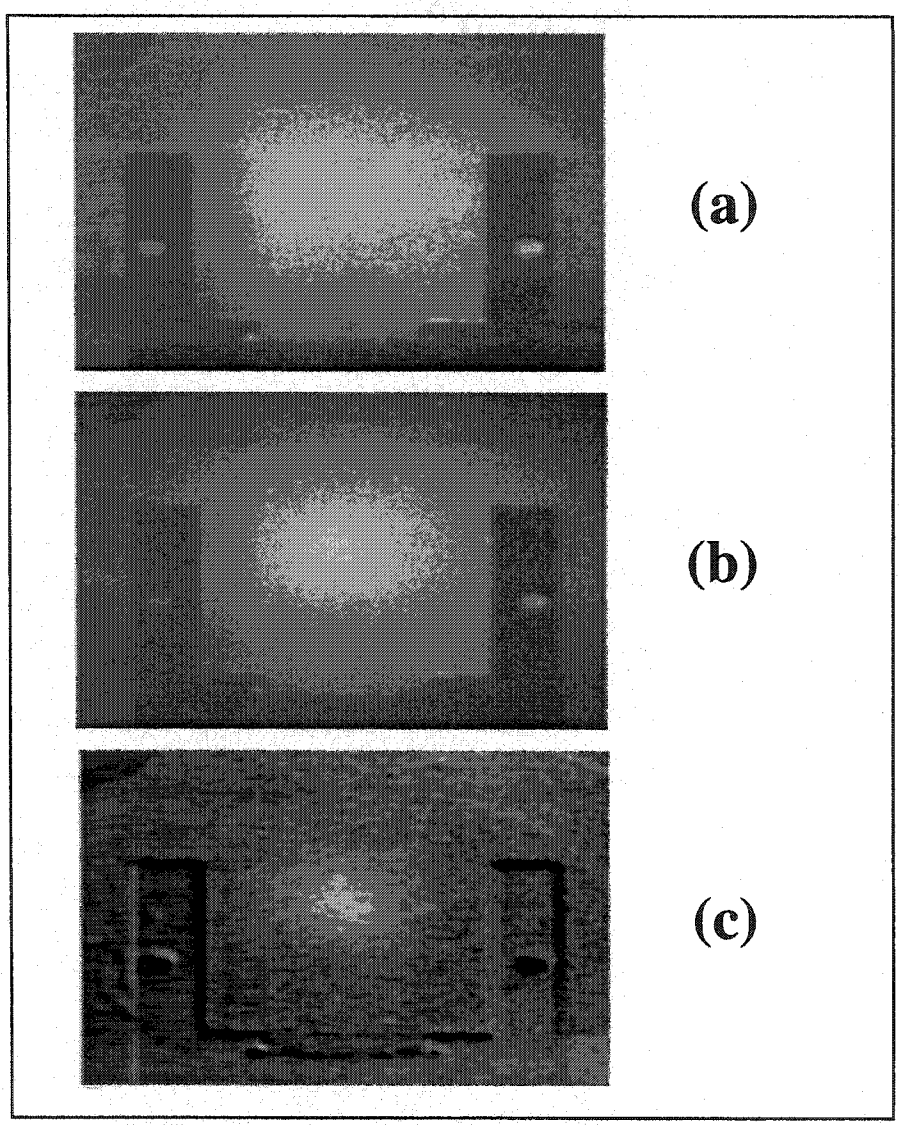

Fig. 4.5: Using SFDI, fluorescence images of a luminous object (1 mm-diameter chicken breast tissue stained by Cardio Green located 3.1 cm underneath the surface of the host chicken breast tissue) recorded when the narrow band filter in front of the CCD detector is (a) 790 nm, and (b) 830 nm; and (c) is the difference image obtained by subtracting image (a) from image (b).

were recorded at different wavelengths. Fig. 4.5a displays the image recorded when the narrow band filter of 790 nm was placed in front of CCD, while Fig. 4.5b shows the

image when the narrow band filter 830 nm was used. Fig. 4.5c displays the fluorescence difference image obtained by subtracting 790 nm image (Fig. 4.5a) from 830 nm image (Fig. 4.5b).

In PFDI method measurements, the polarized fluorescence images of the two 1-mm chicken breast tissue sample stained with Cardio Green located 2 mm below the surface of the larger host tissue (as shown in Fig. 4.3) under 760 nm linearly polarized

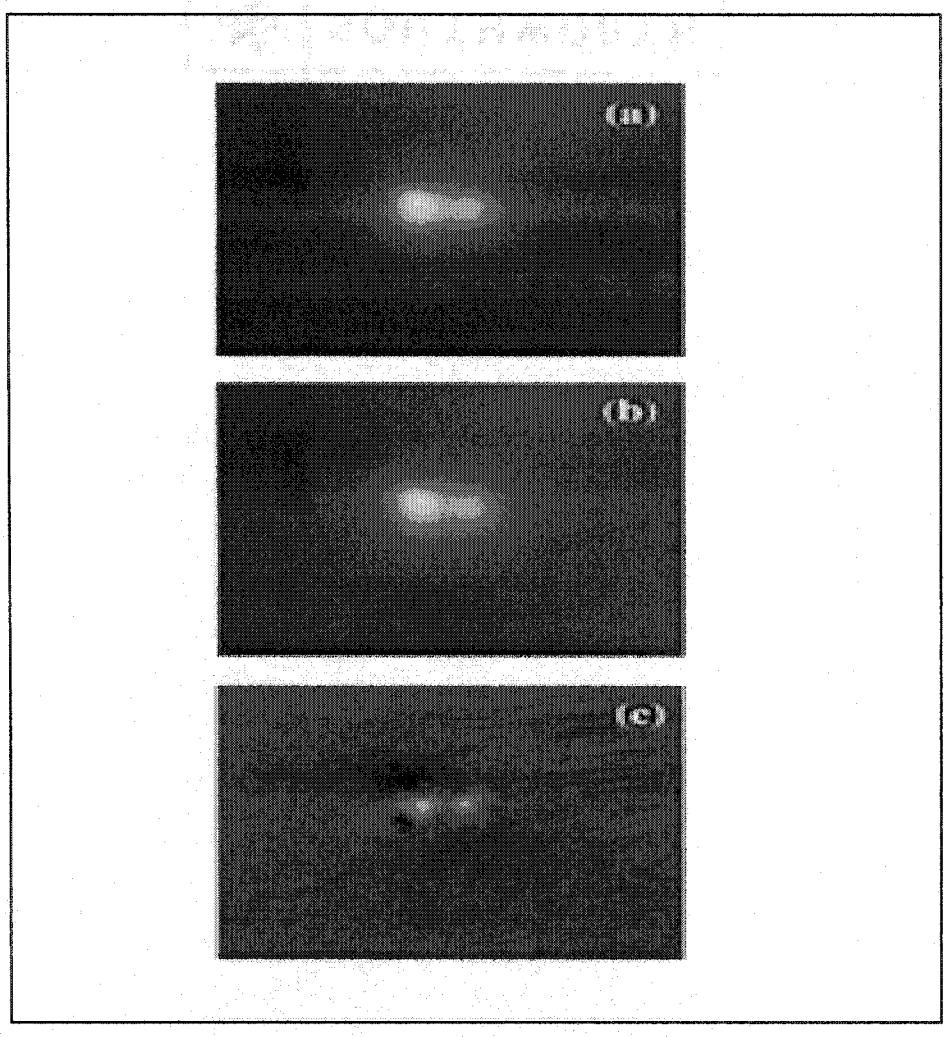

Fig. 4.6: Using PFDI method, fluorescence Images (fluorescence > 830nm) of two 1 mm diameter tissue pieces stained with Cardio Green positioned 1.5 mm apart and placed 2mm underneath the surface of the host chicken breast tissues (a)parallel polarization emission (b)perpendicular polarization emission and (c)polarization difference by subtracting image (b) from (a).

laser illumination are shown in Fig. 4.6. Fig. 4.6a displays the parallel image recorded when the polarization (P_2) in front of CCD is parallel (It) to the polarization of the illuminating beam. Fig. 4.6b displays the perpendicular image recorded when the polarizer P, is perpendicular to the polarization of the illuminating beam. Fig. 4.6c displays the difference image obtained by subtracting the perpendicular image (Fig. 4.6b) from the parallel image (Fig. 4.6a).

4.2.4 Discussion and Outcome

Several salient features can be seen from the images shown in Fig. 4.5:

(1) The quality of the individual 790 nm and 830 nm images shown in Figs. 4.5a and 4.5b are so poor that the presence of the luminous object is not clear or very difficult to be determined. This can be understood because the dyed tissue is deeply embedded inside the host tissue. Although the light emitted from the Cardio Green is strong, the photons emitted from the dye are scattered many times in the host tissue. Consequently, the intensities of the dye fluorescence light is weak when it arrives into the CCD camera. On the other hand, the light emitted from the surface and near-surface area of the host tissue undergoes less scattering before they reach to the detector, which forms a strong background in the surrounding area of the central direct image of the luminous object. As a result, the relative brightness of the direct image formed by the dye emission is not obviously higher than that of the surrounding background formed by the host tissue emission. Consequently, the direct image of the luminous object is very difficult to be observed.

(2) The central peak intensity of the 830 nm image (Fig. 4.5b) is higher than that of the 790 image (Fig. 4.5a). This difference can be explained because the emission of Cardio Green dye at 830 nm is stronger than that at 790 nm. For the reasons as mentioned above, the background intensity formed by the host tissue native emission and diffusion is strong for both the 790 nm and the 830 nm images. As a result, the quality of the 830 nm image is just slightly better than that of the 790 nm image.

(3) The presence of the luminous object can be distinguished in the fluorescence difference image shown in Fig. 4.5c. It can be seen from Fig. 4.5c that the fluorescence difference image is confined nearer the central high intensity area showing its better spatial resolution. In addition, the brightness of the surrounding area of the difference image is much reduced due to the subtraction, and the relative brightness, contrast, of the image of the luminous object is enhanced. These two characteristics indicate the higher quality of the fluorescence difference image.

In order to confirm the improvement of the image quality of the spectral fluorescence difference image with respect to the conventional single wavelength images, digitized intensity profiles across a horizontal line at the center of the 790 nm, 830 nm, and difference images shown in Figs. 4.5a, 4.5b and 4.5c were investigated. The digitized profiles shown in Figs. 4.7a and 4.7b represent the intensity distribution in the transverse position of the conventional 790 nm and 830 nm images, respectively. The peak for the profile of the 790 nm image (Fig. 4.7a) is not clear, which reflects the poor quality of the 790 nm image. The peak of the profile of the 830 nm image (Fig. 4.7b) can be observed, but the high background intensities at the two sides of the peak indicate the poor contrast of the 830 nm image. The profile shown in Fig. 4.7c represents the intensity distribution

of the fluorescence difference image shown in Fig. 4.5c. The peak of this latter plot is very clear which shows a better spatial resolution

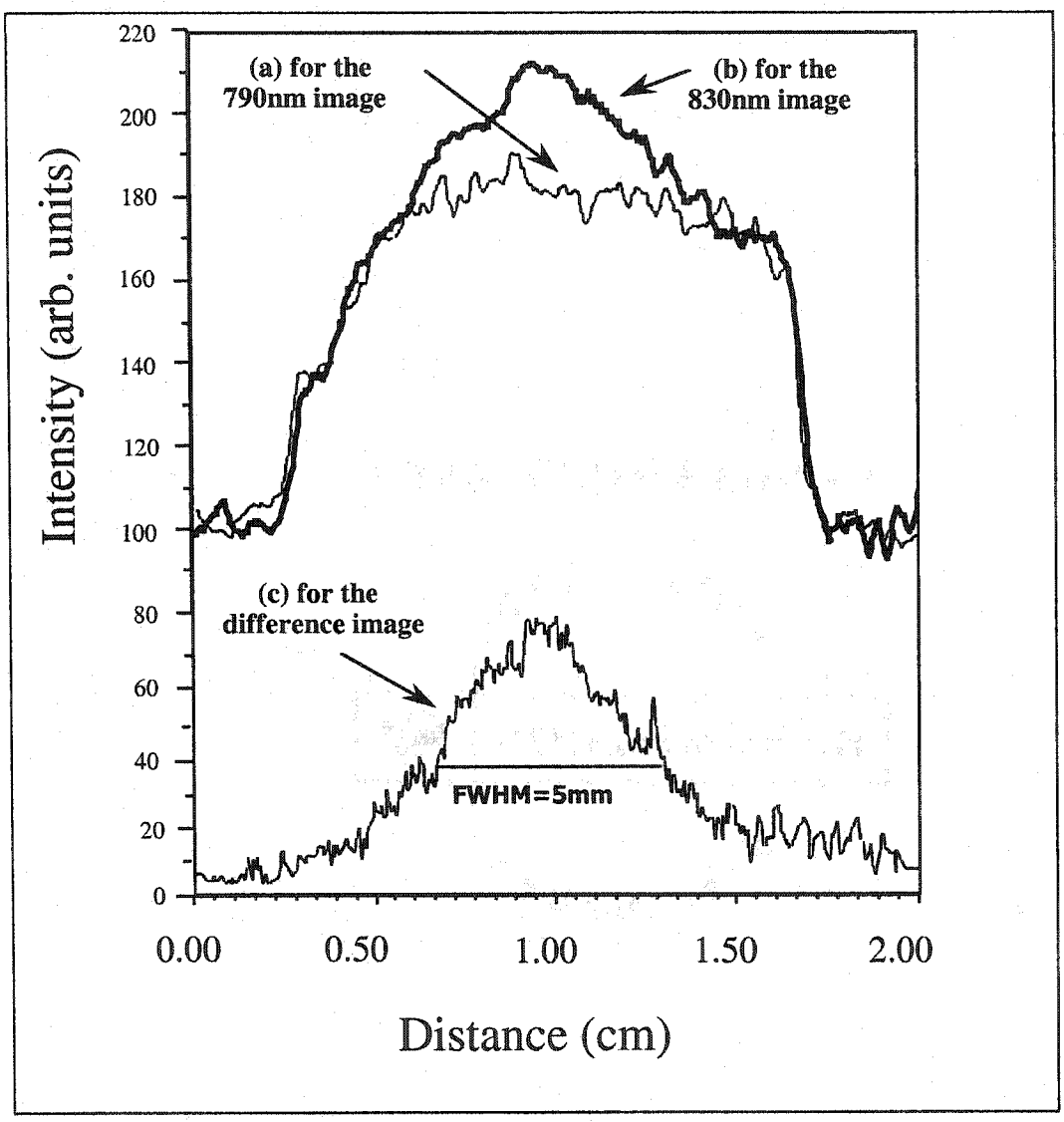

Fig. 4.7: The digitized intensity profiles for (a) the 790 nm, (b) the 830 nm, and (c) the fluorescence difference images shown in Fig.4.5 using SFDI. These profiles clearly show that the spatial resolution and the contrast of the fluorescence difference image are much better than that of the conventional images obtained at the individual wavelength of 790 nm or 830 nm.

of the fluorescence difference image. From Fig.4.7c, the full width at half maximum (FWHM) for the fluorescence difference image of the 1-mm tissue object was found to be

5 mm. This size is reduced by a factors of more than 2 with respect to that of the single wavelength (790 nm or 830 nm) images.

These digitized profiles show that the relative brightness of the central direct image with respect to the surrounding area for the fluorescence difference image is much higher than that of the conventional single wavelength images. Using the data shown in Figs. 4.7a, 4.7b and 4.7c, the contrast defined by $C = (I_{max} - I_{min}) / (I_{max} + I_{min})$ for all of the conventional and fluorescence difference images were calculated. The calculated contrast values are 0.29, 0.34 and 0.84 for the 790 nm, 830 nm and fluorescence difference images, respectively. The fluorescence difference image contrast is 2.9 times higher than that for the 790 nm image and 2.5 times higher than that for the 830 nm image.

The improvement of the quality of the spectral fluorescence difference image arises from the subtraction of the 790 nm image from the 830 nm image, which almost removes the effect of the host tissue native emission and diffusion to the recorded images. The image of the dyed object hidden inside the host tissue is formed by photons emitted from the dye that have undergone coherent scattering (ballistic photons), less scattering (snake photons), and multiple scattering (diffusive photons) [6]. The ballistic photons reaching the CCD contribute to the formation of the central direct image. The diffused photons have suffered multiple scattering before exiting the host tissue; and they are distributed to the area of the image with a large distance off the center. The snake photons undergo a small number of scattering events and as a result, they are distributed to the area of the image within a small distance from the center of the image compared to the diffusive photons. The fluorescence from the surface and the near surface area of the

host tissue undergoing less scattering forms a strong background surrounding the central image. Since the intensities of the native emission from the host tissue at the wavelengths of 790 nm and 830 nm are the same as shown in Fig. 4.4, the subtraction of the 790 nm image from the 830 nm image almost removes the strong background contributed by the native host tissue emission. The subtraction also reduces the effect of the multiple scattering light, which forms the shadow area of the image with a large distance off the image center. Although the emission from the dye at 830 nm is stronger than that at 790 nm, the intensity of the multiple scattering light is inversely proportional to the fourth power of the wavelength [7]. As a result, the difference between the intensities of the multiple scattering light for the wavelengths of 790 nm and 830 nm at the far shadow area of the images is much smaller than that at the center of the image. Therefore, the subtraction of the 790 nm image from the 830 nm image greatly reduces the background intensity of the shadow area with a large distance off the center rather than that of the center area. Since the strong background formed by the host tissue native emission and the strong shadow area formed by the multiple scattering light are almost removed or greatly reduced due to the subtraction, only ballistic and partial snake photons contribute to the formation of the fluorescence difference image. This method improves the spatial resolution and contrast of the fluorescence difference image with respect to the conventional single wavelength images for the contrast agent, Cardio Greens.

In the PFDI method measurements (Fig. 4.6(a-c)), the early arriving photons contribute to the formation of the direct images of the two small pieces of the dyed tissue. Most of the light emitted from the dyed tissue undergoes multiple scattering and loses its polarization information, which contributes to the surrounding area of the image. As a

result, both parallel and perpendicular images similarly consist of a bright surrounding area and a little brighter central direct image. The peak intensity of the parallel image shown in Fig. 4.6a is slightly higher than that of the perpendicular one shown in Fig. 4.6b. This difference can be explained because the light reaching the CCD camera is still partially polarized (although the portion of the polarized light decreases after it passes through the tissue). The preferred polarization is parallel to the polarization of the illuminating laser beam. The fluorescence polarization difference image shown in Fig. 4.6c is different from the primary images shown in Figs. 4.6a and 4.6b. The polarization difference image is confined near to the two central dot-images having a better spatial resolution. In addition, the relative brightness of the image of the dyed tissue in the polarization difference image is enhanced with respect to the brightness of the surrounding area of the image.

In order to confirm the improvement of the image quality, digital intensity profiles across a horizontal line at the center of the difference image shown in Fig. 4.6c, and the conventional image (no polarizers were used) are plotted in Fig. 4.8. The profile shown in Fig. 4.8a represents the intensity distribution in the transverse position of the conventional image which appears identical to images shown in Figs. 4.6a and 4.6b. The plot shows high background intensities at the sides of the two peaks and in the valley between the two peaks. This reflects the poor quality of the conventional image due to the diffusion photons. The profile shown in Fig. 4.8b represents the intensity distribution of the polarization difference image shown in Fig. 4.6c. This latter plot clearly shows a higher spatial resolution. The resolution of full width at half maximum (FWHM) for each peak in Fig. 4.8b is reduced by a factor of 2.3 with respect to that of the conventional

image shown in Fig. 4.8a. The relative brightness of the two central dot-images compared to that of the surrounding area (contrast) for the polarization difference image shown in Fig. 4.8b is obviously higher than that of the conventional image shown in Fig. 4.8*a*. To quantitatively describe the improvement of the relative brightness of the polarization difference image, the contrasts (C) for both conventional and polarization difference images were calculated. For the purpose of distinguishing the two dot-images, the intensities at the left peak, and at the valley between two peaks for both the conventional and polarization difference images were selected for the calculation of C. Using the digital data shown in Figs. 4.8a and 4.8b, the contrast C for the conventional and polarization difference images are calculated to be 0.10 and 0.36, respectively. The contrast of the polarization difference image is more than 3 times higher than that of the conventional image. The improvement of the quality of the polarization difference image arises from the subtraction of the perpendicular image from the parallel image, which almost cancel the diffusion effect to the signal image. The image of the Cardio Green dyed objects hidden inside breast tissue is formed by photons emitted from the dye that have undergone coherent scattering (ballistic photons), less scattering (snake photons), and multiple scattering (diffusive photons) [6]. The ballistic photons reaching the CCD contribute to the formation of the direct image, which is the two small dots located in the middle of the image. The rest of the bright image is formed by the snake and diffusion photons. The diffused photons have suffered multiple scattering before exiting the breast tissue; and they are distributed over a large distance from the center. The snake photons undergo a small number of scattering events and as a result, they are distributed within a small distance from the center of the image compared to the diffusive photons. Due to

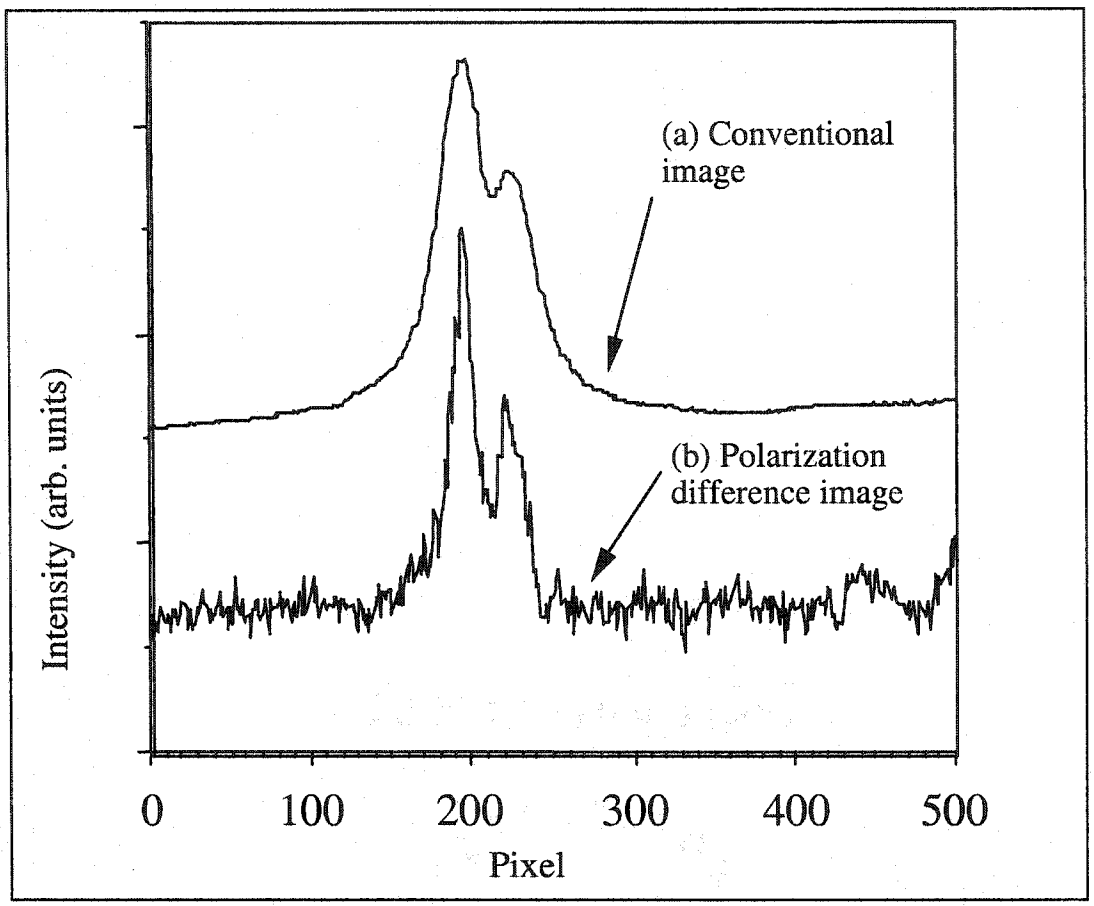

Fig. 4.8: Digital intensity profiles across a line containing the images of the two tissue pieces stained with Cardio Green: (a) for the conventional non-polarized image, and (b) for the polarization difference image using FPDI.

polarization preservation, the dye emits partially polarized light. The ballistic photons recorded by the CCD detector have the same degree of polarization as the photons emitted by the dye since the ballistic photons have not undergone scattering. The snake photons recorded by the detector are still partially polarized but the degree of the polarization is smaller than that of the ballistic photons since the snake photons undergo some scattering. The diffusion photons recorded by the detector are completely depolarized (the two polarization components $I_{//}$ and $I_{\perp}$ have same intensities) because they undergo multiple scattering. Since most of the photons emitted by the dye undergo

multiple diffusive scattering, only small percentage of the photons retain their polarization information while they propagate toward the detector, the intensities of the two image components $I_{//}$ and $I_{\perp}$ have only a small difference. When the two polarization image components are subtracted $(I_{//} - I_{\perp})$, the strong diffusive image component is canceled out. Only ballistic and partial snake photons contribute to the formation of the polarization difference image $(I_{//} - I_{\perp})$. Since the contribution of the diffusive photons is removed using the polarization difference technique, the polarization difference image has small background intensities surrounding to the central direct image. Therefore, the spatial resolution and contrast of the polarization difference image are much better than that of conventional non-polarized optical images.

In conclusion, SFDI and PFDI methods demonstrate the enhancement of visibility of an object embedded inside animal tissues using Cardio Green dye. The imaging depth of 3.1 cm for which the luminous 1 mm dyed tissue object with Cardio Green is embedded beneath the surface of the host tissue is an encouraging distance for the in-vivo medical diagnostic applications using SFDI. The PFDI technique demonstrates the ability to enhance the image quality of objects embedded 2 mm inside animal tissues using Cardio Green dye. The backscattering image geometry shown in this experiment may be suitable for certain medical imaging applications. Specially selected contrast dye agents can be used for detection of cancers and other diseases in the various organs in the human body which can be reached and better imaged using optical probes such as SFDI and FPDI techniques.

4.3 Spectral Polarization Imaging (SPI) of Human Rectum-Membrane-Prostate Tissues

4.3.1 Background

Cancer is a disease characterized by the uncontrolled growth and spread of abnormal body cells. The human body is made up of billions of cells. Normally, cells reproduce themselves by dividing so that growth occurs. Worn-out tissue is replaced and injuries are repaired in this manner. Occasionally, cells grow abnormally, into a mass called a tumor. Some tumors are benign (noncancerous); others are malignant, or cancerous [8]. The growth of a benign tumor may interfere with body function, but these tumors are seldom life-threatening. Malignant tumors, on the other hand, invade and destroy normal tissue. By a process called metastasis, cells break away from a cancerous tumor and spread through the blood and lymphatic system to other parts of the body where they form new tumors. Sometimes cancer grows and spreads rapidly. In other cases, it develops and spreads slowly.

Prostate cancer has a high incidence and mortality rate for men [8]. The detection and treatment of early small prostate cancers are most important to prevent death attributable to prostate cancers. Current techniques for detection of prostate cancers have limited accuracy. The common methods for monitoring prostate cancers are the prostate specific antigen (PSA) blood test and a digital rectal examination (DRE). When the PSA level is elevated or the DRE abnormal, there is a one-in-three chance that cancer is present. This diagnosis can only be confirmed by a needle biopsy of the prostate. In the biopsy, a number of cores of prostate tissue are taken with a thin needle guided into selected regions of the prostate with an ultrasound probe [8]. Since the ultrasound

imaging has poor spatial resolution and contrast, and the needle biopsy is invasive, better methods are needed to develop high resolution and noninvasive techniques for early small prostate cancer detection. Similar to the digital rectal examination through rectum for checking an abnormal prostate in clinical, the best way to optically image prostate tumors is illuminating and imaging the prostate gland through rectum. For this reason, we have imaged objects hidden inside prostate tissues through rectum-membrane-prostate tissues.

When a linearly polarized light is incident on tissues, the state of the light back-scattered and reflected from the surface is still polarized while the light from within tissues at different distance is partially polarized. The polarization portion of the light decreases when the distance that light travels through increases. As a result, the polarization status of the light can be used for imaging objects embedded inside tissues at different distances from the surface. The polarization property of light can be used to evaluate the changes in tissues. In addition to polarization, the spectral properties of the scattered and fluorescent light can also be used to image the state of tissues.

Human rectum-membrane-prostate tissue samples were studied using near infrared spectral polarization imaging technique to detect small objects and structural changes inside prostate tissues through rectum. Modeling samples were made with a small piece of absorber or prostate tissue dyed with a contrast agent (indocyanine green) embedded inside a large piece of prostate tissue in rectum-membrane-prostate structures. The depth of the foreign objects underneath the surface of the rectum-membrane-prostate structures was varied from a millimeter to a centimeter to obtain the critical imaging distance.

In this section we will use (A) scattered light imaging, (B) tissue emission wing imaging, and (C) contrast agent fluorescence imaging methods to image objects hidden inside prostate tissues through rectum-membrane-prostate tissues. These methods will be compared and investigated in terms of penetration depth in prostate tissues.

4.3.2 Experimental Methods

Human rectum-membrane-prostate tissue samples were obtained from autopsy cases at Hackensack University Medical Center (HUMC) and used for the NIR spectral polarization imaging measurements under the IRB approvals from both HUMC and City College of New York (CCNY). The prostate glands were cut into pieces with thickness from ~1 mm to ~3 mm. The slices of the prostate tissue used are uniform. Models of rectum-membrane-prostate tissue samples were made with a small piece of an object such as an absorber as shown in Fig. 4.9a, or a tiny piece of prostate tissue dyed with a contrast agent (Indocyanine Green) embedded inside a large host piece of prostate tissue in a rectum-membrane-prostate tissue structure as shown in Fig. 4.9b.

The depth of the objects beneath the surface of the rectum-membrane-prostate tissue structures were varied by using different prostate tissue slices to obtain the critical imaging depth.

The NIR spectral polarization imaging setup used for the imaging measurements is shown on Fig. 4.10. Light from a white light source is used to illuminate a sample with an average power of ~50 μW/cm^2. The illumination and detection wavelengths are selected by wide-band pass filters placed on two multiple filter wheels, which are located in the illumination and detection paths, respectively, and can be rotated to the desired

filter position controlled by a computer. The wavelengths of the wide-band pass filters change from 550 nm to 900 nm with FWHM = 40 nm for each filters. A CCD camera

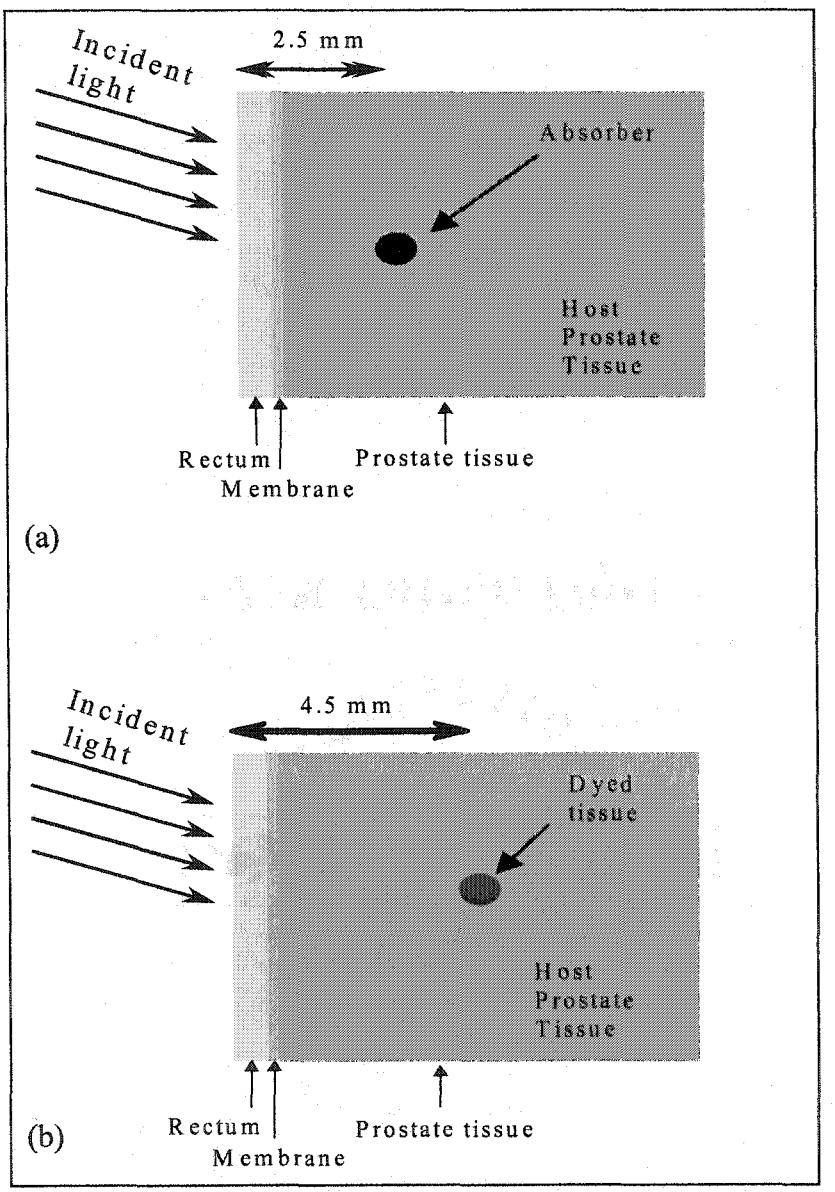

Fig. 4.9: Layer structures of model rectum-membrane-prostate tissue samples made of (a) a small dot piece of black absorber, and (b) a tiny piece of prostate tissue dyed with Indocyanine Green embedded inside a larger piece of host prostate tissue in a rectum-membrane-prostate structure.

records the images formed by light scattered or emitted from the samples. Polarizers P_1 placed in the illumination path, and P_2 placed in front of the CCD, are used to choose the polarization configuration of the illumination and detection. The images can be recorded when the detection polarization is parallel or perpendicular to that of illumination.

In the next section, different imaging methods which include (a) scattered light imaging, (B) tissue emission wing imaging, and (C) contrast agent fluorescence imaging will be performed and compared to image objects inside rectum-membrane-prostate tissue structures. For scattered light imaging, the same illumination and detection band pass filters are used. For emission light imaging, the band pass wavelengths of the detection (imaging) filter are longer than that of the illumination so that the pump light is blocked, and only the light emitted from the sample is collected by the CCD camera. Since the scattering, absorption and emission properties of the hidden foreign objects and prostate tissues are different, both scattered and emitted NIR light images can be used to identify the objects hidden inside prostate tissues.

4.3.3 Experimental Results and Discussion

A. Scattered Light Imaging

The sample used for the scattered light imaging measurements consisted of a small piece of absorber (~ 1mm) embedded inside a large slice of prostate tissue (~30 x 20 mm) in a rectum-membrane-prostate structure with a depth of ~2.5 mm from the surface of the rectum-membrane-prostate tissue structure (see Fig. 4.9a). During the measurements, the illumination and detection wavelengths were synchronously changed so that the detection

wavelengths were always kept as same as that of illumination. In this way, the emission light is blocked, and the CCD camera only collects the light scattered from the sample.

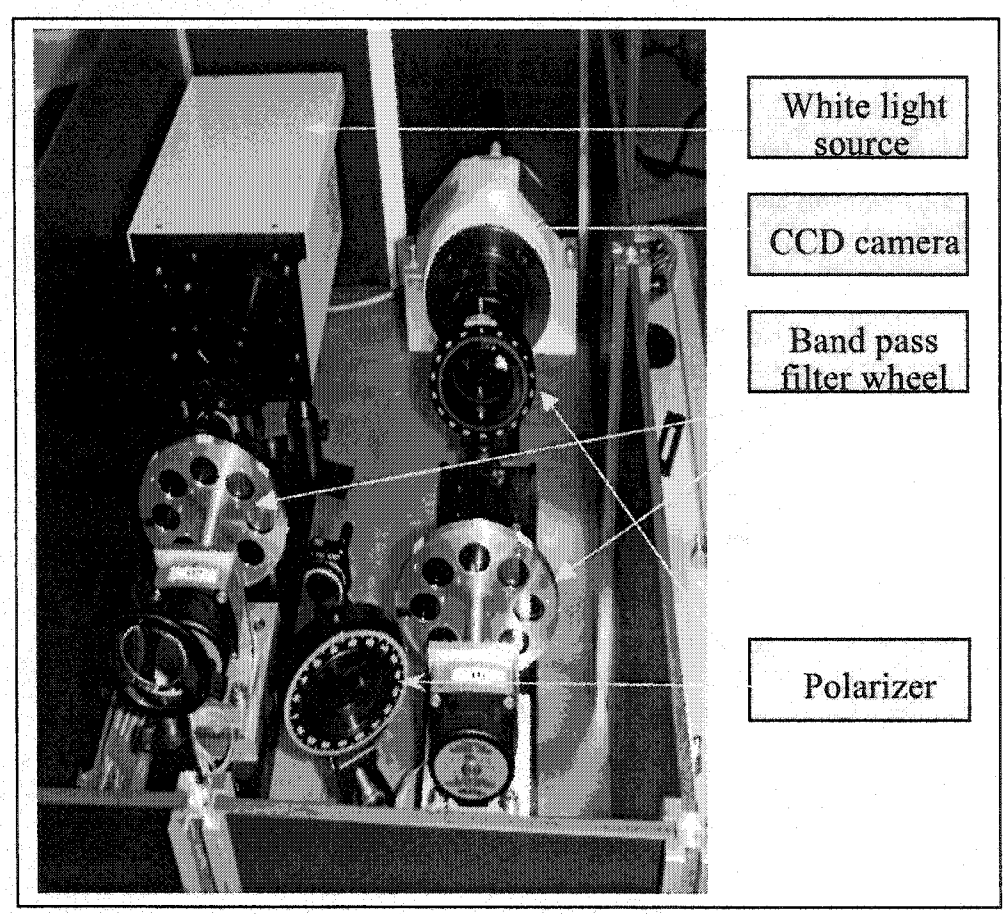

Fig. 4.10: The NIR spectral polarization imaging setup used for the imaging measurements.

The scattered light images recorded at the wavelengths of 600 nm, 700 nm, and 800 nm with the detection polarization perpendicular to that of illumination are shown in Figs. 4.11a – 4.11c. It can be seen that the object (absorber) cannot be distinguished by the 600 nm image, but it can be clearly identified as a dark point by the 800 nm image. As the wavelength increases from 600 nm to 800 nm, the visibility of the object improves.

The wavelength dependence of the image quality of the scattered light images can be explained by the relative absorption spectra of the prostate and rectum tissues shown in Fig. 4.12. The relative absorptions of the prostate and rectum tissues decrease when the wavelength increases from 400 nm to NIR. The short wavelength (such as 600 nm) light

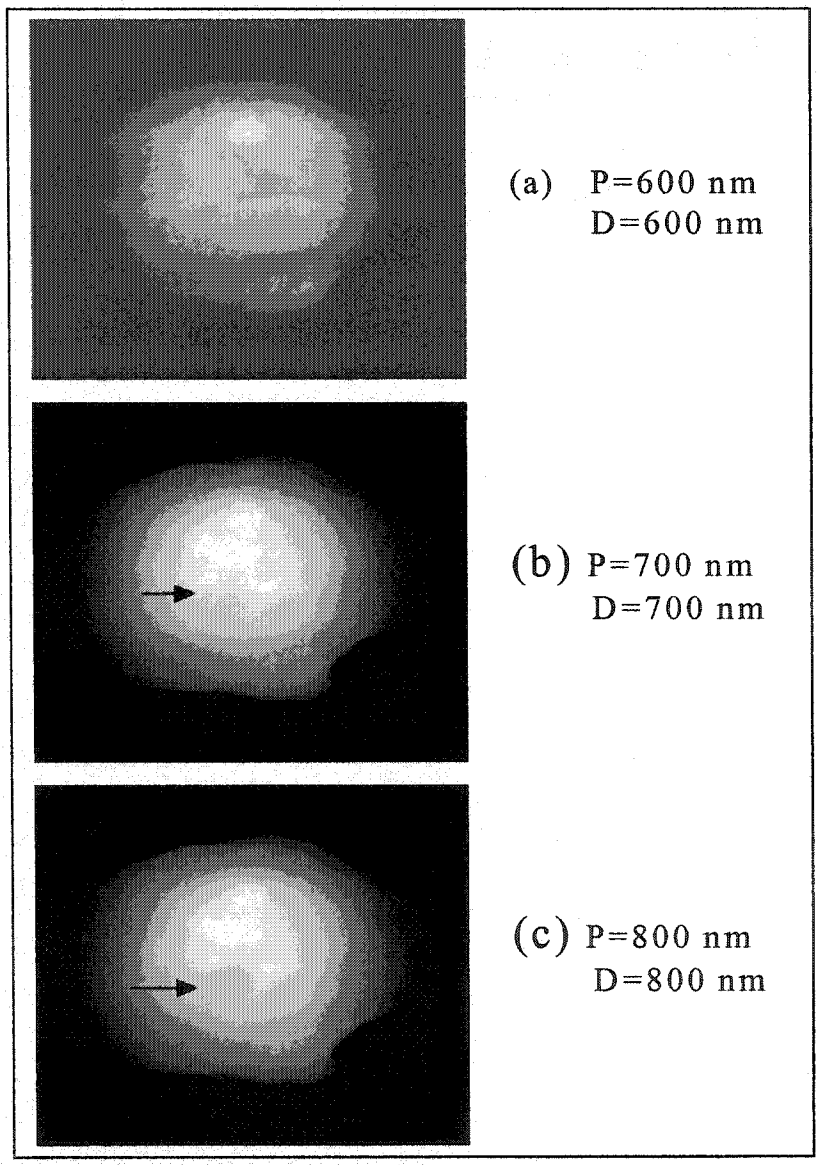

Fig. 4.11: Scattered light images recorded in perpendicular polarization configuration at wavelengths of (a) 600 nm, (b) 700 nm, and (c) 800 nm, respectively, where P: pump, D: detection. The sample consists of a small dot piece of a black absorber hidden inside a large host prostate tissue in a human rectum-membrane-prostate structure at depth of 2.5 mm from the surface of the rectum.

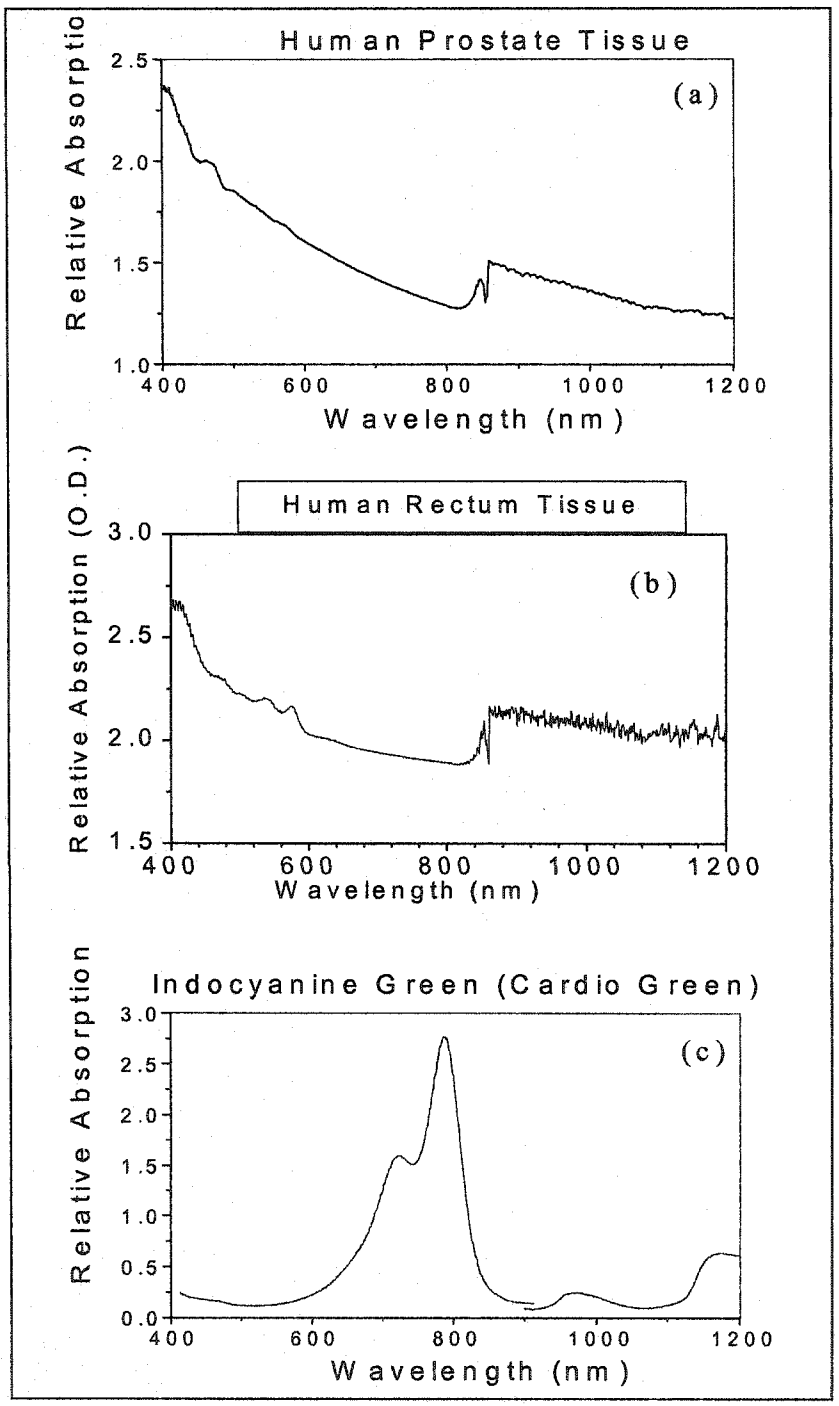

Fig. 4.12 Relative absorption spectrum for (a) human prostate tissue, (b) human rectum tissue, and (c) Indocyanine Green dye.

was absorbed and scattered strongly by the surface and near surface layers of the rectum-

membrane-prostate tissues, and could not reach the object deeply embedded in the host prostate tissue. In this case, the scattered light images are formed by the light scattered only from the surface and near surface tissue layers with almost no contribution from the object, and therefore, the object cannot be identified. In contrast, the larger penetration of the longer wavelength NIR light in rectum-membrane-prostate tissues enables them to reach the deeper object. Once the NIR light reaches the object, the difference of scattering and absorption properties between the foreign object and the surrounding tissues is reflected in the image, and therefore, the foreign object can be identified by the NIR scattering images. The scattered light imaging measurements were extended to other rectum-membrane-prostate tissue samples with objects embedded at depth greater than 2.5 mm. The results show that the image measurements were repeatable for different prostate slices with the same thickness of ~2.5 mm, but, at the same low illumination intensity of ~50 μ W/cm^2, the object could not be observed with depth more than 2.5 mm even from the images obtained at longer wavelengths of 750 nm - 850 nm. To correlate this depth with the time resolved measurements for the prostate tissues using the diffusion model ($\ell_{tr} \sim 0.86mm$ from chapter 3, section 3.4.3), we observed that this depth of 2.5 mm (or 5mm back and forth) is about six times the mean transport free path ($\sim 6\ \ell_{tr}$). Above this limit, the photons that form the image are totally diffused, and diffusive photons dominate strongly over the ballistic and snake photons.

B. Tissue Emission Wing Imaging

The sample used for the tissue emission wing imaging measurements consisted of a small piece of absorber (~1mm) embedded inside a large slice of prostate tissue (~30 x

20 mm) in a rectum-membrane-prostate structure as shown in Fig. 4.9a with a depth of ~4.0 mm from the surface of the rectum-membrane-prostate tissue structure. The tissue emission wing images are formed by the light emitted, not scattered, from the rectum-membrane-prostate sample tissues at the NIR emission wing range. In tissue emission wing imaging measurements, the detection wavelengths used were longer than that of the illumination so that the pump light was blocked, and the images recorded by the CCD camera were formed only by light emitted from tissues.

The tissue emission images recorded at the wavelengths of 650 nm, 700 nm, and 800 nm with pump wavelengths of 550 nm, 600 nm, and 700 nm, are shown in Figs. 4.13a, 4.13b and 4.13c, respectively. It can be seen that the object (absorber) cannot be observed by the 650 nm and 700 nm images, but can be identified by the 800 nm image.

In order to determine the critical detection depth of the tissue emission wing imaging, the measurements were extended to the sample with an object hidden at depth greater than 4.0 mm at the detection wavelength of 800 nm and the illumination wavelength of 700 nm. The results show that the object cannot be observed with a depth more than 4.0 mm. This critical depth of 4.0 mm for which the object can be identified from the tissue emission wing imaging is larger than that from the scattered light imaging. This improvement of detection depth can be understood because the signal light in the tissue emission wing imaging travels much shorter distance than that in the scattering light imaging (photons travel back and forth).

C. Contrast Agent Fluorescence Light Imaging

The sample used for the contrast agent emission light imaging measurements

consists of a tiny piece (~1.0 mm) of prostate tissue dyed with indocyanine green (cardio green) embedded inside a large piece of host prostate tissue (~25 x 15 mm) in a rectum-membrane-prostate structure about 4.5 mm deep from the surface of the rectum-membrane-prostate tissues as shown in Fig. 4.9b. Since the emission from the contrast agents is much stronger and more polarized than tissue emission, introducing contrast

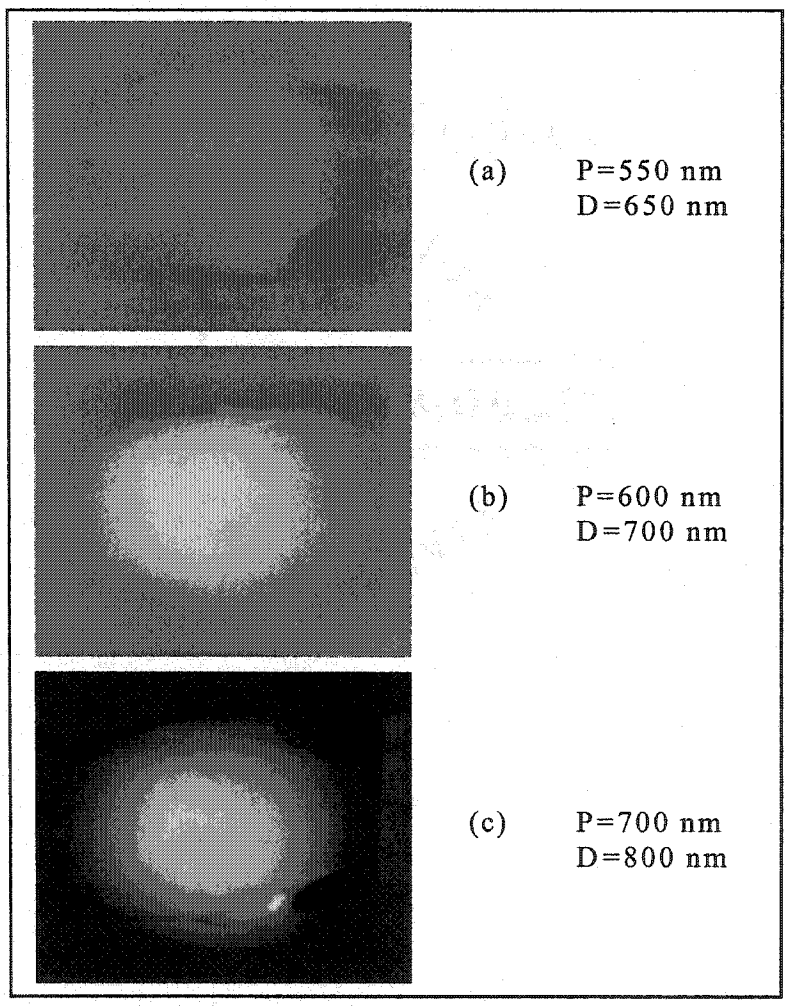

Fig. 4.13: Tissue emission wing images recorded at wavelengths of (a) D=650 nm with P = 550 nm, (b) D=700 nm with P= 600 nm, and (c) D=800 nm with P= 700 nm, respectively, where P: pump, D: detection. The sample consists of a small dot piece of a black absorber hidden inside a large host prostate tissue in a human rectum-membrane-prostate structure at depth of 4.0 mm from the surface of the rectum.

agents to the NIR spectral polarization imaging technique is expected to further improve the imaging depth and resolution.

The contrast agent emission light images for the sample described in Fig. 4.9b recorded at different pump and detection wavelengths varied from 600 nm to 900 nm are shown in Fig. 4.14. The salient feature of the images is that the dyed object cannot be distinguished by images obtained with short pump wavelengths (600 nm and 700 nm), while the object can be clearly identified by the images obtained with longer pump wavelengths (750 nm and 800 nm). When the pump wavelength increases, the visibility of the dyed object increases dramatically. This improvement can be seen more clearly by their image intensity distribution of a cross section taken from a same number row of the different images as shown by curves on the right side of Fig. 4.14. Using the data from these curves, the image contrasts for images with detection wavelengths of 800 nm (Fig. 4.14b), 850 nm (Fig. 4.14c), and 900 nm (Fig. 4.14d) were calculated to be ~ 0%, 17.7 % and 19.3%, respectively. This pump wavelength dependence of the image quality can be explained from the measured relative absorption spectra of prostate and rectum tissues and Indocyanine Green shown in Fig. 4.12c. With longer wavelengths (750 nm and 800 nm) pump, the light can penetrate the rectum-membrane-prostate tissues and reach the dyed object. In addition, the absorption of Indocyanine Green at 750 nm and 800 nm is stronger than that at short wavelengths, and the emission from the dye is much stronger than that of native emission from prostate tissues. As a result, the dyed object can be clearly distinguished by those contrast agent emission light images. The good contrast of the image shown in Fig. 4.14d indicate the possibility of observing the dyed object at depth greater than 4.5 mm, i.e. the object hidden inside the prostate tissue at certain depth

greater than 4.5 mm should be observed. In order to obtain critical depth for the contrast agent fluorescence light imaging, measurements were extended to the samples with the dyed tissue embedded at depths of more than 4.5 mm using the detection wavelength of 900 nm and the illuminating wavelength of 800 nm. The results show that the dyed dot tissue with a diameter of ~1 mm embedded at depth of 7.5 mm inside a large host prostate tissue in a rectum-membrane-prostate structure can be distinguished even if the illumination power was only ~50 μ w/cm^2.

We have performed and compared different spectral polarization imaging methods on human rectum-membrane-prostate samples using light scattered or emitted from tissues, and light emitted from contrast agents. The small foreign objects with a diameter of ~1 mm hidden inside the host prostate tissues in rectum-membrane-prostate structures at depths 2.5 mm, 4.0 mm, and 7.5 mm were imaged and identified using the (A) scattered light imaging, (B) tissue emission wing imaging, and (C) contrast agent fluorescence imaging methods, respectively. These results show that through rectum tissues, small objects hidden inside the host prostate tissues in a rectum-membrane-prostate structure can be imaged and identified at a certain depth without removing tissues using the NIR spectral polarization imaging technique, in particular, by the contrast agent fluorescence imaging methods. Our results indicate the potential of imaging and detecting structural changes and cancers inside prostate tissue through rectum-membrane-prostate tissues using noninvasive spectral polarization and fluorescence imaging techniques.

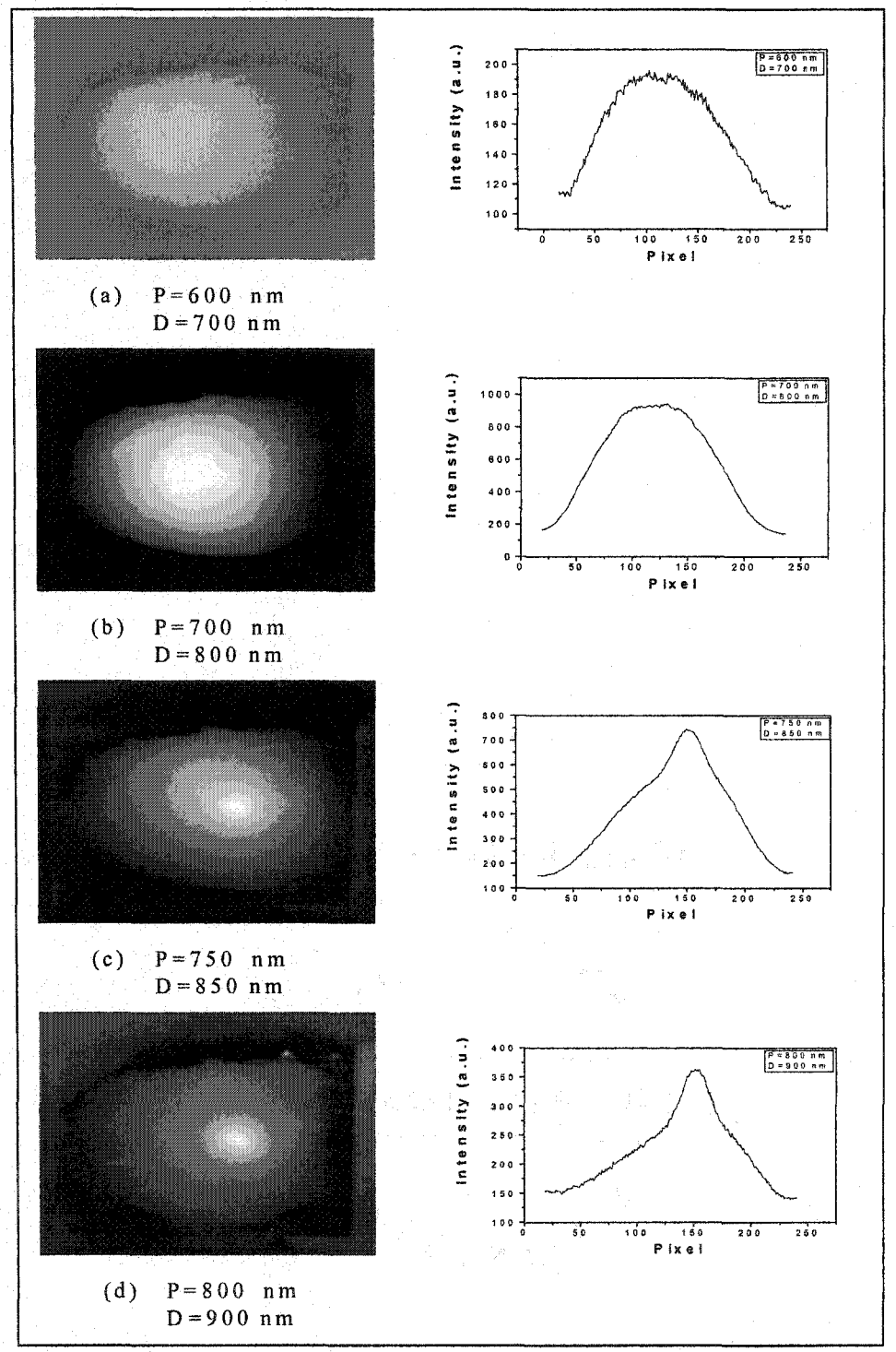

Fig. 4.14: Contrast agent fluorescence images recorded for an object hidden 4.5 mm inside the prostate tissue with (a) P=600nm and D=700nm, (b) P=700nm and D=800nm, (c) P =750nm and D=850nm, and (d) P =800nm and D =900nm, where P: pump, D: detection. The curves on the right side show cross section intensity distributions of corresponding images shown on the left side. The cross sections were taken from a same number row of the different images.

4.4 References

1. T. S. Curry III, J. E. Dowdey, R. C. Murry Jr., in: Christensen's Introduction to the Physics of Diagnostic Radiology, 3rd ed., Lea and Febiger, Philadelphia, 1984.

2. F. J. Green, The Sigma-Aldrich Handbook of Stains Dyes and Indicators, Sigma-Aldrich Corporation, 407, 1991.

3. P. S. Anderson, S. Montan, S. Svanberg, IEEE J. Quantum Electron. QE-23, 1787, 1987.

4. K. M. Yoo, Zhi-Wei Zang, S. A. Ahmad, R. R. Alfano, Optics Lett. 16, 1252, 1991.
5. G. Zhang, Ph. D. Thesis, The City University of New York, 2001.

6. L. Wang, P. P. Ho, C. H. Liu, G. Zhang, and R. R. Alfano, Science 253, 769, 1991.

7. Eugene Hecht, Optics, the Second Edition, Addison-Wesley Publishing Company Inc., Chapter 8, 294, 1990.

8. D. J. Tindall and P. T. Scardino, "Defeating prostate cancer: Crucial directions for research-Except from the report of the Prostate Cancer Progress Review Group (Review)," Prostate, vol. 38, no. 2, pp. 166-171, 1999. P. T. Scardino, "Prostate cancer, treatment, and prevention," Newsweek, Nov. 1, 11, 1999.

Chapter 5

Near Infrared Spectroscopy and Imaging to Detect Water in Normal and Cancer Human Prostate Tissues

5.1 Background

Cancer is a disease characterized by the uncontrolled growth and spread of abnormal body cells. The human body is made up of billions of cells. Normally, cells reproduce themselves by dividing so that growth occurs. Worn-out tissue is replaced and injuries are repaired in this manner. Occasionally, cells grow abnormally, into a mass called a tumor. Some tumors are benign (noncancerous); others are malignant, or cancerous [1]. The growth of a benign tumor may interfere with body function, but these tumors are seldom life-threatening. Malignant tumors, on the other hand, invade and destroy normal tissue. By a process called metastasis, cells break away from a cancerous tumor and spread through the blood and lymphatic system to other parts of the body where they form new tumors.

The interaction between light and tissues are wavelength dependent. Well-defined wavelengths can be absorbed by chromophores naturally present in tissue such as proteins, water, and adipose. Ever since Alfano and coworkers discovered that fluorescence spectroscopy can be used to detect cancer in tissues [2], optical spectroscopy using absorption, emission and scattering of light has been shown to be a novel way to detect diseases. Typically visible and UV light is used to excite the proteins and other chromophores present in tissues. NIR from 0.7 to 1.3 μm is used to deeply probe tissues such as breast and brain. Since water is the main component of the tissue,

water may be important to cancer probing. There are several different grades or stages of cancer, and these may be ranked using a well-known scale that classifies cancerous and precancerous regions into any of five Gleason Grades, usually denoted as Stages 1, 2, 3, 4 and 5 [3]. Precancerous stages (denoted as stages 1 and 2) correspond to the early stages of cancer [4]. These stages are associated with less amount of water content in these regions than at later stages. Water is one of the main components in the body and helps provide for the conversion of mechanical energy developed by contractile proteins into the chemical energy useful in cell processes. Regulating the water volume within the living cell affect the ability of contractile proteins to mechanically control ion selectivity, ion accumulation, and electron transport in mitochondria [5-6]. Within a local region in the tissue, the amount of water varies very little from site to site. H_2O is involved in chemical and physiological reactions activated by light. The free OH stretching vibration in water has a spectral feature at 3463 cm^{-1}. The Raman and infrared spectra of water and ice has been investigated [7-10]. Bonding of H_2O molecules to other components in tissues give rise to a band at 3434 cm^{-1} (or a shift in OH from 3463 cm^{-1} to 3434 cm^{-1} due to hydrogen bonding). Overtones of OH vibrations exist at 1444 nm, 1944 nm and other wavelengths. A great deal of research has focused on nuclear magnetic resonance (NMR) spectroscopy, where the signal is generated by the nuclear spin of the photons present such as in water [11]. NMR is used in tomography to yield images of various parts of the body to detect tumors. Optical vibrational spectroscopy and its use to image H_2O offers a new tool for optical diagnosis. It has been shown that the water spectrum of a rat or a mouse's skeletal muscle is broader than in pure water and this is due to the higher order complexes of water. This is due to the water molecules interaction with

cellular or other macromolecules. Recently, it has been shown that the water heating via absorption band at 1430 nm is correlated to a higher tensile strength of tissue welded by a laser [12]. Optical vibrational spectroscopy of a tissue sample contains information about the biochemical composition and vibrational structure of the tissue. As mentioned earlier, fluorescence and light scattering arising from proteins, nucleic acids, lipids, flavins, NADH, tryptophan, collagen, elastin and other macromolecules have been used to investigate normal, pre malignant, and malignant tissues [2,13-14]. NIR spectral polarization imaging was used to image absorbers dyed with indocyanine green at different depths inside prostate tissues [15].

Current techniques for detection of prostate cancer have a limited contrast and resolution. These are: digital rectal examination (DRE), the prostate specific antigen (PSA) blood test, and the ultrasound imaging. None of the techniques are able to detect early stages of cancer. There are a limited number of spectroscopic studies on the role of water in tissue particularly in tumors. It was shown that there is less water in cancer than normal prostate tissues probably associated with early stages of cancer [16]. The water content may be used as a key native spectral marker molecule for cancer imaging. Water is proposed as a new fingerprint marker to denote changes in the NIR region for prostate, breast, and cervix cancer detection.

We will investigate near-infrared (NIR) spectral and polarization methods to determine the role of water in neoplastic tissues to detect and image, non-invasively, cancer in prostate tissues. The concept for this new approach to detect tumor is that the amount of water is different for normal and neoplastic tissues.

The NIR absorption is directly related to the concentration of water in the biological samples. From optical density measurements or determination of the attenuation coefficient, water content can be determined in both cancer and normal tissues. The concentration of water may be able to monitor the cancer and normal states of tissue. We found that there is a lack of water in neoplastic tissues in comparison to surrounding normal tissues. The work reported here focuses on understanding the scattering and absorption of light by prostate tissue in the visible and NIR region (400-2400 nm). The difference in water absorption is investigated in cancer and normal human prostate tissues by means of spectroscopy, transmission and backscattering of visible and NIR and is due to the different intermolecular bonding by OH in H_2O in neoplastic and normal prostate human tissues. NIR imaging at overtone frequencies is used to distinguish local regions of tissues by their variation in water concentration. Our technique has the advantage over other spectroscopic techniques such as fluorescence and Raman scattering in its being sensitive to chromophores that absorb in the NIR independently of whether these chromophores fluoresce or have a large Raman cross sections. The detected NIR signals in this absorption technique are larger than fluorescence and Raman scattering signals. It is the first time, to the best of our knowledge, that cancer can be detected and imaged based on the water content changes in the tissue.

5.2 Experimental Methods

Fresh prostate tissue specimens were obtained from the National Disease Research Institute (NDRI) under Institutional Review Board (IRB) at CCNY. A photograph of a typical specimen of human prostate tissue is inserted in Fig. 5.1 using a

conventional digital camera. Samples were preserved in saline water. Samples were cut evenly thin. Sample thicknesses were about $330\mu m$, and their areas were about 2X3 cm^2. Samples were arranged such that the right hand side of the specimen was marked as mostly cancerous tissue, while the left hand side was mostly normal tissue. Five different specimens were investigated. For our study, the cancer tissues were harder than normal tissues.

The absorption spectra of normal, cancer prostate tissues, and water were measured using a Perkin-Elmer Lambda 9 UV/VIS/NIR Spectrophotometer with accompanying software. The optical density is defined as $O.D. = \ln(\frac{I_0}{I}) = \ln(\frac{1}{T})$, where I_0 is the incident intensity, I is the transmitted intensity through the sample, and T is the transmission ($T=I/I_0$). Images of the scattered light from human prostate samples were measured using the spectral polarization imaging setup shown in Fig. 5.1. In the imaging measurements, a white light beam of diameter ~ 2 cm was used to illuminate the sample. Wide band filters centered at 700 nm, 800nm, 1200nm, and 1450nm were used to select the desirable spectral range of the illumination and the detected light. The bandwidth of the optical filters is about 60 nm. A polarizer (P_1) is located in the incident light beam pathway to obtain a linearly polarized illumination light. The second polarizer (P_2) is positioned in front of the CCD camera for selecting the detection polarization direction (parallel and perpendicular relative to the orientation of P_1). In the visible and NIR range (600-900 nm) a cooled CCD Silicon camera (Photometric CH250) equipped with a zoom lens of 50-mm focal length is used to record the images in the transmission and backscattering geometry. Similarly, images at 1200 nm and 1450 nm were obtained using an InGaAs NIR CCD camera (for spectral response see Chapter 2).

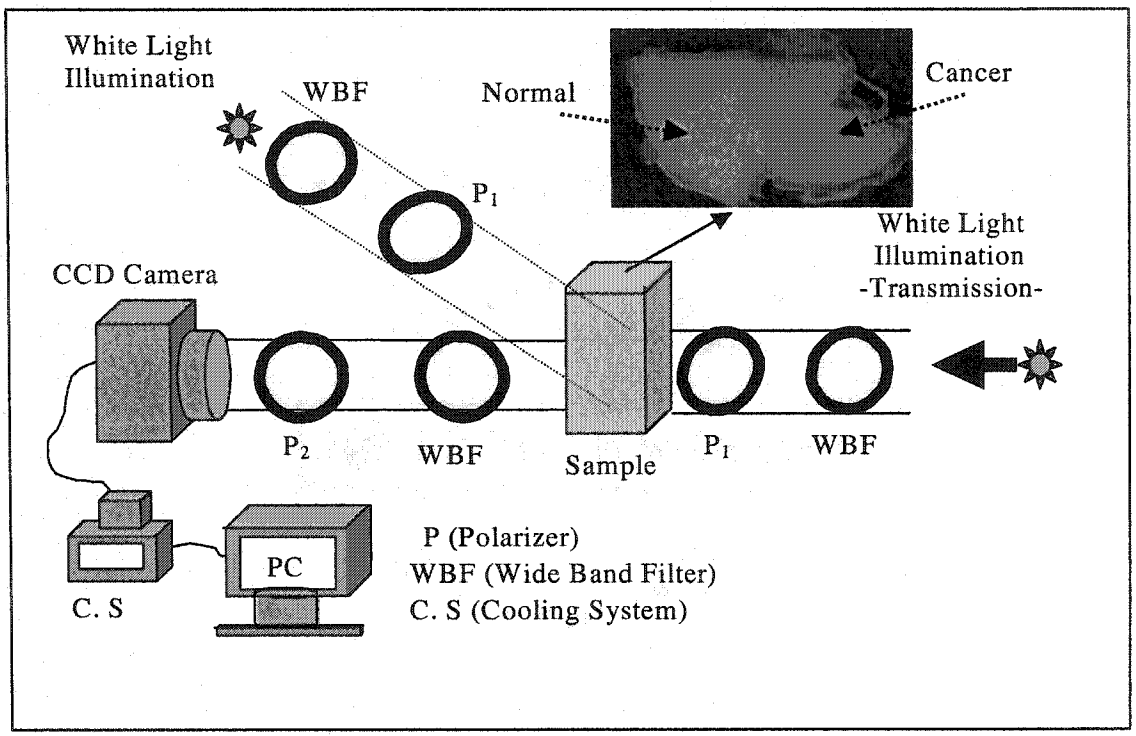

Fig. 5.1: Experimental imaging set up for detection of human prostate cancer and normal tissues using a visible and near-infrared polarization technique. The insert shows the photograph of human cancer and normal prostate tissue using a conventional digital camera.

5.3 Experimental Results and Discussion

The absorption spectra of the five in-vitro samples studied of thicknesses varying from 300 to 380 μm show very similar results. The absorption spectra of normal and cancer prostate tissues (330μm thickness), and a water sample with a 200μm thickness used as a reference between 400 and 2400 nm are shown in Fig. 5.2a. The fingerprints of water absorption in this spectral range are 980 nm (very weak), 1195 nm (weak), 1444 nm (strong), and 1930 nm (very strong). The absorption of water between 400 nm – 800 nm is almost flat and is very small compare to that at longer wavelengths such as 1444 nm and 1930 nm. The absorption at 1444 nm is due to the first overtone of the OH

stretching vibration in water. It is well known that the absorption of the stretching vibration of the O-H bond in a non associated (free) alcoholic or phenolic hydroxyl group produces a strong band at 3600 to 3650 cm^{-1} (2780 – 2740 nm, respectively) in the fundamental region and near 7100 cm^{-1} (1410 nm) for the first overtone [17].

It is well known that scattering is a smooth function of wavelength while absorption is represented by peaks in the NIR spectra [18]. The absorption and scattering spectra of cancer and normal prostate tissues shown in Fig. 5.2a is composed of absorption bands superimposed on a smoothly varying background caused by light scattering. It can be concluded from the optical density data displayed in Fig. 5.2a that scattering from cancer tissue is stronger than the scattering from normal tissue in the forward direction between 400-1200 nm. Both cancer and normal cell nuclei are considered to be large particles (larger than the visible-NIR incident wavelengths) and they obey Mie scattering resulting in a strong forward scattering. Since the nucleus of the cancer cell is larger than that of the normal cell [19], the forward scattering intensity for cancer tissues is larger than that for the normal tissues. So, the transmission of cancer tissue is stronger than that of normal tissue. At 1444 nm and 1944 nm the absorption dominates, so the absorption is stronger than scattering. The profiles show that absorption of normal tissue is stronger than that for cancer tissue at 1444 nm and 1944 nm, which indicates that the content of water in normal tissues is more than that in cancer tissues. These peaks around 1444 nm and 1944 nm in prostate tissue are due to the water-tissue interaction and are shifted toward longer wavelengths from the stretching frequency of a bonded free OH group (shifts towards the lower wave numbers). This is probably due to the higher order phases of water and their interaction with cellular or other macromolecules in prostate tissues.

We noticed that strong forward scattering is still present for a 330 μm thickness. Since the g factor in tissue is large (~ 0.9), the scattering is strongly forward. We can estimate the attenuation length in this tissue based on the exponential decay process (proportional to $e^{-\mu_t x}$), where μ_t is the attenuation (extinction) coefficient. The calculated extinction coefficients (μ_t) of water at different wavelengths are given in Table 5.1. The extinction coefficient of water at 700 nm is ~ 0.433 cm^{-1} (the attenuation length is about 2.31 cm), 1.29 cm^{-1} at 1200 nm, and 9.7 cm^{-1} at 1450 nm. The attenuating length at 1450 is ~ 7.5 times shorter than that at 1200 nm and approximately 22 times shorter than 700 nm in water. To remove the effect of scattering on the profile shown in Fig. 5.2a, a smooth fitted curve reflecting the contribution of scattering is subtracted from the original curve. The smooth fitted curve is obtained by choosing data points along the scattering curve and fitting that to a high-order polynomial function. The result is shown in Fig. 5.2b. The absorption fingerprints in the visible region at 420 nm and 570 nm are due to the blood in the tissue matrix (Hb and HbO_2).

In prostate cancer tissue, the attenuation length at 1450 nm is ~ 1.2 times smaller than that at 1200 nm. In prostate normal tissue, the attenuation length at 1450 nm is ~ 1.3 times smaller than that at 1200 nm. The total attenuation coefficient of normal tissue is larger than that of cancer (as seen in Table 5.1). The attenuation length (equal to $1/\mu_t$) of normal tissue is shorter than that of cancer tissue. This means that the photons traveling in prostate normal tissue will be absorbed and scattered at a shorter distance than that of cancer tissue. The attenuating length ($\ell_t = \frac{1}{n\sigma}$) is inversely proportional to the number of particles per unit volume (n) and the cross section of the scatterer (σ).

Fig. 5.3 shows transmission images of cancer-normal samples at 700 nm, 800nm, 1200 nm, and 1450 nm for parallel and perpendicular polarizations. The left piece of the specimen (mostly normal) has less transmission intensity than that on the right side

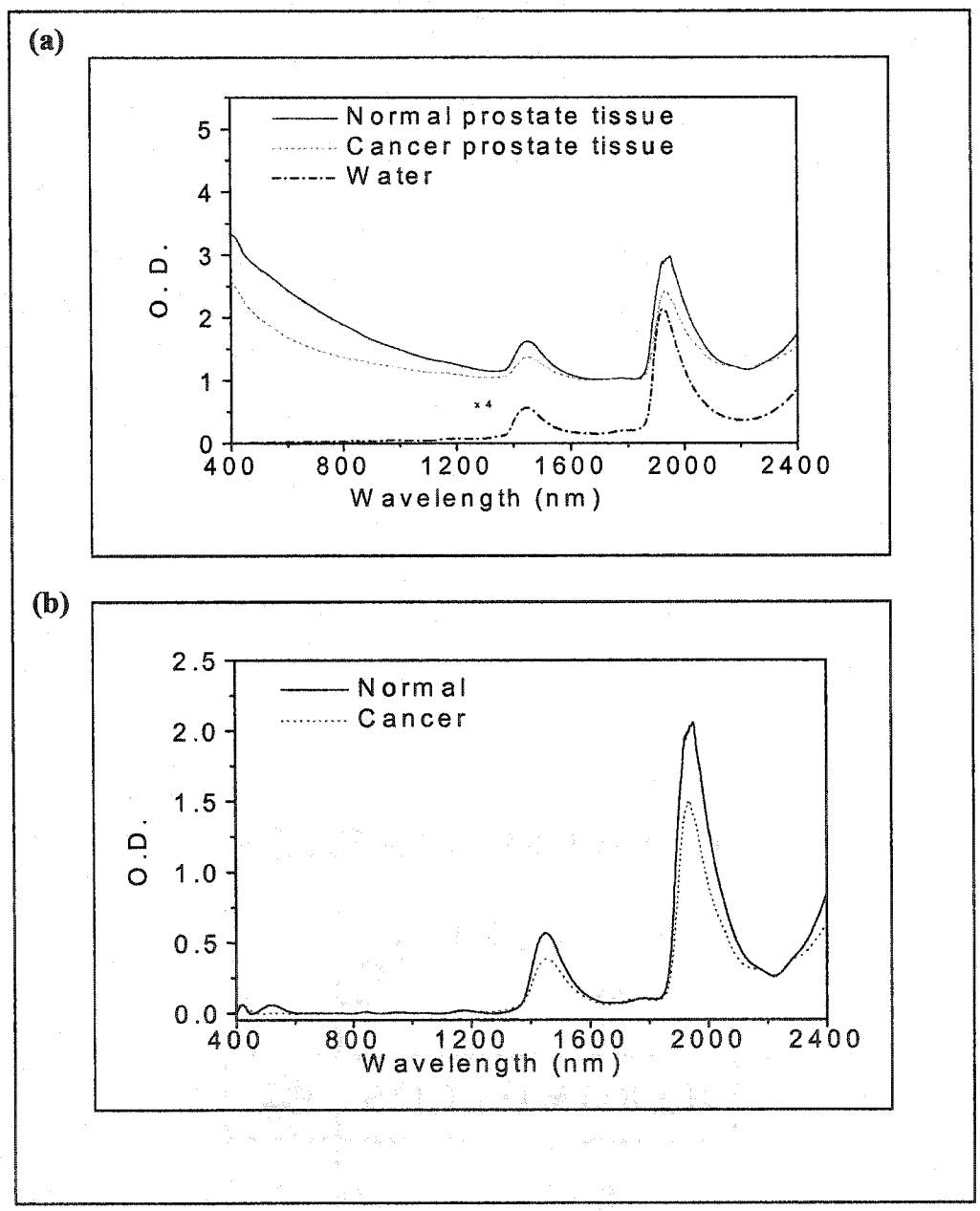

Fig. 5.2: (a) Optical density (O. D.) versus wavelength in the 400-2400 nm region for (__ normal prostate tissuel, ... Cancer prostate tissue, and _._._ water). (b) Optical density for normal and cancer prostate tissues with scattering wing removed by subtracting the scattering effect in (a) using the scattering wavelength fitting function.

(mostly cancer) at all wavelengths (700nm, 800nm, 1200nm, and 1450nm) as shown in

λ (nm)	O.D.			T			μ_t (cm^{-1})		
	C	N	W	C	N	W	C	N	W
700	1.50	2.14	0.0062	0.0326	0.0074	0.9858	104	149	0.433
800	1.37	1.89	0.0077	0.0440	0.0132	0.9824	95	131	0.538
1200	1.10	1.25	0.0185	0.0818	0.0577	0.9583	76	86	1.29
1450	1.36	1.61	0.1394	0.0451	0.0252	0.7254	94	112	9.70

Table 5.1: Extinction coefficient (μ_t), optical density ($O.D.$) and transmission (T) of human prostate normal tissue (N), prostate cancer tissue (C) and water (W).

Fig. 5.3(a-h). Similar results were obtained in normal-cancerous human breast tissues using picosecond temporal time-gated imaging at 800 nm by the use of a Ti:Sapphire pulsed laser [20]. In the large particle case (Mie scattering), the intensity for the forward scattering is higher than that for the backscattering. Since the nuclei of cells in cancer tissue are larger than that for normal tissue, the forward scattering for cancer samples are expected to be larger than that for normal samples in the forward direction [19, 21]. At 1200 nm the scattering is stronger than absorption. The forward scattering intensity from cancer tissues at 1200nm is higher than that from normal tissues as shown in Fig. 4.16a. As a result the transmission through cancer tissues is more than that for normal as shown in the images in Fig. 5.3c (parallel) and 5.3g (perpendicular). At 1450 nm wavelength absorption dominates, so the main reason for the higher transmission in a cancer region is due to less H_2O in cancer than in normal regions, which is related to the microscopic bonding of OH in prostate tissues. The transmission intensity through normal tissues is weaker than that of cancer tissues. The tissue that has more water in it will absorb the

incoming photons more than that which has less water at the absorption peaks of water. This difference in the concentration of water in tissue will also cause difference in the degree of scattering. The difference in the images displayed in Figs. 5.3d and 5.3h result mainly from the smaller absorption of water in cancer tissue (first overtone of the OH stretching vibration); in addition, the forward scattering in cancer tissues is larger than that of normal tissues.

From the curves displayed in Figs. 5.2a and 5.2b, the absorption peak at 1450 nm is stronger than that at 1200nm. The scattering at 1450 nm is less than that at 1200nm. Most of the photons at 1450 nm that are incident on the samples get strongly absorbed by water molecules. Photons at 1200 nm get absorbed less. Since cell nuclei are larger than the incident wavelengths they predominantly scatter light in the forward direction. The scattered intensity is related to the population density of the nuclei. For the perpendicular imaging case, the depolarization is due mostly to multiple scattering events. The depolarization is caused by the cell size and shape, and this will cause photons to be more depolarized in cancer tissue. Cancer cells are more randomized in shape and size. The internal structures of the cancer tissue randomize the light more than for normal tissue in the forward direction, which is highly ordered in water as shown in Fig. 5.3.

In the backscattering geometry, images as shown in Fig. 5.4, the light scattering from cancer tissues is stronger than that from normal tissues. It is known that the index of refraction for cancer tissue is higher than that of normal tissue [17]. The scattering angle θ_S can be written in terms of the scattering wavelength (λ) and the size of the scatterer (a) as $\theta_S \sim \frac{\lambda}{a}$. For objects having small scattering sizes relative to the incident wavelength, such as mitochondria (much smaller than normal cell size),

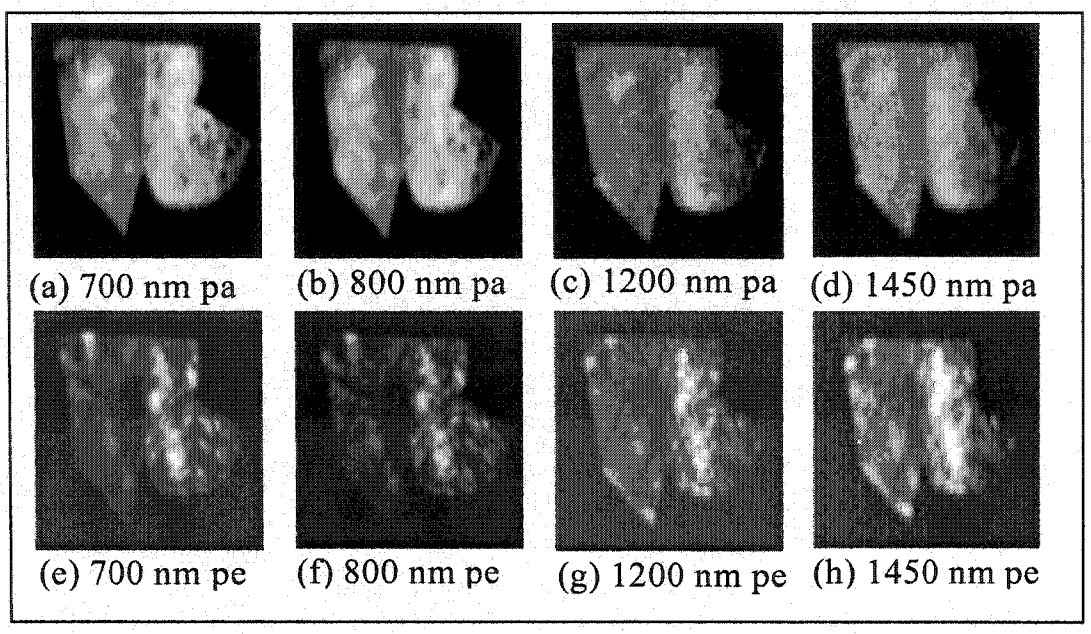

Fig. 5.3: Transmission images of human prostate tissue, normal (left) and cancer (right) at different visible and NIR wavelengths for parallel (top images) and perpendicular (bottom images) polarization configurations. The sample thickness is ~ 330 μm and its area is 2X3 cm^2.

scattering in the backward direction is larger, giving a stronger signal for scattering off small structures. The mitochondria index of refraction for cancer tissues is higher that for normal tissues. This is one of the reasons why small particles such as mitochondria are an important factor in backscattering and for large angle scattering. The index of refraction of tissues is a function of water content varies linearly between 1.33 and 1.50 for water contents between 100 percent and 0 percent, respectively [22]. Consequently, it is generally given by: n = 1.5 – (1.5 - 1.33)*W, where W is the volume fraction of water [22-23]. Accordingly, since cancer tissue has less water than normal tissue it has a higher index of refraction than normal tissue. Due to the following factors: cancer tissue has a higher index of refraction than normal tissues, and as a consequence has weak absorption by water in the NIR, it is expected that the backscattering intensity for cancer tissue is

larger than that of normal tissue as shown in Fig. 5.4. It is also known that smaller particles in tissues such as mitochondria play a major role in the backscattering geometry [21, 24]. Mitochondria from cancer cells have a higher index of refraction than from normal cells. The backscattering signal from tissue is determined mainly by the index of refraction and the particle sizes. The cancer region will be brighter than the normal region due to its higher index of refraction, lower H_2O absorption, and small particle sizes.

Digitized horizontal scans from left to right at the center of the transmission images displayed in Figs. 5.3(a-d) were obtained. The digitized images show that the cancer tissue region scatters more than that of the normal tissue region due to the reasons that have been discussed earlier. Linearly polarized light incident on tissue loses its

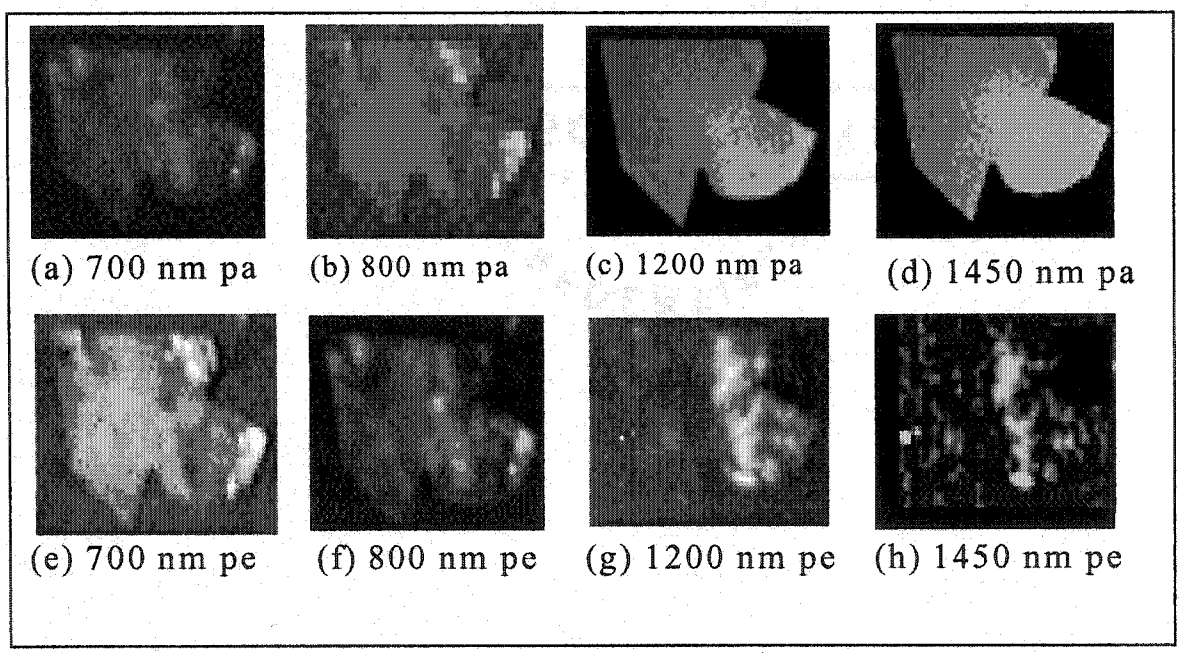

Fig. 5.4: Backscattered images of human prostate normal (left) and cancer (right) tissue at different visible and NIR wavelengths for parallel (top images) and perpendicular (bottom images) polarization configurations. The sample thickness is ~ 330 μm and had an area of 2X3 cm^2.

polarization as it traverses the medium. A portion of the incident light is backscattered by the tissue surface, retaining its polarization in this single scattering event. The remaining light propagates in a turbid medium such as prostate tissues and can be viewed as consisting of three components: ballistic, snake and diffusive. Diffusive light is the dominant component consisting of multiple-scattered photons that travel the longest path, and takes the longest time to exit the sample. Ballistic photons traverse the shortest path, retain most of the characteristics of the incident photons, and carry direct information about the interior structure of the scattering medium. Snake photons follow the ballistic light in time and involve more scattering events; they retain a significant amount of the initial properties and information on structures hidden in the scattering medium.

The calculated contrasts between cancer (I_{max}) and normal tissues (I_{min}) are 0.11 at 700 nm and 800 nm, 0.17 at 1200 nm, and 0.15 at 1450 nm. The main difference between the 1200 nm and 1450 nm contrasts is that at 1450 nm the resulting contrast is due to the microscopic OH bonding in prostate tissue while at 1200 nm the difference may be due to the macroscopic scattering size and population density in the prostate tissue.

The calculated degree of polarization (D) for normal and cancer tissues at different wavelengths is shown in Table 5.2. The values of D for normal tissues are higher than that for cancer tissue at all wavelengths (700nm, 800nm, 1200nm, and 1450nm). This result is expected, arising from the greater randomization (abnormal growth) of the cancer cells while the normal cells are more ordered than cancer in tissues. The degree of polarization of outgoing light depends on the details of the single scattering by the particle and the number of scattering encountered by light. Light is less depolarized in one scattering event if the scattering is more forward-directed, which is

characterized by the anisotropy factor g. Roughly speaking, D is related to the ratio of the sample thickness of the slab over the transport length rather than the size of the particle. D decreases as this ratio increases. Bicout et al. [25] show that for small particle size there is a maximum point of polarization, and is then followed by a decrease in polarization. Tissues, however, have large particles sizes that vary in sizes and shapes that complicate the calculation of the degree of polarization. Assuming spherical particles for normal and cancer nuclei, it can be derived from Mie calculations that the transport length of the normal tissue is larger than that of the cancer tissue. This results in a slower depolarization for normal tissue than that for cancer tissue. The degree of polarization of the cancer and normal tissues increases as the wavelength increases, which suggest that at longer wavelengths the light will scatter less.

Wavelength (nm)	D_{Normal}	D_{Cancer}
700	0.079	0.059
800	0.100	0.088
1200	0.761	0.435
1450	0.849	0.749

Table 5.2: The degree of polarization of the images in Figs. 4.17(a-d).

In conclusion, the amount of water in tissues alters the absorption in the NIR from the OH overtone vibrational bands at 1444 nm and 1944 nm. These key spectra fingerprints are used to distinguish between low concentration and high concentration

region of water. The local deviations in both the concentration of water and cell size in prostate tissue cause differences in the degree of scattering and overtone absorption. The difference in water content in normal and cancer prostate tissues can be imaged and used for prostate cancer detection. This method can be extended to detect cancer in other organs such as breast and cervix. It appears that cancer tissues may contain less water than normal tissues at an early stage of cancer. It was found that the forward scattering intensity for cancer tissues is larger than that for normal tissues. Due to the higher index of refraction of cancer tissues, and the lower absorption of water in cancer, the backscattering intensity for cancer tissue was found to be larger than that of normal tissue. This information can be used to detect cancer regions in prostate tissue using NIR spectral polarization and difference imaging techniques. Water may also be an important spectral fingerprint marker in other tissue types such as breast and cervix to detect cancer at early stages.

5.4 References

1. D. J. Tindall and P. T. Scardino, "Defeating prostate cancer: Crucial directions for research-Expert from the report of the Prostate Cancer Progress Review Group (Review)," Prostate, vol. 38, no. 2, pp. 166-171, 1999. P. T. Scardino, "Prostate cancer, treatment, and prevention," Newsweek, Nov. 1, 11, 1999.

2. R . R. Alfano, D. Tata, J. Cordero, P. Tomashefsky, F. Lonyo, and M. Alfano, IEEE J. Quantum Electron, Vol. 20, 1507, 1984.

3. Juan Rosai. Ackerman's Surgical Pathology, Vol. 2, Mosby Incorporated, 1998.

4. Gleason DF, Mellinger GT. Prediction of prognosis for prostatic adenocarcinoma by combined histological grading and clinical staging. J. Urol. 111, 58, 1974.

5. A . Szent-Gyorgyi, Bioenergetics, Academic Press, New York, 1957.

6. L . Minkoff and R. Damadian, Physiol. Chem. & Physics 8, 349, 1976.

7. N. Ockman and G. B. Sutherland., Proc. Roy. Soc. Vol. A247, 434, 1958.

8. H. K. Shin., J. Chem. Phys., Vol. 69, 1240, 1978.

9. G. E. Walrafen, J. Chem. Phys., Vol. 44, 1546, 1966.

10. Mark Sceats, Stuart A. Rice, and J. E. Butler., J. Chem. Phys., Vol. 63, 5390, 1975.

11. C . Hazlewood, and B. Nicholas, Nature, Vol. 222, 747, 1969.

12. J . Tang, F. Zeng, J. Evans, B. Xu, H. Savage, P. P. Ho, and R. R. Alfano, J. Clin. Laser Med. Surg., Vol. 18, 117, 2000.

13. R . R. Alfano, B. B. Das, J. Cleary, R.Prudente, and E. Celmer, Bull. N. Y. Acad. Med., Vol. 67, 143, 1991.

14. C . H. Liu, B. B. Das, W. L. Sha Glassman, G. C. Tang, K. M. Yoo, H. R. Zhu, D. L. Akins, S. S. Lubicz, J. Cleary, R. Prudente, E. Celmer, A. Caron, and R. R. Alfano, J. Photochem. Photobiol., Vol. 1887, 188, 1992.

15. W .B. Wang, J. H. Ali, J. M. Vitenson, J. M. Lombardo, and R. R. Alfano, SPIE, Vol. 3917, 75, 2000.

16. W. B. Wang, J. H. Ali, M. Zevallos, and R. R. Alfano. Near infrared imaging of human prostate cancerous and normal tissues based on water absorption, in OSA Biomedical Optics Topical Meetings on CD-ROM (The Optical Society of

American, Washington, DC), MF 38, 2004.

17. Dudley Williams, Nature Vol. 210, 194, 1966.

18. Fay A. Marks, Frontiers in Bioscience Vol. 3, a1-10, 1998.

19. V. Backman, R. Gurjar, K. Badizadegan, I. Itzkan, R. Dasari, L. Perelman, and M. Feld, IEEE J. Select. Topics Q. E.,Vol. 5, 1019, 1999.

20. S . K. Gayen and R. R. Alfano, Optics Express, Vol. 4, No. 11, 475, 1999.

21. Y . Shao, A. Maximov, I. Ourdev, W. Rozmus, and C. Capjack, IEEE J. Q. E., Vol. 37, 617, 2001.

22. S. A. Prahl, PhD thesis, University of Texas at Austin, 1988.

23. Private communication with Prof. Steven Jacques, 2003.

24. A. Dunn, and R. Richards-Kortum, IEEE J. Q. E. , Vol. 2, 898, 1996.

25. D. Bicout, C. Brosseau, A. S. Martinez, and J. M. Schmitt Phys. Rev. E 49, 1767, 1994.

Chapter 6

Time-resolved Photon Scattering Measurements in Highly Scattering Paint Medium

6.1 Introduction

This chapter describes the time-resolved photon scattering measurements in a highly scattering paint medium. The optical properties of paint will be obtained using steady state transmission measurements, polarization measurements, and time-resolved measurements techniques. The randomization of coherence and polarization from ballistic to diffusive in paint using steady and time resolved measurements will be investigated. The correlation of coherence (from time-resolved interference) and polarization in a scattering thin paint medium has been determined for the first time for the ballistic, snake, and diffusive regions.

6.2 Optical Properties of Paint

6.2.1 Background

Paint is a mixture of a pigment and a vehicle (a mix of solvent and solid binder) such as oil that together form a liquid. Different types of paint have different macro-structures (size and shape of the main paint structure) and molecular structures (absorption bands). In paint coating, the primary role of pigments is to provide the optical properties of hiding and color. Pigments impact hiding by virtue of their light absorption and scattering abilities.

Imaging of a translucent object hidden in a highly scattering random medium with

light is a challenging problem. However, strong random multiple scattering of light in paint washes out the shadow and renders these techniques ineffective for imaging beneath or through paint. The thickest scattering media to image or detect an object embedded in a random medium can be approximated by the number of scattering mean free lengths or the number of the transport scattering lengths. The first step in attaining ballistic and snake light imaging is to understand the nature of a light pulse propagating through turbid media [1-6]. Characteristics of the incident light pulse - intensity, duration, coherence, and polarization change as the pulse is scattered inside the highly turbid medium, e.g. painted layer. The pulse that emerges from the medium has very different characteristics than that of the incident pulse. The transmitted pulse consists of three temporal components: ballistic, snake and diffusive [4,5]. Three key optical parameters of scattering medium (e.g. paints) are the scattering length ℓ_s, the transport length ℓ_{tr}, and the absorption length ℓ_a. These parameters can be used to predict the intensity distribution of the output signal as a function of time. For a low loss ($\ell_a >> L$) layered sample of thickness L, the intensity of the ballistic component is ~ $\exp(-L/\ell_s)$. Diffusive light is the dominant component consisting of multiple-scattered photons that travel the longest path, and are the last to exit the sample. The diffuse component is temporally broadened, as it consists of photons that have been scattered randomly in all directions and have traversed different path lengths. The temporal profile of a diffuse pulse can be approximated by the diffusion theory when the thickness of the sample is many times larger than the transport mean free path (ℓ_{tr}) of the sample. For a narrow beam of ultrashort laser pulses incident at a point on a slab, the temporal profile of a transmitted pulse at a point on the other side of the slab is predicted by the diffusion theory as [7]

$$I(t) = \frac{1}{4td^2}\exp(-\upsilon t/\ell_a)\sum_1^{\infty} mSin\left(\frac{m\pi L}{d}\right) \times \exp(-(m\pi)^2 Dt/d^2), \tag{6.1}$$

where $d = L + 1.4\ell_{tr}$, v is the speed of light in the medium, D is the diffusion coefficient ($D = v\ell_{tr}/3$), and ℓ_a is the absorption length. For a thin slab, for a short pulse from an isotropic point source, the corresponding 1D photon density is replaced by that of the cumulative solution (as shown in chapter 2, equation 2.42):

$$U(z,t) = \frac{1}{(4\pi Dct)^{1/2}}\exp\left[-\frac{(z-R_Z)^2}{4Dct}\right]\exp(-\mu_a t) \tag{6.2}$$

where the center of particles, R_Z, $R_Z = c[1-\exp(-g_1 t)]/g_1$. Equation 6.1 or/and equation 6.2 can be used to fit the temporal profiles of the transmitted pulses in the forward scattering through a slab of turbid medium to obtain the transport and absorption lengths of a turbid medium. The appendix gives a computer program to fit equation 6.2.

The dynamic wave transport for diffusion approximation for paint film system at different thickness of samples is investigated. For long time exponential decay, the transmitted pulse shape is governed by diffusion which proportional to exp ($^{-t}/_{\tau}$). The transmitted pulse in the diffusion approximation is proportional to exp $(-(\pi^2 D_{eff} t/L^2 + \mu_a vt)$ giving [8,9]:

$$D_{eff} = \frac{L^2}{\pi^2}\left(\frac{1}{\tau} - \mu_a v\right), \tag{6.3}$$

where D_{eff} is the effective diffusion coefficient, L is the sample thickness, τ is the decay time, μ_a is the absorption coefficient, and v is the energy velocity.

The transport length and absorption length are obtained from the attenuation of the transmitted diffusive photons through a paint medium of different thicknesses, L, by

fitting the experimental data with the diffusion model. The diffusion coefficient and energy velocity are obtained for the highly scattering paint medium.

6.2.2 Experimental Methods

The experimental setup is shown below in Fig. 6.1. Ultrashort laser pulses from Ti:Sapphire laser of ~ 150 fs duration, 800 nm wavelength, 82 MHz pulse repetition rate. A part of the incident beam was used to trigger the streak camera with the use of a photodiode. The signal beam was focused by a long-focal-length lens into a

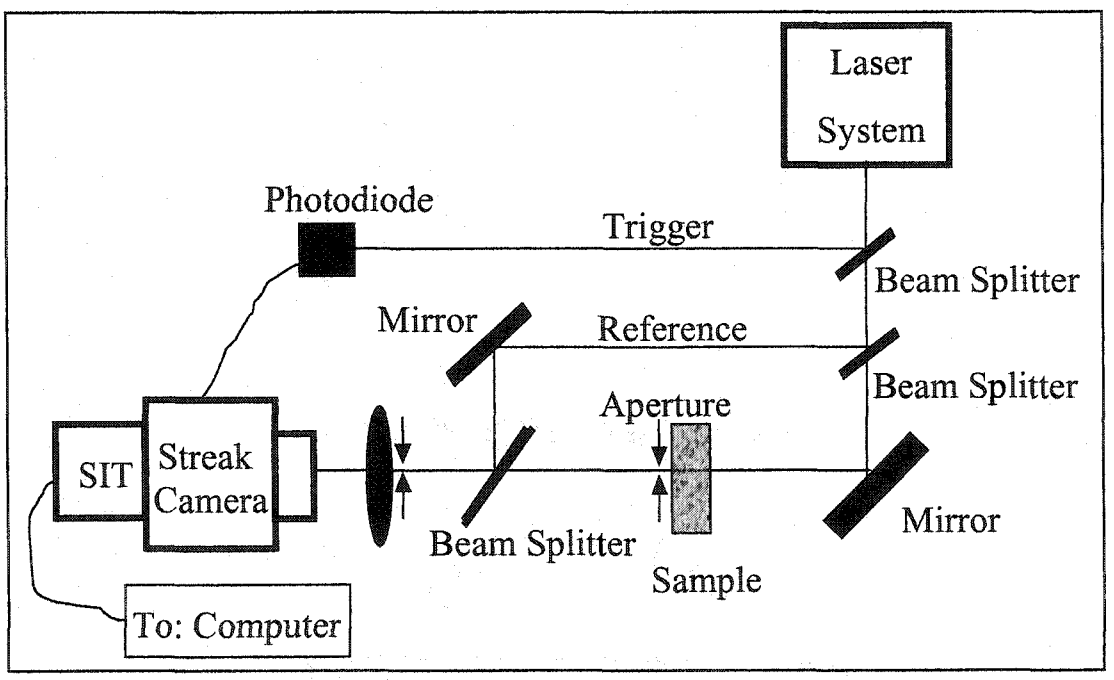

Fig. 6.1: Schematic diagram represents the experimental setup for the time-resolved transmission measurements through paint samples of different thicknesses.

small 1-mm-diameter spot on the sample. The paint sample thickness was varied between 10 and 900 μm. The transmitted signal was detected by a synchroscan streak camera. Small apertures were used to collect the transmitted photons scattered in the forward

direction.

6.2.3 Experimental Results

Figures 6.2a-d display the temporal profile of the transmitted pulses propagating through the $310\,\mu m$, $420\,\mu m$, $580\,\mu m$ and $900\,\mu m$ thicknesses of paint samples. Figs. 6.2a-d show both the experimental and theoretical fitting, where the dotted curve represents the experimental data and the solid curve is computed from equation 6.2. The parameters used in the calculation for the curves in Fig. 6.2 are given in the program at the beginning of the appendix.

6.2.4 Discussion and Outcome

The transport mean free path was obtained by fitting the scattered pulse profile, the photon densities, by the diffusion approximation [10] as shown in Fig. 6.2. The peak of theoretical (solid) curves is normalized to the peak of the experimental data. The solid curves are normalized to the total intensity of the experimental data. Experimental studies were carried out for different thicknesses between $10\,\mu m$ and $900\,\mu m$. None of the theoretical plots from the diffusion approximation agrees with the experimental results when $L < 310\mu m$, see Fig. 6.2a for $50\,\mu m$. For a thick medium, $L \geq 310\mu m$, the diffusion equation holds and the theory clearly fits the experimental data. Figs. 6.2c and 6.2d clearly illustrate an example where the diffusion theory fit the experimental data. The values of transport mean free path, and absorption lengths are measured at 800nm. The ℓ_{tr} and ℓ_a for the paint sample were measured with the pulse transmission technique using equation 6.2. The values of the transport length and absorption length for paint

medium are ℓ_{tr}~ 0.028 mm, *and* ℓ_a~ 27mm, respectively. The transport length represents the average distance traveled by the photon to randomize its direction. It is

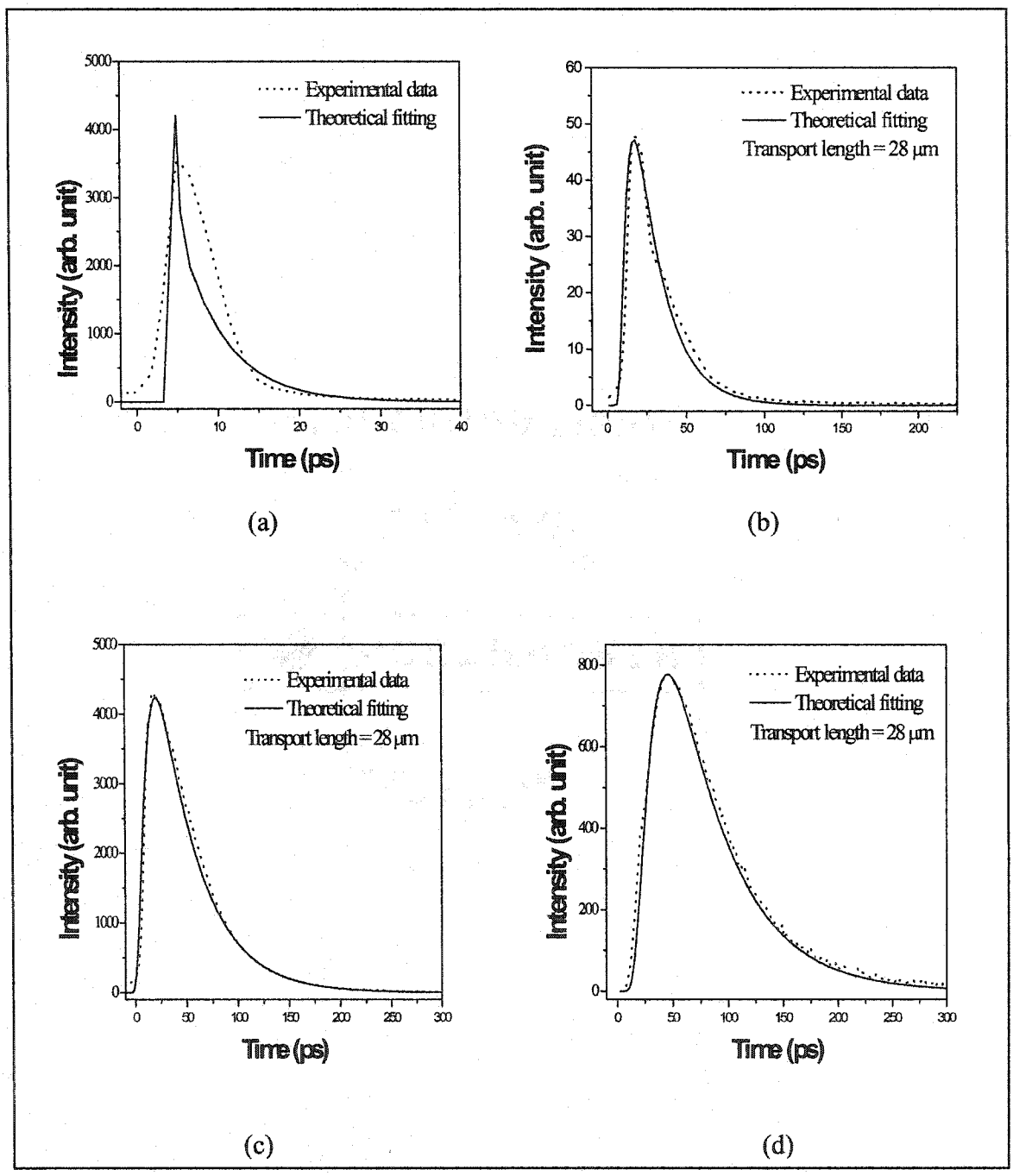

Fig. 6.2 Transmitted pulse profiles of (a)50 μm (b)420 μm, (c)580 μm and (d)900 μm under 800nm laser illumination are fitted to the diffusion equation. The dotted curve represents the experimental data and the solid curve is computed from the diffusion theory. The value of the transport length is 28 μm.

clear from the obtained data that paint medium is dominated strongly by scattering than absorption at 800 nm wavelength. This information will be useful in imaging through the paint. The critical thickness for imaging a hidden object such as corrosion and cracks beneath paint medium can be predicted. Also the explanation of the imaging results in the next chapter (chapter 7) will be possible and clearer.

The transmission intensity profile in here for different paint thicknesses were measured and typical results of the time-resolved transmission of $10\,\mu m$ sample is displayed in Fig. 6.3a. The decay process after a long time, for samples thicker than approximately $310\,\mu m$ as shown in Fig. 6.2, has an exponential decay function. This actually reflects the multiple scattering processes. Typical semi-log plot of transmitted intensity I(t) versus thickness for the 10 and 900 μm samples is shown in the inset of Fig. 6.3a and 6.3b, respectively. The transmission intensity versus thickness for thin samples ($L < 310\ \mu$m) does not follow an exponential decay function and the diffusion model can't explain the dynamic process in the region of ballistic and snake photons.

From the long time decay behavior of the transmitted signal I(t), the diffusion decay time τ can be extracted. Fig. 6.4 shows the relationship between the τ^{-1} versus the paint length L. This shows that τ^{-1} is inverse proportional to L^2 as per equation (6.3). The relaxation time depends on the number of scattering events or the length of the multiple scattering paths. From the time decay values τ, the D_{eff} value can be calculated using equation (6.3) [11]. D_{eff}/D_0, where D_0 is the diffusion constant, is plotted for different L as shown in Fig. 6.5. For thin samples (up to $310\,\mu m$) the effective diffusion coefficient (D_{eff}) is time or thickness dependent. D_{eff} increases approximately linearly with L^2. The increase in D_{eff} value in the near ballistic region has been explained by Cai

et al. [12,13] and has been observed experimentally elsewhere [3,8]. Cai et al. solved analytically the radiative transfer equation and showed that the diffusion coefficient, which represents the spread of half-width of the photon distribution is time dependent at early time and becomes constant at longer time. For larger thickness above 310 μ m, D_{eff} in the diffusion region is almost constant and does not change with sample thickness.

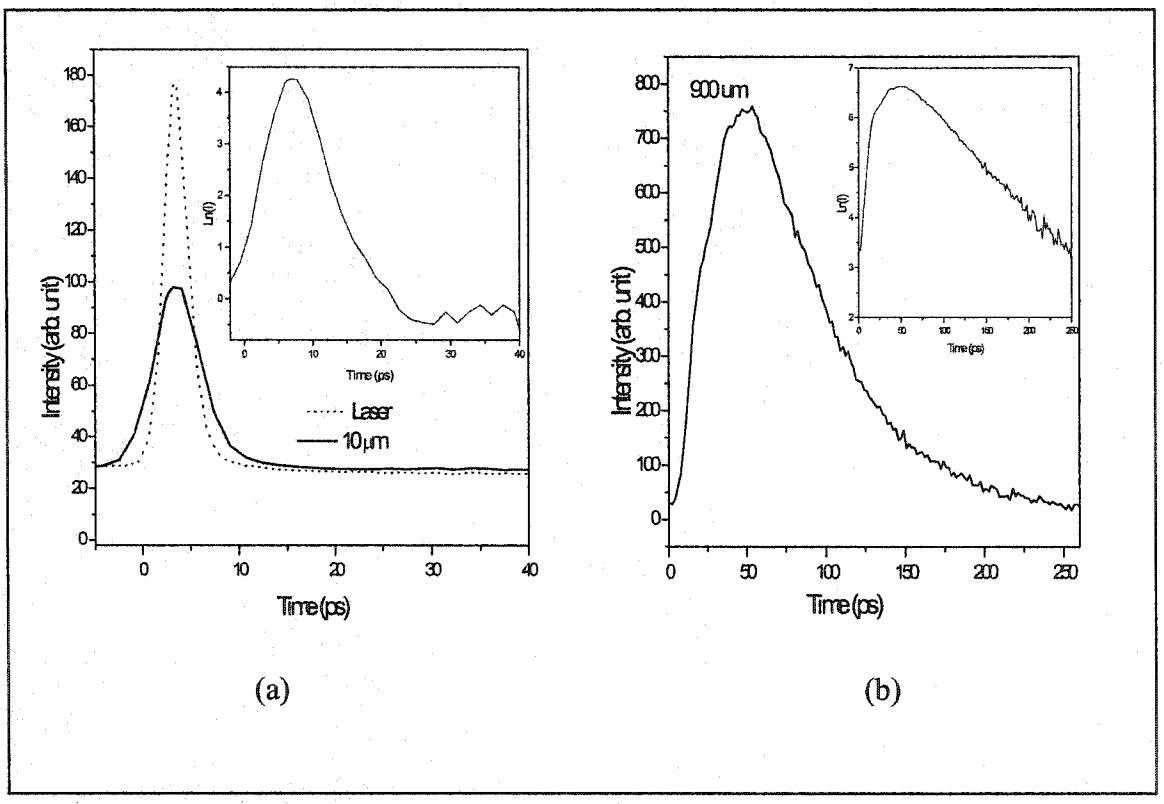

Fig. 6.3: Transmission intensity T versus time T is shown for (a)10 μm and the laser pulse, and (b)900 μm. The Inset shows the temporal profile of the log transmitted intensity pulse of paint samples for 10 μm and 900 μm.

The thick samples ($L \geq 10\ell_{tr}$) are characterized by the diffusion constant D_0 that does not depend on thickness. From our measurements the transport velocity can be calculated as $v = \frac{3D_0}{\ell_t} = \frac{3(908)\mu m^2 / ps}{28\mu m} \approx 1 \times 10^8 m/s$. This transport velocity is slower than the phase and group velocity due to multiple scattering and scattering resonance [14]. While in the non-diffusive region or ballistic and snake regions, $L\langle 3\ell_t$, the velocity will be higher than the transport velocity in the diffusive region for the condensed resonance medium.

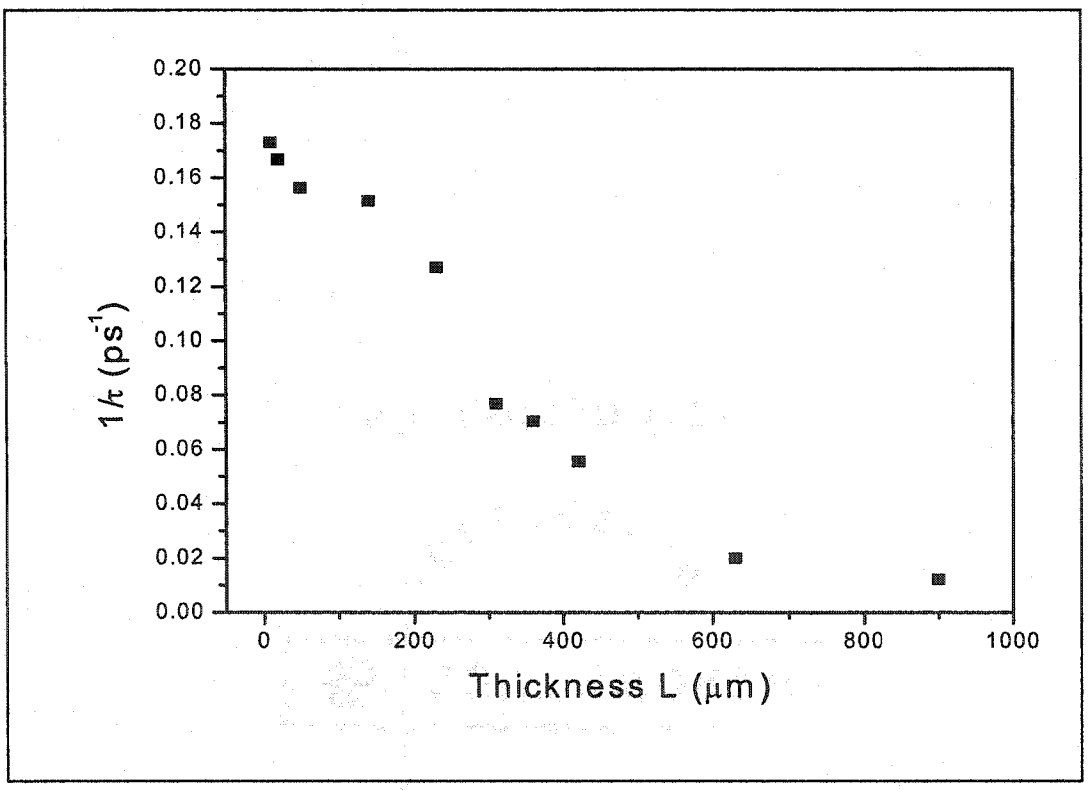

Fig. 6.4: Inverse decay time (τ^{-1}) plotted against the sample thickness L.

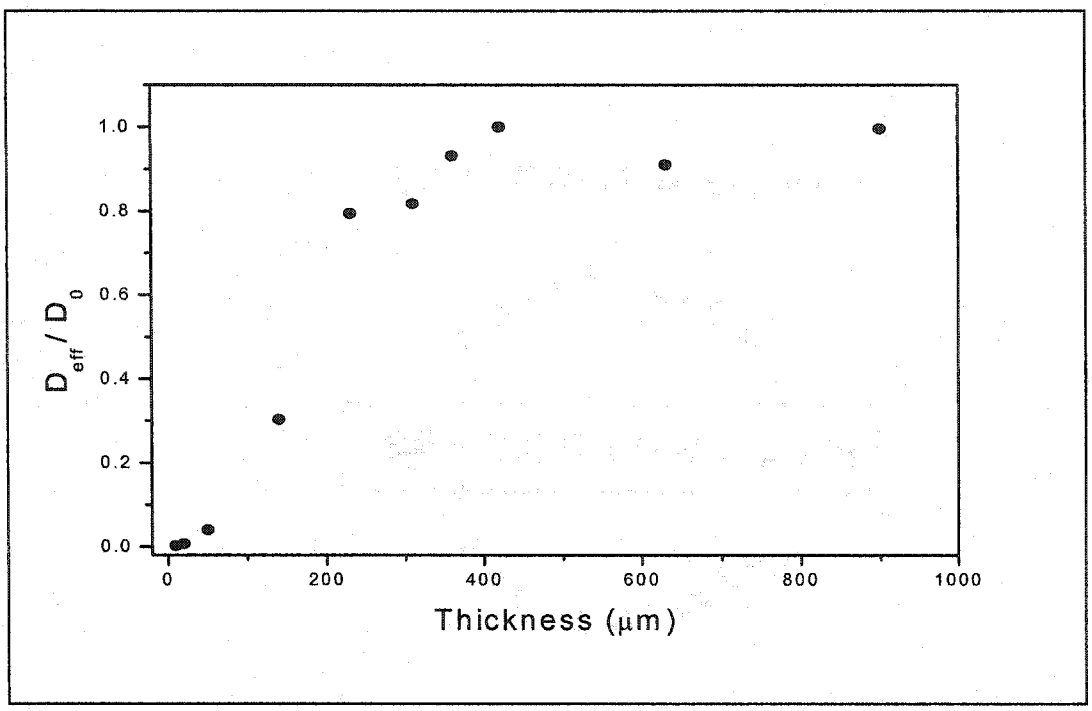

Fig. 6.5: Effective diffusion coefficient, D_{eff}/D_0, versus sample thickness L.

6.3 Randomization of coherence and polarization from the ballistic to the diffusive regimes in a highly scattering paint medium

6.3.1 Background

The direction, coherence, and polarization properties of the light pulses propagating in optically thick random media are altered by multiple scattering in the media. The transmitted pulse consists of ballistic, snake, and diffusive components, which are characterized by scattering length (ℓ_s), and transport scattering length (ℓ_t) of the medium. The transport scattering length gives a measure of the distance traveled to randomize a photon's direction. The ballistic component retains the degree of polarization and coherence while the diffusive component loses both. The intensity of

coherent (ballistic) photons decreases exponentially as L/ℓ_s where L is the sample thickness. The incoherent component can be described by the diffusion approximation when the thickness of the sample is larger than or equal $10\ell_t$ [5-6]. As the scatterer concentration increases, the unscattered light is attenuated and the scattered light is depolarized at different rates depending on the particle size [15,16]. Randomization of the polarization requires many more scattering events than that required to randomize its direction. Most recently, a correlation between the degree of polarization and the degree of coherence has been theoretically demonstrated [17]. Experimentally, this correlation has not yet been explored in scattering media. It is interesting to investigate the ballistic-snake-diffusion transition in the time domain. The understanding of polarization and coherence in scattering media has important consequences in the operation of many new optical applications based on time, coherence and polarization. These include heterodyne detection and confocal spatial filtering [18], optical coherent tomography (OCT) [19-20], temporal gating [4, 21], polarization filtering [17,22], second harmonic generation (SHG) imaging, and two photons fluorescence (TPF) imaging [23-24]. Coherent enhanced backscattering has been used to characterize turbid media, whereas lasing in random media and other applications of strong localization are currently an active area of research [25]. These concepts are used in important micro and macro scale imaging applications of objects in or through turbid media such as biological tissue samples, paint, corrosion and cracks under paint. The predominant approach to the analysis of multiple scattering is the theory of radiative transfer, which assumes an incoherent process ignoring coherence, interference, and polarization effects in the scattering process. The interference fringes are a manifestation of temporal coherence and spatial coherence

between the two light waves. The visibility provides a convenient means of quantifying the light coherence degradation across different path lengths in scattering layers of media of different thickness.

The degree of coherence and polarization and associated lengths will be determined as the medium changes from the ballistic to the diffusion regimes due to multiple scattering in paint layers of different thickness using time-resolved Young's interference approach. The small residual coherence in the diffusive regime is addressed using the Cittert-Zernike theorem. The correlation of time-resolved interference (coherence) and polarization measurements in a highly scattering paint medium has been determined for the first time for the ballistic, snake, and diffusive regions in terms of the mean transport length. The transport length, coherence length, polarization length, and degree of polarization are determined for different degrees of scattering.

When a femtosecond light pulse propagates in a paint film, the pulse broadens in time due to multiple scattering inside the paint medium. The pulse shape of the transmitted light depends on the optical properties of the paint medium. The scattered field E(x,t) from the paint medium passes through a screen containing two slits. The resultant intensity distribution produces a fringe pattern with visibility proportional to the mutual coherence function, $<E_1(t)E_2^*(t+\tau)>$, where $E_1(t)$ and $E_2(t+\tau)$ are the scattered fields from the two slits. The complex degree of coherence between the wave disturbances at the slit points (P_1 and P_2) due to the scattering paint medium is represented by the mutual coherence function $\gamma_{12}(\tau)$, where τ (equal to $\tau=(s_2-s_1)/c$) is the time difference corresponding to the path difference $s_2 - s_1$ between the two disturbances at the point of superposition (on the streak camera slit), and c represents the

speed of light. The intensity at the point of the superposition from P_1 and P_2, which is detected by coherence randomizes the mutual coherence function $\gamma_{12}(\tau)$ and phase $\phi_{12}(\tau)$ [26,27].

The visibility is the Fourier transform of the angular distribution of the scattering from the paint medium. The visibility in an interference pattern is defined as

$$V(p) = \frac{\langle I(p,t)\rangle_{max} - \langle I(p,t)\rangle_{min}}{\langle I(p,t)\rangle_{max} + \langle I(p,t)\rangle_{min}} = V_0\left|\gamma_{12}(\tau)\right|, \tag{6.4}$$

where $\langle I(p,t)\rangle_{max}$ and $\langle I(p,t)\rangle_{min}$ represent the intensity maxima and minima at the point (p) on the screen (streak camera). $\left|\gamma_{12}(\tau)\right|$ is the degree of coherence which is the product of the degree of spatial coherence and the degree of temporal coherence. $\left|\gamma_{12}(0)\right|$ is the degree of spatial coherence at zero path difference (temporal coherence = 1), while at other points the degree of coherence is mixture of both. Under equal intensity conditions from the two slits ($I_1 = I_2$, i.e. $V_0 = 1$) the visibility simplifies to $V(p) = \left|\gamma_{12}(\tau)\right|$.

As the thickness of the scattering paint medium is increased the degree of spatial coherence ($\tau = 0$) will decrease due to the multiple scattering of light by the pigments in the paint. The scattering of light in the paint sample will result in a phase difference in the two arms. The Spatial coherence is given by $\left|\gamma(T)\right| \sim 1 - T/\tau_{coh}$ for $T < \tau_{coh}$ (where T is the average time traveled by a multiply scattered particle and is related to the phase difference). The time $T = \overline{Z}/c = L^2/2c\ell_t$ is used to transform the time (T) dependence into length (L) dependence, where $\overline{Z}$ is the average distance that light travels through the paint sample due to multiple scattering [6,28], τ_{coh} is the coherence time of photons due to scattering ($\tau_{coh} = \ell_c/c$), ℓ_c is the coherence length, L is the thickness of the paint

sample, c is the velocity of light in the paint medium, and ℓ_{tr} is the transport length). The visibility at $\tau=(s_2-s_1)/c=0$ for all L measurements becomes:

$$|\gamma(L)| \sim 1 - L^2/2\ell_c\ell_{tr} \quad L < \sqrt{2\ell_c\ell_{tr}}, \tag{6.5}$$

and $|\gamma(L)| = 0 \qquad L > \sqrt{2\ell_c\ell_{tr}}$.

For a thickness $L > \sqrt{2\ell_c\ell_{tr}}$ the visibility is zero, ($|\gamma(L)|=0$). The visibility in the diffusive region is small but not zero. This nonzero visibility is described by the Van Cittert-Zernike theorem, which implies the existence of spatial coherence region from a completely incoherent source. For a uniform circular source, the degree of spatial coherence can be calculated using the Van Cittert-Zernike theorem, which implies complete incoherence between any pairs of source points, and is given by [26-27]:

$$|\gamma_{12}(0)| = 2J_1(\upsilon)/\upsilon \ , \tag{6.6}$$

where $\upsilon = 2\pi\rho\, d\,/\lambda R$, $J_1(\upsilon)$ represents the Bessel function of the first kind, R is the distance between the pinhole and the second lens that collimated the beam onto a double slit, d is the slit separation, λ is the wavelength, and ρ is the radius of the pinhole.

Since for thin samples, there is strong internal reflection at the boundary of the scattering medium, the extrapolated length z will be added to the transmission in the diffusion equation. The transmission for varying length samples is given by [8-9]:

$$T(z) = \frac{\ell_{tr} + z}{L + 2z}, \tag{6.7}$$

for thickness where ballistic intensity is much smaller than the diffusive light.

The extrapolation length is defined as,

$$z = (2/3)\frac{1+R}{1-R}, \tag{6.8}$$

Where R is the average diffusive reflectivity. The average diffusive reflectivity R, which determines the extrapolation length is given by [29],

$$R = \frac{3C_2 + 2C_1}{3C_2 - 2C_1 + 2}, \tag{6.9}$$

where $C_n = \int_0^1 R(\mu)\mu^n d\mu$. (6.10)

The angular dependent reflectivity, $R(\mu)$, of the entire boundary is

$$R(\mu) = \frac{R_{12} + R_{23} - 2R_{12}R_{23}}{1 - R_{12}R_{23}}, \tag{6.11}$$

where R_{ij} is the average Fresnel reflectivity of the ij interface where a photon strikes the boundary at an angle $\cos^{-1}(\theta)$ from the normal. For light incident on a paint-glass surface, where n=1.33 for paint and n=1.52 for glass, equation 6.7 becomes

$$T(z \sim 1.8\ell_{tr}) = \frac{2.81\ell_{tr}}{L + 5.6\ell_{tr}}. \tag{6.12}$$

Plotting the inverse of transmission (1/T) versus sample thickness (L), enables the transport mean free path l_{tr} for the paint to be obtained.

The degree of linear polarization (P_L) can be used to measure the transport length and the depolarization length of the paint. The degree of polarization of the scattered light is defined as

$$P_L = \left| \frac{P_{11} - P_\perp}{P_{11} + P_\perp} \right|, \tag{6.13}$$

where P_{11} is the intensity of light maintaining its original polarization state, and $P_\perp$ is the intensity of light in the orthogonal polarization state. Bicout et al. [30] derived an expression for the degree of linear polarization, P_L, of light transmitted through a slab of

length L for large particles using "Entropy Analysis Principle". The P_L versus L is given by:

$$P_L \approx \frac{2L}{l_{tr}} Sinh[\frac{\ell_{tr}}{\xi_L}] \exp[-\frac{L}{\xi_L}] , \tag{6.14}$$

where $\xi_L = (\zeta_L \ell_{tr}/3)^{1/2}$, and $\zeta_L = \ell_{tr}/\ln(10/7)$, which is valid for large number (≥ 10) of scattering events. ξ_L is called the characteristic length of linear depolarization, where l_{tr} is the transport mean free path $l_{tr} = \ell_s/(1-g)$, ℓ_s is the mean free scattering path; g is the mean cosine of the scattering angle ($0 \leq g \leq 1$). The value of g=0 represents isotropic scattering for small particles whereas g=1 represents forward scattering for large particles. Kim et al. [31] also derived an expression for P_L, which is valid for a thicker medium than that derived by Bicout. The degree of polarization depends on the number of scattering events and the particle size. The polarization length is expected to be determined by the transport length [30-31]. Both Kim [31] and Bicout [30] claim that the depolarization length is about one transport length. Both don't agree with our experimental results for the condensed paint material, where the paint fraction's volume is ~ 20%.

Most recently, Min Xu [32] demonstrated theoretically a new formula to evaluate the degree of polarization taking into consideration the internal reflection at the boundaries in the scattering media. Min Xu defined the degree of polarization for the high volume fraction scattering media by:

$$P_L \sim \frac{2d}{\xi_L'} Sinhc(\frac{z_1}{\xi_L'}) Sinhc(\frac{z_e}{\xi_L'}) e^{-\frac{d}{\xi_L'}} , \tag{6.15}$$

where $d = L + 2z_e$, $z_1 = z_e + \ell_{tr}$, $\xi_L' = \sqrt{\frac{\ell_{tr}\ell_s}{3\ln(1/a)}}$ is the linear depolarization length, a represents the linear depolarization anisotropy of the scatterer, and Sinhc(x)=Sinh(x)/x.

6.3.2 Experimental Methods

A self mode-locked Ti:sapphire laser was used to generate ultrashort laser pulses of about 150 fs duration at 800 nm, at a repetition rate of 82 MHz. These pulses were incident on the paint sample and the transmitted light was collected by a lens and focused onto an aperture of radius ρ at its focal length. A second lens located at a distance equal to its focal length from the aperture collimated the beam onto a double slit as shown in Fig. 6.6. The beam was expanded and collimated by lenses to cover the double slits. The double slit width was about 40 μm with a slit separation of 250 μm. The temporal behavior of the light interference pattern from the double slit was imaged onto the streak camera slit. The interference pattern obtained at the entrance slit of the Hamamatsu synchroscan streak camera was temporally analyzed when the image of the entrance slit was swept in time with 2 ps resolution. Red Nascar spray paint from Plasti-Kote Co.

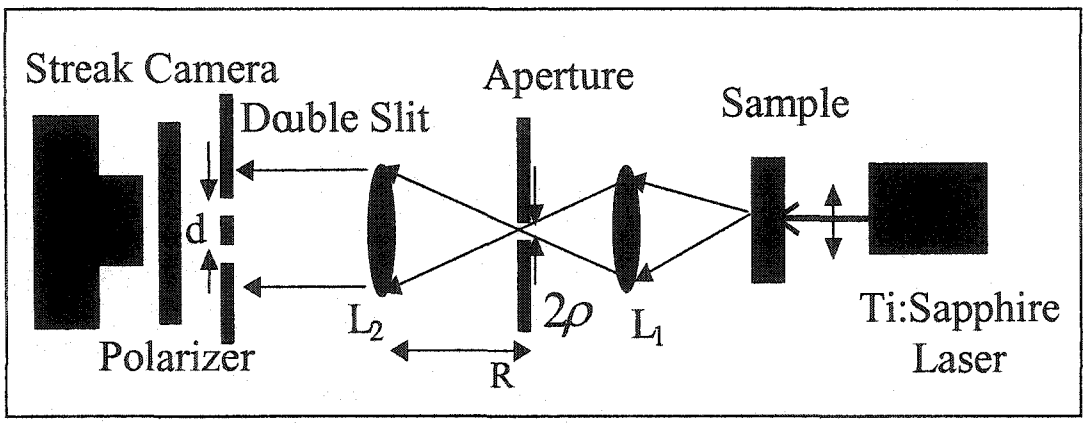

Fig. 6.6 The time-resolved set up for degree of coherence and interference measurements.

(paint # 5727) was used to make layers of different thickness on glass slides. The diameter of the pigments particles of the paint was between 1 μm and 3 μm . The paint thickness ranged from 10 to 900 μm . The paint is large pigmented particles in host scattering medium that scatter the incident light. The propagation distances in the scattering medium are larger than the used wavelength, the radiative transfer theory can be used to describe the propagation of light well in paint.

6.3.3 Results and Discussion

The interference fringes for different thicknesses of paint layers between 10 and 630 μm have been investigated using the Young's and Van Cittert Zernike's experimental double-slit setup. Typical interference fringe patterns in films of thicknesses 10 μm , 230 μm , 310 μm and 420 μm are shown in Fig. 6.7 together with the digitized intensity profiles. The pulse profile on the right is the convoluted response of the instrument and the paint sample. The presence of fringe patterns in the scattered wave implies that visibility (V) is not zero and coherence exists. As the thickness increases the scattered waves are partially coherent at least in the far field, and in a thick scattered medium the mutual coherence between any two points are destroyed, a result that may be derived from the Van Cittert-Zernike theorem [26-27]. A low degree of coherence exhibits a poor depth in the fringe pattern. The sample data displayed in Fig. 6.7 shows the effect of the degree of coherence on the fringe visibility at different thicknesses. The graphs also show the increase in the background (incoherent portion) and the photographs clearly show the decrease in the fringe visibility as the thickness L increases. The changes in the coherence versus time for different paint thicknesses are shown in the digitized graph in

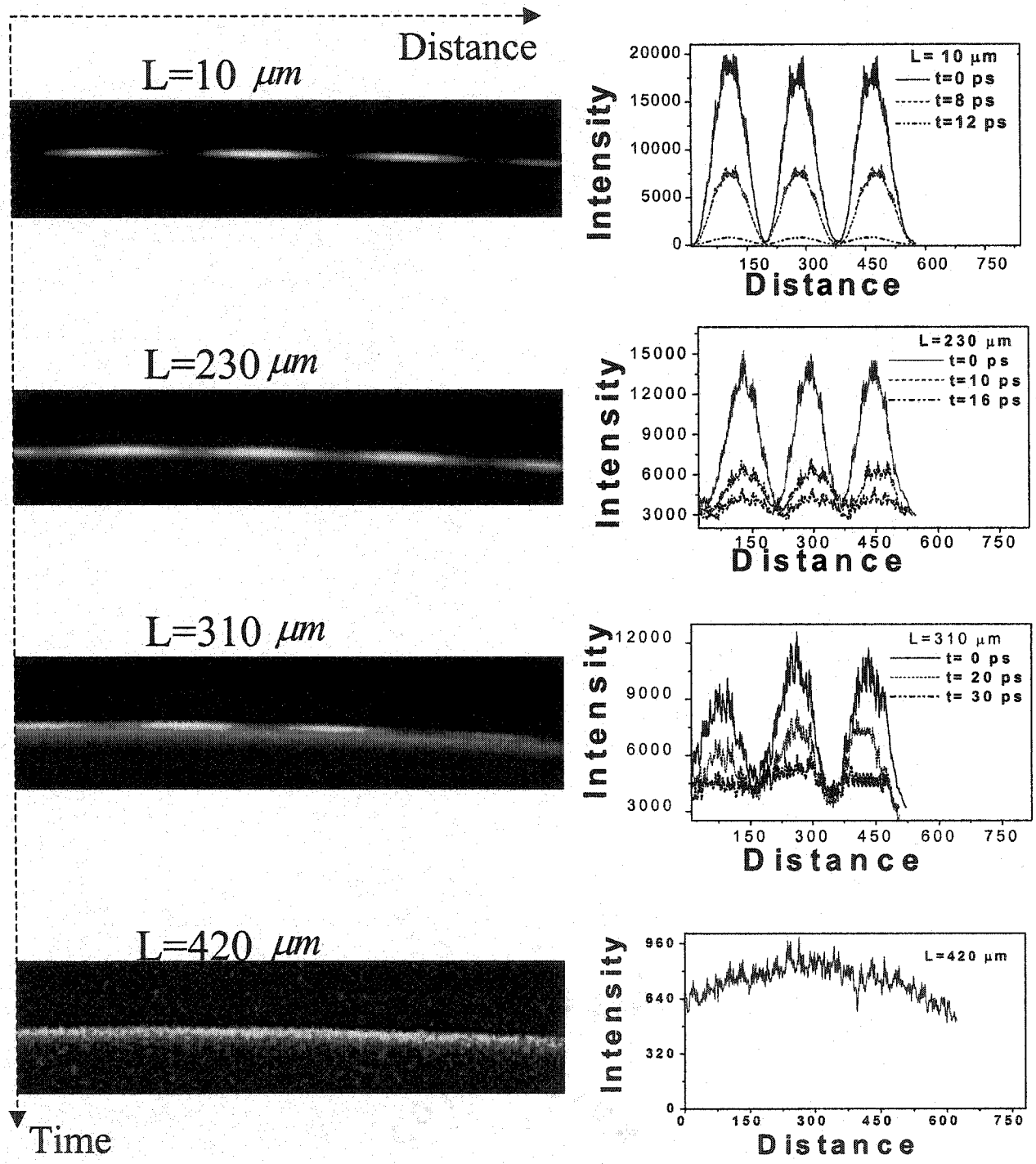

Fig. 6.7: Temporal interferometric fringes and their displayed intensity profiles for different thicknesses L.

Fig. 6.7. The total time domain window along the y-axis in the streak images covers 800 ps in which coherence disappear after ~ 26ps (for L=230 μm), ~ 40ps (for L=310 μm), and ~ 46ps (for L=420 μm). The temporal coherence window represents the dispersed transmitted pulse through the paint medium at different thicknesses.

The degree of spatial coherence is calculated from profile data using equation (6.4). The results of the measured visibility are shown in Fig. 6.8. For uniform random changes in phase a linear relationship between visibility and time can be obtained [33]. For non-uniform random changes of phase $\phi(t)$ and amplitude due to the mixing of short and long paths a more complex relationship between visibility and time occurs. There is a nonlinear relationship between visibility V and thickness L as shown in Fig. 6.8. The visibility reduces to a very small constant value (not zero) of approximately 0.06 at L~420 μm. In scattering media such as paint, the actual mathematical form of the degree of coherence or the fringe visibility will depend on the precise statistical distribution of the lengths of the scattered wave trains in the paint medium. For thin paint layers of thickness less than 50 μm, mostly ballistic photons reach the pinhole and therefore $|\gamma_{12}(0)| \approx 1$ which represents a strong correlation function between the two slits. As the thickness of the paint increased up to ~ 360 μm, then ballistic and multiple scattered photons (believed to be snake photons) will reach the pinhole and $|\gamma_{12}(0)|$ must decrease.

Fitting experimental data to equation (6.5) gives $V = 1-(6*10^{-6})L^2$. Using a transport length of 28 μm (taken from time-resolved measurements as shown in section 6.2.4) gives a coherence length of 2976 μm ($\ell_c = 2976 \mu m$ from V fitting equation as shown in Fig. 6.8). The thickness where coherence disappears is $\sqrt{2\ell_c \ell_{tr}} = 408 \mu m$, or

$L \approx 15\ell_{tr}$. Ballistic photons are overwhelmed by highly scattered photons and the diffusion approximation becomes more valid and therefore the Van Cittert-Zernike theorem can be applied. For some paint thicknesses, the visibility must be the same since complete light diffusion or incoherent photons will be achieved and visibility will depend on the distance between slits, size of the aperture, the distance between the pinhole and lens 2, and the incident wavelength. It is interesting to compare experimental visibility with the Van Cittert-Zernike theorem result. Substituting 1 mm diameter pinhole ($\rho = 500\ \mu m$), d=250 μm, R=15 cm, and $\lambda = 800\ nm$ into equation (6.6) gives $|\gamma_{12}(0)| = 0.05$. Our experimental data as shown in Fig. 6.8 confirm this conclusion, as

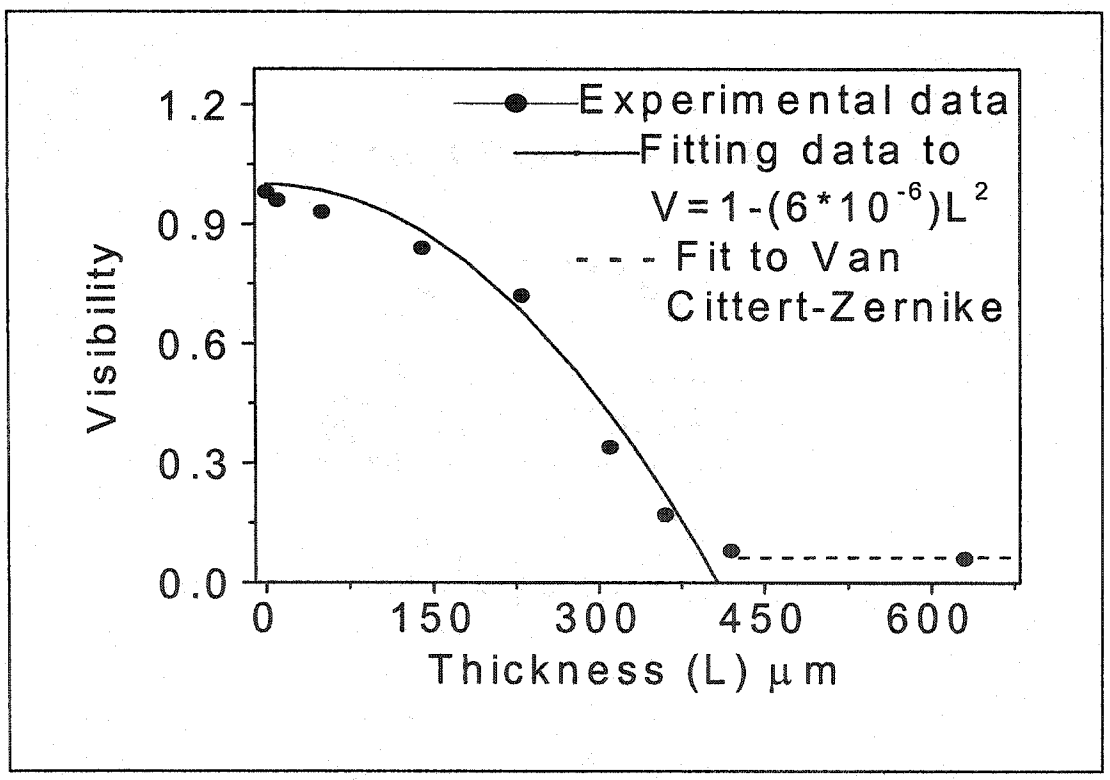

Fig. 6.8 Degree of coherence (visibility) versus sample thickness, L.

the visibility for thickness greater or equal to 420 μm becomes constant ($|\gamma_{12}(0)| \sim 0.06$)

in agreement with the Van Cittert-Zernike theoretical value. It is interesting that both the diffusion approximation and the Van Cittert-Zernike theorem are valid above the thickness of 360 μm when photons are mostly incoherent. This result supports the fundamental theoretical assumption of the diffusion approximation that for this regime the photons are mutually incoherent. The data in Fig. 6.8 can be divided into three regions: $0 \leq L \leq 50$ μm represents the ballistic region, $50 \leq L \leq 310$ μm represents the snake region, and $L \rangle 310$ μm represents the diffusion region.

The inverse of the total transmission data (1/T) vs. thickness (L) is plotted and fitted with equation (6.12) from diffusion theory as shown in Fig. 6.9. To obtain the value

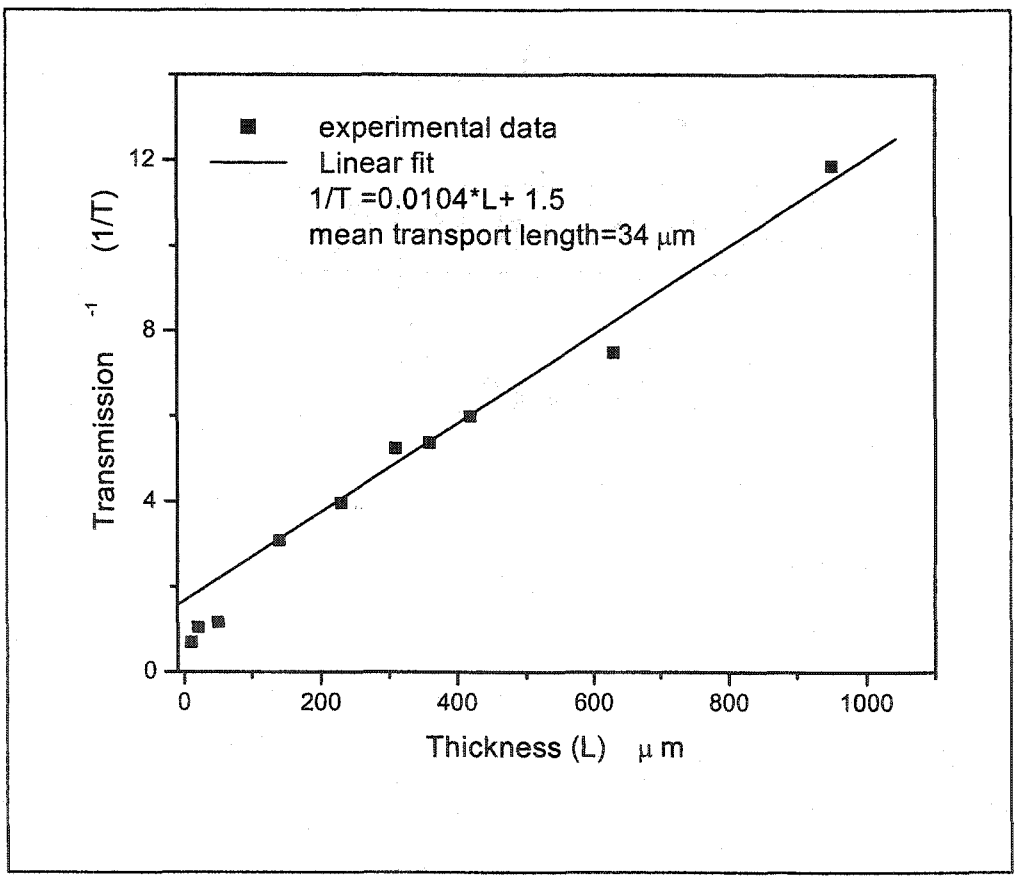

Fig. 6.9: Shows the inverse of transmission (1/T) versus the sample thickness (L) is fitted to equation (6.12), gives $\ell_{tr} = 34 \mu m$.

of ℓ_{tr}, equation (6.12) fits the data shown in Fig. 6.9, where the sample thickness is greater than 100 μm and the ballistic photons intensity e^{-L/ℓ_s} is less than 10^{-4} as shown by the fitted line. The slope of 1/T vs. L gives the transport mean free path ℓ_{tr} of 34 μm.

Parallel polarization (P_{II}) of the transmitted pulse in samples represents the early-arrived photons (ballistic photons) followed by the snake and diffusive photons. The perpendicular polarization ($P_{\perp}$) contains multiple scattering processes. The degree of polarization (P_L) is calculated using equation (6.13) for different thicknesses L. The results of the degree of polarization (P_L) versus thickness (L) are plotted in Fig. 6.10.

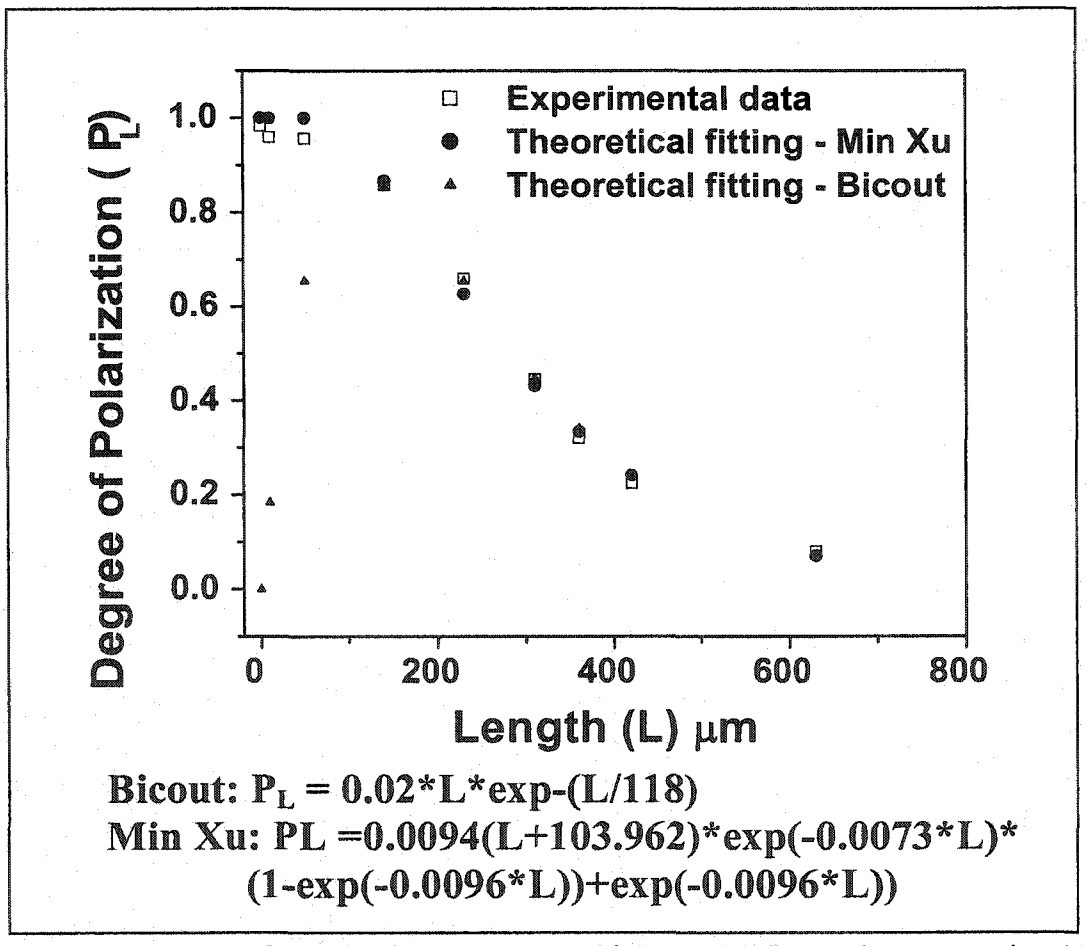

Fig. 6.10: Degree of polarization (P_L) versus thickness (L) fit to Min Xu equation (6.15), gives $\ell_{tr} = 29 \mu m$ while Bicout equation (6.14) gives $\ell_{tr} = 128 \mu m$.

The degree of polarization data shown in Fig. 6.10 is fitted to equation (6.15), which yields the characteristic length of linear depolarization (ℓ_{LP}) of 137 μm, ℓ_{LP}=137 μm, and transport length of 29 μm. The linear depolarization is about five times the transport length ($\ell_{LP} \sim 5\,\ell_{tr}$). The 1/e value of the experimental data of P_L defines the linear depolarization length (ℓ_{LP}) of approximately 310 μm. From Fig. 6.10, the polarization disappears at thickness greater than 420 μm or greater than 15 ℓ_{tr}.

The experimental depolarization length is not in agreement with Bicout [31] and Kim [32] theory of the degree of polarization. The Bicout equation gave a transport length of 128 μm that contradicts the time resolved measurements and the steady state (1/T vs L) measurements, while the Kim equation didn't fit our experimental data. The Kim equation is valid for a very thick scattering media ($L >> \ell_{tr}$). Equation (6.15) is used to fit our experimental data of the degree of polarization. Equation (6.15) takes into consideration the internal reflection at the boundaries of the scattering media and the density of the scatterer. From fitting the experimental data of the degree of polarization to equation 6.15 (see Fig. 6.10), the measured transport length of 29 μm agrees with the time-resolved diffused measurements ($\ell_{tr} = 28 \mu m$). In Fig. 6.10, three regions can be realized: $0 \le L \le 50$ μm represents the polarized coherent ballistic region, $50 \le L \le 420$ μm represents the partially polarized quasi-coherent snake photons, and $L \rangle 420$ μm represents the depolarized diffusive incoherent photons.

The table below, Table 6.1, shows the summary of the obtained transport length in paint using different methods.

In conclusion, the degree of spatial coherence and polarization for paint films of different path lengths has been measured by time resolved measurements. The linear depolarization length of 137 μm and transport length of 29 μm are not in agreement with the current theoretical understanding of the degree of polarization in scattering media [30-31]. The most current theory of polarization in scattering media by Min Xu [34] gives a good result for the transport length that agrees with both the time-resolved measurements and the steady state measurements. The depolarization length for paint is much greater than one transport length ($\ell_{LP} \sim 5\,\ell_{tr}$) which contradicts both Bicout [30] and Kim [31] work. Polarization and coherence disappear at thicknesses greater than or equal to fifteen transport lengths ($> 15\ell_{tr}$). The polarization and coherence gradually decreases in going from the ballistic to the snake to the diffusive regimes. The small residual coherence for $L > 15\ell_{tr}$ is described by the Van Cittert-Zernike theorem, which arises from the correlation of the fields from same single points in the scattering media arriving at the two slits to take part in interference.

Methods of calculations	Transport length ℓ_{tr} (μm)
Pulse transmission	**28**
Steady state transmission	**34**
Polarization transmission	
Min Xu	**29**
Bicout	**128**
Kim	**Fail to fit**

Table 6.1 The measured transport length for paint using different methods.

6.4 References

1. M. Lax, V. Nayaramamurti, and R. C. Fulton, in proceedings of the symposium on laser optics of condensed matter, Leningrad, June 1987, edited by J. L. Birman, H. Z. Cummins, and A. A. Kaplyanskii, Plenum, New York, 1987.

2. E. Akkermans, P. E. Wolf, and R. Maynard, Phys. Rev. Lett. 56, 1471, 1986.

3. D. A. Weitz, D. J. Pine, P. N. Pusey, and R. J. A. Tough, Phys. Rev. Lett. 63, 1747, 1989.

4. L. Wang, P. P. Ho, C. Liu, G. Zhang, and R. R. Alfano, Science 253, 769, 1991.

5. K. M. Yoo and R. R. Alfano, Opt. Lett. 15, 320, 1990.

6. K. M. Yoo, Feng Liu, and R. R. Alfano, Phys. Rev. Lett. 64, 2647, 1990.

7. K. M. Yoo, B. B.Das, and R. R. Alfano, Opt. Lett. 64, 17, 958, 1990.

8. Rik H. J. Kop, Pedro de Vries, Rudolf Sprik, and Ad Lagendijk, Phys. Rev. Lett. 79, 4369, 1997.

9. J. M. Drake and A. Z. Genack, Phys. Rev. Lett. 63, 259, 1989.

10. M. Xu, W. Cai, M. Lax, and R. R. Alfano, Phys. Rev. E. 65, 066609, 2002.

11. J.Ali, M. Xu, W. Cai, to be published.

12. W. Cai, M. Lax, and R. R. Alfano, Phys. Rev. Lett. 61, 3871, 2000.

13. W. Cai, M. Lax, and R. R. Alfano, J. Phys. Chem. B 104, 3996, 2000.

14. B. Tiggelen, Ad Lagendijk, M. Albada, and A. Tip, Phys. Rev. B. 45, 12233, 1992.

15. K. M. Yoo and R. R. Alfano, Phys. Lett. A, 142, 531, 1989.

16. J. M. Schmitt, A. H. Gandjbakhche, and R. F. Bonner, Appl. Opt. 31, 6535, 1992.

17. Emil Wolf, Opt. Lett. 28, 1078, 2003.

18. M. Kempe, A. Z. Genack, W. Rudolph, P. Dorn, J. Opt. Soc. Am. 14, 216, 1997.

19. Michael R. Hee, Joseph A. Izatt, Joseph M. Jacobson, James G. Fujimoto, and Eric Swanson, Opt. Lett. 18, 950, 1993.

20. M. Kempe, A. Z. Genack, W. Rudolph and P. Dorn, J. Opt. Soc. Am. A 14, 216, 1997.

21. B. B. Das, K. M. Yoo, and R. R. Alfano, Opt. Lett 18, 1092, 1993.

22. S. G. Demos and R. R. Alfano, Opt. Lett 21, 161, 1996.

23. J. Ying, F. Liu, P. P. Ho, and R. R. Alfano, Opt. Lett. 25, 1189, 2000.

24. Y. Guo, P. Ho, F. Liu, R. Alfano, Optics Comm. 154, 383, 1998.

25. H. Cao, J. Xu, Y. Ling, A. Burin,E. Seeling, X. Liu, and R. Chang, IEEE Journal of Selected Topics in Quantum Electronics 9, 111, 2003.

26. M. Born and E. Wolf, Principles of Optics, Cambridge University Press, Cambridge, 1999.

27. M. Beran and G. Parrent, Theory of Partial Coherence, Prentice Hall, 1964.

28. K. M. Yoo, Ph. D. Thesis, The City university of New York, 1990.

29. J. X. Zhu, D. J. Pine, and D. A. Weitz, Phys. Rev. A 44, 3948, 1991.

30. D. Bicout, C. Brosseau, A. S. Martinez, and J. M. Schmitt Phys. Rev. E 49, 1767, 1994.

31. A. D. Kim and M. Moscoso, Phys. Rev. E 64, 26612, 2001.

32. Min Xu et al. private communication.

33. Grant R. Fowles, Introduction to Modern Optics, Holt, Rinehart, and Winston, 1975.

Chapter 7

Visible to Mid-IR Imaging Through Paint Using Spectral Polarization and Confocal Scanning Techniques

7.1 Introduction

This chapter describes imaging through paint to detect cracks and corrosion using spectral polarization and confocal scanning imaging techniques from visible to mid-IR. The detection of corrosion and micro-cracks hidden beneath the top coat and primer paint layers using visible to mid-IR spectral polarization imaging techniques will be investigated. This chapter also describes imaging of corrosion beneath paint using the confocal scanning imaging technique.

7.2 Detection of Corrosion Beneath Paint Using Visible to NIR Spectral Polarization Imaging Technique

7.2.1 Background

Aging aircrafts are experiencing increased structural failures due to corrosion. Corrosion of metal surface increases significantly as structure ages. In some applications, metals are being replaced by composites, plastics and ceramics materials. The advantages of this replacement are the low cost, simpler fabrications and corrosion resistance. With sufficient stress and work applied at the atomic level of a material it can cause it to fracture due to the rupture of the bonds that hold the atoms together. Cracks can originate from micro-defects in the material or at points of stress elevation in a member subjected to tensile and fluctuating loads [1,2]. An undetected crack in the systems such as gas

piping and aircraft wings may lead to catastrophic failure. The structural defects from environmental interactions may cause a micro-mechanism fatigue failure. Detection of corrosions and cracks at the earliest stages is an important step towards improving safety and reducing cost. Several methods such as x-ray [3], ultrasonic [4], fractal geometry [5] and electrochemical phenomenon [6] are commonly used today to investigate corrosion. These methods have a limited capability and sensitivity in which corrosion cannot be discovered at the early stage. Detection of hidden corrosion on aircraft structures using ultrasound techniques gives a poor spatial resolution and imaging contrast.

The ability to image corrosion beneath paint is limited by light scattering in the turbid paint (pigmented liquid) medium. Paint is a pigmented liquid composition, which is converted to an opaque solid film after application as a thin layer. Titanium dioxide (TiO_2) is the most important pigment used in paints. The most important function of titanium dioxide when it is used as a pigment is for providing brightness, whiteness, and opacity. In general, the color of a pigment is a function of the absorption constant, refractive index and particle size. Fig. 7.1 shows that the incident and scattered light trajectories for a painted corroded metal surface. A schematic diagram showing how light interacts with a sample (paint-arcyline plexiglass-metal) is displayed in Fig. 7.1. Part of the beam is reflected at the surface (mostly specular reflection and diffuse reflection). The beam will be refracted into the paint layer. The refracted signal will depend upon the density of the paint or the index of refraction. Some of the refracted beam is absorbed, mostly by the pigments and solvent, and the rest is scattered. A portion of this light will reach the metal surface and this will be reflected back. By analyzing the scattered signal,

a smooth, rough and a crack region can be detected. The degree of polarization and scattering angle will be different for surface roughness and cracks of different shapes.

When photons propagate into a scattering medium, they divide into three components: ballistic, snake, and diffusive. The ballistic or coherent component is resulted from photons that travel the shortest path in turbid medium. While the diffusive or incoherent photons travel the largest distance in the turbid medium compare to the ballistic or snake photons. Photons propagating in turbid media have their incident direction, polarization, and phase randomized by multiple scattering. The degree of depolarization depends on the initial polarization state, the number of scattering interactions, the anisotropy of each scatter, and the properties of the surrounding medium.

Photonic techniques offer a rapid and easier approach to detect corrosion in situ. Various defects in highly scattering media at certain depths can be detected using an optical technique [7-10] based on spectral and polarization properties of the scattered light from a turbid media. We will demonstrate the use of the spectral and polarization

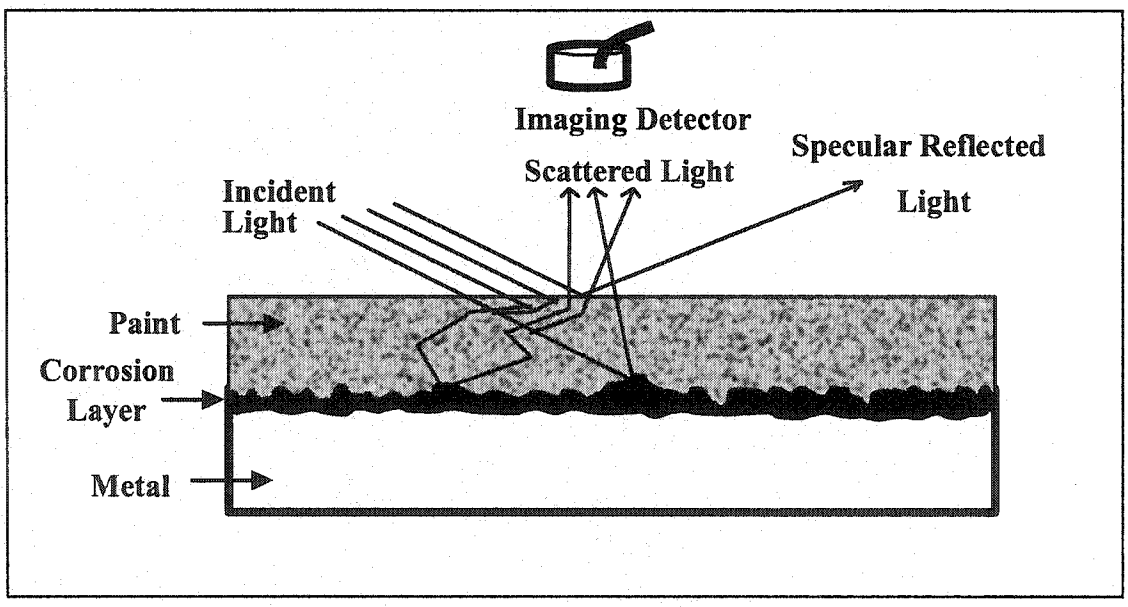

Fig. 7.1: Incident and scattered trajectory waves from the paint-corrosion-metal medium.

properties of the far-red and near-infrared scattered light to detect corrosion beneath thehighly scattering turbid paint media.

It is well known that a uniform corrosive layer can be created when an alloy or metal plate is soaked in a corrosive solution, such as acid or base. The mass loss W as a function of the soaking time t of the sample in an acid solution is given by,

$$W = At^N \ , \tag{7.1}$$

where A and N are constants independent of the soaking time, and $N \rangle 1$ when active dissolution occurs [10]. A high value of N shows low corrosion resistance. A low value of A indicates a high corrosion resistance. The corrosion rate is not constant, it increases with the soaking time. If we take A=5 microgram (high corrosion resistance material), N=1.2, and the soaking time t=20 hours, the calculated mass loss (using equation (7.1)) is ~20 mg. The thickness of the corrosion is ~24 μm .

Understanding the underlying physical principles in detecting corrosion beneath paint will help in improving the image contrast and resolution. The major problems in detecting cracks beneath paint are multiple scattering and absorption of the paint layer due to the chemical compositions of the solvent and the pigments in the paint layer. Colors in paint come from chemical structure of pigments [11]. Black pigments absorb almost all the light falling upon them, whereas white pigments scatter and reflect all the visible light falling on their surface. The degree of color also depends on the size of the scattered particles relative to that of the incident wavelength. Most coating systems are multilayered, and the pigments nature and content will vary from layer to layer. The pigment particles are suspended in an oil solvent fluid. Light passes through the dried oil solvent and strikes the pigments particles. Some of the incident light will be reflected and

the rest will be transmitted through the pigments particles and the latter will result in absorption. This absorption will mainly depend on the optical properties of the pigments and solvent. The strength of light scattering is determined by the relative particle size (d) of pigment and host medium to the incident wavelength (λ) or d/ λ , and relative index of refraction at the interface. A large difference in refractive of index between a pigment and host medium enhances the reflectance at each interface and the smaller the difference the more will be transmitted inside and absorbed. The reflected electric field is proportional to the difference in index of refraction between the pigments medium (n_1) and the host medium (n_2). The intensity of the reflected light is proportional to the square of the electric field (i.e. $(n_1-n_2)^2$) [11],

$$R = \frac{(n_1 - n_2)^2}{(n_1 + n_2)^2}, \tag{7.2}$$

where R is the reflectance.

When a linearly polarized light is incident on the painted metal, the state of the back scattered and reflected light from the surface is partially polarized while the light scattered from within coating is depolarized. Linearly polarized light can be scattered many times in a turbid medium before losing its polarization. Light that is scattered from a thin layer or less pigmented medium may preserve its incident polarization direction. The deeper the photons travel the more depolarized the light will be (lose its initial polarization). At a critical mean free path, the scattered light will be completely depolarized or the parallel and perpendicular polarization intensity will be the same. The degree of polarization of the scattered light decreases when the distance that light travels through the scattering media increases. Light that travels at an angle will travel a longer distance than light that hits the sample at normal incidence to the surface. The longer the

distance that photons travel the longer the time those photons spend in the scattering media. As a result, the polarization status of the light can be used for imaging defects such as cracks at different depths beneath paint.

The degree of polarization is defined as:

$$D = (I_{\parallel} - I_{\perp})/(I_{\parallel} + I_{\perp}), \tag{7.3}$$

where the $I_{\parallel}$ and $I_{\perp}$ are the intensities for the parallel and perpendicular components of the reflected or scattered light from the object, respectively. The contrast is the difference in light intensity in an object or image, and defined as:

$$C = (I_{max} - I_{min})/(I_{max} + I_{min}), \tag{7.4}$$

where the I_{max} and I_{min} are the maximum and minimum intensities of light recorded from the object, respectively.

7.2.2 Experimental Methods

The sample used to detect corrosion in our experiment was an aluminum plate with a circular corrosion disk of ~ 2 cm diameter. The corrosion was induced by the reaction of a base solvent of potassium hydroxide (KOH) with the surface of an aluminum plate for ~ 24 hours. The bottom half of the circular corrosion and aluminum plate was painted with red paint of 40-micrometer thickness. The transmission curve of red paint is shown in Fig. 7.2, which indicates that wavelengths greater than 600 nm are transmitted. The corrosion beneath the red paint was not seen by the eye or conventional camera as shown in Fig. 7.3.

The experimental arrangement for detecting the corrosion beneath the red paint using spectral polarization imaging technique is shown in Fig. 7.4. A beam of a white

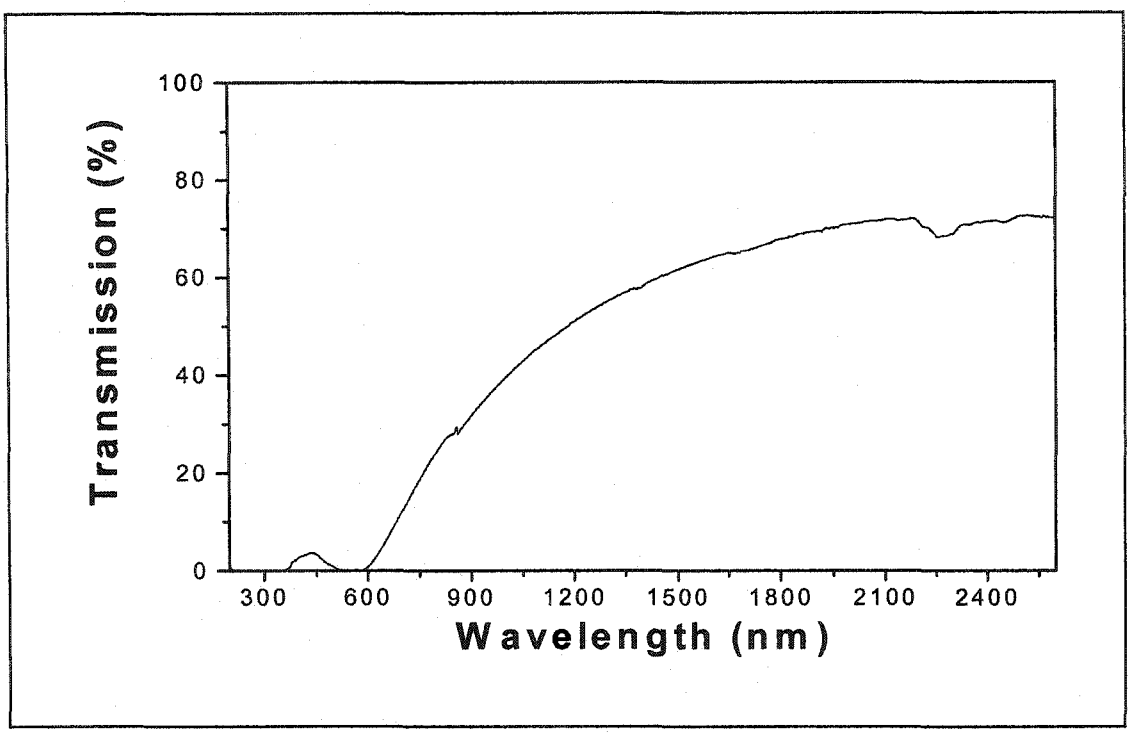

Fig. 7.2: Transmission curve of red paint in the wavelength range from 200 nm to 2600 nm.

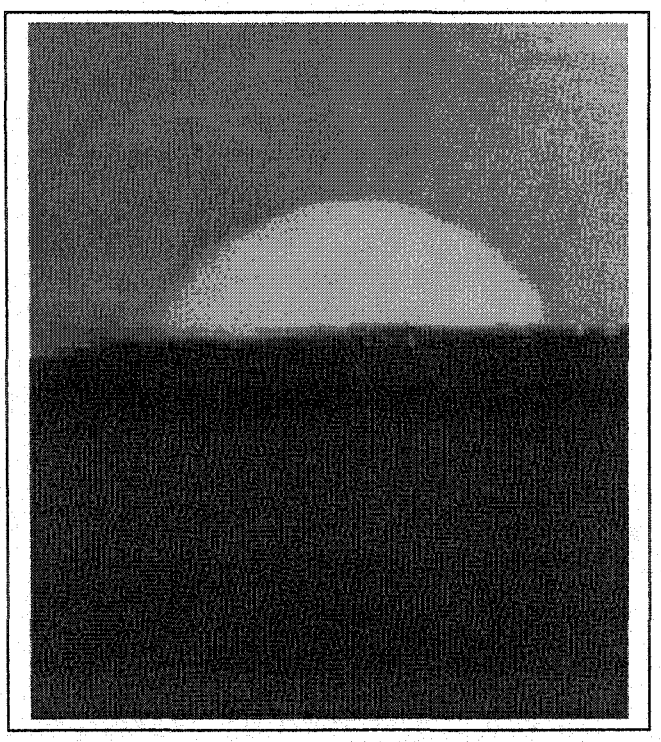

Fig. 7.3: corrosion beneath the red paint, the bottom part of the circular corrosion, was not seen by eye or conventional camera.

light of diameter ~ 2.5 cm was used to illuminate the sample. Wide band filters from 600 nm to 900 nm were alternatively used to select the desirable spectral range of the illumination and the detected light. A polarizer is located in the incident light beam pathway to obtain a linearly polarized illumination light with its polarization oriented parallel and perpendicular to that of the second polarizer orientation. The second polarizer is positioned in front of the CCD camera for selecting the detection polarization direction. A cooled CCD camera (Photometrix CH250) equipped with a zoom lens of 50-mm focal length is used to record the images. The wavelength and polarization dependence of the scattered light images are tested by changing the illumination wavelength (600-900 nm) and rotating the first polarizer (P1).

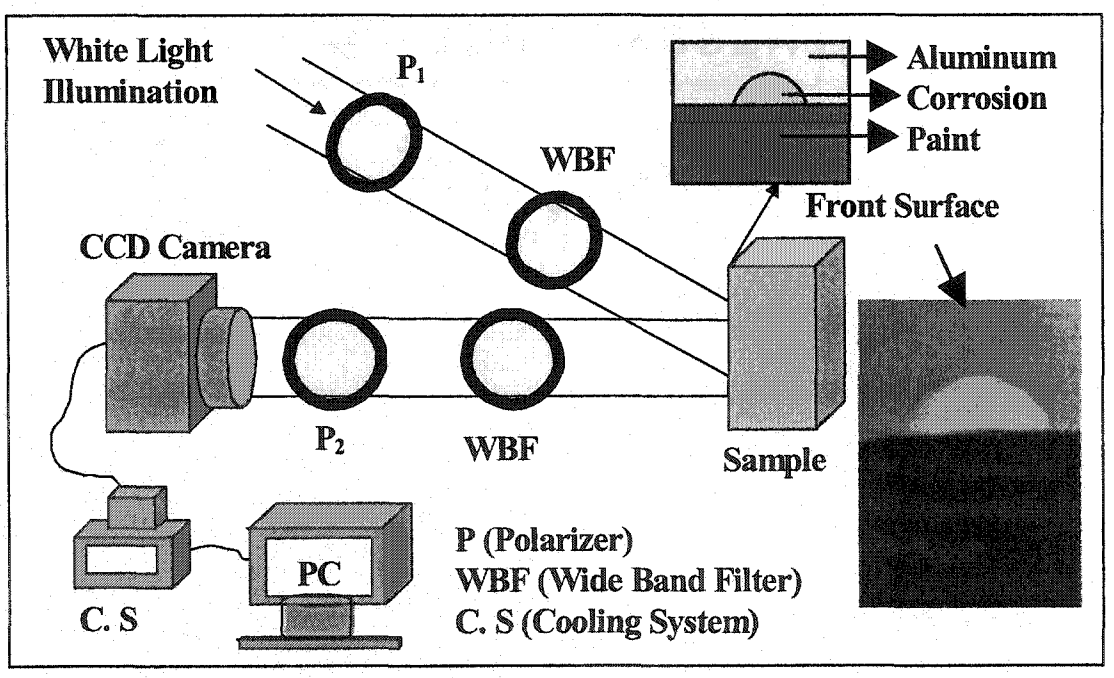

Fig. 7.4: Experimental set up for detection of corrosion beneath paint using spectral polarization imaging technique.

7.2.3 Experimental Results

Figs. 7.5a-c show the parallel scattered light images recorded at different excitation wavelengths of 600 nm, 700 nm, and 800 nm in the parallel polarization configuration. Figs. 7.5d-f show the perpendicular scattered light images recorded with different excitation wavelengths of 600 nm, 700 nm, and 800 nm in the perpendicular polarization configuration.

7.2.4 Discussion and Outcome

It is clear from Fig. 7.5 that the intensity of the scattered light from the bottom half of the circular corrosion increases as the wavelength increases in both parallel and perpendicular states. This can be understood because the transmission of the red paint at 800 nm is higher than that at shorter wavelengths such as 600 nm and 700 nm as shown in Fig. 7.2. As the wavelength gets longer the penetration gets deeper, and so more information can be revealed about the corrosion beneath the paint. Similar results were obtained for blue paint where the transmission wavelength is greater than 700 nm.

Short wavelengths such as 600 nm cannot reach the corrosion layer. In this case, the resulting images are formed from photons that scattered from the surface or subsurface (smaller than 40 μm) of the paint medium. On the other hand the longer wavelengths (such as 700 nm and 800 nm) with a greater penetration had a better chance to pass through the paint medium to reach the corrosion beneath the paint. The resulting images at these wavelengths represent the scattered photons from all layers including the corrosion layer, and therefore, the corrosion layer may be identified. The distortions in

the corrosion layer cause the light to scatter in all directions. Since the CCD camera is fixed along the

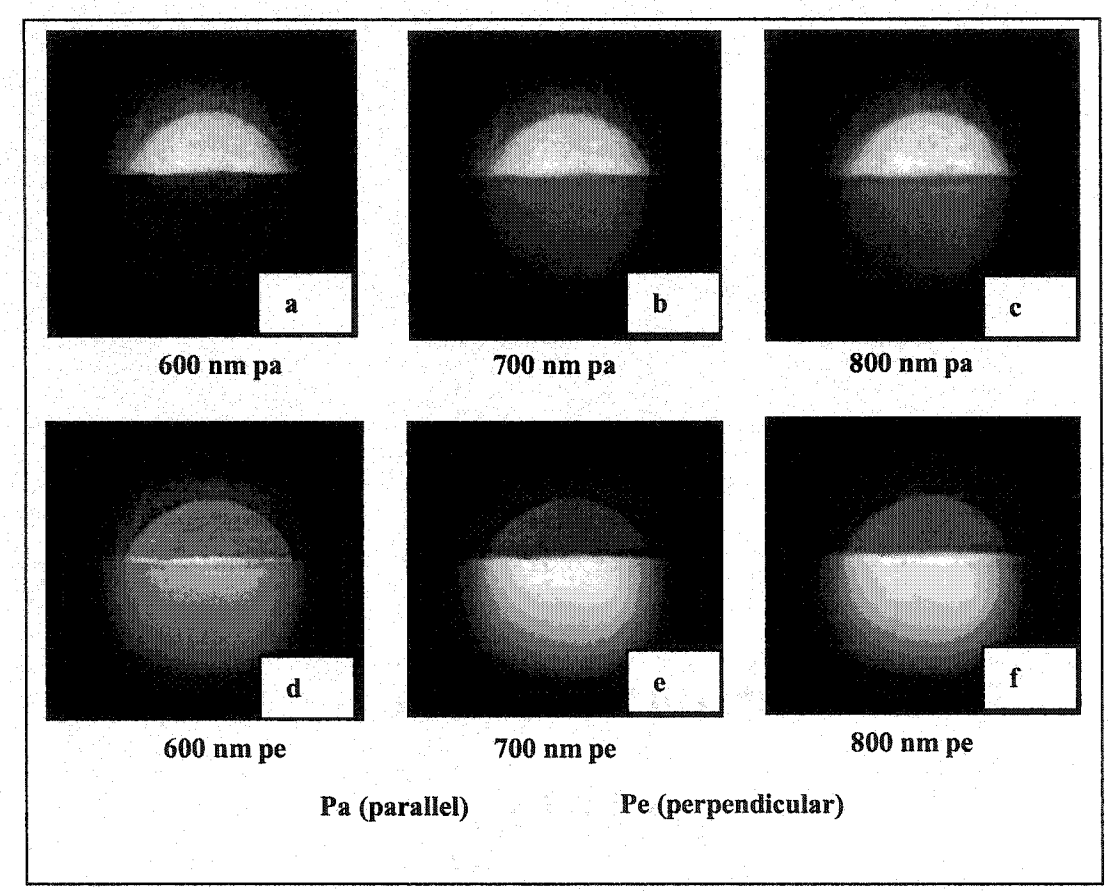

Fig. 7.5 Images of the corrosion on the top of aluminum plate using spectral and polarization properties. The lower half of the circular corrosion and aluminum plate are painted in red. (a-c) represent parallel polarization images, and (d-f) represent perpendicular polarization images.

normal to the sample surface, the reflected light from the paint surface is specularly reflected to the right-hand side of the CCD camera. In Figs. 7.5(a-c), the intensity of the scattered light from the top, unpainted half (low-scattering surface) is stronger than that of the bottom, painted half. Large portions of the scattered photons from the top half are registered in the CCD in the parallel polarization configuration, whereas a small portion of the scattered photons from the corrosion beneath the paint are registered in the CCD

camera in the parallel configuration, owing to scattering (which dominates in the long-wavelength region) and absorption (which dominates in the short-wavelength region) in the paint medium. The multiple-scattering processes through the bottom half cause the scattered light to be depolarized. Absorption in the paint medium is very high in the short-wavelength region, for example, at 600 nm as shown in Fig. 7.5a.

In Figs. 7.5(d-f), the intensities of the perpendicular scattered light from the bottom half of the corrosion at 600 nm, 700 nm, and 800 nm, respectively, are higher than those of the scattered light from the top half. The photons from the bottom half are scattered in all directions as in the top half, but pigments in the paint depolarize the photons more in the bottom half. A large portion of these photons are registered in the CCD camera in the perpendicular configuration. Most of the scattered photons from the top half are still highly polarized in the parallel configuration, and a very small portion is registered in the CCD camera in the perpendicular configuration. The scattering signal in the perpendicular configuration from the bottom half is stronger than that from the top half, as shown in Figs. 7.5(d-f). This observation is confirmed by the degrees of polarization in the two areas, as shown in Table 7.1.

	Location	600 nm	700 nm	800 nm
Degree of Polarization	Upper unpainted Corroded half	0.79	0.82	0.74
	Bottom painted corroded half	0.50	0.12	0.06

Table 7.1: The degree of polarization is measured for Fig. 6.5 for the upper unpainted half and the bottom painted half.

The degree of polarization of the images in Fig. 7.5 at different wavelengths can be calculated using Eq. 7.3. The calculated results, shown in Table 7.1, indicate that as the wavelength gets longer the degree of polarization gets smaller in the bottom half. This can be understood as the scattered signal from the 800 nm photons coming from a region deeper than that from the 600 nm or the 700 nm photons. As the degree of polarization gets smaller, the corrosion beneath the paint appears when the depolarized component is used. The degree of polarization in the top half is high and does not change much with the wavelength in the 600 nm- 800 nm region, as shown in Table 7.1.

It can be seen from Fig. 7.5 that the image contrast of the painted corrosion relative to the unpainted corrosion for perpendicular images is much better than that for the parallel images at each wavelength. The improvement of the perpendicular corrosion images over the parallel images can be seen more clearly in the digitized intensity profiles. Vertical scans from top to bottom in the middle of the images in Figs. 7.5(b) and 7.5(e) were taken for digitization purposes. In Fig. 7.6, curves (a) and (b) represent the intensity distributions of the parallel and the perpendicular polarization images of Figs. 7.5(b) and 7.5(e), respectively. The image contrasts of Figs. 7.5(b) and 7.5(e) (compare the top and bottom portions) were calculated with Eq. 7.4, and the digital data were obtained from Fig. 7.6. The calculated results show that the contrast of the perpendicular image (0.62) is ~ 1.5 times higher than that of the parallel image (0.40).

In conclusion, the visible and near infrared spectral and polarization properties of the scattered light has been used to image corrosion hidden beneath a highly scattering paint medium. These measurements show that the longer the wavelength is, the deeper the penetration, therefore more information on the corrosion structure below the paint

layer can be obtained. The depolarized scattered light imaging (perpendicular imaging configuration) is preferred to detect an object (corrosion) embedded in turbid media (such as paint) than that of the parallel image configuration.

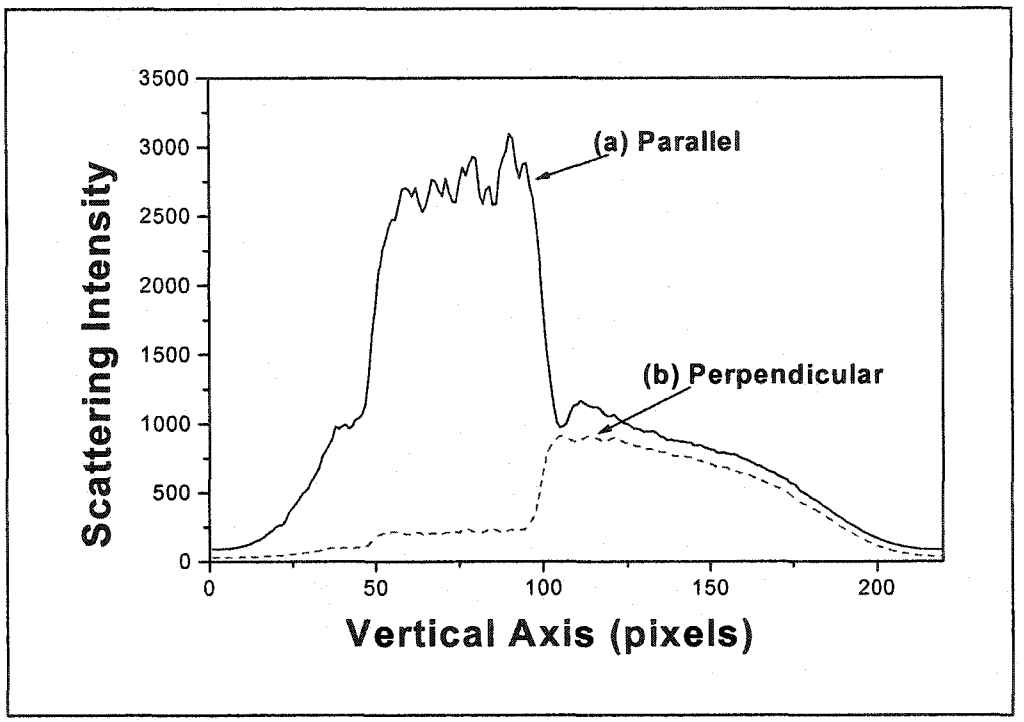

Fig. 7.6: The digitized intensity profiles for 700 nm along the vertical axis at the center of the (a) Parallel polarization image (Fig. 7.5b), and (b) perpendicular polarization image (Fig. 7.5e).

7.3 Detection of Corrosion and Cracks Beneath Paint Using Mid-IR Scanning Imaging Techniques

7.3.1 Background

In general, a structural component fails when it is no longer able to withstand the loads imposed during operation. The majority of structural failures are associated with the presence of cracks A critical crack is one that causes catastrophic break-up of the

component into two or more pieces. Detection of corrosion on a metallic surface beneath a paint layer is most important in determining structural failures. Surfaces on aging aircraft, bridges, electronic components and computer chips, wafers, fuel lines of space shuttles, nuclear reactors, cars or boats are subject to corrosion. There are several methods currently being used to determine structural failures as a result of corrosion including ultrasonic, magneto-optic imaging, active thermography, and speckle correlation. These methods have a poor spatial resolution and sensitivity, and so far corrosion cannot be detected at the earliest stage. Photonic techniques [12-14] offer a potentially rapid, noninvasive and easy approach to detect corrosion *in situ.* Art preservationists use Near-IR (NIR) CCD cameras ($\lambda < 2\ \mu m$) to view paintings that have underdrawings not visible with the human eye. Novel methods of second-harmonic generation (SHG) imaging [12], and spectral polarization optical imaging [13] have been proposed to detect the early stages of corrosion under thin layers of paint using NIR. The confocal enhanced optical coherence tomography has been applied to improve image contrast and depth resolution through a highly scattering paint layer [15].

Absorption and scattering are the dominant mechanisms for paint. When the incident power on the sample at a particular wavelength is large enough, imaging through an absorption layer is possible. The problem of imaging through paint layer is more complicated because of high scattering. It is well known that an image can be produced only by the ballistic and snake photons that provide the limit for the optical thickness of the paint layer of 27 mean free paths (MFP's) for optical coherence tomography [15] and only ~ 6 MFP's for confocal imaging [16].

To achieve spatial resolution of 5 μm, the axial and lateral resolution of the proposed methods should be investigated for two systems in mid-IR at wavelength of ~ 5 μm. The axial resolution of the confocal microscope can be given as $\Delta z = \lambda/2\sin^2(N.A./2)$, where $\lambda = \lambda_0/n$ is the wavelength in the beam path, and N. A. is the numerical aperture of the sample focusing parabolic mirror. For our experimental setup: $\lambda_0 = 4.9\ \mu m$ and N.A. = $d/2f_m$ = 30 mm/20 mm = 1.5 and axial resolution about 5 μm can be achieved using a pinhole of the radius $\upsilon_p \leq 2$ optical units ($\upsilon_p = \pi d_p a/\lambda_0 f$, where d_p is the pinhole diameter, a and f are the effective beam size and the focal length of the parabolic mirror focusing onto the pinhole). The lateral resolution for the confocal microscope is calculated to be $\Delta x = 0.61\lambda/N.A.$ ~1.8 μm. Because of mid-IR diode laser is not a perfect "point" source a detailed investigation needs to be done to achieve a spatial resolution of 5 μm.

We report on the transmission zone of paints in mid-IR and on the use of a scanning imaging technique to detect corrosion beneath a thick paint layer. Two-dimensional (2D) images of the surface region of samples were obtained by scanning with an IR-LED focused beam and mapping the intensity of the reflected signals. These 2D images showed differences between the corrosion and the metal surface beneath a thick paint layer. To the best of our knowledge, our results first report on the mid-IR transmission zone between 3.8 to 5.5 μm in paints and the use of the mid-infrared scanning technique to image corrosion beneath paint layers of thickness, 80 to 100 μm. The best results of imaging corrosion through paint systems were achieved at 4.8 μm.

The use of InSb CCD system will increase the speed at which a large metal painted surface can be imaged.

7.3.2 Experimental Methods

Using the mid-infrared transmission window in paints, a novel scanning imaging technique is presented to detect corrosion beneath a thick paint layer. Two-dimensional (2D) images of the sample were obtained by scanning with an IR-LED focused beam and mapping the intensity of the scattered light signals. These 2D images showed differences between corrosion and a metal surface beneath a thick paint layer. The samples used in our experiment were made from 2024 T3 aluminum plates. The aluminum plates were chemically corroded by the reaction of potassium hydroxide with the surface of the aluminum plate for a period of 24 hours. The thickness of the corrosion was about 35 μm and formed an 8 mm circle. The corrosion was either coated over with paint or covered with glass slides that had been prepared with different paint systems of various thickness. The beam from a LED is focused on the sample that has corrosion beneath a paint layer at a certain angle to the paint surface by an off-axis parabolic mirror (OPM). The reflected light from the paint surface is specularly reflected to the left-hand side of the OPM to be removed from the measurement. Light scattered from the corrosion or metal under the paint is collected by the mirrors. A photodetector (PD) receives this portion of the reflection. The sample is scanned in x and y directions relative to the fixed light beam. The sample is scanning in X-Y or X-Z directions by the linear movements of two translation stages. A lock-in amplifier processes signals from the detector to derive information from the reflected signals. A LN-cooled Indium Antimonide (InSb) PD was

used for the wavelength range of 1.8 μm to 5.5 μm. The experimental setup for detecting corrosion beneath paint using Mid-IR scanning imaging techniques is shown in Fig. 7.7.

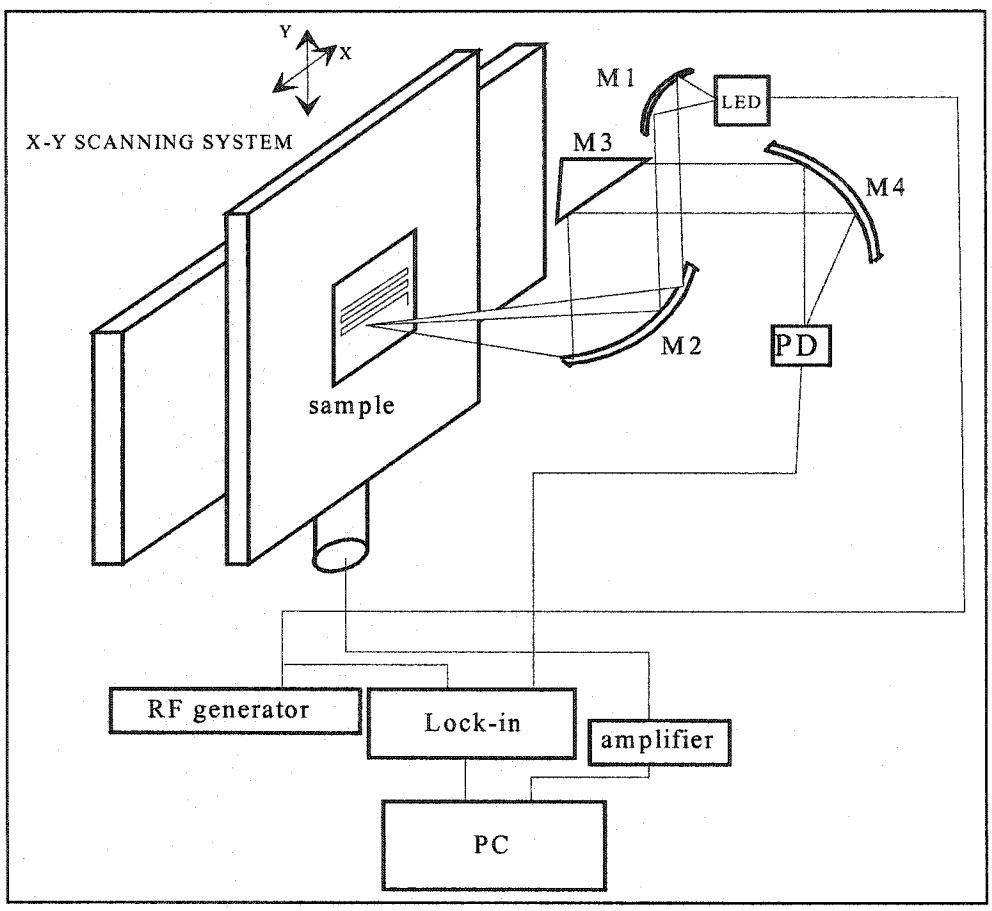

Fig. 7.7: Experimental setup: M1, M2, M4, off-axes parabolic mirrors; M3, plane mirror; PC, personal computer; PD, photodetector (InSb type).

7.3.3 Experimental Results

The coated over glass slides were prepared to measure absorption/transmission characteristics of the individual paints and paint systems. The transmission curve of the paint system # 1 is shown in Fig. 7.8 and indicates that paint has two transmittance zones for wavelengths from 1 μm to 2.8 μm, 3 μm to 3.4 μm and from 3.8 μm to 5.6 μm.

The best zone is 3.8 to 5.6 μm. Paint system # 1 is comprised of a polyurethane primer layer, Strontium Chromate-TT-P-2760 Type 1 Class C, and a polyurethane topcoat, Mil-PRF-85285 Type 1 color 36173 gray. Absorption and scattering are the dominant mechanisms needed to explain the results. When an incident power on the sample at a particular wavelength is large enough, imaging through an absorption layer is possible.

Back reflection geometry is used to image the subsurface structure of the corroded samples covered by a glass slide coated with paint. Glass slides coated with paint systems were generated in order to measure the optical transmission of the paint systems as a function of wavelength. Corrosion detection in the wavelength range from 1.8 μm up to 5.5 μm was investigated. Light emitting diodes (LED) with the following wavelengths and powers were used as sources to illuminate the samples: 1.8 μm (90 μW output power), 3.8 μm (60 μW output power), 4.8 μm (10 μW output power) and 5.5 μm

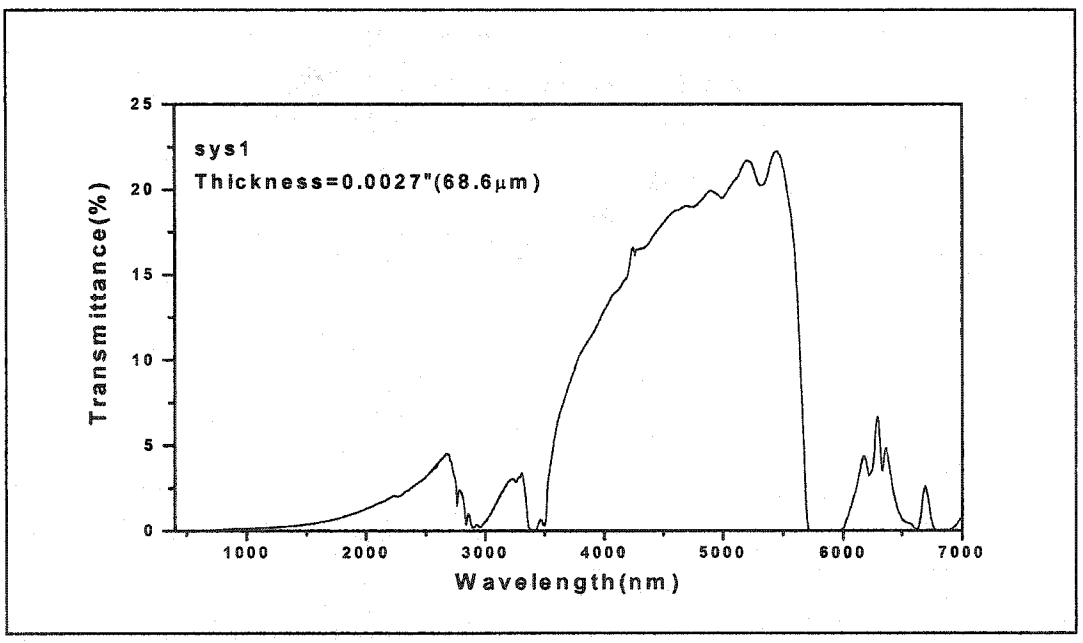

Fig. 7.8: Transmission curve of the paint system #1 in the wavelength range from 500 to 7000 nm

(30 μ W output power).

Figs. 7.9a-d show images at 1.8 μm, 3.8 μm, 4.8 μm and 5.5 μm wavelengths respectively, of corrosion coated over with paint system # 1 (0.004 inches thick).

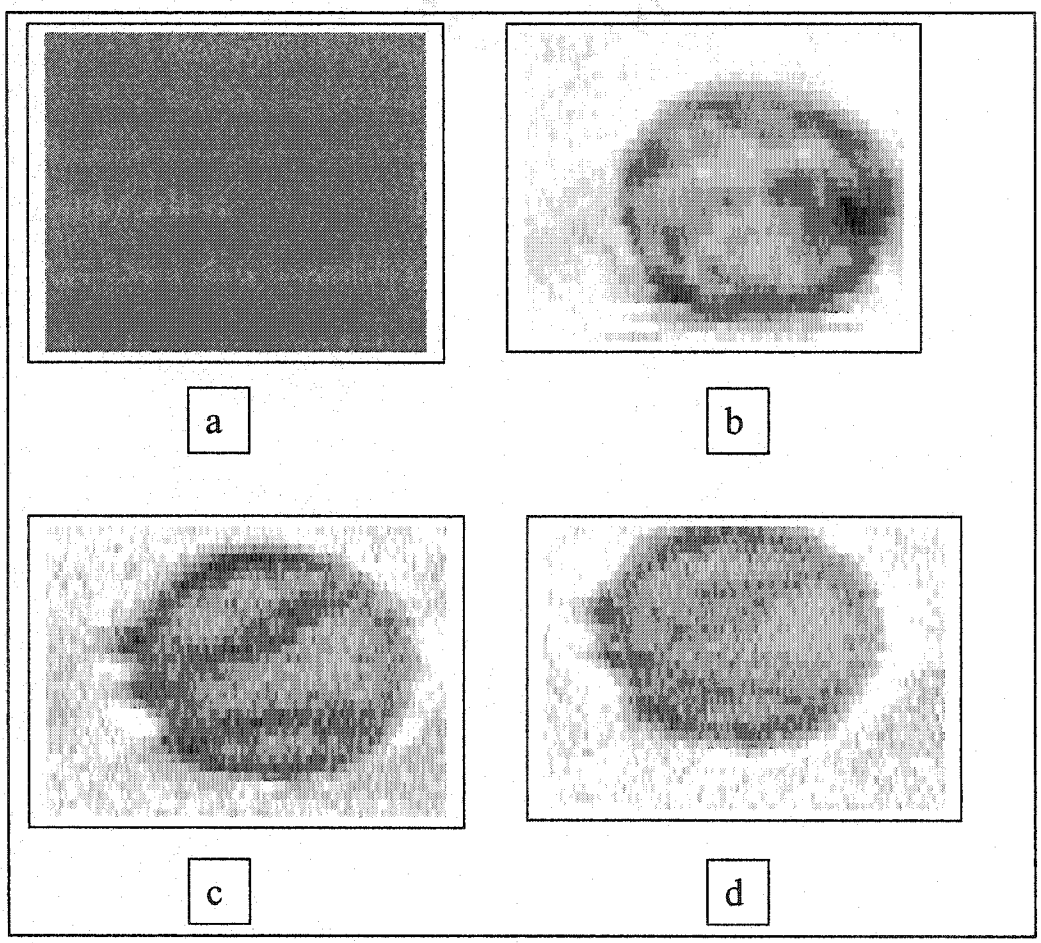

Fig. 7.9: Images of corrosion on the aluminum plate coated over with the paint system # 1 (0.004 inches thick) at 1.8 μm, (b) at 3.8 μm, (c) at 4.8 μm and (d) at 5.5 μm wavelengths, respectively.

7.3.4 Discussion and Outcome

The reflected light from the paint surface is specularly reflected to the left-hand side of the collection mirror M_2 as shown in Fig. 7.7. Only scattered light is collected by the setup. Short wavelengths such as 1.8 μm cannot reach the corrosion layer. In this case,

the resulting images are formed from photons that scattered from the surface or subsurface of the paint medium. On the other hand the longer wavelengths (such as 3.8 μm, 4.8 μm, and 5.5 μm) with a greater penetration (see Fig. 7.8) had a better chance to pass through the paint medium to reach the corrosion beneath the paint. The resulting images at these wavelengths represent the scattered photons from all layers including the corrosion layer, and therefore, the corrosion layer may be identified.

Fig. 7.9a is for the 1.8 μm wavelength. The corrosion region could not be imaged using NIR. At this wavelength the transmission of the light is minimum and scattering is maximum compared to the other wavelengths. As the wavelength increases from 1.8 μm to 3.8 μm (Fig. 7.9b) the paint transmission is higher and more photons are reaching the corrosion surface. The image for MIR of Fig. 7.9c (at 4.8 μm wavelength) has the best contrast, which correlates with the transmission curve of paint system # 1. From the transmission curve in Fig. 7.8, the optical transmission at 5.5 μm wavelength is less then at 4.8 μm wavelength. This results in the slightly poorer image at 5.5 μm compare to that at 4.8 μm as shown clearly in Fig. 7.9d.

We are first to determine the mid-infrared (MIR) transmission zone of paint in the range of 3.8 - 5.5 μm and to use the mid-infrared scanning technique to successfully image corrosion beneath thick paint layers of 80 to 100 μm using low power light emitting diodes. The best results of imaging corrosion through many different paint systems were achieved at about 4.8 μm.

In conclusion, the visible, near infrared, and Mid-IR spectral and polarization properties of the scattered light has been used to image corrosion hidden beneath a highly

scattering paint medium. The depolarized (perpendicular) scattered light component in the visible and NIR spectral polarization imaging technique is preferred to detect corrosion beneath paint layers of 40 μm. The confocal scanning imaging technique in the Mid-IR (3.8 - 5.5 μm) was successfully used to image corrosion beneath paint layers of 80 to 100 μm.

7.4 References

1. M. Fontana, Corrosion Engineering, McGraw-Hill, New York, 1986.

2. Paul E. Mix, P. E., Introduction to Nondestructive Testing, John Wiley and Sons, New York, 1987.

3. D. Liu. F. Wang, Ch. Cao, L. Zhang, and H Lin, Corrosion 46, 975, 1990.

4. Michel de Billy, Frederic Cohen-Tenoudji, Alain Jungman, and Gerard J. Quentin, IEEE Transactions on Sonics and Ultrasonics 5, 356, 1976.

5. Benoit Mandelbrot, Dann Passoja and Alvin Paullay, Nature 308, 721, 1984.

6. M. Stratmann and H. Streckel, Corrosion Science 30, 681, 1990.

7. L. Wang, P. P. Ho, C. Liu, G. Zhang, R. R. Alfano, Science 253, 769, 1991.

8. S. G. Demos, W. B. Wang, J. H. Ali, and R. R. Alfano, OSA TOPS 21, 405, 1998.

9. W. B. Wang, S. G. Demos, J. H. Ali, G. Zhang, and R. R. Alfano, Optics Communications 147, 11, 1998.

10. C. Weiping and Xu Chenghui, Journal of Material Science Letters 16, 113, 1997.

11. S. J.Williamson and H. Z. Cummins, Light and Color in Nature and Art, John Wiley and Sons, USA, 1983.

12. W. B. Wang, J. H. Ali, J. H. Vitenson, J. M. Lombardo, and R. R. Alfano, Technical Program of the SPIE BIOS 2000 Meeting, San Jose, CA, Jan. 22-28, 51, 2000.

13. J. Ying, F. Liu, P. P. Ho, and R. R. Alfano, Opt. Lett. "Nondestructive evaluation of incipient corrosion in a metal beneath paint by second-harmonic tomography", Opt. Lett., 25, 1189, 2000.

13. J. H. Ali, W. B. Wang, P. P. Ho, and R. R. Alfano, Opt. Lett. 'Detection of corrosion beneath a paint layer by use of spectral polarization optical imaging', Opt. Lett.25, 1303, 2000.

14. F. Xu, H. E. Pudavar, P. N. Prasad and D. Dickensheets, 'Confocal enhanced optical coherence tomography for nondestructive evaluation of paints and coatings', Opt. Lett.,24, 808, 1999.

15. M. Kempe, W. Rudolph, and E. Welsh, J. Opt. Soc. Am. A 'Comparative study of confocal and heterodyne microscopy for imaging through scattering media' 13, 46, 1996.

Chapter 8

Conclusion

8.1 Thesis Summary

This dissertation presents an investigation of the structural and molecular changes in scattering media in bio-medical applications such as animal, and human prostate tissues and non-biomedical applications such as corrosion beneath paint in the visible to mid-IR spectral region using steady and time-resolved light spectroscopy and imaging techniques.

In chapter 2, the theoretical background is covered for the work of this thesis. The theoretical work covers: light scattering (single and multiple scattering), polarization in scattering media, absorption and emission, time resolved fluorescence and imaging and scanning principles in scattering media.

In chapter 3, the temporal polarization emission profiles of fluorescein dye-labeled polymers of molecular weight ranging 4 K to 500 K were measured. The polarization decay time of fluorescein dye-polymer conjugates increases with molecular weight. The difference image at high polymer molecular weight was found to be much brighter and clearer than that at low molecular weight. This observation demonstrates that high molecular weight dye-polymer conjugates can be used to enhance the imaging depth and visibility of objects hidden inside tissue media. The fluorescence depolarization of the Cardio Green dye was measured, and found to decay after 400ps. The optical properties of Human prostate tissues using time resolved techniques were measured. The

transport length of prostate tissue was $\ell_{tr} = 0.86$ mm.

Chapter 4 covers the spectral polarization imaging in animal and human prostate tissues imaging. This chapter shows that:

(i)The polarization preservation property of Cardio Green dye and the fluorescence-polarization-difference-imaging (FPDI) technique are introduced to enhance the image quality of an object embedded inside tissues. The difference between the fluorescence spectra emitted from Cardio Green dye and chicken breast tissue in the near-infrared (NIR) region was measured and used to select a pair of fingerprint wavelengths for imaging. The spatial resolution and contrast of the resulted fluorescence polarization difference image (for two 1 mm diameter tissue pieces stained with Cardio Green positioned 1.5 mm apart and placed 2mm underneath the surface of the host chicken breast tissues) were found to be higher than that of the conventional non-polarized optical images by factors of 2.3 and 3.6, respectively. Using spectral fluorescence difference imaging (SFDI) method, a 1mm tissue object stained with Cardio Green dye located 3.1 cm beneath the surface of the host chicken tissue was clearly imaged and identified.

(ii) Small objects hidden inside the host prostate tissues in the rectum-membrane-prostate structures at depths of 2.5, 4.0, and 7.5 mm can be imaged and identified using the scattering light imaging, tissue emission wing imaging, and contrast agent fluorescence imaging methods, respectively. Our results indicate the potential of imaging and detecting structural changes and cancers inside prostate tissue through rectum-membrane-prostate tissues using noninvasive spectral polarization imaging technique.

(iii) The content of water in cancerous and normal human prostate in-vitro tissues was different using near infrared (NIR) spectroscopy. The OH stretching vibrational overtone mode at 1444 nm and other water overtone modes provide key spectroscopic fingerprints to detect, non-invasively, cancer in prostate human tissue. This knowledge about water content offers a new potential imaging method to detect cancer in prostate and in other tissue types such as breast and cervix using the absorption from vibrational overtones of H_2O molecules in the NIR.

Chapter 5 covers the time resolved photon scattering measurements in highly scattering paint media. The value of the transport length ℓ_{tr} for paint medium from time-resolved pulse transmission, steady state, and degree of polarization is $28\,\mu m$, $34\,\mu m$, and $29\,\mu m$, respectively. The polarization and coherence gradually decreases in going from the ballistic to the snake to the diffusive regimes. Polarization and coherence disappear at thickness greater than or equal to fifteen transport lengths ($>15\ell_{tr}$). The small residual coherence for $L > 15\ell_{tr}$ is described by the Van Cittert-Zernike theorem, which arises from the correlation of the fields from same single points in the scattering media arriving at the two slits to take part in interference.

Chapter 6 investigates imaging through paint using spectral polarization and confocal scanning imaging techniques from visible to Mid-IR. The visible to mid-infrared transmission window between 0.5 - $5.5\,\mu m$ has been used to detect corrosion beneath different types of paint layers and thicknesses between 35-100 μm using novel photonics: spectral polarization and confocal scanning imaging techniques.

8.2 Future Work

In this section we briefly review new ideas and potential developments in the investigation of light propagation in highly scattering paint and prostate human tissues.

8.2.1 Diffusion Coefficient and Transport Velocity In Paint Media

In the classical diffusion limit ($\lambda << \ell_{tr}$), the phases of the scattered light are uncorrelated and propagation can be described in terms of the diffusion of the energy density of the wave [1]. The diffusion coefficient is given by $D = \upsilon \ell_{tr}/3$, where v represents the transport velocity. The transport velocity is neither the phase velocity nor the group velocity, where the group velocity describes the propagation of the coherent beam. When scattering is sufficiently intense ($\lambda \sim \ell_{tr}$), extended correlation in scattered waves lead to destructive interference, which reduces the average transport rate [2]. The transport velocity can be much lower than the phase velocity in the resonant scattering case. Transport depends upon the spatial extent of wave correlations. Now the diffusion coefficient D, which depends upon the wavelength of the incident wave and the transport length, can be determined from the transmission of the wave I(t,L), where L is the sample thickness [3,4]. Both the total transmission as a function of the sample thickness, T(L), and fluctuations in the transmitted intensity (I(t,L)) within a single coherence area for various L values are measured. The setup for these measurements is similar to that discussed in chapter five, Fig. 6.5. From these measurements, the optical diffusion coefficient D, the transport mean free path, and transport velocity can be determined in the highly scattering paint medium for different coherence areas. The temporal

propagation of polarization in scattering media such as paint needed to be investigated. More work needs to be done to clarify the issue of transport velocity and temporal polarization in highly scattering media.

8.2.2 Semiconductor Properties of Paint

Various methods have been employed for producing a thermal radiation control surface. Such surfaces have a number of uses, among which are solar collector absorber panels, space vehicle surfaces, and military applications such as a camouflaging military vehicles from detection by infrared. The technology of thermal radiation control surfaces is based on the need to obtain a surface, which absorbs radiation in the range of 300 to 1000 nanometers while at the same time not allowing thermal energy to be radiated. It is necessary to make the surface selective, i.e., as highly absorbing as possible in the visible range and as low emitting as possible in the thermal region. This requirement makes semiconductor pigments highly desirable, as these compounds are highly transparent in the infrared but absorbing in the visible. Not all semiconductor pigments are useful, as those have a high refractive index and thus a high surface reflection. Thus, only those semiconductor pigments having low enough refractive indices to keeping surface reflectivity at a minimum are acceptable. Among such useful semiconductor pigments are copper oxide, iron oxides, chromium oxides, nickel oxide, complexes of nickel-zinc-sufide, lead sulfide, alkali metal silicates and so forth [5,6]. Since thermal and photochemical stability is required of the semiconductor, organic dyes would not be very useful and the preferred semiconductors are, therefore, the inorganic pigments already

enumerated.

The most direct and perhaps the simplest method for probing the band structure of semiconductors is to measure the absorption spectrum. In the absorption process, a photon of a known energy excites an electron from a lower- to a higher-energy state. Thus by inserting a slab of semiconductor at the output of a monochromator and studying the changes in the transmitted radiation, one can discover all the allowed transitions an electron can make and learn much about the distribution of states. Absorption is expressed in terms of a coefficient $\alpha(h\nu)$, which is defined as the relative rate of decrease in light intensity $I(h\nu)$ along its propagation path [7]:

$$\alpha(h\nu) = -\frac{1}{I(h\nu)}\frac{d[I(h\nu)]}{dx} \tag{8.1}$$

The fundamental absorption refers to band-to-band or to exciton transitions, i.e., to the excitation of an electron from the valence band to the conduction band. The fundamental absorption, which manifests itself by a rapid rise in absorption, can be used to determine the energy gap of the semiconductor. The absorption coefficient $\alpha(h\nu)$ for a given photon energy $h\nu$ is proportional to the probability (P_{if}) for the transition from the initial state to the final state and to the density of electrons in the initial state (n_i) and also to the density of available (empty) final states (n_f) and this process must be summed for all possible transitions between states separated by an energy difference equal to $h\nu$:

$$\alpha(h\nu) = A\sum P_{if} n_i n_f \tag{8.2}$$

Let us consider absorption transitions between two direct valleys where all the momentum-conserving transitions are allowed (Fig. 8.1a), i.e., the transition probability

P_{if} is independent of photon energy. Every initial state at E_i is associated with a final state at E_f such that

$$E_f = h\nu - |E_i| \tag{8.3}$$

But in parabolic bands,

$$E_f - E_i = \frac{\hbar^2 k^2}{2m_e^*} \tag{8.4}$$

and

$$E_i = \frac{\hbar^2 k^2}{2m_h^*} \tag{8.5}$$

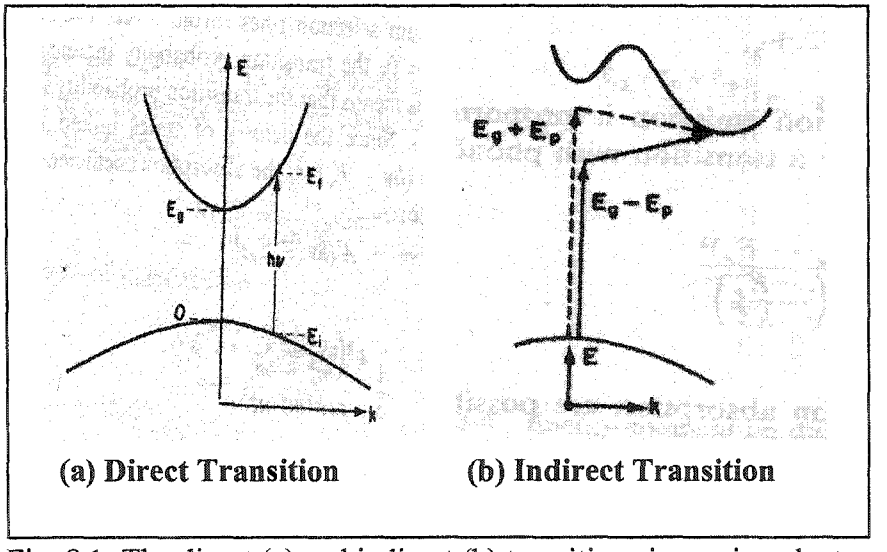

Fig. 8.1: The direct (a) and indirect (b) transitions in semiconductors [7].

Therefore,

$$h\nu - E_g = \frac{\hbar^2 k^2}{2}\left(\frac{1}{m_e^*} + \frac{1}{m_h^*}\right) \tag{8.6}$$

Using equation 8.6 and the density states in the interval E and E+dE in equation 8.1 results in

$$\alpha(h\nu) = A(h\nu - E_g)^{1/2} \tag{8.7}$$

where A is a constant related to the hole and electron effective masses and index of refraction.

When a transition requires a change in both energy and momentum, a double, or two-step, process is required because the photon cannot provide a change in momentum. Momentum is conserved via a phonon interaction as illustrated in Fig. 8.1b. A phonon is a quantum of lattice vibration. Although a broad spectrum of phonons is available, only those with the required momentum change are usable. These are usually the longitudinal- and the transverse-acoustic phonons. Each of these phonons has a characteristic energy E_p. Hence to complete the transition E_i to E_f a phonon is either emitted or absorbed. These two processes are given respectively by

$$h\nu_e = E_f - E_i + E_p \tag{8.8}$$

$$h\nu_a = E_f - E_i - E_p \tag{8.9}$$

In indirect transitions, all the occupied states of the valence band can connect to all the empty states of the conduction band. The number of phonons is given by Bose-Einstein statistics (N_p). The absorption coefficient for a transition with phonon absorption is

$$\alpha_a(h\nu) = \frac{C(h\nu - E_g + E_p)^2}{e^{E_p/kT} - 1} \tag{8.10}$$

for $h\nu > E_g - E_p$, and the absorption coefficient for a transition with phonon emission (proportional to $N_p + 1$) is

$$\alpha_e(h\nu) = \frac{C(h\nu - E_g - E_p)^2}{1 - e^{-E_p/kT}} \tag{8.11}$$

for $h\nu > E_g + E_p$.

Since both phonon emission and phonon absorption are possible when $h\nu > E_g + E_p$, the absorption coefficient is then

$$\alpha(h\nu) = \alpha_a(h\nu) + \alpha_e(h\nu) \tag{8.12}$$

for $h\nu > E_g + E_p$.

The transmission curves of different paints such as white epoxy intermediate and polyurethane coating coat are going to be investigated. The plots of $\sqrt{\alpha}$ versus energy and α^2 versus energy for different paints are going to be investigated. Measuring the I-V curve is a possible way to investigate the optical properties of the paint. From these investigations the semiconductor properties of the paints can be determined. Also from the investigation above, we can design a paint model for surfaces to prevent IR emission or detection in some applications. The size and the shape of the paint components such as pigments can be determined using scanning electron microscope (SEM) to understand the nature of scattering (Rayliegh and Mie scattering) .

8.3 Gleason's Grades in Prostate Cancer

Our technique, described in chapter 5 (Near Infrared Spectroscopy and Imaging to Probe Water in Normal and Cancer Human Prostate Tissues), is related to the microstructure detection, measures the optical vibrational frequency of a bonded OH overtone bands in tissues. To understand the correlation of water to cancer and normal tissues, we used the absorption spectra of side by side normal and cancer prostate tissues. We investigate the spectral absorption, transmission and backscattering imaging techniques to support the key observation that prostate cancer tissues have less water than normal tissues in the samples that we have studied. We investigated the fingerprint of water content in tissues for five different samples. The spectra in all samples showed similar results.

It is believed that the hardness at early stage of cancer arises from the density of cancer cells and its larger nucleus to push out the water. While at later stage these cancer cells are more disperse and not localized and more water will be found in between cancer cells. This can be concluded from the five Gleason Grades as shown in chapter 2 (Fig. 2. 7).

More work and data needed to be collected to support our claim to clarify the detection of cancer and Gleason's Grade based on the water content. In the future, the second phase of our research on this subject will involve data that are correlated with the histopathology studies and to differentiate the Gleason's Grades.

8.4 Publications Resulting From Thesis Work:

A. Publications

1. W. B. Wang, S. G. Demos, J. Ali and R. R. Alfano, "Imaging fluorescent objects embedded inside animal tissues using polarization difference technique", Optics Comm., 142, 161-166 (1997).

2. W. B. Wang, S. G. Demos, J. H. Ali, G. Zhang, and R. R. Alfano, "Enhancement of visibility of fluorescent object hidden in animal tissue using spectral fluorescence difference method", Optics Comm., 147, 11-15 (1998).

3. S. G. Demos, W. B. Wang, J. Ali, and R. R. Alfano, "New optical Difference Approaches for sub-surface imaging of tissues", OSA TOPS Vol. 21, in "Advances in Optical Imaging and Photon Migration", editted by J.G. Fujimoto and M. S. Patterson, 405-410 (1998).

4. W. B. Wang, S. G. Demos, J. H. Ali, G. Zhang, and R. R. Alfano, "Enhancement of contrast agent images using spectral fluorescence difference", OSA TOPS Vol. 22, in "Biomedical Optical Spectroscopy and Diagnostics/ Therapeutic Laser Applications", editted by E. M. Sevick-Muraca, J. A. Izatt, and M. N,. Ediger, 57-60 (1998).

5. W. B. Wang, J. H. Ali, R. B. Dorshow, M. A. McLoughlin, and R. R. Alfano, "Time-resolved fluorescence polarization dynamics and imaging of fluorescein dye attached to different molecular weight chains", in Proceedings of biomedical imaging: reporters, dyes, and instrumentation, SPIE, Vol. 3600, 227 (1999).

6. J. H. Ali, W. B. Wang, P. P. Ho, and R. R. Alfano, "Detection of corrosion beneath a paint layer by use of spectral polarization optical imaging", Optics Letters, Vol. 25, No. 17, 1303 (2000).

7. W. B. Wang, J. H. Ali, J. H. Vitenson, J. M. Lombardo, and R. R. Alfano, "Spectral polarization imaging of human prostate tissues", in Proceedings of optical biopsy III, SPIE, Vol. 3917, 75 (2000).

8. W. B. Wang, J. H. Ali, J. H. Vitenson, J. M. Lombardo, and R. R. Alfano, "Spectral polarization imaging of human prostate tissues", in Proceedings of optical biopsy III, SPIE, Vol. 3917, 75 (2000).

9. I. Zeylikovich, W. Wang, F. Zeng, J. Ali, B. L. Yu, V. Benischek, and R. R. Alfano, "Mid-IR transmission window for corrosion detection beneath paint" Electronics Letters, Vol. 39, 39, 2003.

10. W. B. Wang, J. H. Ali, J. H. Vitenson, J. M. Lombardo, and R. R. Alfano, "Spectral polarization imaging of human rectum-membrane-prostate tissues", IEEE Journal of Selected Topics in Quantum Electronics (JSTQE) on Lasers in Medicine and Biology, Vol. 9, pp 288-293 (2003).

11. J. H. Ali, W. B. Wang, R. R. Alfano, and M. K. Kassir, "Detection of corrosion and cracking beneath paint using photonic techniques", Theoretical and applied fracture mechanics, 28 Nov. 2003.

12. J. H. Ali, W. B. Wang, M. Zevallos, and R. R. Alfano, "Near Infrared spectroscopy, transmission and backscattered imaging to detect water in normal and cancer human prostate tissues", Technology in Cancer Research and Treatment, Vol. 3, October (2004).

13. J. H. Ali, B. Das, D. Kalamidas, I. Zeylikovich, and R. R. Alfano, "Randomization of polarization and coherence from ballistic to diffusive regimes in highly scattering paint medium " submitted to PRL journal, (2004).

B. Patents

1. Apparatus for enhancing the visibility of a luminous object inside tissue and methods for same, Robert R. Alfano, Stavros G. Demos, Wubao Wang, Jamal Ali, # 6,280,386 B1, Aug. 28, 2001.

2. A patent disclosure and provisional U. S. patent application entitled "System and method for corrosion and cracks beneath a paint layer" by R. R. Alfano, I. Zeylikovich, W. B. Wang, J. H. Ali, V. Benischek, and Y. Budansky was filed on 4/23/2002.

3. A patent disclosure and provisional U. S. patent application entitled "Cracks and corrosion detection technique" by R. R. Alfano, I. Zeylikovich, W. B. Wang, J. H. Ali, V. Benischek, and Y. Budansky was filed on 7/17/2002.
4. A patent disclosure and provisional U. S. patent application entitled "Detecting human cancer through spectral optical imaging key water absorption wavelengths" by R. R. Alfano, J. H. Ali, Wubao Wang, and Manuel Zevallos was filed on 4/17/2004.

C. Presentations

1. W. B. Wang, S. G. Demos, J. H. Ali, and R. R. Alfano, "Spectral and polarization imaging", presented at 1997 OSA Annual Meeting, Longbeach, CA, Optics & Photonics News, 8, 107 (1997).

2. J. H. Ali, W. B. Wang, P. P. Ho, and R. R. Alfano, "Detection of corrosion beneath a painted metallic surface", presented at 2000 OSA Annual Meeting, in Providence, Rhode Island, Oct. 22-26, 2000.

3. J. H. Ali, W. B. Wang, P. P. Ho, and R. R. Alfano, "Corrosion detection beneath a painted metallic surface", presented at 2001 SPIE Meeting in Rochester, New York, May 8-10, 2001.

4. J. H. Ali, W. B. Wang, M. K. Kassir and R. R. Alfano, "Detection of corrosion and cracking beneath paint using photonic techniques", presented at the "International Symposium of Multiscaling in Mechanics", in Messini, Greece, on September 2-6, 2002.

5. W. B. Wang, I. Zeylikovich, J. H. Ali, F. Zeng, V. Benischek, F. Pellegrino, R. D'Italia and R. R. Alfano, "Middle-IR zone for corrosion and crack detection beneath paints", presented at OSA annual meeting in Tucson, Arizona on October 5-9, 2003.

6. W. B. Wang, J. H. Ali, M. Zevallos, and R. R. Alfano. Near infrared imaging of human prostate cancerous and normal tissues based on water absorption, in OSA Biomedical Optics Topical Meetings on CD-ROM (The Optical Society of American, Washington, DC), MF 38, 2004.

8.5 References

1. R. Loudon, The Quantum Theory of Light, first edition, Oxford, 1973.

2. Ping Sheng ed., Scattering and Locatisation of Classical Waves in Random Media, World Scientific, Singapore, 1990.

3. T. M. Nieuwenhuizen, A. Lagendijk, and B.A. van Tiggelen, Phys. Lett. A. 169, 191, 1992.

4. B.A. van Tiggelen, A. Lagendijk, M.P. van Albada and A.Tip, Phys. Rev. B 45, 12233, 1992.

5. P. Kittle, Patent # 4034129, Methods for forming an inorganic thermal radiation control, Philadelphia, PA, 1977.

6. K. Nassau, The physics and chemistry of color, John Wiley & Sons, USA, 1983.

7. J. I. Pankove , Optical processes in semiconductors, Dover publications, New York, 1971.

Appendix

This program is written by Dr. W. Cai, Physics Department, IUSL.

Parameters used in this program are:

Anisotropic factor, gg (0.88)

Refractive index of up and down boundary, up: n1(1.35) ,n2 (1.45) ,n3 (1)

Thickness of the layer, 1d, fit to different thicknesses

Calculate ze for boundaries at both sides of the layer up and down boundaries

Incident wavelength 800 nm

The Program:

```
#fit_lmdif1.r
include "head1.h"
real*8 ld, c, lt, gg, mus, mua, r0(3), s0(2), rd(3), sd(2), gl(LL)
real*8 n1(2),n2(2),n3(2),alpha(2),nfun_full, nfun_scat,ta,step,t
real*8 t_profile(2,NDATA),x(NX),fvec(NDATA),dt,base,base1,tol,ratio
real*8 wa(NX*NDATA+5*NX+NDATA+100),x1,xb(2),f1,mus,mua
integer m, n, i, j, k, info, iwa, lwa, id
common /parameter/alpha,ld,c,gl,r0,rd,s0,dt,base,id
common /data/t_profile
external fcn1, fcn2, ini
open(10, "input")
open(11, "data")
open(12, "result")
```

```
read(10,*) gg        # anisotropic factor
read(10,*) n1,n2,n3   # refractive index of up and down boundary
#n1:for layer n2:for wall n3:for outside (1): inject side (2) other side
read(10,*) ld        # thickness of the layer
read(10,*) tol       # tolorance for fitting
read(10,*) xb        # the possible range of initial 1/lt
write(1,*)"xb=",xb
# read experimental data
do i=1,NDATA  {
 read(11,*) t_profile(1,i), t_profile(2,i)
   }
dt=(t_profile(1,NDATA)-t_profile(1,1))/(NDATA-1)
# using Mie theory
#rfn2=IndexRefractionObject/IndexRefractionBG
#rb=DimeterObject/WaveLength*IndexRefractionBG/2
#call phase(rfn2, rb, pfn, qext, qsca, g)
#open(25,file="gl.data")
#n=LL
#call getgl(pfn,n,gl)
#write(25,*)"gl:"
#write(25,*)gl
#write(25,*)"g:", g
```

```
#write(25,*)"extinct coeff.=", qext

#write(25,*)"scattring coeff.=", qsca

# Using H-G phase function

gl(1)=0

gl(2)=gg

do n=3,LL {

 gl(n)=gl(n-1)*gg

 gl(n-1)=1-gl(n-1)

 }

gl(LL)=1-gl(LL)


c=300/n1(1)  # unit um/psec

#calculate ze for boundaries at both sides of the layer

call calc_ze(n1,n2,n3,alpha)

write(1,*)"alpha=",alpha

# put source and detector

r0(1)=0      #source -x

r0(2)=0      #source -y

r0(3)=0      #source -z

s0(1)=0      #theta incident

s0(2)=0      #phi incident

rd(1)=0      #receiver -x
```

```
rd(2)=0      #receiver -y

rd(3)=ld     #receiver -z  #for transmission

sd(1)=0      #theta received

sd(2)=0      #phi   received

#determine the initial value

x(2)=0.00001   # asuume mua=0

x(NX)=1. # the inital value of the ratio at max of profile

# determine initial mus by compare half_width of theory and experiment

call rtbis(ini,x1,xb)

x(1)=x1

#x(1)=1./27

write(1,*)"ini_lt=",1/x(1)

#determine the base ratio

call calc_base(x,base1)

base=base1

write(1,*)"base=",base

n=NX

m=NDATA

iwa=n

lwa=m*n+5*n+m+1000

call lmdif1(fcn1,m,n,x,fvec,tol,info,iwa,wa,lwa)

write(1,*)"info=",info
```

```
#call lmdif1(fcn2,m,n,x,fvec,tol,info,iwa,wa,lwa)
#write(1,*)"info=",info
write(12,*)"lt=", 1/x(1)
write(12,*)"1/la=", x(2)
ratio=x(NX)*base
write(12,*)"ratio=", ratio
mus=c*x(1)/gl(2)
mua=c*x(2)
do i=1,LL { gl(i)=gl(i)*mus}

do i=1, NDATA  {
 t=t_profile(1,i)
 call slab_dens_1d_full(alpha,ld,t,c,mus,mua,gl,r0,rd,s0,nfun_full)
 write(12,*)t, nfun_full*ratio
 }
stop
end
include "head1.h"
subroutine fcn1(m,n,x,fvec,iflag)
real*8 x(NX), fvec(NDATA)
real*8 alpha(2),ld,c,gl(LL),ggl(LL),r0(3),rd(3),s0(2),ratio,base
real*8 t_profile(2,NDATA),den_max,prof_max,dens(2,NDATA)
```

```
real*8 t,dt, nfun_full,mus,mua

integer m,n,iflag,i,max_den,max_prof,id

common /parameter/alpha,ld,c,gl,r0,rd,s0,dt,base,id

common /data/t_profile

mus=c*x(1)/gl(2)

mua=c*x(2)

ratio=x(NX)*base

do i=1,LL { ggl(i)=gl(i)*mus}


# the maximum times in theory and experiment are matched

den_max=0.

prof_max=0.

max_den=0

do i=1, NDATA  {

 if(t_profile(2,i) > prof_max) {

   prof_max=t_profile(2,i)

   max_prof=i

   }

 t=dt*i

 call slab_dens_1d_full(alpha,ld,t,c,mus,mua,ggl,r0,rd,s0,nfun_full)

 dens(1,i)=t

 dens(2,i)=nfun_full
```

```
 if(nfun_full > den_max) {
   den_max=nfun_full
   max_den=i
   }
 }
id=max_prof-max_den
if(id >= 0) {
 do i=1, NDATA-id {
  fvec(i)=dens(2,i)*ratio-t_profile(2,i+id)
  }
 if(id > 0) {
  do i=NDATA-id+1, NDATA  {
    fvec(i)=0.
    }
  }
 }
else  { #id <0
 do i=1, -id {
  fvec(i)=0.
  }
 do i=-id+1, NDATA  {
  fvec(i)=dens(2,i)*ratio-t_profile(2,i+id)
```

```
   }
  }
return
end
include "head1.h"
subroutine fcn2(m,n,x,fvec,iflag)
real*8 x(NX), fvec(NDATA)
real*8 alpha(2),ld,c,gl(LL),ggl(LL),r0(3),rd(3),s0(2),ratio,base
real*8 t_profile(2,NDATA),den_max,prof_max,dens(2,NDATA)
real*8 t,dt, nfun_full,mus,mua
integer m,n,iflag,i,max_den,max_prof,id
common /parameter/alpha,ld,c,gl,r0,rd,s0,dt,base,id
common /data/t_profile
mus=c*x(1)/gl(2)
mua=c*x(2)
ratio=x(NX)*base
do i=1,LL { ggl(i)=gl(i)*mus}
do i=1,NDATA {
  t=dt*i
  call slab_dens_1d_full(alpha,ld,t,c,mus,mua,ggl,r0,rd,s0,nfun_full)
  dens(1,i)=t
  dens(2,i)=nfun_full
```

```
 if(t < 0) fvec(i)=0
 else     fvec(i)=dens(2,i)*ratio-t_profile(2,i)
 }
return
end
# By comparing the half-width of the time profile to determine
# the initial value of mus, assuming initial value mua=0
include "head1.h"
subroutine ini(x,f)
real*8 x,f,t,dt,nfun_full,mus,mua
real*8 alpha(2),ld,c,gl(LL),ggl(LL),r0(3),rd(3),s0(2),base
real*8 t_profile(2,NDATA)
real*8 sum_den,sum_den_one,sum_den_two,den_one,den_two
real*8 sum_pro,sum_pro_one,sum_pro_two,pro_one,pro_two,pro
integer i,id
common /parameter/alpha,ld,c,gl,r0,rd,s0,dt,base,id
common /data/t_profile
mua=0.
mus=c*x/gl(2)
do i=1,LL { ggl(i)=gl(i)*mus}
sum_den=0.
sum_den_one=0.
```

```
sum_den_two=0.
sum_pro=0.
sum_pro_one=0.
sum_pro_two=0.
do i=1, NDATA  {
 t=dt*i
 call slab_dens_1d_full(alpha,ld,t,c,mus,mua,ggl,r0,rd,s0,nfun_full)
 sum_den=sum_den+nfun_full
 sum_den_one=sum_den_one+nfun_full*t
 sum_den_two=sum_den_two+nfun_full*t*t
 t=t_profile(1,i)
 pro=t_profile(2,i)
 sum_pro=sum_pro+pro
 sum_pro_one=sum_pro_one+pro*t
 sum_pro_two=sum_pro_two+pro*t*t
 }
den_one=sum_den_one/sum_den              #average time
den_two=(sum_den_two/sum_den)**2-den_one**2  #half_width
pro_one=sum_pro_one/sum_pro              #average time
pro_two=(sum_pro_two/sum_pro)**2-pro_one**2  #half_width
f=pro_two - den_two
return
```

```
end
include "head1.h"
subroutine rtbis(ini,x,xb)
real*8 x,xb(2),f1,f2,f,dx,xmid,fmid
integer jmax,j
external ini
jmax=30
call ini(xb(1),f1)
call ini(xb(2),f2)
while(f1*f2 > 0) {
if(f1<0)  {
 x=xb(1)
 dx=xb(2)-xb(1)
 }
else  {
 x=xb(2)
 dx=xb(1)-xb(2)
 }
do j=1,jmax {
 dx=dx*0.5
 xmid=x+dx
 call ini(xmid,fmid)
```

```
 if(fmid<0) x=xmid
 }
return
end

include "head1.h"
subroutine calc_base(x,base1)
real*8 x(NX), base1,t,dt
real*8 alpha(2),ld,c,gl(LL),ggl(LL),r0(3),rd(3),s0(2),base
real*8 t_profile(2,NDATA), den_max, prof_max,mus,mua,nfun_full
integer i,id
common /parameter/alpha,ld,c,gl,r0,rd,s0,dt,base,id
common /data/t_profile
mus=c*x(1)/gl(2)
mua=c*x(2)
do i=1,LL {ggl(i)=gl(i)*mus}
# the maximum times in theory and experiment are matched
den_max=0.
prof_max=0.
do i=1, NDATA  {
 if(t_profile(2,i) > prof_max) {
   prof_max=t_profile(2,i)
```

```
    }
  t=dt*i
  call slab_dens_1d_full(alpha,ld,t,c,mus,mua,ggl,r0,rd,s0,nfun_full)
  if(nfun_full > den_max) {
    den_max=nfun_full
    }
  }
base1=prof_max/den_max
return
end
#density_1d_full.r
#this density includes the ballistic component and scattered component
#this program does not work for g_factor=0, but work if g=0.01
# this program works at distance > 0.3 lt
# for the highly anisotropic case, g=0.9, there is no difference between
# full and scat if distance > 0.5*lt, exp(-5) become very small.
# the program includes para, n_func, semi_nfunc, slab_nfunc
# this program produces the photon density distribution function
# input: t: time
#         mus: the scattering constant
#         mua: the absorption constant
#       gl(LL): input from phase function, (* mus in this program)
```

```
#         r0(3): the source position
#         rd(3): the detector  position
#         s0(2): the source direction
#        ld:   the thickness of a slab:wq
#       alpha: the extrapolated length for different wall
#              calculated by calc_ze
#              accoding to Phys. Rev. 53 p3215 (1996)
# output: nfun: the photon density in an infinite uniform medium
# output: snfun: the photon density in a semi_infinite medium
# output: sb_nfun: the photon density in a slab medium
include "head1.h"
subroutine dens_1d_full(t,c,mus,mua,gl,r0,rd,s0,nfun)
real*8 t,c,mus,mua,gl(LL),r0(3),rd(3),s0(2),rc,dx,dz,nfun
call para(t,c,mus,gl,rc,dx,dz)
call nfunc_1d_full(t,c,mus,mua,gl,r0,rd,s0,rc,dx,dz,nfun)
return
end
include "head1.h"
subroutine semi_dens_1d_full(alpha,t,c,mus,mua,gl,r0,rd,s0,snfun)
real*8 t,c,mus,mua,gl(LL),r0(3),rd(3),s0(2),rc,dx,dz,snfun,alpha(2)
call para(t,c,mus,gl,rc,dx,dz)
call semi_nfunc_1d_full(alpha,t,c,mus,mua,gl,r0,rd,s0,rc,dx,dz,snfun)
```

```
return
end
include "head1.h"
subroutine slab_dens_1d_full(alpha,ld,t,c,mus,mua,gl,r0,rd,s0,sb_nfun)
real*8 ld,t,c,mus,mua,gl(LL),r0(3),rd(3),s0(2),rc,dx,dz,sb_nfun,alpha(2)
call para(t,c,mus,gl,rc,dx,dz)
call slab_nfunc_1d_full(alpha,ld,t,c,mus,mua,gl,r0,rd,s0,rc,dx,dz,sb_nfun)
return
end
include "head1.h"
subroutine nfunc_1d_full(t,c,mus,mua,gl,r0,rd,s0,rc,dx,dz,nfun)
real*8 c,mus,mua,gl(LL),r0(3),rd(3),s0(2)
real*8 t,rr(3),nfun,rc,dz,dx
rr(1)=0
rr(2)=0
rr(3)=rd(3)-r0(3)
if(t< 0.01 ) {
        if(dabs(rr(3)-c*t)<0.01) {
          nfun=dexp(-mua*t)
          }
        else
          nfun=0.
```

```
        }
else {
        nfun=1./dsqrt(4.*PI*dz*c*t)*_
        dexp(-(rr(3)-rc)*(rr(3)-rc)/(4.*dz*c*t) -mua*t)
        }
return
end

include "head1.h"
subroutine semi_nfunc_1d_full(alpha,t,c,mus,mua,gl,r0,rd,s0,rc,dx,dz,snfun)
real*8 t,c,mus,mua,gl(LL),r0(3),rd(3),s0(2),rc,dx,dz
real*8 snfun,nfun1,nfun2,alpha(2),r(3),cs11
#alpha=0.7
call nfunc_1d_full(t,c,mus,mua,gl,r0,rd,s0,rc,dx,dz,nfun1)
cs11=dcos(s0(1)*PI/180)
r(1)=r0(1)
r(2)=r0(2)
r(3)=-r0(3)-2.0*(cs11+alpha(1))*c/gl(2)
call nfunc_1d_full(t,c,mus,mua,gl,r,rd,s0,rc,dx,dz,nfun2)
snfun=nfun1-nfun2
return
end
```

```
include "head1.h"
subroutine slab_nfunc_1d_full(alpha,ld,t,c,mus,mua,gl,r0,rd,s0,rc,dx,dz,sb_nfun)
real*8 ld,t,c,mus,mua,gl(LL),r0(3),rd(3),s0(2),rc,dx,dz,sb_nfun
real*8 ll,r(3),alpha(2),nfun1,nfun2,cs11
integer n
#alpha=0.7
ll=ld+(alpha(1)+alpha(2))*c/gl(2)
r(1)=r0(1)
r(2)=r0(2)
cs11=dcos(s0(1)*PI/180)
sb_nfun=0.
do n=-3,3  {
  r(3)=r0(3)+2*n*ll
  call nfunc_1d_full(t,c,mus,mua,gl,r,rd,s0,rc,dx,dz,nfun1)
  r(3)=-r0(3)-2.0*(cs11+alpha(1))*c/gl(2)+2*n*ll
  call nfunc_1d_full(t,c,mus,mua,gl,r,rd,s0,rc,dx,dz,nfun2)
  sb_nfun=sb_nfun+(nfun1-nfun2)
}
return
end
include "head1.h"
subroutine para(t,c,mus,gl,rc,dx,dz)
```

```
real*8 t,c,gl(LL),mus,rc,dx,dz,davg,f1,f2
f1=(1.-dexp(-gl(2)*t))/gl(2)
f2=(1.-dexp(-gl(3)*t))/gl(3)
rc=c*f1
dz=c/(3.*t)*(t/gl(2)-(3.*gl(2)-gl(3))/(gl(2)*(gl(2)-gl(3)))*f1 _
   +2./(gl(2)-gl(3))*f2 -3./2.*f1*f1)
dx=c/(3.*t)*(t/gl(2)+gl(3)/(gl(2)*(gl(2)-gl(3)))*f1 _
   -1./(gl(2)-gl(3))*f2)
davg=c/(3.*t)*(t/gl(2)-1/gl(2)*f1-f1*f1/2)
   #write(1,*)"t",t,"c",c,"gl",gl(2),gl(3)
   #write(1,*)t*118/(300*1.5), davg*3
return
end
#calc_ze.r for scalar case
# n1(2): the reflective index of scattering medium
# n2(2): the reflective index of wall (i.e. glass)
# n3(2): the reflective index of outside (i.e. air)
# ze(2): extrapolation length ratio (to transport mean free path)
# for both side of a medium
# Formula come from PHYS. REV. E 53 p3215(1996) M.U.Vera & D. J. Durian
#real*8 n1(2),n2(2),n3(2),ze(2)
#n1(1)=1.35
```

```
#n2(1)=1.45
#n3(1)=1.
#n1(2)=1.35
#n2(2)=1
#n3(2)=1
#call calc_ze(n1,n2,n3,ze)
#write(1,*)"ze=",ze(1),ze(2)
#stop
#end
subroutine calc_ze(n1,n2,n3,ze)
real*8 n1(1),n2(2),n3(2),cosi,sini,cosr,sinr,re_par,re_pen,temp
real*8 r12,r23,RR,R2,R1,ze(2)
integer i,j
do j=1,2 {
 R1=0.
 R2=0.
 do i=1,1001 {
  cosi=(i-0.99999)/1000.00002
  sini=dsqrt(1.-cosi*cosi)
  if(dabs(n1(j)-n2(j)) < 1.d-06) r12=0.
  else {
   sinr=sini*n1(j)/n2(j)
```

```
if(sinr > 0.999999999) {
  re_par=1.
  re_pen=1.
  }
else {
  cosr=dsqrt(1.-sinr*sinr)
  re_par=(n2(j)*n2(j)*cosi-n1(j)*n2(j)*cosr)/(n2(j)*n2(j)*cosi+n1(j)*n2(j)*cosr)
  re_pen=(n1(j)*cosi-n2(j)*cosr)/(n1(j)*cosi+n2(j)*cosr)
  }
r12=0.5*(re_par*re_par+re_pen*re_pen)
}
if(dabs(n2(j)-n3(j)) < 1.d-06) r23=0.
else {
 if(n3(j)-n2(j)*sinr < 1.d-06) {
  re_par=1.
  re_pen=1.
  }
 else {
  cosr=dsqrt(1.-sinr*sinr)
  temp=dsqrt(n3(j)*n3(j)-n2(j)*n2(j)*sinr*sinr)
  re_par=(n3(j)*n3(j)*cosr-n2(j)*temp)/(n3(j)*n3(j)*cosr+n2(j)*temp)
  re_pen=(n2(j)*cosr-temp)/(n2(j)*cosr+temp)
```

```
    }
  r23=0.5*(re_par*re_par+re_pen*re_pen)
  }
  RR=(r12+r23-2.*r12*r23)/(1.-r12*r23)
  # write(1,*)"cosi=", cosi," RR=",RR
  if(i==1 && i==1001)  {
    R1=R1+0.5*2.*cosi*RR
    R2=R2+0.5*3.*cosi*cosi*RR
    }
  else {
    R1=R1+2.*cosi*RR
    R2=R2+3.*cosi*cosi*RR
    }
  }
  ze(j)=2*(1.+R2/1000.)/3/(1.-R1/1000.)
}
return
end
```

lmdif1.f

```
c     subroutine lmdif1 is a standard minimization routine, which can be downloaded from
http://www.netlib.org/minpack.
include "head1.h"
```

```
real*8 x(NDATA),y(NDATA),xx(NDATA),yy(NDATA)
real*8 dstak
integer n,i
common /cstak/dstak(10000)
call istkin(10000,4)
open(11, "exp_data")
open(12, "data")
n=NDATA
# read experimental data
do i=1,n  {
 read(11,*) x(i), y(i)
   }
dt=(x(n)-x(1))/(n-1)
do i=1,n  {
 xx(i)=x(1)+dt*(i-1)
 }
call dcspin(x,y,n,xx,yy,n)
do i=1,n {
 write(12,*)xx(i),yy(i)
 }
stop
end
```

Bibliography

Chapter 1

1. A. Ishimaru, Wave propagation and scattering in random media, Vol. 1 and 2, Academic Press, NY , 1978.

2. P. Sheng, Introduction to wave scattering, localization, and mesoscopic phenomena, Academic Press, NY 1995.

3. K. M. Yoo, Feng Liu, and R. R. Alfano, Phy. Rev. Lett. 64, 2647, 1990.

4. B. B. Das, Feng Liu and R. R. Alfano, Rep. Prog. Phys. 60, 227, 1997.

5. Rik H. J. Kop, Pedro de Vries, Rudolf Sprik, and Ad Lagendijk , Phys. Rev. Lett 79, 4369, 1997

6. W. Rudolph; M. Kempe , J. Mod. Opt. 44, 1617, 1997.

7. Luther E. Preuss, A. Edward Profio, Appl. Opt. 28, 2207, 1989.

8. R. R. Alfano, D. Tata, J. Cordero, P. Tomashefsky, F. Lonyo, and M. Alfano, IEEE J. Quantum Electron, Vol. 20, 1507, 1984.

9. E. Solomon and P. Davis, Human anatomy and physiology, CBS college publishing, 1983.

10. L. Wang, P. P. Ho, C. Liu, G. Zhang, R. R. Alfano, Science 253, 769, 1991

11. N. Ometto, Ed. , Analytical Laser Spectroscopy, NY Wiley, 1979.

12. R. R. Alfano and L. L. Shapiro, Physics Today, 28, 7, 1975.

13. R. R. Alfano and S. S. Yao, J. Dent. Res. 60, 120, 1981.

14. K. M. Yoo and R. R. Alfano, Opt. Lett. 15, 320, 1990.

15. B. B. Das, Feng Liu and R. R. Alfano, Rep. Prog. Phys. 60, 235, 1997.

16. F. J. Green, The Sigma-Aldrich Handbook of Stains Dyes and Indicators, Sigma-Aldrich Corporation, 1991.

17. P. S. Anderson, S. Montan, S. Svanberg, IEEE J. Q. E. 23, 1798, 1987.

18. K. M. Yoo, Zhi-Wei Zang, S. A. Ahmed, R. R. Alfano, Opt. Lett. 16, 1252, 1991.

19. Xu, F., Pudavar, H.E.,Prasad, P.N., and Dickensheets, D., Opt. Lett., 24, 1808, 1999.

20. Ying, J., Liu, F., Ho, P.P., and Alfano, R. R., Opt. Lett., 25, 1189, 2000.

21. Michael R. Hee, Joseph A. Izatt, Joseph M. Jacobson, James G. Fujimoto, and Eric A. Swanson, Opt. Lett. 18, 950, 1993.

22. Faming Xu, Haridas E. Pudavar, Paras N. Prasad, and David Dickensheets, Opt. Lett. 24, 1808, 1999.

23. M. Kempe, W. Rudolph, and E. Welsch , J. Opt. Soc. Am. A 13, 46, 1996.

24. T. Wilson and C. J. R. Sheppard, Theory and practice of scanning optical microscopy, Academic, London,1984.

25. T. Wilson, ed., Confocal microscopy, Academic, London, 1991.

26. J. M. Drake and A. Z. Genack, Phys. Rev. Lett. **63**, 259 (1989).

27. Emil Wolf, Opt. Lett. 28, 1078, 2003.

Chapter 2

1. http://www-class.unl.edu/bios201a/spring97/group6/

2. http://www.nku.edu/~dempseyd/SKIN.htm

3. Alberts, D. Bray, J. Lewis, M. Raff, K. Roberts, and J. D. Watson, Molecular biology of the cell, Garland, New York, 1994.

4. Private communication with Prof. Steven Jacques, 2003.

5. http://www.brucerosemanmd.com/id53.htm

6. http://www.upmccancercenters.com/cancer/prostate/dre.html

7. The Cancer Book, Geoffery M. Cooper, Jones and Bartlett Publishers, London, England, 1993.

8. Ackerman's Surgical Pathology, Juan Rosai, V. 2, Mosby Incorporated, 1998.

9. Ramzi S. Cotran, Vinay Kumar, Tucker Collins, Robbins pathology basis of disease, Elsevier Science, 6th edition, 1998.

10. H. C. Van de Hulst, Light scattering by small particles, Dover, New York, 1981.

11. C. F. Bohren and D. R. Huffman, Absorption and scattering of light by small particles, John Wiley and Sons, New York, 1983.

12. A. Ishimaru, Electromagnetic wave propagation radiation and scattering, Prentice-Hall Englewood Cliffs, New Jersey, 1995.

13. S. Chandrasekha, Radiative transfer, Dover, New York, 1960.

14. J. R. Lakowicz, Principles of fluorescence spectroscopy, 1999.

15. Oliver Howarth, Theory of spectroscopy, John Wiley and Sons, 1973.

16. R. Chang, Basic principles of spectroscopy, McGraw-Hill, 1971.

17. Cantor and Schimmel, Biophysical Chemistry, 1990.

18. G. R. Fleming, J. M. Morris and G. W. Robinson, Chem. Phys. 17, 91, 1976.

19. T. J. Chuang and K. B. Eisenthal, J. Chem. Phys. 57, 5094, 1972.

20. T. Tao, Biopolymers 8, 609, 1969.

21. F. J. Perrin, J. Phys. Radium 5, 497, 1934.

22. G. Porter, P. J. Sadkowski and C. T. Tredwell, Chem. Phys. Lett. 49, 416, 1977.

23. J. R. Mourant, J. P. Freyer, A. H. Hielscher, A. A. Eick, D. Shen, and T. M. Johnson, Apl. Opt. 37, 3586, 1998.

24. A. Ishimaru, Wave propagation and scattering in random media, New York, Academic press, 1978.

25. S. T. Flock, B. C. Wilson, and M. S. Ptterson, Med. Phys. 14(5), 835, 1987.

26. B. C. Wilson and S. L. Jacques, IEEE J. Q. Elec. 26 (12), 2186, 1990.

27. M. S. Patterson, B. C. Wilson, and D. R. Wyman, Lasers Med Sci 6, 155, 1991.

28. R. Haskell, L. Svaasand, T. Tsay, T. McAdams, and B. Tromberg, J. Opt. Soc. Am. A 11, 2727, 1994.

29. A. Ishimaru, Appl. Opt. 28, 2210, 1989.

30. K. M. Case and P. F. Zweifel, Linear Transport Theory, Addison-Wisley, Reading, Mass., Sec. 1.3, 1967.

31. J. J. Duderstandt and L. J. Hamilton, Nuclear Reactor Analysis, wiley, New York, 1976.

32. T. Durduran, A.Yodha, B. Chance, and D. Boas, J. Opt. Soc. Am. A14, 3358, 1997.

33. M. Lax, V. Nayaramamurti and R. C. Fulton in Laser Optics of Condense Matters edited by J. L. Birman, H. Z. Cummins, A. A. Kaplyaskii, Plenum, New York, 229, 1987.

34. G. H. Watson, S. L. McCall, P. A. Fleury and K. B. Lyons, Phys. Rev. B, 41, 10947, 1990.

35. X. Zhang and Z. Q. Zhang, Phys. Rev. E66, 016612, 2002.

36. R. Elalounfi, R. Carminati, and J. J. Greffet, J. Opt. A: Pure Appl. Opt. 4, S103, 2002.

37. B. B. Das, Thesis, The City University of New York, 1993.

38. Rik H. J. Kop, Pedro de Vries, Rudolf Sprik, and Ad Lagendijk, Phys. Rev. Lett. 79, 4369, 1997.

39. J. M. Drake and A. Z. Genack, Phys. Rev. Lett. 63, 259, 1989.

40. D. Bicout, C. Brosseau, A. Martinez, and J. Schmitt, Phys. Rev. E. 49, 1767, 1994.

41. D. Bicout and C. Brosseau, J. Phys. I(France) 2, 2047, 1992.

42. A. D. Kim and M. Moscoso, Phys. Rev. E., 64, 26612, 2001.

43. Ming Xu et al. to be published.

44. Parker, C. A., Photoluminescence of solution with application to photochemistry and analytical chemistry, Elsevier pub. Cor., 1968.

45. Alan G. Marshall, Biophysical Chemistry, John Wiley & Sons, 1978.

46. N. H. Schiller, A. Dagen and R. R. Alfano, Optical Spectra 15, 56, 1982.

47. R. R. Alfano, ed. " Biological events probed by ultrafast laser spectroscopy",

Academic press, New York, 1982.

48. Y. Tsuchiya, Quantum Electronic QE-20, 1516, 1984.

49. B. B. Das, Feng Liu, and R. R. Alfano, Rep. Prog. Phys. 60, 235, 1997.

50. Jenkins, FA., White HE., Fundamentals of Optics, New York, McGraw-Hill, 1976.

51. T. Wilson and C. J. R. Sheppard, Theory and practice of scanning optical microscopy, Academic, London,1984.

52. T. Wilson, ed., Confocal Microscopy, Academic, London, 1991.

53. James B. Pawley, ed. "Handbook of biological confocal microscopy", Plenum press, 1995.

Chapter 3

1. T. S. Curry III, J. E. Dowdey, R. C. Murry Jr., in: Christensen's Introduction to the Physics of Diagnostic Radiology, 3rd ed., Lea and Febiger, Philadelphia, 1984.

2. P. S. Anderson, S. Montan, S. Svanberg, IEEE J. Quantum Electron. QE-23, 1787, 1987.

3. K. M. Yoo, Zhi-Wei Zang, S. A. Ahmed, R. R. Alfano, Optics Lett. 16, 1252, 1991.

4. F. J. Green, The Sigma-Aldrich Handbook of Stains Dyes and Indicators, Sigma-Aldrich Corporation, 407, 1991.

5. G. R. Fleming, J. M. Morries and G. W. Robinson, Chemical Physics, 17, 91, 1976.

6. G. Porter, P. J. Sadkowski and C. J. Tredwell, Chem. Phys. 49, 416, 1977.

7. S. G. Demos and R. R. Alfano, Appl. Optics, 36, 150, 1997.

8. J. M. Schmitt, A. H. Gandjbakhele, and R. F. Bonner, Appl. Opt. 31, 6535, 1992.

9. S. G. Demos, W. B. Wang, and R. R. Alfano, Appl. Optics, 37, 792, 1998.

10. K. M. Yoo and R. R. Alfano, Opt. Lett. 15, 320, 1990.

11. D. J. Tindall and P. T. Scardino, "Defeating prostate cancer: Crucial directions for research-Except from the report of the Prostate Cancer Progress Review Group (Review)," Prostate, vol. 38, no. 2, pp. 166-171, 1999.

12. B. B. Das, K. M. Yoo and R. R. Alfano, Opt. Lett. 18, 1002, 1993.

13. F. Liu, K. M. Yoo, and R. R. Alfano, Opt. Lett. 16, 351, 1991.

14. L. Wang, P. P. Ho, C. Liu, G. Zhang, and R. R. Alfano, Science 253, 769, 1991.

15. B. B. Das, Ph. D. Thesis, The City University of New York, 1993.

Chapter 4

1. T. S. Curry III, J. E. Dowdey, R. C. Murry Jr., in: Christensen's Introduction to the Physics of Diagnostic Radiology, 3rd ed., Lea and Febiger, Philadelphia, 1984.

2. F. J. Green, The Sigma-Aldrich Handbook of Stains Dyes and Indicators, Sigma-Aldrich Corporation, 407, 1991.

3. P. S. Anderson, S. Montan, S. Svanberg, IEEE J. Quantum Electron. QE-23, 1787, 1987.

4. K. M. Yoo, Zhi-Wei Zang, S. A. Ahmed, R. R. Alfano, Optics Lett. 16, 1252, 1991.

5. G. Zhang, Ph. D. Thesis, The City University of New York, 2000.

6. L. Wang, P. P. Ho, C. H. Liu, G. Zhang, and R. R. Alfano, Science 253, 769-771, 1991.

7. Eugene Hecht, "Optics", the Second Edition, Addison-Wesley Publishing Company Inc., Chapter 8, 294, 1990.

8. D. J. Tindall and P. T. Scardino, "Defeating prostate cancer: Crucial directions for research-Except from the report of the Prostate Cancer Progress Review Group (Review)," Prostate, vol. 38, no. 2, pp. 166-171, 1999. P. T. Scardino, "Prostate cancer, treatment, and prevention," Newsweek, Nov. 1, 11-12, 1999.

Chapter 5

1. D. J. Tindall and P. T. Scardino, "Defeating prostate cancer: Crucial directions for research-Except from the report of the Prostate Cancer Progress Review Group (Review)," Prostate, vol. 38, no. 2, pp. 166-171, 1999. P. T. Scardino, "Prostate cancer, treatment, and prevention," Newsweek, Nov. 1, 11, 1999.

2. R . R. Alfano, D. Tata, J. Cordero, P. Tomashefsky, F. Lonyo, and M. Alfano, IEEE J. Quantum Electron, Vol. 20, 1507, 1984.

3. Juan Rosai. Ackerman's Surgical Pathology, Vol. 2, Mosby Incorporated, 1998.

4. Gleason DF, Mellinger GT. Prediction of prognosis for prostatic adenocarcinoma by combined histological grading and clinical staging. J. Urol. 111, 58, 1974.

5. A . Szent-Gyorgyi, Bioenergetics, Academic Press, New York, 1957.

6. L . Minkoff and R. Damadian, Physiol. Chem. & Physics 8, 349, 1976.

7. N. Ockman and G. B. Sutherland., Proc. Roy. Soc. Vol. A247, 434, 1958.

8. H. K. Shin., J. Chem. Phys., Vol. 69, 1240, 1978.

9. G. E. Walrafen, J. Chem. Phys., Vol. 44, 1546, 1966.

10. Mark Sceats, Stuart A. Rice, and J. E. Butler., J. Chem. Phys., Vol. 63, 5390, 1975.

11. C . Hazlewood, and B. Nicholas, Nature, Vol. 222, 747, 1969.

12. J . Tang, F. Zeng, J. Evans, B. Xu, H. Savage, P. P. Ho, and R. R. Alfano, J. Clin. Laser Med. Surg., Vol. 18, 117, 2000.

13. R . R. Alfano, B. B. Das, J. Cleary, R.Prudente, and E. Celmer, Bull. N. Y. Acad. Med., Vol. 67, 143, 1991.

14. C . H. Liu, B. B. Das, W. L. Sha Glassman, G. C. Tang, K. M. Yoo, H. R. Zhu, D. L. Akins, S. S. Lubicz, J. Cleary, R. Prudente, E. Celmer, A. Caron, and R. R. Alfano, J. Photochem. Photobiol., Vol. 1887, 188, 1992.

15. W .B. Wang, J. H. Ali, J. M. Vitenson, J. M. Lombardo, and R. R. Alfano, SPIE, Vol. 3917, 75, 2000.

16. W. B. Wang, J. H. Ali, M. Zevallos, and R. R. Alfano. Near infrared imaging of human prostate cancerous and normal tissues based on water absorption, in OSA Biomedical Optics Topical Meetings on CD-ROM (The Optical Society of American, Washington, DC), MF 38, 2004.

17. Dudley Williams, Nature Vol. 210, 194, 1966.

18. Fay A. Marks, Frontiers in Bioscience Vol. 3, a1-10, 1998.

19. V. Backman, R. Gurjar, K. Badizadegan, I. Itzkan, R. Dasari, L. Perelman, and M. Feld, IEEE J. Select. Topics Q. E.,Vol. 5, 1019, 1999.

20. S . K. Gayen and R. R. Alfano, Optics Express, Vol. 4, No. 11, 475, 1999.

21. Y . Shao, A. Maximov, I. Ourdev, W. Rozmus, and C. Capjack, IEEE J. Q. E., Vol. 37, 617, 2001.

22. S. A. Prahl, PhD thesis, University of Texas at Austin, 1988.

23. Private communication with Prof. Steven Jacques, 2003.

24. A. Dunn, and R. Richards-Kortum, IEEE J. Q. E. , Vol. 2, 898, 1996.

25. D. Bicout, C. Brosseau, A. S. Martinez, and J. M. Schmitt Phys. Rev. E 49, 1767, 1994.

Chapter 6

1. M. Lax, V. Nayaramamurti, and R. C. Fulton, in proceedings of the symposium on laser optics of condensed matter, Leningrad, June 1987, edited by J. L. Birman, H. Z. Cummins, and A. A. Kaplyanskii, Plenum, New York, 1987.

2. E. Akkermans, P. E. Wolf, and R. Maynard, Phys. Rev. Lett. 56, 1471, 1986.

3. D. A. Weitz, D. J. Pine, P. N. Pusey, and R. J. A. Tough, Phys. Rev. Lett. 63, 1747, 1989.

4. L. Wang, P. P. Ho, C. Liu, G. Zhang, and R. R. Alfano, Science 253, 769, 1991.

5. K. M. Yoo and R. R. Alfano, Opt. Lett. 15, 320, 1990.

6. K. M. Yoo, Feng Liu, and R. R. Alfano, Phys. Rev. Lett. 64, 2647, 1990.

7. K. M. Yoo, B. B.Das, and R. R. Alfano, Opt. Lett. 64, 17, 958, 1990.

8. Rik H. J. Kop, Pedro de Vries, Rudolf Sprik, and Ad Lagendijk, Phys. Rev. Lett. 79, 4369, 1997.

9. J. M. Drake and A. Z. Genack, Phys. Rev. Lett. 63, 259, 1989.

10. M. Xu, W. Cai, M. Lax, and R. R. Alfano, Phys. Rev. E. 65, 066609, 2002.

11. J.Ali, M. Xu, W. Cai, to be published.

12. W. Cai, M. Lax, and R. R. Alfano, Phys. Rev. Lett. 61, 3871, 2000.

13. W. Cai, M. Lax, and R. R. Alfano, J. Phys. Chem. B 104, 3996, 2000.

14. B. Tiggelen, Ad Lagendijk, M. Albada, and A. Tip, Phys. Rev. B. 45, 12233, 1992.

15. K. M. Yoo and R. R. Alfano, Phys. Lett. A, 142, 531, 1989.

16. J. M. Schmitt, A. H. Gandjbakhche, and R. F. Bonner, Appl. Opt. 31, 6535, 1992.

17. Emil Wolf, Opt. Lett. 28, 1078, 2003.

18. M. Kempe, A. Z. Genack, W. Rudolph, P. Dorn, J. Opt. Soc. Am. 14, 216, 1997.

19. Michael R. Hee, Joseph A. Izatt, Joseph M. Jacobson, James G. Fujimoto, and Eric Swanson, Opt. Lett. 18, 950, 1993.

20. M. Kempe, A. Z. Genack, W. Rudolph and P. Dorn, J. Opt. Soc. Am. A 14, 216, 1997.

21. B. B. Das, K. M. Yoo, and R. R. Alfano, Opt. Lett 18, 1092, 1993.

22. S. G. Demos and R. R. Alfano, Opt. Lett 21, 161, 1996.

23. J. Ying, F. Liu, P. P. Ho, and R. R. Alfano, Opt. Lett. 25, 1189, 2000.

24. Y. Guo, P. Ho, F. Liu, R. Alfano, Optics Comm. 154, 383, 1998.

25. H. Cao, J. Xu, Y. Ling, A. Burin,E. Seeling, X. Liu, and R. Chang, IEEE Journal of Selected Topics in Quantum Electronics 9, 111, 2003.

26. M. Born and E. Wolf, Principles of Optics, Cambridge University Press, Cambridge, 1999.

27. M. Beran and G. Parrent, Theory of Partial Coherence, Prentice Hall, 1964.

28. K. M. Yoo, Ph. D. Thesis, The City university of New York, 1990.

29. J. X. Zhu, D. J. Pine, and D. A. Weitz, Phys. Rev. A 44, 3948, 1991.

30. D. Bicout, C. Brosseau, A. S. Martinez, and J. M. Schmitt Phys. Rev. E 49, 1767, 1994.

31. A. D. Kim and M. Moscoso, Phys. Rev. E 64, 26612, 2001.

32. Min Xu et al. private communication.

33. Grant R. Fowles, Introduction to Modern Optics, Holt, Rinehart, and Winston, 1975.

Chapter 7

1. M. Fontana, Corrosion Engineering, McGraw-Hill, New York, 1986.

2. Paul E. Mix, P. E., Introduction to Nondestructive Testing, John Wiley and Sons, 1987.

3. D. Liu. F. Wang, Ch. Cao, L. Zhang, and H Lin, Corrosion 46, 975, 1990.

4. Michel de Billy, Frederic Cohen-Tenoudji, Alain Jungman, and Gerard J. Quentin, IEEE Transactions on Sonics and Ultrasonics 5, 356, 1976.

5. Benoit Mandelbrot, Dann Passoja and Alvin Paullay, Nature 308, 721, 1984.

6. M. Stratmann and H. Streckel, Corrosion Science 30, 681, 1990.

7. L. Wang, P. P. Ho, C. Liu, G. Zhang, R. R. Alfano, Science 253, 769, 1991.

8. S. G. Demos, W. B. Wang, J. H. Ali, and R. R. Alfano, OSA TOPS 21, 405, 1998.

9. W. B. Wang, S. G. Demos, J. H. Ali, G. Zhang, and R. R. Alfano, Optics Communications 147, 11, 1998.

10. C. Weiping and Xu Chenghui, Journal of Material Science Letters 16, 113, 1997.

11. S. J.Williamson and H. Z. Cummins, Light and Color in Nature and Art, John Wiley and Sons, USA, 1983.

12. W. B. Wang, J. H. Ali, J. H. Vitenson, J. M. Lombardo, and R. R. Alfano, Technical Program of the SPIE BIOS 2000 Meeting, San Jose, CA, Jan. 22-28, 51, 2000.

13. J. Ying, F. Liu, P. P. Ho, and R. R. Alfano, Opt. Lett. "Nondestructive evaluation of incipient corrosion in a metal beneath paint by second-harmonic tomography", Opt. Lett., 25, 1189, 2000.

13. J. H. Ali, W. B. Wang, P. P. Ho, and R. R. Alfano, Opt. Lett. 'Detection of corrosion beneath a paint layer by use of spectral polarization optical imaging', Opt. Lett.25, 1303, 2000.

14. F. Xu, H. E. Pudavar, P. N. Prasad and D. Dickensheets, 'Confocal enhanced optical

coherence tomography for nondestructive evaluation of paints and coatings', Opt. Lett.,24, 808, 1999.

15. M. Kempe, W. Rudolph, and E. Welsh, J. Opt. Soc. Am. A 'Comparative study of confocal and heterodyne microscopy for imaging through scattering media' 13, 46, 1996.

Chapter 8

1. R. Loudon, The Quantum Theory of Light, first edition, Oxford, 1973.
2. Ping Sheng ed., Scattering and Locatisation of Classical Waves in Random Media, World Scientific, Singapore, 1990.
3. T. M. Nieuwenhuizen, A. Lagendijk, and B.A. van Tiggelen, Phys. Lett. A. 169, 191, 1992.
4. B.A. van Tiggelen, A. Lagendijk, M.P. van Albada and A.Tip, Phys. Rev. B 45, 12233, 1992.
5. P. Kittle, Patent # 4034129, Methods for forming an inorganic thermal radiation control, Philadelphia, PA, 1977.
6. K. Nassau, The physics and chemistry of color, John Wiley & Sons, USA, 1983.
7. J. I. Pankove , Optical processes in semiconductors, Dover publications, New York, 1971.